Analysis of Tilt-to-Length Coupling in the GRACE Follow-On Laser Ranging Interferometer

Von der QUEST-Leibniz-Forschungsschule der Gottfried Wilhelm
Leibniz Universität Hannover
zur Erlangung des Grades

Doktor der Naturwissenschaften
– Dr. rer. nat. –

genehmigte Dissertation von

M. Sc. Henry Wegener

2022

Abstract

GRACE Follow-On (GFO), launched in May 2018, is the nearly identical successor of the Gravity Recovery and Climate Experiment (GRACE) mission, which was in operation from 2002 until 2017. Both missions consist of two satellites in a low Earth orbit (LEO), with the goal of measuring the Earth's gravity field with a special focus on its temporal variations. The essential observable for this purpose is the inter-satellite range-rate, measured by the so-called K/Ka-band ranging (KBR) instrument. In addition to the established KBR instrument, GFO carries a laser interferometer named laser ranging interferometer (LRI) as a technology demonstrator, to measure the same observable. One important noise source of the LRI at low frequencies is the so-called tilt-to-length (TTL) coupling, caused by unavoidable deviations from the nominal satellite attitudes with respect to each other. The main motivation of the work presented here is to analyze the LRI TTL error with in-flight data, in order to generate a deeper understanding of the LRI as well as comparable future laser interferometers.

In this thesis, the different stages in the large context of LRI TTL analysis are illuminated. As a basis, a mathematical formalism for the description, sensing, and control of spacecraft (S/C) attitude is given. Then, a linear TTL coupling model for the LRI is derived as a function of the inter-satellite pointing angles. The model parameters are estimated by utilizing GFO data recorded during the so-called center-of-mass calibration (CMC) maneuvers. These are S/C rotation maneuvers which provide a stimulus to evoke a TTL error, although their original purpose is unrelated to the LRI. Several parameter estimation methods are scrutinized, the respective mathematical formulas are derived, and the potential of each individual approach is evaluated. Finally, the results of the LRI TTL estimations are presented in the form of linear coupling factors, all of which fulfill the pre-launch requirements.

Moreover, the linear coupling factors contain information about the spatial offsets between the satellites' centers-of-mass (CoM) and the LRI reference points (RP). Estimations of nadir and cross-track components of these offsets are derived in this thesis. This provides an independent method to track the CoM movement over time. Furthermore, during the study presented here, another error source of the LRI was discovered, which is here denoted by angular rate coupling (ARC). While the TTL error term is a function of the attitude deviation, ARC is a function of the rate of change of this attitude deviation. It is therefore relevant for the analysis of TTL coupling. A theoretical explanation of the ARC effect is given here, as well as a formula to compute the ARC error term. This formula is confirmed by analyzing CMC maneuver data.

This thesis is also intended as a detailed guide to TTL mitigation in inter-satellite laser interferometers in general, with emphasis on the utilization of S/C rotation maneuvers. To this end, a technique to simulate satellite rotation maneuvers is developed. The design of dedicated TTL calibration maneuvers is investigated, starting by defining the relevant parameters that determine such a maneuver. A method is developed to assess the suitability of an arbitrary maneuver for the purpose of TTL estimation. Thereupon, the maneuver parameters are optimized for the case of the LRI. Furthermore, some simulated rotation maneuvers are highlighted, and their performance with regard to TTL estimation is compared to the performance of the CMC maneuvers.

Keywords: GRACE Follow-On, Laser Ranging Interferometer, Tilt-to-Length Coupling

Zusammenfassung

GRACE Follow-On (GFO), gestartet im Mai 2018, ist die nahezu baugleiche Nachfolgemission zur Mission Gravity Recovery and Climate Experiment (GRACE), im Betrieb von 2002 bis 2017. Beide Missionen bestehen aus zwei Satelliten in einem niedrigen Erdorbit, mit dem Ziel der Messung des Erdschwerefeldes mit besonderem Fokus auf dessen zeitlichen Variationen. Die wesentliche Messgröße zu diesem Zweck ist die Änderungsrate des Abstands der Satelliten voneinander, gemessen vom sogenannten K/Ka-band ranging (KBR) Instrument. Zusätzlich zum etablierten KBR Instrument ist in die GFO Satelliten ein Laserinterferometer integriert, genannt laser ranging interferometer (LRI), welches als Technologiedemonstrator ebenfalls die Abstandsänderungen misst. Eine wichtige Rauschquelle des LRI bei niedrigen Frequenzen ist die sogenannte tilt-to-length (TTL) Kopplung, hervorgerufen durch unvermeidbare Abweichungen von der nominellen Ausrichtungen der Satelliten zueinander. Die Hauptmotivation der hier präsentierten Arbeit ist die Analyse des LRI TTL Fehlers mittels der gemessenen Daten, um ein tieferes Verständnis des LRI sowie vergleichbarer zukünftiger Laserinterferometer zu generieren.

In dieser Doktorarbeit werden die verschiedenen Schritte im Zusammenhang mit der LRI TTL Analyse beleuchtet. Als Grundlage wird ein mathematischer Formalismus zur Beschreibung, Messung und Kontrolle der Satellitenorientierung gegeben. Darauffolgend wird ein lineares Kopplungsmodell für das LRI hergeleitet, als Funktion der Eulerwinkel, welche die Orientierungsabweichungen der Satelliten beschreiben. Die Modellparameter werden geschätzt unter Nutzung von GFO Daten, welche während der sogenannten center-of-mass calibration (CMC) Manöver aufgezeichnet wurden. Dies sind Satellitenrotationsmanöver, welche einen Stimulus liefern können um einen TTL Fehler hervorzurufen, wenngleich der ursprüngliche Zweck der CMC Manöver unabhängig vom LRI ist. Etliche Methoden zur Parameterschätzung werden eingehend untersucht, die jeweiligen mathematischen Formeln werden hergeleitet, und das Potenzial der einzelnen Ansätze wird individuell ausgewertet. Zuletzt werden die Ergebnisse der LRI TTL Parameterschätzung präsentiert, in Form von linearen Kopplungsfaktoren, welche allesamt innerhalb der Missionsanforderungen liegen.

Im Weiteren enthalten die linearen Kopplungsfaktoren Informationen über die räumlichen Versätze zwischen den Masseschwerpunkten der Satelliten und den Referenzpunkten des LRI. Schätzungen der Komponenten in Nadirrichtung sowie seitwärts senkrecht zur Flugrichtung dieser räumlichen Versätze werden in dieser Arbeit hergeleitet. Dies liefert eine unabhängige Methode, die zeitliche Verschiebung der Masseschwerpunkte zu verfolgen. Ferner wurde während der hier dargestellten Untersuchung eine weitere Fehlerquelle des LRI entdeckt, welche hier angular rate coupling (ARC) genannt wird. Während der TTL Fehlerterm eine Funktion der Orientierungsabweichungen ist, ist der ARC Fehlerterm eine Funktion der Änderungsrate dieser Abweichungen. ARC ist daher auch relevant für die Analyse der TTL Kopplung. Für diesen Effekt wird hier eine theoretische Erklärung geliefert, sowie eine Formel zur Berechnung des ARC Fehlerterms. Diese Formel wird durch die Analyse von CMC Manöverdaten bestätigt.

Diese Arbeit ist ebenfalls als detaillierte Anleitung zur Mitigation von TTL Kopplung in LRI-ähnlichen Laserinterferometern im Allgemeinen gedacht, mit besonderem Schwerpunkt auf der Nutzung von Rotationsmanövern. Zu diesem Zweck wird eine Technik zur Simulation solcher Manöver entwickelt. Die Gestaltung dedizierter TTL Kalibrierungsmanöver wird untersucht, beginnend mit der Definition der relevanten Parameter, welche ein solches Manöver festlegen. Es wird eine Methode entwickelt, um die Eignung eines beliebigen Manövers hinsichtlich der TTL Parameterschätzung zu bewerten. Daraufhin werden die Manöverparameter für den Fall des LRI optimiert. Des Weiteren werden einige simulierte Manöver hervorgehoben und ihre Eignung für die TTL Analyse mit der Eignung der CMC Manöver verglichen.

Contents

Acronyms

ACC accelerometer.

ACS attitude control system.

AEI Albert Einstein Institute.

AF accelerometer frame.

AOC antenna offset correction.

AOCS attitude and orbit control system.

APC antenna phase center.

ARC angular rate coupling.

AS amplitude spectrum.

ASD amplitude spectral density.

ATD atmospheric drag.

BS beam splitter.

CESS coarse Earth and Sun sensors.

CF coupling factor.

CMC center-of-mass calibration.

CoM center-of-mass.

CP compensation plate.

DLN differential linear non-gravitational.

DWS differential wavefront sensing.

ECEF Earth-centered Earth-fixed.

ECI Earth-centered inertial.

EGM08 Earth Gravitational Model 2008.

FSM fast steering mirror.

GF1 GFO satellite 1.

GF2 GFO satellite 2.

GFO GRACE Follow-On.

GFR gravity field recovery.

GFZ Deutsches GeoForschungsZentrum.

GPS Global Positioning System.

GRACE Gravity Recovery and Climate Experiment.

IERS International Earth Rotation and Reference Systems Service.

IGRF12 International Geomagnetic Reference Field (12$^{\text{th}}$ generation).

IMU inertial measurement unit.

ITRS International Terrestrial Reference System.

JPL Jet Propulsion Laboratory.

KBR K/Ka-band ranging.

KF K-frame.

LEO low Earth orbit.

LFN laser frequency noise.

LISA Laser Interferometer Space Antenna.

LLA latitude, longitude, altitude.

LoS line-of-sight.

LOSF line-of-sight frame.

LPF LISA Pathfinder.

LRI laser ranging interferometer.

LRP laser ranging processor.

LSQ least squares.

LTPDA LISA Technology Package Data Analysis.

MAP maximum a posteriori.

MDM magnetic dipole moment.

MoI moment of inertia.

MTR magnetic torque rod.

NASA National Aeronautics and Space Administration.

NED north-east-down.

NGGM Next Generation Gravity Mission.

NSF noise shape function.

OBA optical bench assembly.

OBE optical bench electronics.

PCHIP piecewise cubic hermite interpolating polynomial.

PDF probability density function.

QPD quadrant photodiode.

RMS root mean square.

RP reference point.

S/C spacecraft.

SCA star camera assembly.

SDS Science Data System.

SF satellite frame.

SH spherical harmonic.

SRF science reference frame.

SRP solar radiation pressure.

SST satellite-to-satellite tracking.

STD standard deviation.

TDI time delay interferometry.

TMA triple mirror assembly.

TTL tilt-to-length.

VP vertex point.

ZARM Zentrum für Angewandte Raumfahrttechnologie und Mikrogravitation.

Chapter 1

Introduction

1.1 Topic of study

The climate change may be the greatest challenge of humankind in the 21$^{\text{st}}$ century. Hence, it is more urgent than ever for us to study the climate system of our planet, the Earth. An important contribution to this is made by the field of geodesy, which, in particular, examines the Earth's gravitational field and its temporal variations. During the past decades, a novel branch has been developing, the satellite geodesy, which is utilizing the steadily growing amount of satellite observation data.

An overview of satellite geodesy missions is provided on the website of the Global Geodetic Observing System (GGOS) [GI], which is the observing system of the International Association of Geodesy (IAG). A well established method is to deploy satellites as small mass test objects, whose motion is mainly determined by the mass of the Earth and the gravitational law. By tracking the distance between a satellite and either a ground station or another satellite, the satellite's motion is measured precisely. From the data gathered in this way, often in combination with Global Navigation Satellite System (GNSS) measurements, information about the Earth's gravitational field can be inferred, and thus about the mass distribution in the Earth system. Observing time variations thereof is considered one of the most important measurements for the National Aeronautics and Space Administration (NASA) to obtain during this decade [NAS18].

This thesis focuses on science data from the mission called GRACE Follow-On (GFO) [Kor+19], which is the successor mission of the Gravity Recovery and Climate Experiment (GRACE) mission [Tap+04b; Tap+04a; Wou+14; Tap+19]. The principle that underlies these missions has been described already in [Wol69]. Like GRACE, GFO has been very successful in measuring the Earth's gravitational field. It consists of two basically identical spacecraft (S/C), orbiting in an almost circular low Earth orbit (LEO) about 500 km above ground, with an inclination of 89 °. While one S/C is trailing the other at a varying distance of 220 ± 50 km, the biased range between the two is measured using a K/Ka-band ranging (KBR) instrument [KL09]. Here the term biased range means the separation between the two satellites' centers-of-mass (CoM), measured up to a constant, i.e. with an unknown bias. Once the surface of the Earth is sampled well enough by the satellite ground track, after about one month, an Earth gravity model is fitted to the data obtained from these observations. Comparing the results of this process, which is called gravity field recovery (GFR), of many subsequent months enables a detailed study of the time variability of the Earth's gravitational field. The temporal and spatial resolution of GRACE-derived gravity fields is a matter of discussion [VDS18], and a matter of tradeoff between temporal and spatial accuracy, however, about 1 month temporal and 200-300 km spatial resolution may serve as approximate values.

1.1.1 Applications of GRACE / GFO data

Applications of the GRACE mission, which has been in operation and recording data from 2002 until 2017, are manifold and of great importance. To mention a few, these applications include the monitoring of ice sheet and glacier mass balance, terrestrial water storage, and sea level change. Recent overviews of the contributions of the GRACE science data to climate change research are given in [Wou+14] and [Tap+19]. A comprehensive list of GRACE and GFO related publications is provided in [FK], counting more than 2500 references. Several of these were cited in the 2013 Fifth Assessment Report of the International Panel on Climate Change (IPCC-5)[Cli14], due to their tremendous impact in the field of climate research. Rodell et al. have listed and quantified 34 regional trends of terrestrial water storage, distributed all over the Earth, e.g. the decline of the Aral Sea and the Caspian Sea [Rod+18]. GRACE / GFO data is also the basis for the European Gravity Service for Improved Emergency Management (EGSIEM) project, currently in the prototype phase [Jäg+19]. In the following, three examples are presented which shall demonstrate the wide range of GRACE applications, their importance, as well as the essentiality of continuing these measurements and improving upon their accuracy and precision.

Example 1 The availability of fresh water is a crucial basis for human civilization. Unfortunately, this basis is threatened in many regions, where aquifers diminish, often caused by unsustainable groundwater consumption [Fam14]. For instance, southern California, USA, is facing a historical drought, as the groundwater storage cannot replenish at nearly the same rate at which it is being withdrawn, mostly due to the high agricultural demands [SLL12; Rod+18]. The groundwater depletion in India is studied for example in [RVF09], where it could be shown that, during the period of August 2002 to October 2008, groundwater equivalent to a net amount of 109 km^3 was lost, over the Indian states of Rajasthan, Punjab, and Haryana. An anthropogenic cause of this observation is likely, and it was concluded that there may be severe consequences for the respective regions in India, unless appropriate measures are taken soon. Notably, only part of the terrestrial water storage can be monitored by means other than GRACE data, so that satellite geodesy can be expected to be indispensable in the future for similar applications.

Example 2 The monitoring of ice mass loss near the poles may be one of the most prominent applications of the GRACE data. Both Greenland and Antarctica ice mass balances showed a significant negative trend already after a few years of GRACE mission operation [VW05; VW06], which unfortunately continued in an undamped way [Vel09]. Due to the high quality satellite data, very consistently provided over a time span of 15 years, scientists understanding of these mass changes has considerably increased. The consistency of data from the GFO mission has been demonstrated [Vel+20], revealing for example a dramatic loss of 600 Gt of Greenland ice within the record-breaking summer of 2019. From 2002 until 2017, the average annual balance of Greenland mass was determined to be -258 ± 26 Gt yr^{-1}, and the respective value for Antarctica was determined to be -137 ± 41 Gt yr^{-1}. For comparison, note the average mass loss of the glaciers and ice caps of the Earth of about 280 Gt yr^{-1} [CVS20], which is also an alarming value. A portion of about 200 Gt yr^{-1} could be linked to glacier mass loss alone [WGM19].

A spatial resolution of 200 km enables a regional breakdown of the mass balance. With a temporal resolution of 1 month, seasonal variations are also well resolved. This even allows for a more detailed analysis of the different causes of certain mass changes [Tap+19]. Furthermore, a strong correlation between the Antarctic ice mass balance, the precipitation there, and the ocean-atmosphere phenomenon La Niña, which is the colder counterpart of El Niño, could be shown in [Sas+10]. The importance of the ice sheets at the poles for the climate of the entire Earth is undisputed.

Example 3   Earthquakes permanently change the mass distribution within the Earth, and hence can in principle be measured by gravimetric missions such as GRACE / GFO. One of the most devastating earthquakes in the past decades was the 2004 Sumatra-Andaman earthquake, with a moment magnitude $M_w > 9$. This event produced a crustal dilatation of a strength which is readily detectable by GRACE [Han+06]. An analysis of the seven largest earthquakes during the era of GRACE, between 2002 and 2017, is presented in [CL19]. The permanent solid Earth mass change caused by the 2011 Tohoku-Oki earthquake was examined using GRACE data in [Wan+12]. With temporally and spatially better resolved gravity fields, in the future, even more valuable studies of such seismic events will become feasible, aspiring towards the ambitious goal of real-time earthquake monitoring.

1.1.2   GRACE Follow-On and the LRI

In order to continue the valuable measurements of GRACE, a successor mission named GFO has been brought to life [Kor+19]. The continuation of science output in the form of gravity fields from GFO, qualitatively comparable to GRACE-derived gravity fields, has already been demonstrated [Lan+20; Che+21; Pei+22]. The GFO satellites are quasi replica of the GRACE satellites, except for some minor improvements. The single big novelty aboard the GFO satellites is the laser ranging interferometer (LRI), with the purpose of demonstrating an innovative satellite-to-satellite tracking (SST) technique [Abi+19; She+12]. The LRI measures the biased inter-satellite range, as does the KBR, and both instruments are operated independently in the GFO mission. By means of laser interferometry, the LRI is able to reach unprecedented SST precision.

The GFO satellites have been launched with a SpaceX Falcon 9 rocket from the Vandenberg Airforce Base in California, USA, on 22 May 2018. The twin satellites were deployed at an altitude of 491 km, and with an orbit inclination of 89 °. The launch and early operations phase (LEOP), during which the satellites were maneuvered into their nominal constellation, 220 km apart, see also [Sch+15a], lasted until 26 May. The in-orbit commissioning (IOC) phase followed, where, after all LRI subsystems were checked out, the laser link acquisition procedure was carried out, which is described in [Mah14; Koc+18]. On 14 June 2018, the interferometric link was established on first attempt, and the LRI started to measure the inter-satellite biased range [Abi+19; Weg19]. The in-orbit commissioning phase ended on 28 January 2019, heralding the mission's science phase.

A public homepage maintained by NASA / JPL provides plenty of interesting information, figures and links concerning the satellites, the mission, as well as climate research applications [JPL]. In particular, the homepage provides a downloadable 3D model of the satellites. Regular newsletters with GFO related news are made public via [Lan+]. These newsletters provide science related updates including detailed reports on mission operations and data availability.

1.1.3   LRI tilt-to-length coupling

The precision of the biased range measured by the LRI is limited at high frequencies by the laser frequency noise (LFN), down to less than 1 nm/$\sqrt{\text{Hz}}$ for Fourier frequencies above 200 mHz. The frequency of the LRI laser is stabilized by an optical cavity. Since the LRI measures distance variations via the Doppler shift due to the relative motion of the two S/C, laser frequency jitter couples into the beatnote measurement of the interferometer. A posteriori, the LFN in the LRI data cannot be mitigated further. In the Laser Interferometer Space Antenna (LISA) mission, so-called time delay interferometry (TDI) will be used, which suppresses laser frequency noise to a large extent, by linearly combining independent time-shifted Doppler measurements in a certain way [TD20]. For future satellite geodesy missions with multi-satellite formations, TDI may be utilized as well [Con+21].

Apart from the LFN, the other main noise source of the LRI is the so-called tilt-to-length

(TTL) coupling, caused by S/C attitude jitter which couples into the measured range. It is expected to limit the LRI accuracy at frequencies below 20 mHz. As opposed to the LFN, the TTL coupling can in principle be estimated and subtracted from the measurements in post-processing. The topic of study examined in this thesis is the error in the GFO LRI measurements due to TTL coupling. This includes the investigation of

- the contribution of TTL coupling to the total LRI ranging error

- the different effects that cause TTL coupling in the LRI

- ways of mitigating TTL coupling in post-processing, in particular by utilizing satellite rotation maneuvers

In the following, an overview of the state of the art of this topic of study is presented, as well as directly related topics.

1.2   State of the art

With the LRI, for the first time, distance variations between two satellites in space are being measured using laser interferometry. Since the LRI is the first instrument of its kind, there exist no in-situ studies of TTL coupling in inter-satellite laser interferometers yet. Thus, an overview of the theoretical and experimental investigations about LRI TTL coupling is given here, in Sec. 1.2, which have been carried out on ground prior to the launch of GFO. Besides, some studies on adjacent subjects are highlighted, beginning with a recapitulation of the general LRI performance and its contribution to geodesy up to now. Afterwards, an outline of pre-flight studies on LRI TTL coupling is given. The focus in the last part of this section lies on satellite rotation maneuvers, which can be utilized to estimate TTL coupling.

1.2.1   LRI performance and its scientific meaning

Since the LRI started to collect data, it has proven to be able to measure the same observable as the KBR instrument, with lower noise at least at high frequencies. The ranging data contains occasional phase jumps, which are modeled and subtracted, so that they do not influence the performance of the instrument [Abi+19]. A first unpublished description of the phase jump modeling was given in [Hei18]. In addition to the biased range, the LRI measures pitch and yaw angles of the S/C with high precision, using the differential wavefront sensing (DWS) technique and a fast steering mirror (FSM), demonstrating its usefulness, not only for keeping the interferometer aligned, but also for attitude determination. Furthermore, the LRI has shown that it can take measurements for many orbits without interruption. From June 2018 to May 2020, there have been 10 distinct periods during which the LRI was switched off for longer than a day. Merely two of these downtimes were longer than 8 days, and those were due to reasons unrelated to the LRI. By the time of writing, some working groups produce gravity fields using LRI data on a regular basis. The gravity fields that have been derived from LRI data achieve at least the same accuracy as those derived from KBR data [Lan+20]. Hence, it is likely that future satellite geodesy missions will utilize laser interferometry as the primary SST technique, which the LRI was designed to demonstrate.

Although the LRI range has significantly lower noise than the KBR range, the improvement in terms of the quality of gravity fields is at the moment still marginal, which does not come unexpected [Fle+16]. There may be further improvements to come, after gaining more experience with the LRI data, which is still new to the community. After all, each instrument poses its own challenges for data processing. Regardless of that, the accuracy of GFR is currently mostly limited by factors other than the ranging precision. This is the main reason for the low amount of improvement from KBR to LRI. For future satellite geodesy missions which are based on SST, this is likely going to change.

For instance, short term mass variations in the atmosphere or the oceans are undersampled by the satellite measurements. Hence, such high frequency signals become indistinguishable from lower frequency components, an effect called temporal aliasing. This is one of the most challenging error sources in the processing of GRACE and GFO data. Scientists attempt to dealias the data, for example using the AOD1B data product [Dob+13; Fle15]. There are limitations e.g. due to uncertainties in the available atmospheric data, which the AOD1B product is based on. Possible paths towards mitigating aliasing in future geodesy missions are investigated for example in [Dob+16] and [DP17].

Another major error source for GFR is the performance of the accelerometers at low frequencies. The GFO satellites are equipped with improved versions of the Super STAR (Space Three-axis Accelerometer for Research) accelerometers, which were operated on GRACE [TFW99; Tou+99; Tou+12], in order to remove the nongravitational acceleration contributions from the range when fitting the gravity field model [Tap+04b]. The linear accelerations measured by the Super STAR have a specified resolution of 10^{-10} m/s$^2/\sqrt{\text{Hz}}$ for Fourier frequencies between 0.1 and 100 mHz [Tou+12]. Lowering the impact of accelerometer data noise is, hopefully, merely a matter of time, as better space qualified accelerometers are being developed [Chr+15; Chr+19]. A gravitational reference sensor for future geodesy satellite missions is presented in [Alv+21], which could potentially significantly improve the precision of measuring nongravitational accelerations. For GRACE and GFO, not only the noise of the instrument, but also disturbing signals within the accelerometer data influence the quality of gravity field solutions. Several types of artifacts in the accelerometer data have been identified, studied and modeled [FBT08; PFS12; Pet14; KM16]. To this day, 4 years after the end of the lifetime of GRACE, there is still room left for improving the data. Moreover, superior processing methods may yield further improvements of gravity field solutions [PP19].

Different concepts for future gravity missions have been studied extensively [Ces+10; Sil+12; WNL12; Pan+13; CS13; GN14; Mül17; Els+14]. A promising satellite constellation, consisting of two GRACE-type pairs utilizing two different orbit inclinations, is the so-called Bender-type constellation [BWN08], however, other concepts are certainly possible. As a representative for the variety of different potential mission concepts, in this thesis, the common term Next Generation Gravity Mission (NGGM) is used. Such mission studies are typically presuming the utilization of inter-satellite laser interferometry.

Apart from NGGM, there are other potential applications of laser interferometry in space, e.g. in the field of gravitational wave research. For instance, the planned space-borne gravitational wave detector LISA [Dan+93; Jen09; Ama+17] will also apply inter-satellite laser interferometry, with much stricter requirements on the ranging noise. LISA is currently planned for launch in the 2030's. A pathfinder mission called LISA Pathfinder (LPF) [Bra+04; MVa08] has been very successful in demonstrating key LISA technologies in free space [Arm16]. Since the main science instrument on both missions is also a laser interferometer, TTL coupling plays an important role for LPF [Wa17], as well as for LISA [Trö+18; Sch17; Sch+15b; Sch+16; Chw+20]. For the sake of completeness, the two Chinese LISA-type mission designs should be mentioned, called TianQin [Luo+16] and Taiji [HW17], which are currently also in the planning process, in parallel to LISA.

It is thus important to study the LRI, its noise and error sources, and it is essential to contribute to even higher precision laser ranging instruments in the future. A recent study suggests that even GFO itself, or similar NGGM missions, may theoretically be applied to gravitational wave astronomy [Ros+20], although it is unlikely that gravitational waves can ever be detected by the LRI, since the instrument was not designed for this purpose. With only a single arm, which is much shorter than each of the three arms of LISA, the LRI does not reach the sensitivity to enable it to detect gravitational waves from any expected source.

1.2.2 Pre-flight studies of TTL coupling in the LRI

A key component of the LRI is the so-called triple mirror assembly (TMA). On each of the two S/C, a TMA is responsible for reflecting the local laser light back in the direction of the received beam. It consists of three mirrors in a corner cube reflector arrangement. The three mirror planes are pairwise perpendicular, and their virtual intersection point is called the vertex point (VP). Loosely speaking, the LRI measures the distance between the two VPs, one at each S/C, up to a constant offset due to integer phase ambiguity and other uncalibrated delays and offsets. Consequently, due to the special properties of a corner cube, the measured range is invariant under small satellite rotations around the VPs. On each S/C, the VP is placed in the satellite CoM, to the accuracy of integration tolerances. Due to residual offsets between the VPs and CoMs of the order of 100 µm, there is a difference between the distance from VP to VP on the one hand, and the distance from CoM to CoM on the other hand. This difference is varying, when the S/C rotate around their CoMs. Hence, S/C attitude variations cause an error in the measured biased range. This effect, in this thesis referred to as the TMA vertex point (TMAVP) effect, is assumed to be the main cause of TTL coupling in the LRI.

The TTL coupling of the LRI is already minimized by design, e.g. by careful placement and alignment of the TMA, i.e. such that the virtual VP is colocated with the satellite CoM. Clearly, TTL coupling can never be avoided completely. Some mechanisms, both geometrical and optical, of TTL coupling in satellite laser interferometers are investigated in [Sch17]. There it is further studied how a part of the TTL coupling can be suppressed in the first place, e.g. by the use of a well designed imaging system, which is also utilized in the LRI. In the following, some studies are highlighted which have been carried out before the launch of GFO and which are concerned, among other topics, with the TTL coupling of the GFO LRI.

In a paper by Sheard et al. [She+12], the top-level architecture of the LRI is presented in a compact form. An overview of the working principle, key components and the noise sources of the LRI is given. Pre-flight requirements are discussed as well. In particular, the TMAVP effect is mentioned and a linearized equation for the resulting pathlength error is given, depending on the S/C pitch and yaw angles, and on the offset between the TMA VP and the accelerometer (ACC) reference point (RP), which nominally coincides with the S/C CoM.

A detailed study of the LRI based on simulations is given in [Mül13]. The measurement equations for the LRI are derived, and from that the LFN, which scales with the absolute inter-satellite distance. The TMAVP effect is also stated to be the largest TTL effect in the LRI, and a second order formula of the resulting pathlength error is given. Moreover, the following TTL contributors are identified and analyzed in [Mül13]:

1. The optical pathlength change due to the beamsplitter on each optical bench is derived. Since it depends on the incident beam angle, this is a TTL effect. It is shown that the linear coupling is cancelled by the utilization of a second beam splitter, a so-called compensation plate. The magnitude of the residual coupling, which is quadratic in the pitch and yaw angles, is estimated.

2. The center of phase front curvature of the transmitted laser beam is not colocated with the center of beam rotation. Due to this, S/C attitude variations yield variations of the phase detected at the distant S/C. A formula is given, which comprises only second order pitch and yaw terms, i.e. there is no linear coupling and no roll coupling.

3. So-called off-racetrack pathlength noise, i.e. ranging noise which originates from light travel paths outside the LRI racetrack, otherwise called stray light or ghost beams, is discussed. Changes in those paths may occur, e.g., due to thermal expansion or due to steering mirror motion. The contributions of such pathlength changes are likely to be negligible.

4. For many studies, it is assumed that the TMA itself is perfectly aligned, i.e. the angle between each pair of mirrors is exactly 90 °. A more general pathlength coupling formula for S/C rotations, in case of a possibly misaligned TMA, is derived. The formula is given in terms of pointing angles, VP offset, and the relative angles between the TMA mirror planes called dihedral angles.

In [Mül17], the TMAVP effect is explained in detail. A second order formula for the TTL coupling due to this effect is derived, which is compatible with the formulas given in [She+12] and in [Mül13]. Ideas how to calibrate TTL were mentioned and rough estimates on the estimation accuracy were given. It is concluded that TTL calibration for the LRI is theoretically possible using calibration signals in form of periodic pointing variations. However, it is stated that the feasibility of producing such a pointing variation requires further investigation. It is also shown that the LRI RP is in fact the TMA VP, which means that the LRI effectively measures distance changes between the two VPs, assuming a perfect placement and alignment of all components. Moreover, in [Mül17], it is revisited how S/C rotations couple into the pathlength in case of misaligned TMA mirrors. According to the given formula, the additional TTL coupling due to TMA misalignments, i.e. on top of the TMAVP effect, is below $500 \, \mathrm{mm \, rad^{-1}}$ per rad of mirror misalignment. I.e., if all mirrors have a misalignment of less than 20 µrad, the additional TTL coupling is less than $10 \, \mathrm{\mu m \, rad^{-1}}$.

In [Sch15], the TMA is extensively studied. Originally, the VP was defined for an ideal TMA to be the point where the three mirror planes intersect. If these planes are not mutually perpendicular, such a point does not exist. Thus, the so-called point of minimal coupling (PMC) is defined and studied, which should be referred to instead of the VP. As the name suggests, it is the point which yields the least pathlength coupling, when the TMA is rotated around that point. Different types of TMA units are studied experimentally, with a focus on TTL coupling and the PMC. Furthermore, the suppression of the linear TTL coupling of the beamsplitter by using a compensation plate is experimentally verified.

As suggested for example in [Mül17], one way of estimating TTL coupling may be by means of satellite rotation maneuvers. In the following it is illustrated which kinds of rotation maneuvers were already utilized for other purposes in the GRACE mission.

1.2.3   Satellite rotation maneuvers

Among other instruments, each of the GFO satellites carries an accelerometer (ACC), in order to measure the nongravitational accelerations, and remove its contributions from the range in the process of GFR [Tap+04b]. To ensure the correct measurement of accelerations, the CoM of the proof mass of this ACC, called the ACC reference point (RP), must be colocated with the S/C CoM. Due to residual offsets, S/C rotations couple into the measured linear accelerations. For the purpose of estimating this offset, so-called center-of-mass calibration (CMC) maneuvers are scheduled regularly. The satellites are commanded to perform small periodic rotations, individually, around one axis at a time. By fitting a model to the linear accelerations that are induced by these rotations, the CoM positions of the GFO satellites w.r.t. the ACC RP can be estimated [Wan03; Wan+10]. Occasionally, the S/C CoM are shifted back towards the ACC RP by moving trim masses on the satellites, a procedure which is called mass trim maneuver.

The CMC maneuvers, as well as techniques of estimating the ACC RP offset, are described in [Wan00; Wan03; Wan+10]. The torque required to perform the S/C rotations is obtained by using magnetic torque rods (MTR). Three of these rods per S/C produce a magnetic dipole moment, which produces a torque in combination with the surrounding magnetic field of the Earth. The maneuvers have a duration of 180 seconds, a signal period of 12 seconds, and can achieve angular acceleration amplitudes of about 20, 4, and 2 $\mathrm{\mu rad \, s^{-2}}$, for rotations in the roll, pitch, and yaw axes, respectively [Wan+10]. Moreover, a S/C state simulation using the

dynamics equations of motion, in particular simulation of the S/C attitude state, is described therein.

The rectangular torque pattern of the CMC maneuvers, with a period of 12 seconds, yields a pointing angle stimulus at a frequency of $83.\bar{3}$ mHz. However, whether these maneuvers can be used for the LRI TTL calibration as well, is yet to be examined. A further open question is, what maneuver configuration would be ideal for that purpose. As will become clear within this thesis, the CMC maneuvers are not too far away from what would be ideal for a calibration of LRI TTL coupling.

There is one other rotation maneuver which is exercised in the GRACE and GFO missions. The KBR data contains an error, which is also a kind of TTL error, since it can also be modeled as a function of the S/C pointing angles. It is caused by an offset between the S/C CoM and the antenna phase center (APC), the RP of the KBR range. A correction term is provided as part of the Level-1B KBR data product, called antenna offset correction (AOC) [Hor+11]. To this end, the true APC position must be estimated by once again utilizing satellite rotation maneuvers. These maneuvers are also described in [Wan03], and they differ significantly from the CMC maneuvers. The angles are oscillating with a much larger amplitude, around a nonzero initial offset value. This starting point of the maneuver is $\pm$ 2 ° and the oscillation amplitude is 1 °, which is too large for the LRI to cope with. It cannot be operated during a KBR calibration maneuver. Therefore, KBR calibration maneuvers can be excluded right away, when searching for a calibration maneuver for the LRI.

Based on the discussion of the state of the art above, the main objectives of the study presented in this thesis are formulated below.

1.3   Objectives

To summarize the setting that has been drawn up to this point, TTL is a potential issue for all laser interferometers, including NGGM, LPF, LISA, and the LRI, whereas the latter is mandated to pave the way for other space interferometers to follow. Though the full potential of the LRI cannot yet be exploited for the purpose of GFR, due to other dominating error sources, the LRI has already proven to be very valuable. E.g., the LRI data is used for the characterization of disturbances caused by thruster firings, as well as the monitoring of micrometeorite impacts on the outer satellite surfaces, to mention just a few. Further improvement of the ranging precision is expected to be of great scientific benefit in the future. As will be shown within this thesis, it is possible to estimate the LRI TTL coupling by utilizing satellite rotation maneuvers, yet no detailed studies of such a procedure have been carried out before the launch of GFO. Based on this, the goals of this research are formulated in the following.

A way to estimate the TTL error shall be identified, in order to assess its impact on the overall performance of the instrument. In particular, a first milestone is reached if it can be shown that the pre-flight requirements on the TTL coupling are met. In case the spectrum of the measured LRI range is dominated by TTL in any frequency band, it shall be attempted to improve the data by subtracting the previously estimated TTL error.

The CMC maneuvers and their suitability for the estimation of LRI TTL coupling shall be tested. Apart from that, it shall be explored how to design a dedicated rotation maneuver for the purpose of estimating TTL coupling. What are the defining maneuver parameters, and what parameters are optimal for the LRI? Other strategies of TTL estimation, apart from using rotation maneuvers, shall be assessed and compared.

Estimating the TTL error in any case requires the handling of ranging data, as well as inter-satellite pointing data. Developing the necessary processing algorithms is also part of the work presented in this thesis. Pointing angles shall be computed from various attitude sensors, in order to analyze their noise behavior. In particular, it shall be confirmed that

pitch and yaw angles with high accuracy can be obtained from LRI steering mirror data, which enables the LRI to be calibrated using exclusively its own data. Once the required data processing infrastructure is established, a suitable parameter estimation method must be identified. Different methods, as well as their strengths and weaknesses shall be investigated.

Past studies have named a few possible TTL effects, with the TMAVP effect as the premier one. These studies shall be revisited. In particular, it shall be investigated whether the TMAVP effect is indeed the dominating TTL effect in the LRI. In case this assumption proves to be correct, it should be possible to use the estimated coupling factors to derive the S/C CoM positions relative to the LRI RP. This derivation shall be done, if possible, yielding additional useful information for the GFO mission.

When pursuing the above mentioned goals, any unexpected artifacts in the LRI data or in the auxiliary data, which constitute obstacles on the way to TTL estimation, shall be studied and, if possible, removed or mitigated. Any lessons learnt along the way shall be formulated, with regard to future inter-satellite laser interferometers, as these will likely face similar challenges. All the previously mentioned steps shall be archived in this thesis with much detail, such that they are quickly reproducible and easily adaptable to a different mission scenario.

1.4   Structure

The structure of this thesis is as follows. Chapter 2 is an introduction to S/C attitude. Within this work, the LRI TTL error is expressed in terms of S/C pointing angles, called roll, pitch, and yaw, which describe the deviation of a satellite's attitude w.r.t. a reference attitude. The definition of these pointing angles and a derivation of the formulas by which they can be calculated is given in Sec. 2.1. This includes a summary of the mathematical formalisms of S/C attitude description. There are different types of instruments which can provide information about the attitude of a S/C. An overview of such instruments, called attitude sensors, and how to utilize their data, is given in Sec. 2.2. The third related topic which is relevant for the studies presented in this thesis is attitude control. Several means of attitude actuation are discussed in Sec. 2.3, not restricted to but with a focus on GFO attitude control.

Once the pointing angles are defined, one is able to describe the TTL error in the LRI measurements. This shall be done in Chap. 3. In Sec. 3.1, an introduction to the working principle of the LRI is given, as well as a description of those of its components, which are relevant for this study. Then, different effects that can cause TTL coupling in the LRI are discussed in Sec. 3.2, and each of them is given as a function of the pointing angles. Based on this, a general strategy of estimating TTL coupling in the LRI is explained in Sec. 3.3. In particular, a linear model of the LRI TTL error is developed. This model is later to be fitted to the LRI range together with the pointing angles.

The estimation strategy may require to intentionally evoke a TTL error by exciting the pointing angles, i.e. creating a stimulus. Such can be achieved by means of satellite rotation maneuvers, which is the topic of Chap. 4. There exists already one procedure to produce such a stimulus, which is regularly carried out on GFO. This procedure, called CMC maneuver, is presented in Sec. 4.1. Since the original purpose of CMC maneuvers is unrelated to the LRI, it is likely that dedicated TTL calibration maneuvers would yield better estimation results. With this in mind, it shall be investigated how such maneuvers can be designed, for GFO or similar missions in the future. To this end, a simulation technique is developed in Sec. 4.2. Afterwards, in Sec. 4.3, a design strategy with the specific target of optimizing TTL estimation is discussed. While the focus lies on maneuvers where the stimulus is produced exclusively via so-called MTRs, a potential alternative is discussed as well, namely the use of attitude control thrusters. In the end of the chapter, a selection of simulation cases is presented and compared to the CMC maneuvers.

In the chapters mentioned so far, the capability of deriving pointing angles from several attitude sensors has been developed, the LRI TTL model has been given as a function of the pointing angles, and satellite rotation maneuvers have been studied. These form the basis for the TTL estimation with in-flight GFO data, which is the topic of Chap. 5. In particular, the remaining steps of data processing are discussed in Sec. 5.1, including data filtering and synchronization of different data streams. In Sec. 5.2, different parameter estimation methods are presented and the relevant formulas are derived in detail. The results, i.e. estimated coupling factors, are shown in Sec. 5.3, where also the performance of the individual estimation methods is evaluated. Moreover, estimates of the offsets between S/C CoMs and the LRI RPs are derived. Afterwards, the results are interpreted and some conclusions are drawn. In Sec. 5.4, some analysis is presented investigating the subtraction of TTL from the LRI range, not only with the goal of mitigating the TTL error and improving the LRI data, but also as a confirmation of the estimation results.

In Chap. 6, the findings of this thesis are summarized. Conclusions are drawn and a prospect of future research is provided.

Chapter 2

Spacecraft attitude

In this thesis, in the context of the LRI, TTL coupling is referred to as an error in the measured range, which can be described as a function of the so-called pointing angles of the two GFO satellites. This function is derived in Chap. 3. However, the first step towards estimating the LRI TTL error is to develop the formalism which is necessary to describe S/C attitude. This chapter is meant to provide a detailed description of this formalism, and to give an overview of some related topics, as a basis for the main part of this thesis.

Given the positions of the two GFO satellites, each of them has a uniquely defined target attitude, i.e. a desired orientation. It is given in terms of a coordinate frame, which is in one axis aligned with the line-of-sight (LoS), the line connecting the two S/C CoMs, which should coincide with the optical axis of the instrument. Pointing angles describe the deviation of a satellite's attitude from this nominal attitude. They can either be measured directly, or derived from other measurements. In the latter case, the pointing angles can be obtained by combining information on the S/C positions with information on their attitudes w.r.t. inertial space.

There are different ways to describe the attitude of a rigid object such as a satellite. In general, it is done by choosing two coordinate frames, one fixed to the object and one which serves as a reference. The attitude of the object may then be defined by the rotation which transforms between these two frames. The classic form of representing 3D rotations are orthogonal 3x3 matrices, however, there are other possibilities. Some of these are listed and discussed in Sec. 2.1, after introducing the coordinate frames which are relevant for this thesis. In particular, the quaternion number system is introduced. These numbers, in this context called attitude quaternions, constitute a useful method to represent 3D rotations. Moreover, inter-satellite pointing angles are defined for the GFO satellites, and it is elaborated how they can be computed.

Section 2.2 shall give an overview of S/C attitude determination. GFO hosts different science instruments, whose measurements can be used to derive the attitude of a satellite. These attitude sensors are discussed, with emphasis on the measured observables rather than the measurement principles. For each sensor, it is described how its measurement data can be used to determine the S/C attitude, and subsequently the pointing angles, defined in the preceding section. Furthermore, an overview of some attitude sensors is given, which are not incorporated in GFO.

In Sec. 2.3, the attitude control system (ACS) of GFO is described. The attitude control mechanisms which are used for GFO are magnetic torque rods (MTR) and cold gas thrusters. The working principles behind these mechanisms are sketched. Again, for completeness, other possible ways of attitude control are given and described briefly.

2.1 Attitude description

In general, the orientation or attitude of an object must be described with respect to a reference coordinate frame. Once such a reference is given, the objects attitude is fully defined by a single rotation around a fixed, uniquely determined axis. There are different ways in which such a rotation can be represented. The most common ways, also depending on the type of application, are using either rotation matrices, attitude quaternions, or Euler angles.

By Euler's rotation theorem, any volume- and orientation-preserving transformation of $\mathbb{R}^3$, which has a fixed point, is equivalent to a single rotation around that fixed point. For some theoretical background, the reader is referred to [GPS02]. In particular, the composition of any number of rotations is again a rotation. Hence, the set of 3D rotations has the structure of a group. In fact, this group is called $SO(3)$, and it has dimension 3. Thus, a minimum of three coordinates is required to represent a rotation. However, for any such representation using no more than three coordinates, there is at least one orientation where the coordinates are singular. Hence, it is most common to use a form of representation which is built on at least four independent coordinates. Note also that a three-dimensional matrix R is a rotation if and only if it fulfills

$$
\begin{aligned}
RR^T = R^T R &= I, \\
\det R &= +1,
\end{aligned}
\tag{2.1}
$$

with the identity matrix I.

The coordinate frames which are required to establish the formalism for the estimation of LRI TTL coupling are defined in Sec. 2.1.1. The quaternion number system is introduced in Sec. 2.1.2. For the purpose of TTL analysis, mainly so-called inter-satellite pointing angles are used, which are the Euler angles of the rotation between the satellite frame (SF) and the line-of-sight frame (LOSF). The exact definition of these pointing angles, known as roll, pitch, and yaw, is given in Sec. 2.1.3.

2.1.1 Coordinate frames

In this section, the coordinate frames which are relevant for the purpose of this thesis are defined. All described frames are right-handed orthonormal systems. Some authors may use different names for these frames, or they may define them according to slightly different conventions. The descriptions given here are used for the analysis presented in this thesis.

Earth-Centered Inertial (ECI) frame

The Earth-centered inertial (ECI) frame is a geocentric inertial coordinate system. The origin is defined to be the CoM of the Earth, according to the World Geodetic System 1984 (WGS84), identical to the origin of the Earth-centered Earth-fixed (ECEF) frame. The axes of the ECI frame are defined according to the International Celestial Reference System (ICRS) [PL10]. This frame is usually used as a reference for the attitude of a S/C. I.e., the attitude of the S/C is defined by the rotation between ECI and SF, the latter of which is defined further below.

Earth-Centered Earth-Fixed (ECEF) frame

The Earth-centered Earth-fixed (ECEF) frame is a geocentric coordinate system, which is fixed to the Earth, and hence rotating w.r.t. inertial space. The origin of the ECEF is defined to be the CoM of the Earth. Its axes are fixed to the surface of the Earth, hence the name Earth-Fixed. Within this thesis, it is referred to the International Terrestrial Reference System (ITRS), with its most recent realization of the origin and axes, the ITRF2014 [Alt+16].

In the ITRS, the z axis of the ECEF is the mean rotation axis of the Earth, directed towards the geodetic north pole, which is defined by the International Earth Rotation and Reference Systems Service (IERS). The geodetic north pole is also called IERS Reference Pole (IRP), and it differs from the magnetic north pole. The x axis is aligned with the prime meridian, also called IERS Reference Median (IRM), maintained by IERS. The y axis completes the right-handed system, and is thus pointing to the east of the IRM.

For one thing, the computation of atmospheric drag forces is carried out in the ECEF, cf. Sec. 4.2.2. Also, the ECEF is used for the S/C positions provided in the GNV1B data product [Wen+19], which also adopts the ITRF2014 realization, see also Sec. 5.1.1.

For several purposes throughout this thesis, the S/C positions are required in ECI rather than ECEF. An implementation of the rotation between the ECI and ECEF frames is available within the Matlab software, with the function *dcmeci2ecef*. The exact computation requires so-called Earth orientation parameters, which are provided by IERS for public access. However, GFO satellite positions are also reported in the ECI frame, in the GNI1B data product.

Satellite Frame (SF) and Science Reference Frame (SRF)

The definition of the satellite frame (SF) is given in [Wen+19]. Its origin is defined to be the CoM of the accelerometer proof mass. The x axis of the SF is called the roll axis, which is defined by the line joining the origin and the nominal reference point (RP) of the KBR instrument. This KBR RP is called antenna phase center, see also App. C. The y- and z-axes are called pitch axis and yaw axis, respectively. Figure 2.1 shows the satellite body fixed frames which are used for GFO.
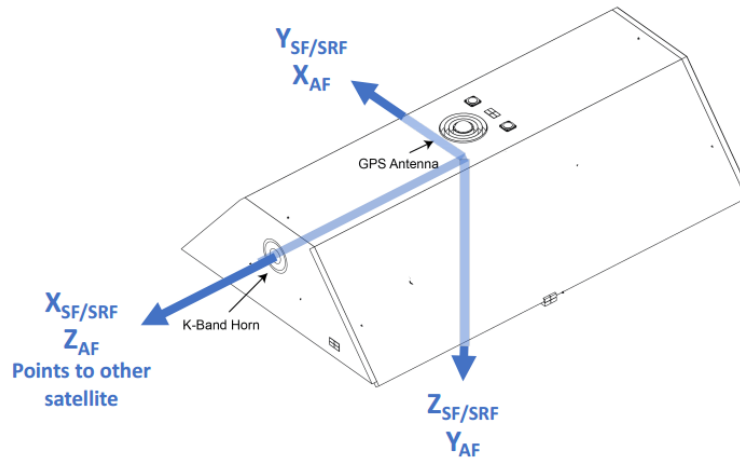
Figure 2.1: GFO satellite body fixed frames: SF, science reference frame (SRF), accelerometer frame (AF). Image adopted from [Wen+19].

In this thesis, the SF is used to describe the attitude of the S/C. Generally, satellite body fixed frames are required to interpret the data measured by the different instruments onboard a S/C. For GFO, most official Level-1 data products provided by the Science Data System (SDS) are referring to the SRF, which has the same origin and axes as the SF [Wen+19].

It shall be remarked here that the LRI measures inter-satellite pointing angles in addition to the range, see Secs. 2.1.3 and 2.2.1. More precisely, it measures pitch and yaw angles with respect to the LRI optical axis. This optical axis can be defined in two ways, which are nominally identical. These definitions refer to the fast steering mirror (FSM) and the differential wavefront sensing (DWS) of the LRI beam steering mechanism, which is described in Sec. 3.1.4. Then, the optical axis can be defined either by the beam axis of the outgoing beam when the FSM is centered, or by the beam axis of the received beam when the FSM is

centered and the DWS error signal is zero. However, with both these definitions, the optical axis nominally coincides with the SF x axis. The potential residual deviation between optical axis and SF x axis is assumed to be small and static. Therefore, in this thesis, the SF x axis will be referred to instead of the LRI optical axis.

The accelerometer frame (AF) is introduced below.

Accelerometer Frame (AF)

A third relevant body fixed reference frame is the accelerometer frame (AF). It has the same origin as SF and SRF, and nominally differs from those frames merely by a permutation of the axes, cf. Fig. 2.1. The Level-1 data product ACC1A, containing the accelerometer measurements, is given in this reference frame, whereas the ACC1B data product is given in the SRF.

Vectors can be rotated from the AF to the SF by multiplication from the left with the matrix

$$R_{\mathrm{AF}}^{\mathrm{SF}} = \begin{pmatrix} 0 & 0 & 1 \\ 1 & 0 & 0 \\ 0 & 1 & 0 \end{pmatrix}. \tag{2.2}$$

Line-of-sight frame (LOSF)

The line-of-sight frame (LOSF) of a GFO satellite is defined w.r.t. the other satellite. Within this thesis, the following definition of the LOSF is used. The origin is the CoM of the S/C. Let $\vec{p}$ denote the position of the S/C, given in ECI. Denoting by $\vec{p}_{\mathrm{other}}$ the position of the other S/C, let the LOSF axes be defined as

$$\vec{X}_{\mathrm{LOSF}} = \frac{\vec{p}_{\mathrm{other}} - \vec{p}}{|\vec{p}_{\mathrm{other}} - \vec{p}|}$$

$$\vec{Y}_{\mathrm{LOSF}} = \frac{\vec{X}_{\mathrm{LOSF}} \times \vec{p}}{|\vec{X}_{\mathrm{LOSF}} \times \vec{p}|}$$

$$\vec{Z}_{\mathrm{LOSF}} = \vec{X}_{\mathrm{LOSF}} \times \vec{Y}_{\mathrm{LOSF}},$$

with $|X_{\mathrm{LOSF}}| = |Y_{\mathrm{LOSF}}| = |Z_{\mathrm{LOSF}}| = 1$. Here $\times$ denotes the cross product. Then, the matrix $R_{\mathrm{ECI}}^{\mathrm{LOSF}}$, transforming a vector from ECI representation to LOSF representation, is obtained by

$$R_{\mathrm{ECI}}^{\mathrm{LOSF}} = \begin{pmatrix} \vec{X}_{\mathrm{LOSF}}^{T} \\ \vec{Y}_{\mathrm{LOSF}}^{T} \\ \vec{Z}_{\mathrm{LOSF}}^{T} \end{pmatrix} \tag{2.3}$$

Within this thesis, this frame is used as a reference for S/C pointing. That is, in the absence of S/C internal misalignments, it is said that the S/C has perfect pointing, or zero pointing deviation, if the LOSF aligns perfectly with the SF. Note further that $\vec{X}_{\mathrm{LOSF}}$ is pointing roughly in flight direction for the trailing satellite, while it is pointing backwards for the leading satellite.

K-frame (KF)

The KBR reference frame is called the K-frame (KF). Its origin is chosen to be the S/C CoM. The axes are defined, according to [Bet12], by

$$\vec{X}_{\mathrm{KF}} = \frac{\vec{v}}{|\vec{v}|}, \tag{2.4}$$

where $\vec{v}$ is the vector pointing from the CoM to the KBR ranging reference point (RP), i.e.
the antenna phase center (APC). The z axis of the KF is defined via

$$\vec{Z}_{\mathrm{KF}} = \frac{\vec{X}_{\mathrm{KF}} \times \vec{y}_{\mathrm{SF}}}{|\vec{X}_{\mathrm{KF}} \times \vec{Y}_{\mathrm{SF}}|},$$ (2.5)

and the y axis completes the right handed triad:

$$\vec{Y}_{\mathrm{KF}} = \vec{Z}_{\mathrm{KF}} \times \vec{X}_{\mathrm{KF}}.$$ (2.6)

In order to realize this frame, the APC position, i.e. $\vec{v}$, has to be determined. This is done
at first via calibration on ground, and during the mission via the KBR calibration maneuvers,
see also App. C.

North-East-Down (NED) frame

In the studies presented in this thesis, the north-east-down (NED) frame is merely used for
the computation of the Earth's magnetic field, i.e. for the implementation of the International
Geomagnetic Reference Field (12$^{\mathrm{th}}$ generation) (IGRF12) model, see Sec. 4.2.2. Its axes are
north, east, and down, and the origin is taken to be the S/C CoM.

The matrix rotating vectors from the ECEF frame to the NED frame is given by [SL92]

$$R_{\mathrm{ECEF}}^{\mathrm{NED}} = \begin{pmatrix} -\sin(\alpha)\cos(\beta) & -\sin(\alpha)\sin(\beta) & \cos(\alpha) \\ -\sin(\beta) & \cos(\beta) & 0 \\ -\cos(\alpha)\cos(\beta) & -\cos(\alpha)\sin(\beta) & -\sin(\alpha) \end{pmatrix},$$ (2.7)

with α and β denoting latitude and longitude, respectively, expressed in units of rad. Matlab
provides implementations of the coordinate transformations between NED and ECEF with
the functions *ecef2ned* and *ned2ecef.*

Latitude, Longitude, Altitude (LLA)

Although not a Euclidean frame, the commonly known latitude, longitude, altitude (LLA)
coordinates are useful on or above the surface of the Earth. In this thesis, it will be used for
illustration purposes, whenever it is beneficial to refer some data to geographic locations. The
reference meridian for the longitude is taken to be the international prime meridian, i.e. the
meridian of the British Royal Observatory in Greenwich, in southeast London, England. For
the data analysis presented here, the Matlab functions *ecef2lla* and *lla2ecef* are used, in order
to transform between ECEF and LLA coordinates.

2.1.2   Attitude quaternions

It has been mentioned in the beginning of Sec. 2.1 that an object's attitude is described
by a rotation. Here one way of representing rotations is introduced which is making use of
quaternion numbers. Other methods to represent rotations are rotation matrices or Euler
angles. Matrices and angles may be more intuitive, however, quaternions have proven to be
very well suited for describing and processing the attitude of a S/C. A good reference for
S/C attitude determination is [Wer78]. A more recent reference is [FB16]. An overview of
developments in the field of quaternion based attitude determination is given in [Yan12]. In the
following, the quaternion number system is presented, as well as how quaternions can describe
rotations, how quaternions can be derived from rotation matrices, and how quaternions can
be obtained via S/C state integration.

Quaternion number system

Quaternions are an extension of the complex number system. The complex numbers $\mathbb{C}$ are defined as $\mathbb{R}^2$, equipped with a complex structure i, which fulfills $i^2 = -1$. Similarly, quaternions are defined as $\mathbb{R}^4$, together with an additional algebraic structure. Instead of one real and one imaginary part, a quaternion has one real and three imaginary parts. A quaternion q can be written as

$$q = q_0 + iq_1 + jq_2 + kq_3, \tag{2.8}$$

with $q_0, \dots, q_3 \in \mathbb{R}$.

Like for complex numbers, addition and scalar multiplication are inherited from $\mathbb{R}^4$, and the multiplication operation is fully defined by requiring

$$i^2 = j^2 = k^2 = ijk = -1. \tag{2.9}$$

The product of two quaternions p and q is then given by

$$\begin{aligned}
p \cdot q &= (p_0 + ip_1 + jp_2 + kp_3) \cdot (q_0 + iq_1 + jq_2 + kq_3) \\
&= p_0 q_0 - p_1 q_1 - p_2 q_2 - p_3 q_3 \\
&\quad + i \cdot (p_0 q_1 + p_1 q_0 + p_2 q_3 - p_3 q_2) \\
&\quad + j \cdot (p_0 q_2 - p_1 q_3 + p_2 q_0 + p_3 q_1) \\
&\quad + k \cdot (p_0 q_3 + p_1 q_2 - p_2 q_1 + p_3 q_0).
\end{aligned} \tag{2.10}$$

Note that this multiplication of two quaternions is not commutative.

In analogy with complex numbers, one can assign to a quaternion $q = q_0 + iq_1 + jq_2 + kq_3$ its conjugate, q^*:

$$q^* = q_0 - iq_1 - jq_2 - kq_3. \tag{2.11}$$

The norm $\|q\|$ of a quaternion is given by

$$\|q\| = \sqrt{qq^*} = \sqrt{q^*q} = \sqrt{q_0^2 + q_1^2 + q_2^2 + q_3^2}. \tag{2.12}$$

Every nonzero quaternion has an inverse, also called the reciprocal quaternion, defined to be

$$q^{-1} = \frac{q^*}{\|q\|^2}, \tag{2.13}$$

such that $qq^{-1} = q^{-1}q = 1$. A quaternion with norm 1 is called a unit quaternion. For any unit quaternion, one has $q^{-1} = q^*$.

The quaternion number system is often denoted by $\mathbb{H}$, after *William Rowan Hamilton*, who first described quaternions. In the following section, it is illustrated how quaternions provide a formalism to describe three-dimensional rotations.

Rotations described by quaternions

Similar to complex numbers, quaternions are related to geometry, in the sense that they provide an alternative representation of three-dimensional rotations. Consequently, quaternions can describe the attitude of an object, by describing the rotation between a body fixed frame and a reference frame. This is elaborated in the following.

It will be beneficial to identify three-dimensional vectors with imaginary quaternions. More precisely, if $\vec{p}$ is a vector, assign to it an imaginary quaternion $\mathcal{Q}(\vec{p})$:

$$\vec{p} = \begin{pmatrix} p_1 \\ p_2 \\ p_3 \end{pmatrix} \quad \longmapsto \quad \mathcal{Q}(\vec{p}) = 0 + ip_1 + jp_2 + kp_3.$$

Reversely, denote by $\mathcal{V}(q)$ the vector obtained by taking the imaginary components of a quaternion q as vector components:

$$q = q_0 + iq_1 + jq_2 + kq_3 \quad \longmapsto \quad \mathcal{V}(q) = \begin{pmatrix} q_1 \\ q_2 \\ q_3 \end{pmatrix}.$$

In this manner, one can switch from vectors to quaternions and back.

Now, let R be a rotation matrix, which describes a rotation through angle φ around an axis which is given by a normalized vector $\vec{e} = (e_1, e_2, e_3)^T$, i.e. $\|\vec{e}\| = 1$. Let further $\vec{p} \in \mathbb{R}^3$ be any vector, and let $\vec{r} = R\vec{p}$ denote the rotated vector. From φ and $\vec{e}$, construct a quaternion q_R:

$$q_R = \cos\left(\frac{\varphi}{2}\right) + (ie_1 + je_2 + ke_3) \cdot \sin\left(\frac{\varphi}{2}\right).$$

Then, with the notations given above, one has

$$\vec{r} = \mathcal{V}(q_R \mathcal{Q}(\vec{p}) q_R^{-1}). \tag{2.14}$$

That is, multiplication by the matrix R is equivalent to conjugation by q_R. This can be proven by rearranging the expression $q_R \mathcal{Q}(\vec{p}) q_R^{-1}$ and by using Rodrigues' rotation formula [FB16]. Note also that q_R is by construction a unit quaternion, i.e. has norm $\|q_R\| = 1$, and thus $q_R^{-1} = q_R^*$. Hence, formula (2.14) is equivalent to

$$\vec{r} = \mathcal{V}(q_R \mathcal{Q}(\vec{p}) q_R^*). \tag{2.15}$$

As to the other direction, if a rotation is given as a quaternion number $q = q_0 + iq_1 + jq_2 + kq_3$, it can be easily seen that the rotation axis $\vec{e}$ and angle φ can be obtained back via

$$\varphi = 2\arccos(q_0),$$

$$\vec{e} = \frac{1}{\sin\left(\frac{\varphi}{2}\right)} \begin{pmatrix} q_1 \\ q_2 \\ q_3 \end{pmatrix},$$

if $\varphi \neq 2k\pi, k \in \mathbb{Z}$. Note that if $\varphi = 2k\pi$, R is simply the identity matrix and $\vec{e}$ is not determined. The corresponding rotation matrix R is given by [Wer78]

$$R = \begin{pmatrix} 1 - 2q_2^2 - 2q_3^2 & 2(q_1q_2 - q_3q_0) & 2(q_1q_3 + q_2q_0) \\ 2(q_1q_2 + q_3q_0) & 1 - 2q_1^2 - 2q_3^2 & 2(q_2q_3 - q_1q_0) \\ 2(q_1q_3 - q_2q_0) & 2(q_2q_3 + q_1q_0) & 1 - 2q_1^2 - 2q_2^2 \end{pmatrix}. \tag{2.16}$$

Recovering quaternions from rotation matrices

Assume now that a rotation is given as a matrix, not via angle and axis. One of the most simple ways to recover a quaternion $q = q_0 + iq_1 + jq_2 + kq_3$ from a rotation matrix R is found by taking a close look at Eq. (2.16). Denoting by tr the trace of a matrix, it is immediately seen that $\operatorname{tr}R + 1 = 4 - 4(q_1^2 + q_2^2 + q_3^2)$, and hence $\operatorname{tr}R + 1 = 4q_0^2$, since q is a unit quaternion, which yields q_0. Note that the quaternion $-q$ describes the same rotation as q, see e.g. Eq. (2.15). Thus, the positive root can be taken without loss of generality, when computing q_0. Formulas for q_1, q_2, q_3 can be derived by forming linear combinations of the nondiagonal entries of R, cf. Eq. (2.16). Introducing an auxiliary variable s, one has

$$\begin{aligned} q_0 &= \frac{1}{2}\sqrt{1 + \operatorname{tr}R}, \\ s &= \frac{1}{4q_0}, \\ q_1 &= (R_{23} - R_{32}) \cdot s, \\ q_2 &= (R_{31} - R_{13}) \cdot s, \\ q_3 &= (R_{12} - R_{21}) \cdot s. \end{aligned} \tag{2.17}$$

Note that this computation is only numerically stable, as long as $\mathrm{tr}\,R$ is greater than and not close to -1, since otherwise the computation of the term denoted by s would require to divide by a number close to zero. This problem can be circumvented by considering three different cases, depending on which of the diagonal entries R_{11}, R_{22}, R_{33} is the largest. One of the values q_1, q_2, q_3 can be found by regarding linear combinations of the diagonal entries of R. Formulas for the other quaternion components can be derived subsequently, again by using Eq. (2.16). The pseudocode of a numerically stable implementation for recovering a quaternion $q = q_0 + iq_1 + jq_2 + kq_3$ from a rotation matrix R is given in algorithm 1 below, which was extracted from the method presented in [She78].

Algorithm 1: Conversion from rotation matrix to quaternion

---

if $R(1,1) \geq R(2,2)$ *and* $R(1,1) \geq R(3,3)$ **then**

> $r = \sqrt{1 + R(1,1) - R(2,2) - R(3,3)}$;
> $s = 1/(2 \cdot r)$;
> $q0 = (R(3,2) - R(2,3)) \cdot s$;
> $q1 = r/2$;
> $q2 = (R(2,1) + R(1,2)) \cdot s$;
> $q3 = (R(1,3) + R(3,1)) \cdot s$;

else if $R(2,2) > R(1,1)$ *and* $R(2,2) >= R(3,3)$ **then**

> $r = \sqrt{1 + R(2,2) - R(1,1) - R(3,3)}$;
> $s = 1/(2 \cdot r)$;
> $q0 = (R(1,3) - R(3,1)) \cdot s$;
> $q1 = (R(1,2) + R(2,1)) \cdot s$;
> $q2 = r/2$;
> $q3 = (R(3,2) + R(2,3)) \cdot s$;

else

> $r = \sqrt{1 + R(3,3) - R(1,1) - R(2,2)}$;
> $s = 1/(2 \cdot r)$;
> $q0 = (R(2,1) - R(1,2)) \cdot s$;
> $q1 = (R(1,3) + R(3,1)) \cdot s$;
> $q2 = (R(2,3) + R(3,2)) \cdot s$;
> $q3 = r/2$;

end

It may occur that the rotation matrix R cannot be assumed to be free of errors, e.g. due to propagation of numerical errors. In fact, R may not even be a rotation matrix, i.e. slightly violating properties (2.1). In this case, the method introduced in [Bar00] can be used. It requires to form a 4×4 matrix K, which depends on the matrix entries of R. Then, the eigenvector corresponding to the largest eigenvalue of K is computed. If the input matrix is a rotation matrix fulfilling equations (2.1), the largest eigenvalue is 1. In any case, the eigenvector will be of the form (q_0, q_1, q_2, q_3), defining the quaternion q corresponding to the rotation matrix, which is the closest orthogonal matrix to R w.r.t. the Euclidean norm on $R^{3\times3}$.

Quaternions from integration

For integrating angular velocities or angular accelerations in order to obtain quaternions, one uses the 7-dimensional state vector $\vec{X}_{\text{att}}$:

$$\vec{X}_{\text{att}} = \begin{pmatrix} \vec{X}_q \\ \vec{X}_\omega \end{pmatrix} = \begin{pmatrix} \vec{q} \\ \vec{\omega} \end{pmatrix} \tag{2.18}$$

with derivatives [Wer78]

$$\dot{\vec{X}}_q = \frac{1}{2}\Omega(\vec{\omega}) \cdot \vec{q} \tag{2.19}$$

and

$$\dot{\vec{X}}_\omega = J^{-1}(\vec{\tau} - \vec{\omega} \times (J\vec{\omega})). \tag{2.20}$$

In this thesis, the state vector $\vec{X}_{\text{att}}$ as defined in Eq. (2.18) will be called the attitude state vector. The following notation is used in equations (2.18)-(2.20):

- $q = (q_0, q_1, q_2, q_3)^T$ are the attitude quaternions, interpreted as a 4-dimensional vector. Here and throughout this thesis, q_0 is the real part, describing the rotation angle, and $(q_1, q_2, q_3)^T$ is the imaginary part, describing the rotation axis.

- $\vec{\omega} = (\omega_x, \omega_y, \omega_z)^T$ are the S/C angular velocities. They must be given in SF.

- $\Omega(\vec{\omega})$ is a skew-symmetric 4x4-matrix given by

$$\Omega(\vec{\omega}) = \begin{pmatrix} 0 & -\omega_x & -\omega_y & -\omega_z \\ \omega_x & 0 & \omega_z & -\omega_y \\ \omega_y & -\omega_z & 0 & \omega_x \\ \omega_z & \omega_y & -\omega_x & 0 \end{pmatrix}$$

  Note that in the notation used here, the angle part is given in the first element of $\vec{q}$, that is, q_0. Some authors define $\vec{q}$ such that the angle part is the fourth element. In that case, the matrix $\Omega(\vec{\omega})$ must also be adjusted.

- $\vec{\tau} = (\tau_x, \tau_y, \tau_z)^T$ is the total torque acting on the satellite, given in SF.

- J denotes the satellite's moment of inertia (MoI) tensor w.r.t. the S/C CoM, which is given below.

Adopting SF coordinates, the MoI tensor w.r.t. the S/C CoM is defined as the matrix

$$\begin{aligned} J &= \begin{pmatrix} \int (y^2 + z^2)\, dm & -\int xy\, dm & -\int xz\, dm \\ -\int xy\, dm & \int (x^2 + z^2)\, dm & -\int yz\, dm \\ -\int xz\, dm & -\int yz\, dm & \int (x^2 + y^2)\, dm \end{pmatrix} \\ &= \begin{pmatrix} J_{xx} & J_{xy} & J_{xz} \\ J_{xy} & J_{yy} & J_{yz} \\ J_{xz} & J_{yz} & J_{zz} \end{pmatrix}, \end{aligned} \tag{2.21}$$

where dm is the mass element with coordinates $(x, y, z)^T$ given in the SF. In [Wen+19], the MoI matrices in SF for the GFO satellites are specified as

$$J_{\text{GF1}} = \begin{pmatrix} 110.49 & -1.02 & 0.35 \\ -1.02 & 580.67 & 0.03 \\ 0.35 & 0.03 & 649.69 \end{pmatrix} \text{kg m}^2 \tag{2.22}$$

and

$$J_{\mathrm{GF2}} = \begin{pmatrix} 109.64 & -0.50 & 0.36 \\ -0.50 & 579.76 & 0.06 \\ 0.36 & 0.06 & 648.80 \end{pmatrix} \, \mathrm{kg\,m^2}. \tag{2.23}$$

For comparison, the MoI matrix for a GRACE satellite was approximately given by, cf. [Wan03] p. 139,

$$J_{\mathrm{GRACE}} \approx \begin{pmatrix} 80 & -3 & -3 \\ -3 & 420 & -0.3 \\ -3 & -0.3 & 470 \end{pmatrix} \, \mathrm{kg\,m^2}.$$

Simulations published in [Woe21] are based on a diagonal MoI matrix for GRACE, with slightly different values, $J_{\mathrm{GRACE}} \approx \mathrm{diag}(104.3, 408.0, 473.4) \, \mathrm{kg\,m^2}$.

2.1.3 Inter-satellite pointing angles

A measure of the deviation of the attitude of a GFO satellite from the nominal attitude can be given by the three Euler angles of the rotation which transforms between the SF and the LOSF, similar as for the GRACE satellites [BFK12]. In this context, the angles of rotation around SF x, y, and z axes are called roll, pitch, and yaw angles, respectively. Here the SF x axis is roughly aligned with the LoS, and the SF z axis is roughly the nadir direction. When regarding the z direction as bottom and the x direction as forward, the SF y axis is pointing to the right of the S/C. See Sec. 2.1.1 for the definition of the SF. Here the definition of the inter-satellite pointing angles is stated, as it is used in this thesis, and it is described how these angles can be computed from the rotation matrix $R_{\mathrm{SF}}^{\mathrm{LOSF}}$.

Definition

The pointing angles used in this thesis are defined by

$$R_{\mathrm{SF}}^{\mathrm{LOSF}} = R_z(\theta_z) R_y(\theta_y) R_x(\theta_x), \tag{2.24}$$

where $R_x(\theta_x)$ denotes a rotation around the x axis by an angle θ_x, which is called the roll angle. $R_y(\theta_y)$ and $R_z(\theta_z)$ denote rotations around y and z axes, by angles θ_y and θ_z, called pitch and yaw, respectively. $R_{\mathrm{SF}}^{\mathrm{LOSF}}$ denotes the rotation which transforms a vector given in SF to its representation in LOSF, cf. Sec. 2.1.1. In general, if $R_{\mathrm{SF}}^{\mathrm{LOSF}}$ is replaced by an arbitrary rotation matrix, the angles θ_x, θ_y and θ_z are called Euler angles. With this notation, the pointing angles are defined as the Euler angles of the rotation $R_{\mathrm{SF}}^{\mathrm{LOSF}}$. In the following, it is described how the pointing angles are computed.

Computing Euler angles

By Euler's theorem, any composition of rotations can be described by a single rotation. In return, having fixed a coordinate system, a single rotation can also be described by the composition of three rotations, each around one of the coordinate axes. The corresponding rotation angles are called Euler angles. These angles can be computed as follows.

Given a rotation matrix R, the relation between R and the Euler angles is given by

$$R = \begin{pmatrix} R_{11} & R_{12} & R_{13} \\ R_{21} & R_{22} & R_{23} \\ R_{31} & R_{32} & R_{33} \end{pmatrix} = R_z R_y R_x, \tag{2.25}$$

where R_x stands short for a (counter-clockwise) rotation around the x axis by an angle θ_x, i.e.

$$R_x = \begin{pmatrix} 1 & 0 & 0 \\ 0 & \cos(\theta_x) & -\sin(\theta_x) \\ 0 & \sin(\theta_x) & \cos(\theta_x) \end{pmatrix}, \tag{2.26}$$

and accordingly for y and z. Written out explicitly, one has

$$R = \begin{pmatrix} \cos(\theta_z) & -\sin(\theta_z) & 0 \\ \sin(\theta_z) & \cos(\theta_z) & 0 \\ 0 & 0 & 1 \end{pmatrix} \cdot \begin{pmatrix} \cos(\theta_y) & 0 & \sin(\theta_y) \\ 0 & 1 & 0 \\ -\sin(\theta_y) & 0 & \cos(\theta_y) \end{pmatrix} \cdot \begin{pmatrix} 1 & 0 & 0 \\ 0 & \cos(\theta_x) & -\sin(\theta_x) \\ 0 & \sin(\theta_x) & \cos(\theta_x) \end{pmatrix}. \quad (2.27)$$

With the abbreviations $s_x = \sin \theta_x$, $c_x = \cos \theta_x$, etc., one obtains

$$R = \begin{pmatrix} c_z & -s_z & 0 \\ s_z & c_z & 0 \\ 0 & 0 & 1 \end{pmatrix} \cdot \begin{pmatrix} c_y & s_x s_y & c_x s_y \\ 0 & c_x & -s_x \\ -s_y & s_x c_y & c_x c_y \end{pmatrix}$$

$$(2.28)$$

$$= \begin{pmatrix} c_y c_z & s_x s_y c_z - c_x s_z & c_x s_y c_z + s_x s_z \\ c_y s_z & s_x s_y s_z + c_x c_z & c_x s_y s_z - s_x c_z \\ -s_y & s_x c_y & c_x c_y \end{pmatrix}.$$

After this computation, it follows that

$$\theta_x = \arctan \left(\frac{R_{32}}{R_{33}} \right),$$

$$\theta_y = -\arcsin \left(R_{31} \right), \quad (2.29)$$

$$\theta_z = \arctan \left(\frac{R_{21}}{R_{11}} \right).$$

The order of the composition of the rotations R_x, R_y, and R_z can be chosen differently. There are indeed twelve different ways to define the order of rotation, involving either rotations around two of the axes, or rotations around all three axes, see App. A.1. Due to this and other ambiguities, such as the choice of the (direction of the) matrix R, there is the potential of confusion concerning the sign of each pointing angle. Figure 2.2 illustrates how the sign of each angle is defined, according to the convention applied throughout this thesis. Expressed in yet another way, for any of the SF axes, imagine that the axis is pointing towards the observer. Then, a positive angle is obtained by rotating the S/C counter-clockwise, from that point of view.

In the case of GFO pointing angles, the matrix R is taken here to be $R_{\text{SF}}^{\text{LOSF}}$. It can be computed by

$$R_{\text{SF}}^{\text{LOSF}} = R_{\text{ECI}}^{\text{LOSF}} \cdot R_{\text{SF}}^{\text{ECI}}, \quad (2.30)$$

where $R_{\text{SF}}^{\text{ECI}}$ can be derived, for instance, from the S/C attitude quaternions provided as SCA1B data, via Eq. (2.16). The matrix $R_{\text{ECI}}^{\text{LOSF}}$ can be derived using Eq. (2.3), for which inertial positions of both S/C are needed as input.

In the following section, it is described how the S/C attitude can be determined, with a focus on attitude sensors for the GFO mission. In particular, different types of sensors will be presented, and it will be discussed how the pointing angles, roll, pitch, and yaw, can be derived in each case.

2.2   Attitude determination

In the previous section, it was discussed how S/C attitude can be described. This section is meant to give an overview of ways to determine S/C attitude, focusing on the GFO mission. Various methods and sensors for attitude determination are presented, commencing with dedicated attitude sensors in Sec. 2.2.1. A more general approach of attitude determination, known as Wahba's problem, is introduced in Sec. 2.2.2. In Sec. 2.2.3, a summary and comparison is given.
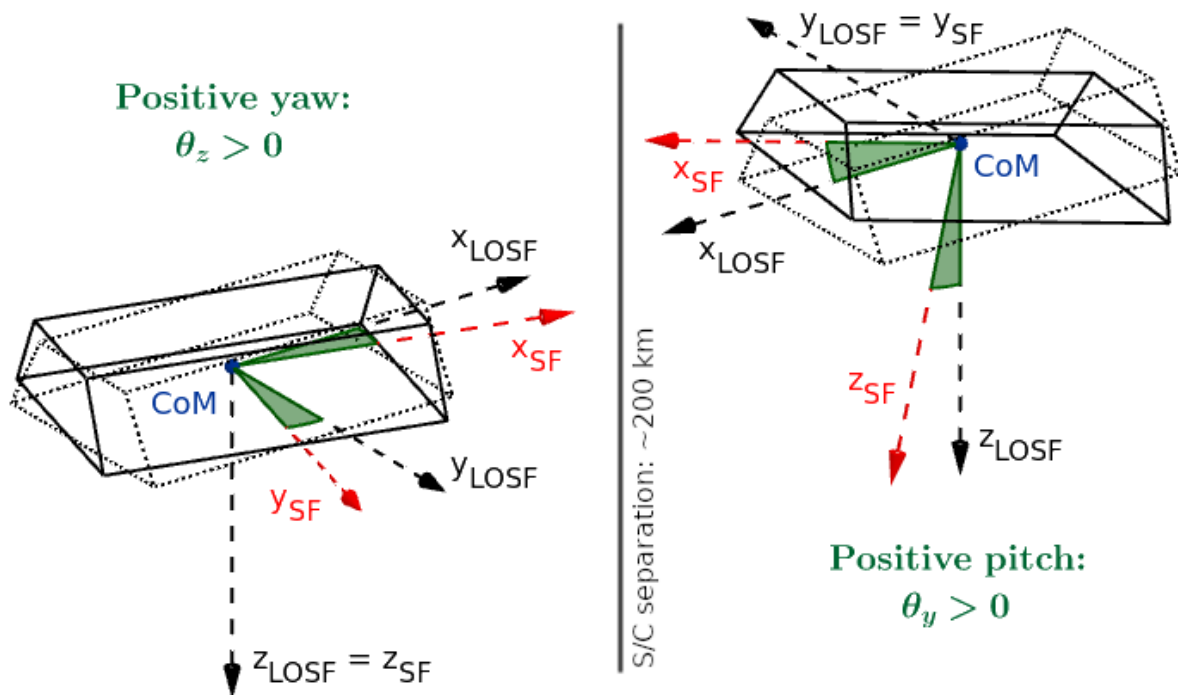
Figure 2.2: Sketch of the GFO satellites, indicating the definition of the signs of the pointing angles. By the definition used in this thesis, the left satellite has a small **positive** yaw angle, and the right satellite has a small **positive** pitch angle.

2.2.1   Attitude sensors

GFO hosts a variety of science instruments, whose measurements are related to the S/C attitude, and thus the pointing angles, which is of interest in this thesis. Figures 2.3-2.5 depict the accomodation of some of the GRACE instrumentation, which is similar for GFO. The most relevant attitude sensors on board GFO are the LRI fast steering mirror (FSM), the star camera assembly (SCA), the inertial measurement unit (IMU), and the accelerometer (ACC). The FSM measures pitch and yaw angles directly, independent of other sensors, however, it does not measure the roll angle. The IMU and the ACC measure angular velocities and accelerations, respectively, both of which can be integrated to obtain attitude quaternions w.r.t. inertial space. The SCA measures these quaternions directly, from which the matrix $R_{\mathrm{SF}}^{\mathrm{ECI}}$ can be derived. Once this matrix is obtained, pointing angles can be computed according to Sec. 2.1.3, using GPS-derived S/C positions, as provided in the GNV1B data product.

In the following, it is described how to obtain inter-satellite pointing angles from the main GFO attitude sensors mentioned above. Apart from these main sensors, measurements from other instruments also contain information on the S/C attitude, when combined with a priori knowledge, which is discussed afterwards. Finally, a comparison of the different attitude sensors is made.

LRI steering mirror

In the nominal fine-pointing mode, the ACS of a GFO S/C keeps the absolute values of the pitch and yaw angles below a few hundred microradian. While the LRI is not as sensitive to the roll angle, regarding pitch and yaw it requires more accurate pointing of the laser beam. This is ensured by the use of a fast steering mirror (FSM) on the optical bench, controlled by a feedback loop using the DWS technique [Abi+19]. The steering mirror orientation is downlinked at the same sampling rates as the LRI phase measurements, and can be directly
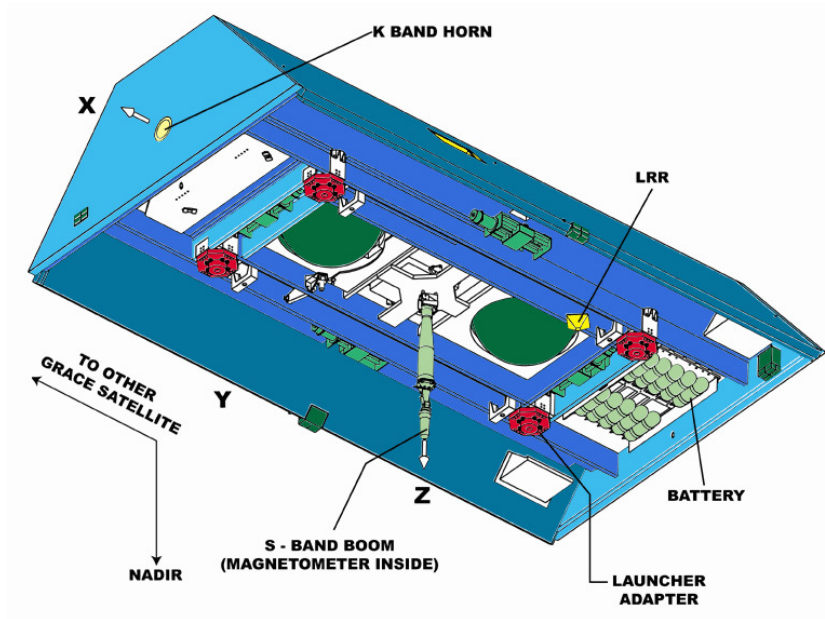
Figure 2.3: GRACE bottom view. Image credit: www.gfz-potsdam.de
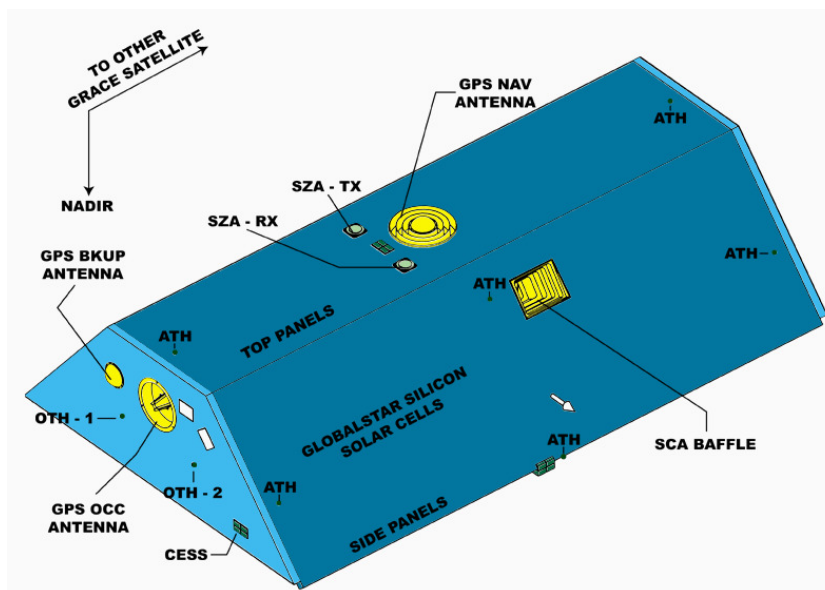
Figure 2.4: GRACE top view. Image credit: www.gfz-potsdam.de

converted to pitch and yaw angles. This conversion process was recently described in [Gos+21]. The FSM does not provide roll angles. The resolution of the measured and downlinked pitch and yaw angles is limited due to quantization of the steering mirror readout to about 1-2 μrad/$\sqrt{\text{Hz}}$ for each angle, cf. Figs. 2.6 and 2.7. When required for the data analysis within this thesis, white noise with a level of 1.3 μrad/$\sqrt{\text{Hz}}$ and 1.85 μrad/$\sqrt{\text{Hz}}$ was assumed for the pitch and yaw angles, respectively, based on experience with in-flight data. A more detailed description of the LRI laser beam steering is given in Sec. 3.1.
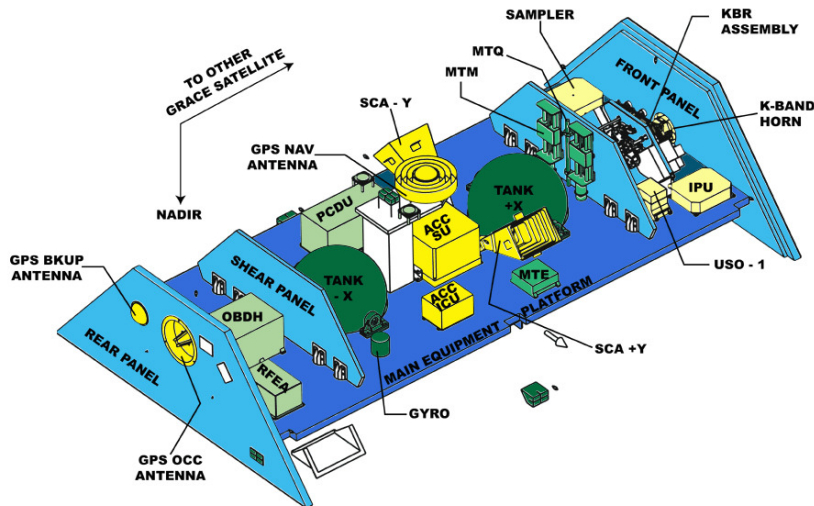
Figure 2.5: GRACE internal view. Image credit: www.gfz-potsdam.de

Star cameras

The working principle of the star camera assembly (SCA) is as follows. Rigidly mounted cameras take images of the surrounding celestial objects, i.e. stars. The positions of the stars identified in these images, their brightnesses and spectral types, are compared to a so-called star catalogue. An integrated computer determines the LoS vectors from the S/C towards the observed stars, and derives the rotation quaternions between the camera fixed frame and inertial frame. The mathematical problem of attitude determination based on vector measurements is called Wahba's problem [FB16], cf. Sec. 2.2.2. Solutions from different star camera heads can be combined, as described for example in [03].

For the GRACE mission, each satellite was equipped with two star camera heads, each having a field of view of ± 7 ° by ± 9.5 °, with both cameras being consistent down to below 0.1 mrad [Her+04]. The star cameras for GRACE and GFO were developed by the Technical University of Denmark (DTU). Occasionally, one of the cameras is blinded by incident light emitted by the Sun or reflected by the Moon. A lot of studies exist about SCA noise and errors, and its impact on GFR, e.g. [BF14; Iná+15; Har16; Gos+18; Gos18]. For instance, it has been shown in [Gos18] that during the periods when only data from one of the cameras is available, the quality of gravity field recovery is lowered significantly. Different reasons for this were identified, e.g. the AOC term in the KBR measurement can be determined less accurately. Also, the rotation of accelerometer data requires SCA data and is thus susceptible to degraded attitude information. On average, for GRACE, both heads were available at the same time merely about two thirds of the time, during some periods only half of the time [Gos+18].

In order to mitigate the disturbances due to camera blindings, three star camera heads were mounted on each GFO satellite, instead of two as for GRACE. Thus, if one camera is blinded by the Sun, there are still two functioning cameras available. During the entire year of 2019, according to the SCA1B RL04 data, roughly 72 % of the time, all three heads were used to generate SCA1B data; 28 % of the time, two heads were used; about 0.05 % of the time, only 1 head was used. Here 37 days during this period were excluded, i.e. 10 % of the whole time span, because there was no SCA1B data available. Similar numbers have been published in [Löw+19] for the first year in orbit. The amount of available cameras significantly influences the attitude determination and control. This even shows up in the LRI data, which records larger ranging variations during periods with a blinded camera, due to more frequent attitude thruster activations, cf. [Mis19]. Note that these ranging variations are not a measurement

error, but reflect actual S/C motion due to nongravitational accelerations. This topic will be investigated in detail in App. E.

The SCA1A data product contains the attitude quaternions provided by the individual star camera heads. For the purpose of this thesis, merely the SCA1B data product is used. The quaternions in the SCA1B data describe the rotation between SF and inertial frame, cf. Sec. 2.1.2. In the current release RL04 of Level-1B data, SCA1B data contains quaternions generated from SCA1A and IMU1A data, which are fused using a Kalman filter [Wen+19; HS19]. Without using IMU data, angles derived from star camera quaternions have significantly higher noise of about 20 µrad/$\sqrt{\text{Hz}}$. Even the fused attitude solution seems to have a slightly elevated spectrum for Fourier frequencies between 10 and 100 mHz. One possible cause of this could be suboptimal processing, which is being improved continuously. A promising attempt has been made recently in [Yan+22], for instance. See also Figs. 2.6 and 2.7 further below, which show amplitude spectral densities (ASD) of pointing angles measured by different attitude sensors.

Gyroscopes

Each GFO satellite carries an Astrix-120 inertial measurement unit (IMU) manufactured by Airbus Defence & Space [Gat16]. Each IMU hosts 4 laser fiber gyroscopes, measuring the angular velocities in 4 different axes. The angular velocities, measured for the individual gyroscope axes, are accumulated, yielding integrated angles. These angles are reported in the IMU1A and IMU1B data products, both with a sampling frequency of 8 Hz, and with the unit degree. The gyroscope axes, arranged in a tetrahedral configuration, are given in [Wen+19]. In the GRACE mission, unfortunately, the IMU on GRACE-1 failed shortly after launch, and the IMU on GRACE-2 was switched off [HS12; Her+12]. As opposed to GRACE, the GFO IMU seem to work well and have proven to provide useful data.

Since the IMU data provides accumulated angles, which are wrapped when reaching a certain limit, they have to be unwrapped first. Let the time series of the unwrapped angles referring to gyroscope i be denoted by $\alpha_i(t)$, $i = 1, 2, 3, 4$. These can be converted from degree to radian. Afterwards, angular velocities are obtained by taking the derivative, i.e. the angular velocities $\gamma_i(t)$ referring to gyroscope i are given by

$$\gamma_i(t) = \frac{\pi \text{ rad}}{180\,^{\circ}} \cdot \frac{\mathrm{d}}{\mathrm{dt}} \alpha_i(t), \tag{2.31}$$

for a given point in time t. This way, $\gamma_i(t)$ has the unit rad s^{-1}. In the following, it is described how these angular velocities can be transformed to angular velocities referring to the SF.

Let $\vec{g}_i = (g_{i,x}, g_{i,y}, g_{i,z})^T$ denote the reference axis for gyroscope i, given in SF, with $|\vec{g}_i| = 1$ for all i. Then, the angular velocity $\gamma_i(t)$ measured by this gyroscope can be decomposed as

$$\gamma_i(t) = g_{i,x}\omega_x(t) + g_{i,y}\omega_y(t) + g_{i,z}\omega_z(t) = \vec{g}_i^T \vec{\omega}(t), \tag{2.32}$$

where $\vec{\omega}(t) = (\omega_x(t), \omega_y(t), \omega_z(t))^T$ is the angular velocity vector of the S/C, given in SF. Since Eq. (2.32) holds for each gyro, this can be written in matrix form as

$$\begin{pmatrix} \gamma_1(t) \\ \gamma_2(t) \\ \gamma_3(t) \\ \gamma_4(t) \end{pmatrix} = G \cdot \begin{pmatrix} \omega_x(t) \\ \omega_y(t) \\ \omega_z(t) \end{pmatrix} = G \cdot \vec{\omega}(t), \tag{2.33}$$

where G is the 4x3-matrix

$$G = \begin{pmatrix} \vec{g}_1^T \\ \vec{g}_2^T \\ \vec{g}_3^T \\ \vec{g}_4^T \end{pmatrix}. \tag{2.34}$$

With $\omega_x(t), \omega_y(t), \omega_z(t)$ being the unknowns, for each t, Eq. (2.33) is an overdetermined system of linear equations. It can be solved by computing the pseudo-inverse of G, denoted by G^+, which is a 3x4-matrix. Then,

$$\vec{\omega}(t) = G^+ \cdot \begin{pmatrix} \gamma_1(t) \\ \gamma_2(t) \\ \gamma_3(t) \\ \gamma_4(t) \end{pmatrix} \tag{2.35}$$

is the best fit of the system (2.33) in the least squares sense. This way, the measured angular velocities can be converted to SF. An alternative way is to use only three of the four gyros, since in theory one of the four is redundant. In that case, G is a 3x3 matrix, e.g. $G = (\vec{g}_1, \vec{g}_2, \vec{g}_3)^T$, and the usual inverse G^{-1} can be used in place of the pseudo-inverse in order to compute $\vec{\omega}(t)$. In fact, in the current release RL04 of the official Level-1 data, merely the measurements of gyroscopes 1-3 are reported. The gyroscope axes measured in the IMU frame are provided in [Wen+19], for both GFO satellites, as well as the transformation matrices needed to rotate these axes to the SF. The axis vectors, rotated to SF according to [Wen+19], above denoted by $\vec{g}_i$, $i = 1, 2, 3, 4$, are given in Tab. 2.1.

Table 2.1: Gyroscope axes in SF for GFO satellite 1 (GF1) and GFO satellite 2 (GF2).

Satellite	Axis	Components in SF		
		x	y	z
GF1	$\vec{g}_1$	-0.471053692158870	0.817220193736133	-0.332053571059512
	$\vec{g}_2$	0.942798065066750	0.000479684579529	-0.333364032866619
	$\vec{g}_3$	-0.471543331201393	-0.815925135929739	-0.334534092967415
	$\vec{g}_4$	-0.000547156582651	-0.001133931001332	0.999999207409765
GF2	$\vec{g}_1$	-0.472161373934852	0.816056005487263	-0.333341015886321
	$\vec{g}_2$	0.942760507517236	0.001274336049879	-0.333468141706936
	$\vec{g}_3$	-0.470935739138852	-0.816832866273961	-0.333172024900661
	$\vec{g}_4$	-0.000079129944766	0.000412221502813	0.999999911905939

Once the angular velocities in SF are obtained, they can be integrated using Eq. (2.19). Initial values can be taken from SCA data. The obtained quaternions can be used to derive pointing angles from Eq. (2.24). Because of error propagation in the integration process, the integrated quaternions are only useful when regarding relatively short time spans, or when the IMU data is fused with other sensors, as is done to obtain the SCA1B data [Wen+19]. For the purpose of this thesis, the IMU1B RL04 data product is used. However, the IMU1A data has the same format as the IMU1B data, and it can be used to derive attitude quaternions or pointing angles in the same way.

Another crucial part in the derivation of pointing angles from IMU data is to estimate the angular velocity bias for each gyroscope, and subtract it before the integration. Otherwise, the bias accumulates during integration and results in an artificial drift of the pointing angles, which propagates quickly, rendering the resulting quaternions useless. Since the SCA observations seem to be very reliable at lower frequencies, the IMU bias can be estimated by comparison with SCA data. However, note that the bias stability of the Astrix-120 over 1 hour is of the order of $0.01\,°\,h^{-1}$, approximately $0.0485\,\mu rad\,s^{-1}$, according to the data sheet provided by the manufacturer Airbus Defence & Space. This suggests that it is not sufficient to estimate the bias once and apply that bias for all times.

The specification of the Astrix-120 IMU on the noise of the measured angular rates is, according to the data sheet, an angle random walk (ARW) of $0.0016\,°/\sqrt{h}$. In terms of an ASD, this is equivalent to $0.6582\,\mu rad/s/\sqrt{Hz}$, assuming white measurement noise. By

integration, this translates to pink Euler angle noise:

$$\text{ASD}(\theta) = 0.1048 \left(\frac{f}{\text{Hz}} \right)^{-1} \text{µrad}/\sqrt{\text{Hz}}, \tag{2.36}$$

where θ denotes the integrated angle. I.e., the angle noise is approximately 1 µrad/$\sqrt{\text{Hz}}$ at f=100 mHz, decreasing with a f^{-1} slope. This number is compatible with the author's analysis of the real data, cf. Figs. 2.6 and 2.7 further below.

Accelerometers

One Super STAR (Space Three-axis Accelerometer for Research) accelerometer on board each S/C measures nongravitational angular accelerations, in addition to the nongravitational linear accelerations [Tou+12; Kor+19]. The accelerometers (ACCs) for GRACE and GFO were built by the French national aerospace research centre (ONERA). The measured angular accelerations are reported in the ACC1A data product, with a sampling frequency of 10 Hz. They are given in the AF, cf. Sec. 2.1.1, which differs from the SF merely by a permutation of the frame axes. Namely,

$$\dot{\vec{\omega}}_{\text{SF}} = \begin{pmatrix} 0 & 0 & 1 \\ 1 & 0 & 0 \\ 0 & 1 & 0 \end{pmatrix} \cdot \dot{\vec{\omega}}_{\text{AF}}, \tag{2.37}$$

where $\dot{\vec{\omega}}_{\text{SF}}$ and $\dot{\vec{\omega}}_{\text{AF}}$ denote the angular accelerations, given in SF and in AF, respectively.

Once the angular accelerations are available in SF, they can be integrated using Eq. (2.19), in order to obtain quaternions. From these quaternions, the pointing angles can be derived in the same manner as from the star camera quaternions, by using Eq. (2.24).

Because of error propagation in the integration process, pointing angles derived from accelerometer data is only useful for a very short time. Note that this restriction is, naturally, even more serious than for the IMU, since here one has to integrate twice. Nevertheless, the noise of the derived pointing angles is decreasing rapidly towards higher Fourier frequencies, with a f^{-2} slope, so that ACC data is well suited for observing very fast angular S/C movements. ACC angular accelerations can be fused with other attitude sensors such as the SCA, although this requires some care due to aliasing of linear into angular accelerations and 1/rev tone errors [HS19].

Coarse Earth and Sun Sensors

The coarse Earth and Sun sensors (CESS) provide attitude information by estimating the vectors pointing from the S/C to the Sun and to the Earth, based on thermistor measurements. The CESS for GRACE and GFO were manufactured by SpaceTech Immenstaad. The system consists of six sensor heads, orthogonally mounted to the S/C, with one head at each side. The accuracy of the derived attitude is about 5-10 ° for the Earth vector, and 3-6 ° for the Sun vector, depending on the orbit geometry [Her+04]. The CESS can provide a crude sense of orientation, if the satellite has to switch into a safe mode, cf. Sec. 2.3.

Magnetorquer input currents

Previously, it has been shown that the orientation of a S/C can be obtained by integrating angular accelerations, assuming that these angular accelerations are available, as well as initial conditions. Now, apart from accelerometer data, the angular accelerations can also be obtained via Eq. (2.20), provided the torque and the S/C moment of inertia matrix are known. In the GFO mission, part of the control torque is realized using MTRs, cf. Sec. 2.3.1 further below. There are periods, where the magnetic control torque is in fact the dominating torque, namely

during a rotation maneuver. Since the MTR input currents are reported in the MAG1B data, one can compute the magnetic control torque. Hence, for this short period, the pointing angles can be approximated by integrating these torques, neglecting environmental torques which are acting on the S/C. This method will indeed prove to be useful, e.g. for the considerations on the design of satellite rotation maneuvers, in Sec. 4.3.

2.2.2 Wahba's problem

A general way to estimate a satellite's attitude is by comparing local vector measurements to an a priori model of the same observable. The mathematical problem of determining the best estimate of the attitude, given a set of vector measurements and their modeled values, has become known as *Wahba's problem*, after Grace Wahba, who first defined it in 1965 [Wah65]. In fact, many attitude determination methods are based on solving this problem. Here the problem is described, and some well established methods to solve it are listed. The reader is referred to [FB16] for a more detailed description of Wahba's problem and related topics.

Suppose one is given a set of vector observations in the satellite-fixed frame, for example the ambient magnetic field measured by a magnetometer. If one has accurate knowledge of the same observable in a known reference frame such as ECI, e.g. from a model, the measurement contains information about the relative orientation of the two frames, and thus about the S/C orientation. To convey the principle of this idea, consider an Earth orbiting S/C, knowing that it is currently located above the geomagnetic north pole. If this S/C measures the ambient magnetic field, it gains some information on its attitude, since it is known that the geomagnetic field lines are nearly radial in this region. That raises the question, whether it is possible to derive the corresponding rotation matrix in this case. Namely, one is interested in the rotation matrix $R_{\mathrm{SF}}^{\mathrm{ECI}}$. It turns out that while one such vector measurement is not sufficient, two independent vector measurements already yield an estimation of the matrix $R_{\mathrm{SF}}^{\mathrm{ECI}}$.

In order to state the problem in a stringent way, let $\vec{v}_i, i = 1, \ldots, N$ denote a set of vector observations in SF, and $\vec{w}_i, i = 1, \ldots, N$ the corresponding vectors predicted by a model, given in ECI. Desired is a rotation matrix R satisfying

$$\vec{w}_i = R\vec{v}_i, \tag{2.38}$$

for $i = 1, \ldots, N$. Recall that the group $SO(3)$ of three-dimensional rotations has itself dimension 3. Therefore, the system (2.38) is overdetermined if $N \geq 2$. Moreover, both the measurements and the model contain uncertainties, which is why the equations (2.38) would anyway not be expected to hold. Rather, one is interested in the rotation matrix R which minimizes the residuals in the least squares sense. That is, find

$$\min_R \sum_{i=1}^{N} \|\vec{w}_i - R\vec{v}_i\|^2. \tag{2.39}$$

A variety of algorithms for solving Wahba's problem exist. The most prominent ones are based on Davenport's q-method [Kea81], which reduces the problem to finding the largest eigenvalue of a specific matrix that can be constructed from the vectors $\vec{v}_i, \vec{w}_i, i = 1, \ldots, N$. Some popular algorithms with references are listed below.

- three-axis attitude determination (TRIAD) [SO81]

- quaternion estimator (QUEST) [SO81]

- estimator of the optimal quaternion (ESOQ) [CBO04]

- singular value decomposition (SVD) [Mar88]

- polar decomposition (PD) [Bar92]

- Euler-n [Mor95b]

- fast optimal matrix algorithm (FOAM) [Mar93]

- energy approach algorithm (EAA) [Mor95a]

- factored quaternion algorithm (FQA) [YBM08]

All of these methods are capable of finding an optimal estimation, they differ mainly in the computational efficiency of the algorithms.

Moreover, the problem can be generalized by applying weights a_i, in order to incorporate the level of confidence in the different observations, i.e. find

$$\min_R \sum_{i=1}^N a_i \left\| \vec{w}_i - R\vec{v}_i \right\|^2 . \tag{2.40}$$

Most systems of S/C attitude determination are applying a solution to Wahba's problem. Perhaps one of the most prominent examples for a vector observation $\vec{v}_i$ is the Earth's magnetic field. Determining the direction towards any object is also a vector measurement. If the same vector is known from an independent source, such measurements can yield attitude information. Most apparent examples are the direction towards the Sun or the Earth, as in the CESS. The other most obvious vector observable in the vicinity of the Earth is the gravity gradient, which can be measured with a gravity gradiometer.

Thus, the sensors and methods discussed so far are almost exhaustive. Certainly, there exists some variety in the details, such as different techniques of determining the direction of the incoming light, resulting e.g. in different types of Sun sensors. Moreover, there exist alternative types of Earth sensors, or Earth horizon sensors, either scanning or static, which can determine the direction towards the geocenter with an accuracy up to 1 °. Finally, a few more words shall be spent on two specific ways of attitude determination, one using magnetometers and one using Global Positioning System (GPS) receivers.

Magnetometers

In the sense of Wahba's Problem, magnetometer measurements contain information on the S/C attitude, by measuring the ambient magnetic field, which is that of the Earth. Since there are relatively accurate models of this magnetic field, these are the type of vector observations which can be used for attitude determination, as has been illustrated previously. Magnetometers are in fact part of the ACS for GRACE and GFO, when the system is in safe mode [Her+04], cf. Sec. 2.3.1. However, the magnetometer must be combined with at least one more vector observation, in order to yield an attitude solution.

Same as for GRACE, the GFO magnetometers are installed at the nadir side of each S/C. The actual measurement of the magnetic field is taken outside the S/C, in the S-Band boom, cf. Fig. 2.3, whereas the processing unit is located inside the S/C. The accessible measurement range is $\pm$ 50 µT and the resolution is about 25 nT.

When a S/C is in the vicinity of other planets, magnetometers could be used for attitude determination as well, provided the object has a measurable magnetic field, and a model of it as well as the S/C positions are available.

GPS-based attitude determination

The measurements of GPS receivers can also be utilized for attitude determination, e.g. by using multiple antennas. The task is then to determine the vectors towards the GPS satellites

by comparing phase measurements, resulting in another application case of Wahba's problem. For further reading, the reader is referred to [Gio17; AW96; CP01; DKL09; TP12]. The GFO satellites also host GPS antennas, cf. Figs. 2.3 and 2.5, however, to the knowledge of the author, vector measurements from GPS data have not been used for GRACE attitude determination.

GPS-based attitude determination has some disadvantages, such as low accuracy, i.e. possible errors of the order of 1 °. It requires direct view of a sufficient amount of GPS satellites. Nonetheless, there are also some advantages, e.g. principally low implementation effort. Moreover, it requires no moving parts, and thus has no disturbing effect on any of the science instrumentation.

2.2.3   Comparison of attitude sensors

Although there are other sources of S/C attitude information, the main attitude sensors on board GFO, which are suited for deriving pointing angles, are: FSM, SCA, IMU, ACC. Figures 2.6 and 2.7 show examples of time series and ASDs of pointing angles, for GF1 and GF2, respectively. The angles were derived from SCA data without sensor fusion (gray; labeled *SCA only*), steering mirror data (red; labeled *FSM*), fused SCA1B data (blue; *SCA1B*), and IMU1B data (green; *IMU1B*), based on data from a period of 1000 seconds in January 2019. Note that the angles from IMU1B data were obtained by integration, which requires the initial S/C attitude state at $t = 0$ as input, cf. Sec. 2.2.1. This initial attitude in terms of quaternions was taken from SCA1B RL04 data. For the time series plots, the mean value over the 1000 s period was subtracted for each of the shown time series, for the sake of comparability. The spectra were computed using the LPSD method [TH05].

Using ACC angular accelerations, after 1000 seconds, the integrated pointing angles already accumulate a large integration error. However, when regarding short time intervals, the angles derived from ACC data are compatible with angles derived from other attitude sensors, see Fig. 2.8. The left plot exemplarily shows the GF1 pitch angle, derived from different sources, here including ACC1A data, but excluding *SCA only* data. The plotted data was measured during a CMC pitch maneuver, cf. Sec. 4.1, executed on 16 January 2019. Again, the angles derived from IMU1B as well as from ACC1A data were obtained by integration, as described in Sec. 2.2.1. For each time series, the mean over the shown 180 s period was subtracted, for better comparability. The right plot of Fig. 2.8 shows the difference between the SCA1B time series and each of the other time series. All angles for these plots were filtered according to Sec. 5.1.6. For longer time spans, the potential of ACC angular accelerations lies in sensor fusion, i.e. in the combination with other data.

Table 2.2 summarizes the sources of attitude information that were treated in this section. In the following section, methods of attitude control will be discussed, focusing on the GFO ACS.

2.3   Attitude control

Most satellite missions require attitude control, since there is usually a preferred S/C orientation. This topic is especially important for GRACE and GFO, where the main science observable, the biased range, can only be measured if accurate pointing is assured. The KBR instrument is able to continue measurements with a pointing deviation of several degrees, where 1 ° corresponds to 17.45 mrad. However, the quality of the KBR measurements suffers from imperfect pointing, so that the deviation should still be kept low [Ko08]. The LRI needs even more accurate pointing control, down to a few mrad, to ensure instrument operation. The laser beam itself has to be steered with even better accuracy, below 100 µrad. However, this beam steering is performed by the LRI, using the FSM, cf. Sec. 3.1.

Figure 2.6: Roll (top), pitch (middle) and yaw (bottom) angles of **GF1**, based on different data types. Here for a period of 1000 seconds during January 14, 2019. Left: ASDs. Right: time series.

An attitude and orbit control system (AOCS) is a system of sensors and actuators, together with a control loop, which controls the S/C attitude, as well as the orbit. Here one is not interested in orbit control, thus the term attitude control system (ACS) is used, albeit the two things are connected and AOCS is the common term. The attitude control mechanisms utilized by the ACS of the GRACE and GFO missions are magnetic torque rods (MTR) and cold gas thrusters. Both of them are of some relevance for the work presented in this thesis. They are therefore described in detail in the following section. Afterwards, an overview of other types of attitude actuation is given. The attitude control devices / mechanisms discussed in this section are summarized in Tab. 2.4.
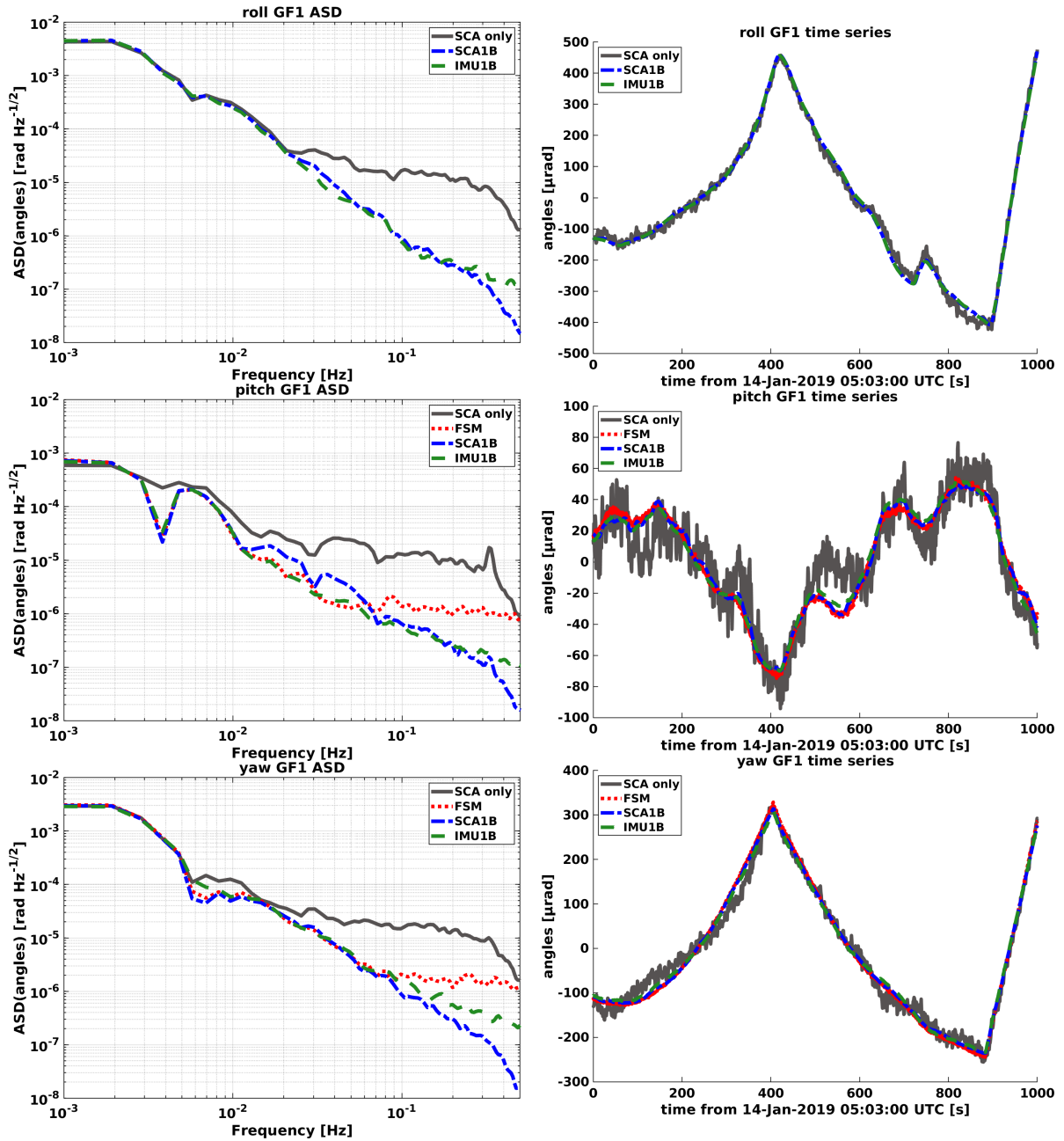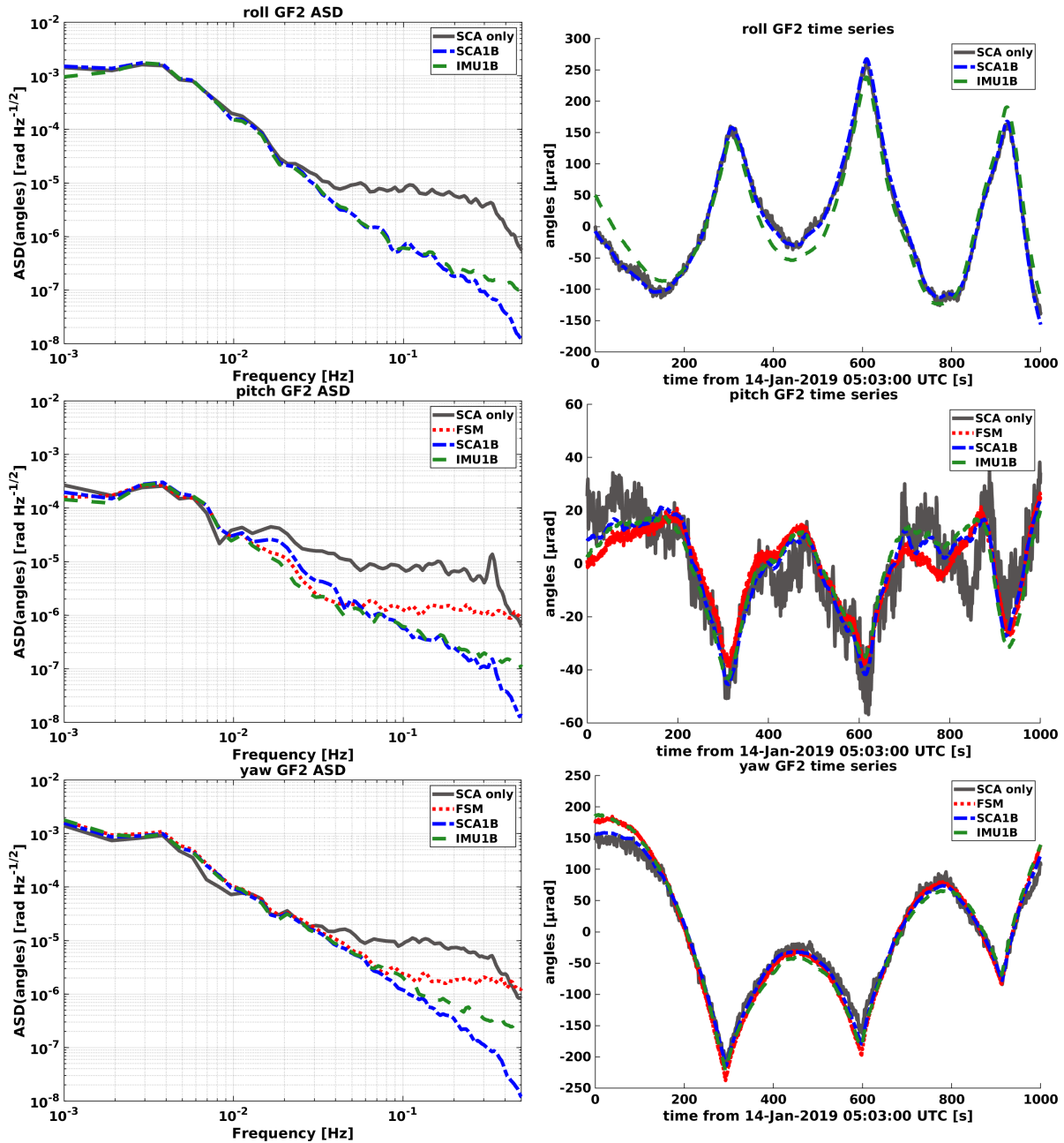
Figure 2.7: Roll (top), pitch (middle) and yaw (bottom) angles of **GF2**, based on different data types. Here for a period of 1000 seconds during January 14, 2019. Left: ASDs. Right: time series.

2.3.1 Attitude control from GRACE to GFO

Many aspects of the ACS for the GRACE satellites, which is described in [Her+04], were adapted for the GFO mission. The GFO ACS is described in [Cos+21]. It consists of a toolkit of sensors, actuators, and data handling. The attitude sensors which are available to the ACS are the SCA, the CESS, and the IMU. The GFO ACS benefits from a third star camera head, whereas GRACE had merely two to its disposal. Further improvement of the attitude information is due to the availability of a high precision IMU with four axes. Measurements from the fluxgate magnetometers may be used additionally. Furthermore, GPS receivers are used to obtain the S/C positions, which are used by the ACS directly, but also downlinked

Figure 2.8: Comparison of different attitude sensors, from a pitch GF1 maneuver during 23 June 2019. Left: bandpass filtered pointing angles from different sources. Right: residuals (differences to SCA1B).

and processed on ground. High-precision orbit predictions are uploaded back to the S/C. Note that attitude information from the LRI FSM is not used by the GFO ACS, however, this may be done in future missions.
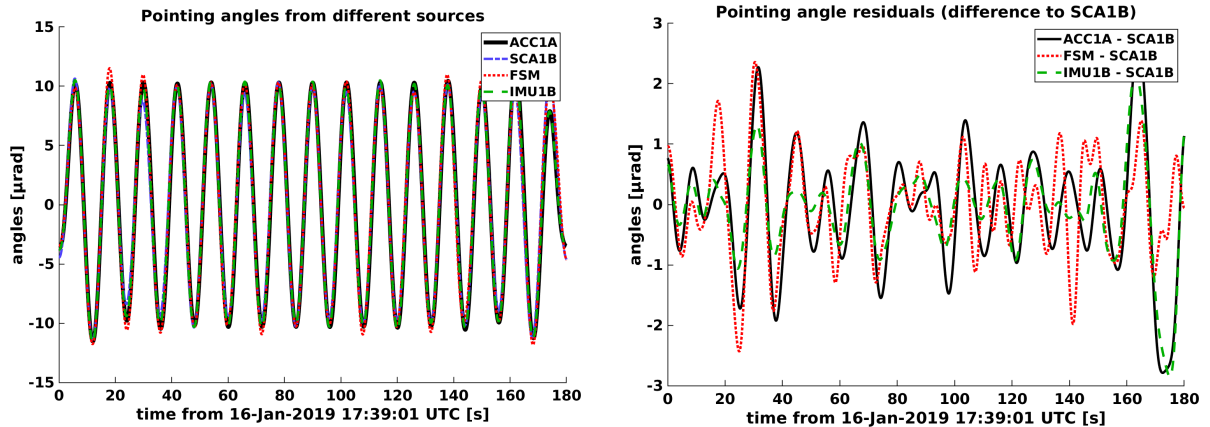
The sensors mentioned above enable the ACS to determine the actual attitude of the S/C, as well as the desired attitude. With this input, the required action of the control mechanism is computed, resulting in commands to the attitude actuators. These are, for GRACE as well as GFO, MTRs and a cold gas propulsion system, i.e. attitude thrusters. These actuators shall be characterized in dedicated sections below. The pointing requirements have been tightened for GFO, which is good in general and vital for the LRI. I.e., the deadbands of the thruster control have been lowered to 250 µrad for pitch and yaw, and to 2.5 mrad for roll (default values in the nominal fine-pointing mode) [tea19]. The deadbands on the GRACE satellites had been 3, 3, and 4 mrad for roll, pitch, and yaw, however, these values were varied slightly throughout the mission, cf. [HS12]. There is significantly less fuel consumption on GFO compared to GRACE [Lan+20]. Battery capacity was increased from 18 to 78 A h, allowing to dispense with the fuel-intensive yaw steering during ACS safe mode, see [Löw+19] for details.

The GRACE ACS was designed to have a minimum life time of 5 years, which it exceeded by more than 10 years. Among other reasons, the prolonged lifetime was possible due to an optimized fuel and battery management, cf. [HS12; Her+12]. By mid 2017, on both S/C some of the battery cells failed and the rest were continuously degrading [Löw+19; Mül+19]. This limited the usage of MTRs, which significantly increased N_2 gas consumption due to attitude thruster activation. As a consequence, controlled decommissioning of the satellites was performed in the end of 2017, more than 15 years after mission launch.

In the following, the attitude control via MTRs and cold gas thrusters is described.

Magnetic torque rods

At the altitude of the GFO satellites of about 500 km, the magnitude of the Earth's magnetic field is of the order of some tens of µT, cf. Fig. 4.6. This is sufficiently strong for the purpose of S/C attitude control by means of MTRs. An MTR, also called magnetic torquer or magnetorquer, consists of an electromagnetic coil, i.e. a conductive wire, which is twisted

Table 2.2: Overview of different attitude sensors available in the GFO mission. The given noise levels for FSM, SCA, IMU, and ACC, are empirical values from the author's experience with the data, which are merely meant to allow a rough comparison. In reality, the noise levels may be slightly different for the different angles (roll, pitch, yaw), and they may vary with time.

Device / technique	Advantage	Disadvantage	Noise level of derived pointing angles
FSM	low noise; measures pitch and yaw angles, referring to the LoS; completely independent of other sensors	does not measure roll	~ 1.3 µrad/$\sqrt{\text{Hz}}$ for pitch and ~ 1.85 µrad/$\sqrt{\text{Hz}}$ for yaw (due to quantization)
SCA	measures the absolute S/C attitude w.r.t. inertial space; very low long-term error	less accurate than other sensors for high Fourier frequencies	~ 20 µrad/$\sqrt{\text{Hz}}$ white noise above 40 mHz (without sensor fusion)
IMU	accurate measurement of angular velocities; good attitude determination at high frequencies	angular rates must be integrated to obtain the S/C attitude; does not measure the orientation in inertial space	$\sim 0.1 \left(\frac{f}{\text{Hz}} \right)^{-1}$ µrad/$\sqrt{\text{Hz}}$; e.g. 1 µrad/$\sqrt{\text{Hz}}$ at 0.1 Hz
ACC	accurate measurement of angular accelerations; good attitude determination at high frequencies	angular rates must be integrated twice to obtain the S/C attitude; does not measure the orientation in inertial space	$\sim 0.013 \left(\frac{f}{\text{Hz}} \right)^{-2}$ µrad/$\sqrt{\text{Hz}}$; e.g. 1.3 µrad/$\sqrt{\text{Hz}}$ at 0.1 Hz
CESS	robust & reliable	coarse	**no pointing angles**
derivation from MTR currents (not used in the GFO mission)	useful as additional information during S/C rotation maneuvers, and for maneuver simulation	restricted to short time spans, during which the magnetic torque is the dominating torque	depends on the accuracy of modeled torques, magnetic field information, and numerical integration

around a nickel alloy core [Pet10]. By applying a voltage, a magnetic dipole moment (MDM) in the direction of the core is created. Due to the Lorentz force, the combination of the MDM with the geomagnetic field produces a mechanical torque, which will tend to align the two vectors of MDM and magnetic field [Wer78].

The MT30-2 rods for GRACE and GFO were designed and manufactured by the Zentrum für Angewandte Raumfahrttechnologie und Mikrogravitation (ZARM) in Bremen, Germany. The material of the core is nickel alloy. There is one MTR for each SF axis, each having a mass of about 1400 g and a length of 40 cm. A schematic of the MTR is depicted in Fig. 2.9. The second coil has been integrated merely for redundancy [Pet10]. By controlling the input current of the individual rods, a magnetic dipole moment in any desired direction can be achieved. For each rod, the dipole moment can be computed by

$$\vec{m} = \vec{I} \cdot 250 \text{ m}^2, \tag{2.41}$$

Table 2.3: Overview of different attitude control devices / techniques. Magnetic torque rods and cold gas thrusters (in bold letters) are used in the GFO mission.

Device or technique	Advantage	Disadvantage	Limitations
Magnetic torque rods	pure torque; high accuracy; no fuel consumption	requires ambient magnetic field; possible hysteresis	strength of geomagnetic field $\vec{B}$; maximum MTR input current; angle between $\vec{B}$ and torque rod; electrical power consumption
Cold gas thrusters	large torques; high reliability	fuel consumption; strict requirements on S/C integration; residual linear accelerations; fixed torque; tendency to overshoot	available amount of fuel; potential disturbance of sensitive science instruments
Reaction wheels	high accuracy; large torque range; low power consumption; high reliability	not quiet; saturation; large volume and mass	maximum spin rate
Control moment gyros	high accuracy; high power efficiency	not quiet; saturation; large volume and mass; singularities	maximum spin rate
Solar sails	no internal power consumption	small effect; requires direct view of the Sun; S/C more prone to space debris	incident light has a fixed direction
Spin stabilization	beneficial for specific applications	no active attitude control	maximum tolerance on angular rates
Gravity gradient stabilization	no power consumption	no active attitude control; S/C more prone to space debris; may need damping	strength of gravitational field
Aerodynamic stabilization	no internal power consumption	decreases orbit altitude	atmospheric density; only feasible in low Earth orbit

Table 2.4: Overview of different attitude control devices / techniques. Magnetic torque rods and cold gas thrusters (in bold letters) are used in the GFO mission.

with $\vec{m}$ being the MDM of one of the torque rods, and I the input current. For GFO, these currents are provided in the MAG1B data product. Denoting by $\vec{B}$ the Earth's magnetic field, the resulting torque $\vec{\tau}_m$, called the magnetic torque, is then given by

$$\vec{\tau}_m = \vec{m} \times \vec{B}. \tag{2.42}$$

$\vec{\tau}_m$ is one of many components of the total torque acting on the S/C.

The torque rods can use a current of up to 120 mA, however, the maximum current has been limited to 110 mA for GFO. This results in a maximum MDM of 27.5 A m^2, as opposed to 30 A m^2 for GRACE. The achievable magnetic control torque has lowered due to this and
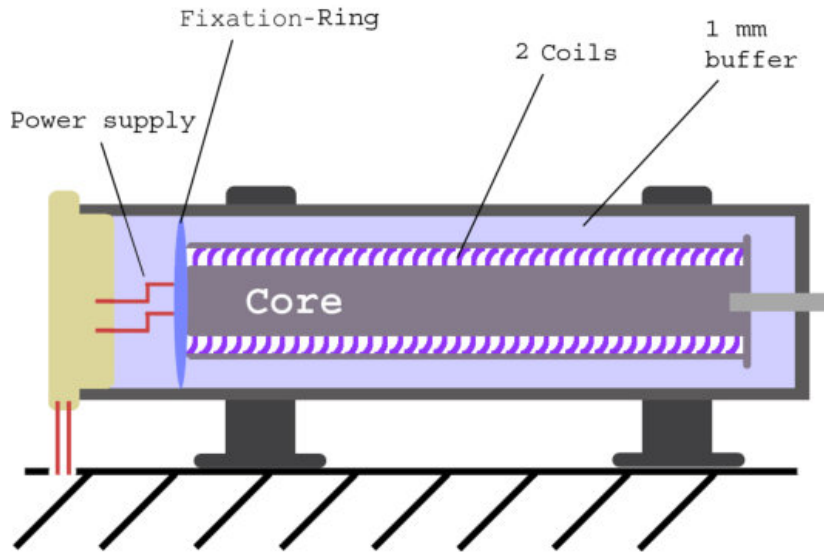
Figure 2.9: Schematic of a magnetic torque rod for GRACE, manufactured by the ZARM. Image adopted from [Pet10].

the fact that the mass of the satellites has been increased from roughly 475 kg per S/C for GRACE [Gat16] to 601 kg mass at launch for GFO [Wen+19; Kor+19]. Based on measured orbit, attitude, and magnetic field data for a GFO satellite, magnetic control torques as large as 1.5 mN m, 1.7 mN m, and 0.9 mN m for roll, pitch, and yaw axes, respectively, could be possible. This is assuming that all torque rods were to be used to full capacity, which they are typically not, except during rotation maneuvers.

The MTRs are used by the ACS with priority, because they need no fuel and produce no linear accelerations. When the required control torque axis is nearly parallel to the Earth's magnetic field vector, e.g. near the equator for roll and near the poles for yaw, the magne-torquers cannot produce a torque around that axis. In such a case, the attitude thrusters are activated, which are described in the following.

Cold gas thrusters

The cold gas propulsion system for GFO is very similar to that of GRACE, which is described in detail in [Sch00]. The ACS for GFO utilizes a Gaseous Nitrogen (GN2) cold gas system with six pairs of thrusters, with a force of 10 mN per thruster, in addition to the orbit control thrusters. These function by using valves, which can be opened in order to expel the gas, which creates a thrust, i.e. a force $\vec{F}$ in the direction opposite to the outstreaming gas. The torque τ due to an attitude control thruster is given by the cross-product of the position vector $\vec{r}$ of the location at which the force $\vec{F}$ is acting, and the force vector itself, i.e.

$$\vec{\tau} = \vec{r} \times \vec{F}. \tag{2.43}$$

In addition to the torque, attitude control thrusters always produce a linear acceleration in the direction of the thrust force $\vec{F}$. Thus, they must be used in pairs, pointed in opposite directions, in order to cancel this linear acceleration. It is also possible to choose constellations of three or more thrusters per rotation axis, as long as the linear accelerations cancel out. Due to residual misalignments, the S/C will always be subject to a residual linear acceleration, when a thruster is firing, cf. App. E.1. The gas storage and consumption should be organized in such a way that the CoM is not shifted by thruster usage.

As mentioned above, the attitude thrusters are only activated if the control with torque rods is insufficient. More precisely, the GFO ACS uses so-called deadbands, i.e. fixed limits

for the pointing angles. Only if the estimated pointing deviation moves out of this deadband, the attitude thrusters are activated. This type of control is also referred to as "bang-bang" control. The GFO attitude thrusters apply an adaptive strategy, whereby the length of a pulse depends upon the strength and the result of the preceding ones [Her+04]. Figure 2.10 shows the placements of attitude thrusters for the GFO satellites. They are always activated in pairs. The activation of one such pair results in a torque of the order of 10 mN m.
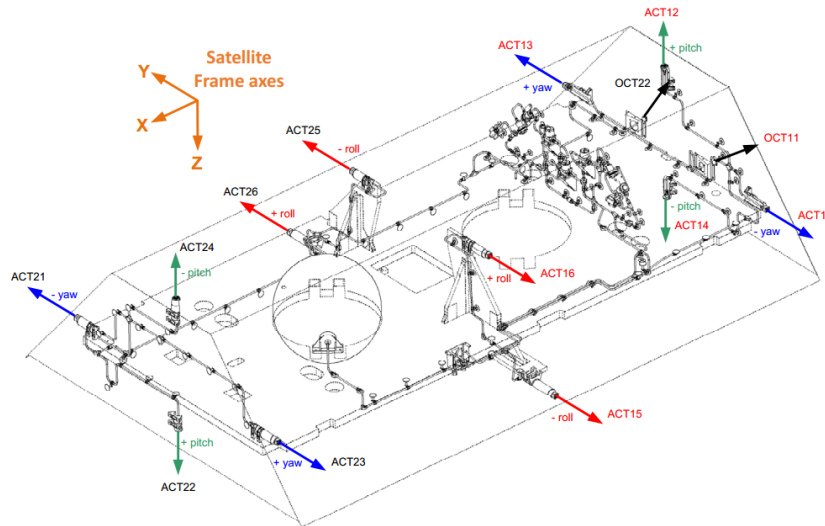

Figure 2.10: GFO thruster accomodation. Image credit: [Wen+19].

2.3.2   Other attitude control mechanisms

In general, attitude control can be divided into active and passive control, where active means that there is a control loop, which causes some kind of reaction based on the inputs from the ACS sensors. Some principles of attitude control can be used either in an active or passive way. A few methods are listed here. A good reference for some background on S/C attitude control is [MC14], for example.

- Attitude control via **magnetic dipole moments** are described below.

- Angular momentum storage and exchange devices (**reaction wheels**, **control moment gyros**) are described below.

- There are other types of **thrusters**, e.g. ion thrusters, which accelerate ions using electricity, which can be gained e.g. from solar panels, whereas the ion material is being used up.

- **Solar sails** use the fact that incident photons, i.e. from the Sun, transmit kinetic energy to the S/C. When the solar sails are placed and oriented appropriately, this yields a torque which can be utilized for S/C attitude control.

- **Spin stabilization**: The attitude can be stabilized by spinning the entire S/C or a part of it, if the mission concept allows for it.

- **Gravity gradient stabilization** uses the fact that the gravitational force decreases with the square of the distance. If the S/C body extends much further in one axis than in the other two axes, the S/C will tend to align with the gravity gradient, due to the tidal force.

- **Aerodynamic stabilization** uses atmospheric drag to stabilize the attitude, which is only feasible in low Earth orbit, and will accelerate the decrease of orbit altitude.

Attitude control mechanisms using magnetic dipole moments, reaction wheels, and control moment gyros are briefly described in the following.

Magnetic dipole moments

Magnetic dipole moments, as produced by an MTR, can also be used in a different way. Instead of controlling the amount of MTR input current, there could be one rod which can be turned actively. Then, the direction of the rod tends to align with the magnetic field vector. Theoretically, such a rod could also be fixed to the S/C body for a passive attitude control. Instead of coils, in principle, permanent magnets could also be used.

Reaction wheels

A reaction wheel, also called momentum wheel, can be thought of a momentum exchange device. The working principle is to have a spinning wheel, where the amount of spin can be controlled. By conservation of angular momentum, when the angular momentum of the wheel is changed, the S/C must gain an angular momentum to cancel that of the wheel. The conservation of angular momentum can be written as

$$I_{\mathrm{rw}}(\omega_{\mathrm{rw}} + \omega_{\mathrm{sc}}) + I_{\mathrm{sc}}\omega_{\mathrm{sc}} = 0, \tag{2.44}$$

where I_{rw} and I_{sc} denote the moments of inertia of the reaction wheel and of the S/C, respectively, and ω_{rw} and ω_{sc} denote the angular velocities of the reaction wheel and of the S/C, respectively.

Reaction wheels cannot produce an external torque. Therefore, the wheel may accumulate angular momentum and has to be desaturated occasionally ("momentum unload") in order to maintain its functionality, which requires using other attitude actuators. Reaction wheels can thus usually not be used independently. Moreover, their use is limited by size and mass constraints, as well as a maximum rotation rate of the wheel. Due to friction, reaction wheels should not be operated near 0 rotations per minute. Since they have moving parts, they could produce mechanical vibrations of the satellite body, potentially disturbing sensitive science instruments.

Control moment gyros

A control moment gyroscope (CMG), or gyrotorquer, is a rotor spinning at a constant rate, together with either one or two additional gimbals. Through the gimbals, the direction of the rotor w.r.t. the S/C body can be changed, which constitutes the difference to reaction wheels. This changes the angular momentum of the rotor, which induces a torque on the S/C, called gyroscopic torque. While a single-gimbaled CMG is more energy efficient, a dual-gimbaled CMG can turn around two independent axes and is thus more flexible. A CMG is much more power efficient than other types of attitude control such as reaction wheels. A disadvantage of this method is that gimbal lock can occur, which means that two of the gimbal axes are parallel, causing a singularity in the control system.

It is theoretically possible to construct a CMG with a variable spinning rate. There is no great advantage over constant rate gyrotorquers, although they can provide some more flexibility for the ACS. Moreover, they can function as a mechanical battery, by transforming electric into kinetic energy, and vice versa.

Chapter 3

Tilt-to-length coupling in the LRI

The goal of this chapter is to describe the TTL coupling in the LRI, and thereby build a basis for the main part of this thesis. In general, TTL coupling in laser interferometers is the phenomenon that a tilt of some part of the interferometer causes an error in the measured interferometric range. It is a common error source which is present in all laser interferometers in some form. In the context of the LRI and this thesis, the TTL error is referred to as an error in the LRI range measurements that can be expressed as a function of the inter-satellite pointing angles, which have been defined in Sec. 2.1.3. Recall that the pointing angles describe the deviation of a satellite's actual attitude from its nominal attitude, where the former is to be measured and the latter is defined via the LoS. In a more general context, different denotations for TTL coupling exist, such as "rotation-to-pathlength coupling", "pointing jitter coupling", "pointing induced errors", or similar.

The first section of this chapter, Sec. 3.1, is dedicated to describing the design and functionality of the LRI. Special focus will be laid on those functionalities of the LRI which are important for the further understanding of this thesis in general, and of the effects treated in the rest of this chapter in particular.

There are several different effects that can cause TTL coupling. Those effects which are assumed to be present in the LRI, are treated in Sec. 3.2, starting with the supposedly most impactful effect, which is due to the offset between triple mirror assembly (TMA) vertex point (VP) and S/C CoM. Other effects are discussed subsequently. In addition to TTL effects, a related effect is introduced, called angular rate coupling (ARC), which will prove to be important for the TTL analysis in the further course of this thesis.

In Sec. 3.3, a strategy of estimating TTL coupling in the LRI is presented. A linear TTL coupling model for the LRI is stated, which is based on the preceding discussion of TTL effects. All the working steps, which are required in order to pursue this estimation strategy, are named, giving a foretaste of what is treated in detail in Chap. 5.

3.1   LRI design and functionality

The LRI is a heterodyne optical interferometer, built and operated in a US-German cooperation led by NASA/JPL and the Albert Einstein Institute (AEI) Hannover. Figure 3.1 shows some of the most relevant GFO payload, including LRI units and displaying contributors to the individual components. Since the LoS connecting the two satellites' CoMs is blocked by the KBR assembly and the N_2 gas tanks (depicted as spherical orange objects in Fig. 3.1), and since the S/C CoM is occupied by the accelerometer, the LRI could not be conceptually designed as an on-axis interferometer. Instead, it has been implemented as an off-axis interferometer in a so-called racetrack configuration, i.e. the laser light is entering the S/C through an aperture on one side of the front panel and, after being guided around the CoM, it leaves the S/C through a different aperture on the other side of the front panel.
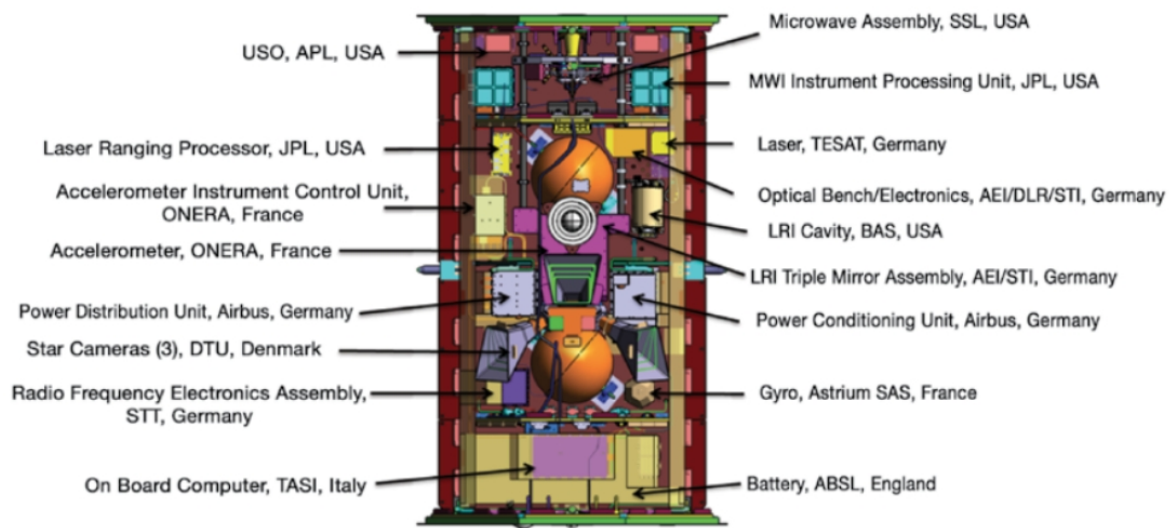
Figure 3.1: GFO payload. Image credit: Airbus Defence and Space, Germany.

The LRI was built into the GFO satellites with the role of a technology demonstrator, in addition to the KBR instrument. Since it was switched on for the first time on 14 June 2018, the LRI is in operation as the first inter-satellite laser interferometer. Figure 3.2 shows a functional overview of the LRI, cf. also [She+12; Abi+19]. A brief summary including more of the components can be viewed in Tab. 3.1.
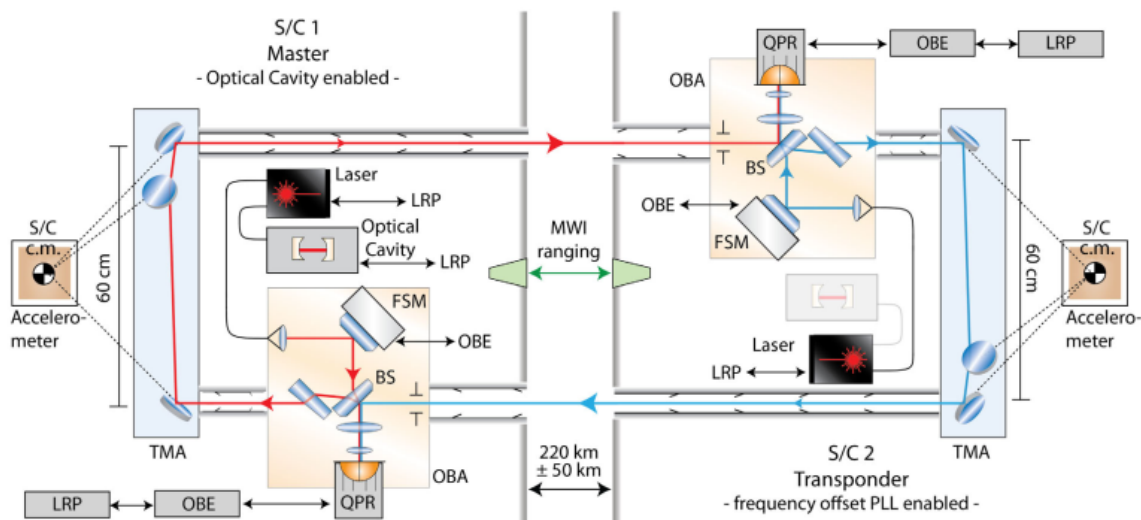
Figure 3.2: Functional overview of the LRI units on both spacecraft. The LRI units include the laser, cavity, Laser Ranging Processor (LRP), optical bench electronics (OBE), TMA, and optical bench assembly (OBA) with FSM. Figure and caption adopted from [Abi+19].

In the following section, 3.1.1, a brief overview of the pre-flight noise allocation for the LRI is provided. Then, the measurement principle of the LRI is sketched in Sec. 3.1.2. The reader is referred to [Mül13] for a more comprehensive description of the LRI subsystems and the derivation of the formula for the final beatnote phase measurement. Subsequently, a few of the components and functionalities of the LRI are briefly described, focusing on those aspects

Table 3.1: LRI components: overview of contributions.

Component	Country	Manufacturer
Optical Bench Assembly (OBA)	Germany	SpaceTech Immenstaad
Fast Steering Mirror (FSM)	Germany	Airbus Defence & Space
Photo Receiver Frontend (PRF)	Germany	DLR
Optical Bench Electronics (OBE)	Germany	Apcon Aerospace and Defence
Laser Ranging Processor (LRP)	USA	JPL / Ball Aerospace
Triple Mirror Assembly (TMA)	Germany	SpaceTech Immenstaad
Optical baffles	Germany	SpaceTech Immenstaad
Optical cavity	USA	Ball Aerospace / JPL
Optical fibers	USA / Switzerland	Diamond USA / Diamond Losone
Optical Ground Support Equipment (OGSE)	Germany / USA	DLR / AEI / JPL
Nd:YAG laser	USA / Germany	TESAT

that are relevant for a broader understanding of TTL coupling in the LRI. Namely, the OBA is treated in Sec. 3.1.3, the laser beam steering mechanism including DWS and FSM principles in Sec. 3.1.4, and the TMA in Sec. 3.1.5. In Sec. 3.1.6, the laser frequency noise (LFN) is discussed, which is one of the major noise sources of the LRI and thus relevant for estimating TTL coupling. Finally, a summary of the laser link acquisition procedure is given in Sec. 3.1.7.

3.1.1 Pre-flight noise allocation

The conservative pre-flight total noise budget of the LRI of $80 \text{ nm}/\sqrt{\text{Hz}} \times$ noise shape function (NSF) at high frequencies, cf. [She+12], comprises the root mean square (RMS) sum of the requirement values for LFN, total TTL coupling, temperature induced pathlength changes, and several sources of readout noise, plus a top-level margin. The suballocation is given in Tab. 3.2.

Table 3.2: Suballocation of the LRI noise budget. The RMS sum of these components, plus a margin, yields a ranging requirement of $80 \text{ nm}/\sqrt{\text{Hz}}$. The NSF is given in Eq. (3.1).

Noise source	Requirement (ASD)	Remark
LFN	$40 \text{ nm}/\sqrt{\text{Hz}} \times \text{NSF}$	cf. Sec. 3.1.6
TTL	$40 \text{ nm}/\sqrt{\text{Hz}} \times \text{NSF}$	flight performance depends on ACS performance; cf. Sec. 3.2
thermal effects	$30 \text{ nm}/\sqrt{\text{Hz}} \times \text{NSF}$	i.e. temperature induced pathlength changes
readout noise	$3 \text{ nm}/\sqrt{\text{Hz}} \times \text{NSF}$	e.g. clock noise, shot noise, laser power noise, photodetector electronic noise, parasitic signals, analog-to-digital quantization noise, spurious electronic phaseshifts

The requirements are relaxed towards lower Fourier frequencies, by multiplying them by the NSF given by

$$\text{NSF}(f) = \sqrt{1 + \left(\frac{f}{3\text{mHz}}\right)^{-2}} \cdot \sqrt{1 + \left(\frac{f}{10\text{mHz}}\right)^{-2}}. \tag{3.1}$$

This yields a flat spectrum for high frequencies, a $1/f$ slope between 3 and 10 mHz and a $1/f^2$ slope below 3 mHz.

Note that a requirement on the TTL error cannot be translated in a uniquely determined way to requirements on the coupling factors (CF) for the individual pointing angles. For one thing this is because TTL is the sum of the contributions from different pointing angles, so that there a tradeoff is possible. E.g., a relaxed requirement on the roll coupling factor and a stricter requirement on the pitch coupling factor may yield the same total TTL error budget. Moreover, the amount of satellite pointing jitter was not perfectly known before the launch. However, based on pointing jitter simulations performed by Airbus Defence & Space, the AEI internal pre-flight requirements on the linear TTL CFs for each S/C were 20, 200, and 200 μm rad^{-1} for roll, pitch, and yaw, respectively. A more detailed discussion of different TTL effects is presented further below in Sec. 3.2.

3.1.2 LRI measurement principle

The measurement principle of the LRI can be sketched as follows. One of the S/C is assigned the "transmitter" role, while the other S/C is in "transponder" mode. Both S/C carry the same components and can fulfill either of these roles. On the transmitter S/C, light is emitted by a laser with a wavelength of $\lambda_0 = 1064.5$ nm, i.e. with a nominal frequency ν_0 of approximately 282 THz, where an optical cavity is utilized for stabilization of the laser frequency [Fol+10; Tho+11; Pie+12]. The operating temperature of the lasers is 27-33 ° [Kor+19]. The laser beam is steered by the FSM on the OBA, so that it is parallel to the beam coming from the transponder S/C. By means of a beam splitter (BS), a small part of the light is guided to the quadrant photodiode (QPD), where it is used as the reference beam, whereas the larger part is routed through the TMA towards the distant S/C. Omitting any noise or error terms in the following, denote the frequency of the light transmitted by the transmitter S/C by $\nu_{\text{TX, transmitter}}$. Due to the relative velocity of the two satellites, the frequency of the light received at the transponder S/C differs from the frequency of the transmitted light by a Doppler shift:

$$\nu_{\text{RX, transponder}} = \nu_{\text{TX, transmitter}} + \nu_{\text{Doppler}}. \tag{3.2}$$

The cavity on the transponder side is not used, it serves as cold redundant backup, instead the transponder laser beam is phase locked to the received light using a frequency-locked loop, and a constant frequency offset $\nu_{\text{off}} \approx 10$ MHz is added to $\nu_{\text{RX, transponder}}$. Thus, the apparent beatnote frequency at the transponder QPD is given by

$$\nu_{\text{QPD, transponder}} = (\nu_{\text{RX, transponder}} + \nu_{\text{off}}) - \nu_{\text{RX, transponder}} = \nu_{\text{off}}. \tag{3.3}$$

The transponder TX beam with frequency

$$\nu_{\text{TX, transponder}} = \nu_{\text{TX, transmitter}} + \nu_{\text{Doppler}} + \nu_{\text{off}} \tag{3.4}$$

is also routed through a TMA and sent back towards the transmitter S/C. There the roundtrip closes and the light, which has gained another Doppler shift on its way, i.e.

$$\nu_{\text{RX, transmitter}} = \nu_{\text{TX, transmitter}} + 2\nu_{\text{Doppler}} + \nu_{\text{off}}, \tag{3.5}$$

is interfered with the reference beam from the laser on the transmitter S/C. Due to the frequency offset $\nu_{\text{off}} \approx 10$ MHz and Doppler shifts of the order of a few MHz, a beatnote is detected on the transmitter S/C QPD with a frequency which is varying around 10 MHz:

$$\nu_{\text{QPD, transmitter}} = \nu_{\text{RX, transmitter}} - \nu_{\text{TX, transmitter}} \tag{3.6}$$

$$= \nu_{\text{off}} + 2\nu_{\text{Doppler}}. \tag{3.7}$$

The phase of this beatnote is measured by a phasemeter and contains the ranging information in the form of the integrated Doppler shift, i.e.

$$\psi_{\text{QPD, transmitter}}(t) = \psi_{\text{QPD, transmitter}}(t_0) + 2\pi \int\limits_{t_0}^{t} \nu_{\text{QPD, transmitter}}(\tau) \ d\tau \tag{3.8}$$

$$= \psi_{\text{QPD, transmitter}}(t_0) + 2\pi \int\limits_{t_0}^{t} \left[\nu_{\text{off}} + 2\nu_{\text{Doppler}}(\tau)\right] \ d\tau \tag{3.9}$$

Note that, since the relative S/C velocity Δv is small compared to the speed of light c, the Doppler shift is approximately given by

$$\Delta\nu_{\text{Doppler}} \approx -\frac{\Delta v}{\lambda_0}. \tag{3.10}$$

A second order relativistic correction of $\Delta v/c \approx 10^{-8}$, where c is the speed of light, is neglected here. Moreover, the Doppler shift will be slightly different on the way back, due to the different frequency and due to the light travel time, which is about 1.5 ms. This difference is neglected as well here.

The initial phase $\psi_{\text{QPD, transmitter}}(t_0)$ in Eq. (3.9) is arbitrary, since t_0 is arbitrary. The LRI cannot measure the absolute distance, merely the biased range, i.e. up to an unknown constant. Hence,

$$\psi_{\text{QPD, transmitter}}(t) = 2\pi\nu_{\text{off}}t - \frac{4\pi}{\lambda_0} \int\limits_{t_0}^{t} \Delta v(\tau) \ d\tau. \tag{3.11}$$

The linear ramp due to the constant frequency offset can be cancelled by subtracting the phase at the transponder QPD from the phase at the transmitter S/C QPD, i.e. by regarding

$$\bar{\psi} = \psi_{\text{QPD, transmitter}} - \psi_{\text{QPD, transponder}}. \tag{3.12}$$

With Eq. (3.3), one can compute the biased range $\rho(t)$ as

$$\rho(t) = -\frac{\lambda_0}{4\pi}\bar{\psi}(t), \tag{3.13}$$

disregarding laser frequency noise.

3.1.3 Optical bench

The LRI OBA, developed by SpaceTech Immenstaad (STI), is visible in Fig. 3.2. It comprises

- an ultra-stable Fibre Injector Assembly (FIA) for injecting the local laser light,

- an FSM for beam steering,

- a BS for beam superposition of the local beam with the received beam,

- two photoreceiver frontends, including QPDs, for measuring the beatnote and DWS signals,

- imaging optics for mapping the aperture as well as the FSM surface onto the photoreceivers and suppressing beamwalk.

A compensation plate (CP) is placed in the beam path between the BS and the TMA, i.e. before the beam leaves the OBA, in order to compensate for part of the TTL effect which is caused by the BS, see Sec. 3.2. The OBA is connected to the OBE, which establishes the link between photoreceivers and the Laser Ranging Processor (LRP), and which is also enabling power supply of FSM and the photoreceivers. The OBA and OBE are part of the German contribution to the LRI [Nic+17; Abi+15; Bac+17; Dah+17], see also Tab. 3.1.

3.1.4   Laser beam steering

The LRI requires accurate pointing of the laser beam, in order to transmit a sufficient amount of light power to the other S/C. The S/C pointing uncertainty and attitude variations are in the order of a few hundred µrad, much larger than the LRI pointing requirement [Sch+14]. Thus, active beam steering is employed by means of control loops and FSMs. This requires the application of QPDs, which measure the tip and tilt of the local beam with respect to the incoming beam, using the DWS technique [Mor+94; And84].
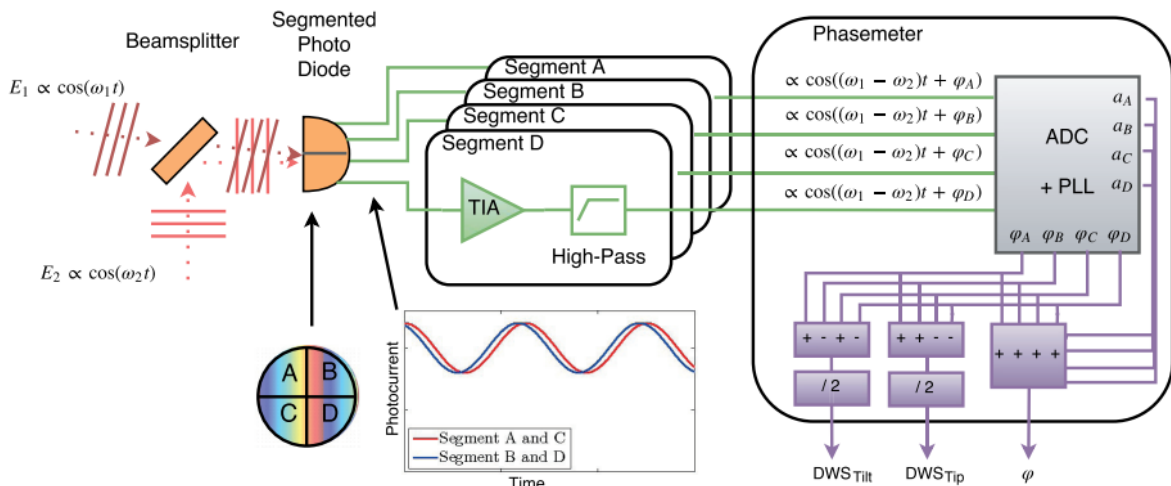

Figure 3.3: DWS principle. In case the two interfering wavefronts are not parallel, different QPD segments detect different phases. Tip and tilt of the beam can be inferred from different combinations of the four QPD segments. Image credit: [Mül13]

The principle of the DWS technique is depicted in Fig. 3.3. The four segments of a QPD detect the two interfering light beams. If the two beams are perfectly aligned, the signals detected at the four segments are in phase. If the beams are tilted w.r.t. one another, the interfering beam is detected with different phases at the different QPD segments. The average phase of the four segments is used to derive the interferometric range, whereas suitable combinations are used as tip and tilt signals, i.e.

$$\text{DWS}_{\text{tip}} = \frac{\varphi_A + \varphi_B - \varphi_C - \varphi_D}{2}, \tag{3.14}$$

$$\text{DWS}_{\text{tilt}} = \frac{\varphi_A + \varphi_C - \varphi_B - \varphi_D}{2}. \tag{3.15}$$

The DWS signal is fed back to the control loop, commanding the FSM in such a way that the DWS signal is driven towards a programmed set point. If the components are perfectly placed and aligned, this set point is zero. With a closed control loop and zero DWS set point, the incoming phasefront is parallel to the outgoing phasefronts on the OBA. This ensures that, after retro-reflection at the TMA, the emitted light is propagating in the direction of the received light and thus towards the distant S/C, as long as the TMA mirrors are correctly aligned w.r.t. each other. The DWS set points can be updated and uploaded to the S/C when necessary. This way, the set point compensates for misalignments, whereas the FSM control loop compensates for a mispointing of the local S/C, and hence maximizes the heterodyne efficiency and corresponding signal-to-noise ratio (SNR) of the phase readout. The FSM principle is illustrated in Fig. 3.4. The correct DWS set point was determined with an initial acquisition scan, which is described in Sec. 3.1.7.

Since the FSM is permanently commanded to compensate for the misalignment of the received light field and the local laser beam, the FSM positions provide very accurate information
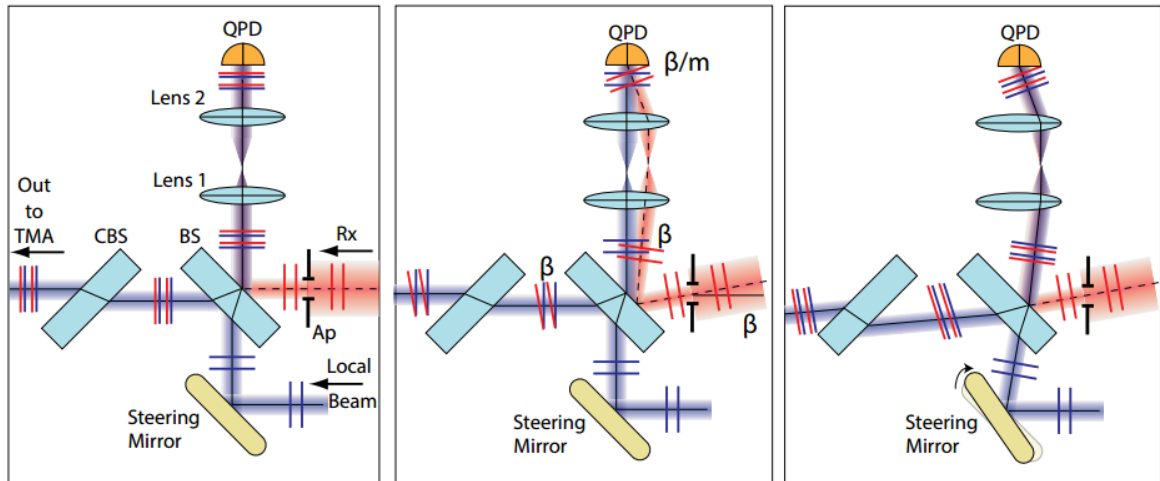
Figure 3.4: FSM principle. Left: beams are aligned, DWS signal is zero. Middle: beams are not aligned, DWS signal is not zero. Right: the FSM guides the local beam, such that it is parallel to the incoming beam, DWS signal is zero. Image credit: [Mül13]

about the alignment of the S/C with respect to the LoS, and hence about the S/C pointing angles. This method measures the pointing angles, i.e. the deviation of the local frame from the LOSF. As opposed to that, the star cameras measure the satellites' attitudes compared to inertial space, which must then be combined with orbit data in order to obtain pointing angles. However, the LRI does not measure the S/C roll angle, which is the angle around the LoS, but merely the vertical and horizontal angles which correspond to the so-called pitch and yaw angles, cf. Sec. 2.1.3.

3.1.5   Triple mirror assembly

The racetrack configuration of the LRI, as described above, is realized with the use of the so-called triple mirror assembly (TMA). It consists of three pairwise perpendicular mirrors, connected by a tube made of carbon fiber reinforced polymer (CFRP). The TMA thus uses the principle of a corner cube which acts as a retroreflector. Since the entry point and the tilt of the incoming beam is varying only by a very small amount, not an entire corner cube is needed. Instead, merely three small circle-shaped parts of it, where the beam is reflected, are incorporated in the TMA. The accomodation of the TMA in the S/C is described in [Kor+19].

The planes defined by the three mirrors intersect in one point, which is called the vertex point (VP). This VP is a virtual point, i.e. it is not physically a part of the TMA, but lies outside of the TMA. Figure 3.5 shows an illustration of such a corner cube reflector. This allows for the VP to be placed in the S/C CoM, which is physically occupied by the accelerometer proof mass.

Properties of the TMA

The TMA has been studied extensively before the launch of GFO [War+14; Sch+14; Sch15; Fle+14]. It has many advantageous geometrical properties. In particular, the following observables are invariant under rotations of the TMA around its VP:

- the direction of reflected beam leaving the TMA, which is always antiparallel to the incoming beam.
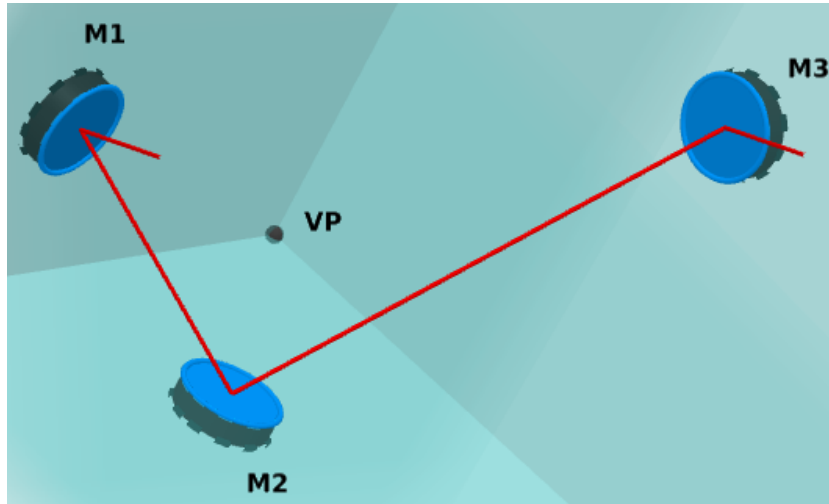
Figure 3.5: Geometrical model of a retroreflector in a corner cube arrangement. Three pairwise perpendicular mirrors can reflect light back towards its source.

- the path from an invariant reference plane through the TMA and back to the reference plane, e.g. the red path in Fig. 3.6, which is identical to two times the distance between VP and this reference plane, i.e. two times the blue path in Fig. 3.6. Considering both TMAs on both S/C, it follows that the round trip path length is invariant as well, being always twice the distance between the two VPs.

- the lateral offset between incident and outgoing beam, approximately 60 cm.

These properties can be verified theoretically, for example by analytical raytracing, as performed in [Mül13]. The same technique can be used to describe the TTL error which occurs if the TMA is rotated around a point other than the VP. Furthermore, it yields an analytical description of TTL coupling if the TMA mirrors are not perfectly aligned, cf. Sec. 3.2. The properties mentioned above and the results of the analytical raytracing have been verified experimentally as well, cf. [Sch15].

TMA coalignment

If all the TMA mirrors are perfectly aligned, the beam that enters the TMA is antiparallel to the beam that leaves the TMA, cf. Sec. 3.1.5. The term TMA coalignment describes how well these two beams, incoming and outgoing, are aligned. The coalignments of the TMAs on both GFO S/C have been measured on 18 July 2018, shortly after the launch. Both TMAs showed a significant misalignment close to 50 µrad, for GF1 in the pitch angle and for GF2 mainly in the yaw angle. The measurement was repeated a few times since then, confirming that the misalignment had decreased over time to below 10 µrad. This change had been anticipated and was likely due to volatilization of humidity in the glue connecting the TMA components. Tables 3.3 and 3.4 summarize the results of TMA coalignment tests, according to [MM20] (AEI internal document).

The laser beam is steered by a control loop. The local beam is aligned with the incoming (RX) beam by orienting the FSM in such a way that the DWS signal is driven to a certain set point. When the control loop is active, the RX and transmit (TX) beams are aligned on the optical bench. Subsequently, the TX beam is then reflected by the TMA, and thus antiparallel to the RX beam, unless the TMA mirrors are not perfectly aligned w.r.t. each other. The measurement of such misalignments is performed by varying the DWS set point and fitting a model to the intensity profile of the beam measured at the distant S/C.
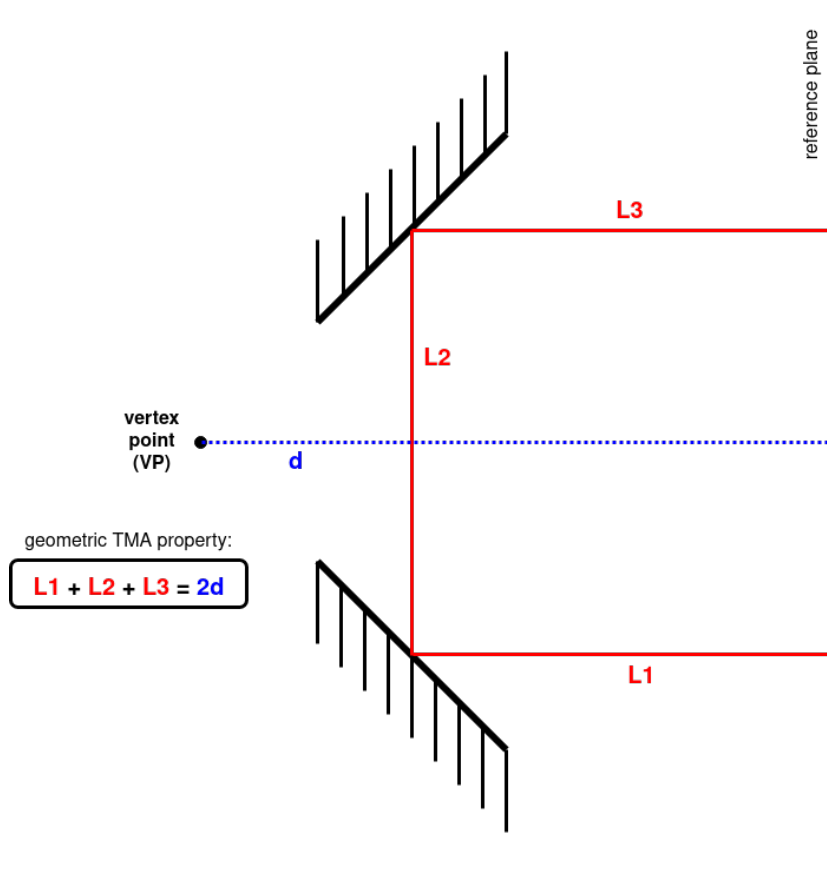
Figure 3.6: This sketch illustrates the path invariance property of the TMA. The given relation is independent of small rotations of the setup around the VP. Here, for the purpose of illustration, merely two of the three TMA mirrors are depicted.

Table 3.3: TMA misalignment results for GF1 in terms of pitch and yaw offsets, given in µrad.

Date	$\delta\theta_y$	$\delta\theta_z$	TRP temp. [°C]	Note
2018-07-18	47.4 ± 0.3	1.3 ± 0.2	14.5	
2019-06-13	5.8 ± 0.8	9.9 ± 1.0	20.2	warm TMA
2019-06-14	6.0 ± 0.8	9.7 ± 0.9	19.3	cold TMA
2019-10-10	6.0 ± 0.1	4.8 ± 0.2	17.6	

Table 3.4: TMA misalignment results for GF2 in terms of pitch and yaw offsets, given in µrad.

Date	$\delta\theta_y$	$\delta\theta_z$	TRP temp. [°C]	Note
2018-07-18	-4.7 ± 0.2	52.3 ± 0.3	14.5	
2019-06-14	-0.4 ± 0.4	5.8 ± 0.5	14.7	run 1
2019-06-14	-0.1 ± 0.5	5.1 ± 0.6	14.7	run 2
2019-09-26	1.0 ± 0.1	5.9 ± 0.1	14.5	
2019-10-10	-2.3 ± 0.1	10.4 ± 0.2	17.3	

3.1.6   Laser frequency noise

Within the measurement band of the LRI, the range spectrum is expected to be limited by LFN at the high end, whereas TTL is assumed to be dominant at the low end. To put it into perspective, the quality of gravity field solutions is thought to be limited by accelerometer

noise for low frequencies, and by aliasing for high frequencies, both of which should be larger than the contributions from LFN and TTL together. This proposition shall be confirmed within this thesis. It implies that the quality of gravity fields derived from LRI range is not limited by the ranging noise, which seems to be confirmed by comparisons of gravity fields derived from KBR and LRI range products [Lan+20].

As mentioned above, the laser on the transmitter S/C is stabilized by an optical cavity. The remaining frequency jitter couples into the range measured by the LRI. The coupling formula for the ranging error due to laser frequency noise according to [She+12] is

$$\widetilde{\delta\rho} = \frac{L}{\nu} \cdot \widetilde{\delta\nu}, \tag{3.16}$$

i.e. it is proportional to the inter-satellite distance L. Here $\widetilde{\delta\nu}$ and $\widetilde{\delta\rho}$ denote the ASDs of the laser frequency noise and the resulting ranging error (LFN), respectively. The absolute laser frequency is

$$\nu = \frac{c}{1064.5\text{nm}} \approx 282 \text{ THz}, \tag{3.17}$$

and the S/C separation fulfills $L \leq 270$ km. If one is aiming at a ranging noise requirement of

$$\widetilde{\delta\rho} \leq 30 \text{ nm}/\sqrt{\text{Hz}}, \tag{3.18}$$

this roughly yields a requirement for the laser frequency stabilization of

$$\widetilde{\delta\nu} \leq 30 \text{ Hz}/\sqrt{\text{Hz}}. \tag{3.19}$$

This requirement for the cavity performance, i.e. $30 \text{ Hz}/\sqrt{\text{Hz}}$ multiplied by the NSF given in Eq. (3.1), is depicted in Fig. 3.7 as a black line. The frequency noise of the actual flight unit, shown in blue, was measured on ground before the launch of GFO. It was below $30 \text{ Hz}/\sqrt{\text{Hz}}$ for Fourier frequencies above 1 mHz, cf. [KM], so the confidence was high that the resulting ranging noise in the mission would not surpass the $30 \text{ nm}/\sqrt{\text{Hz}}$ budget.

The frequency noise can be roughly approximated by a line, see the red line in Fig. 3.7. This line, converted to ranging noise according to Eq. (3.16), is the basis of the model for the LFN that is used in this thesis. With slight modifications based on the actual flight data, the formula for the modeled LFN in the LRI range reads

$$\widetilde{\delta\rho}(f) = 0.32 \cdot \frac{L}{\nu} \cdot \left(\frac{f}{\text{Hz}}\right)^{-0.6} \cdot \sqrt{\text{Hz}}. \tag{3.20}$$

In fact, it shall be seen in this thesis that it appears to fit well with the LRI in situ data, at least in the frequency regimes where LFN is the dominant noise source, see for example Fig. 3.13.

3.1.7 Laser link acquisition

The LRI has a field-of-view of about ± 6.5 mrad, provided that the beam steering mechanism is active. The field-of-view is designed to be larger than the pointing variations of the satellites and initial uncertainties, e.g. due to alignment tolerances during instrument integration. It is nevertheless required to perform a search within this field-of-view, in order to close the interferometric link. This pointing offset, which is unknown initially, has to be determined in flight. Furthermore, the laser frequency difference between transmitter and transponder lasers is required to be in the measurable range between 4 and 16 MHz. To this end, an initial acquisition scan is performed on both spacecraft simultaneously ("initial line of sight calibration procedure" [Koc+18]). Afterwards, the pointing offset is determined from the steering mirror positions recorded at the instances when the phasemeter detects flashes, i.e.
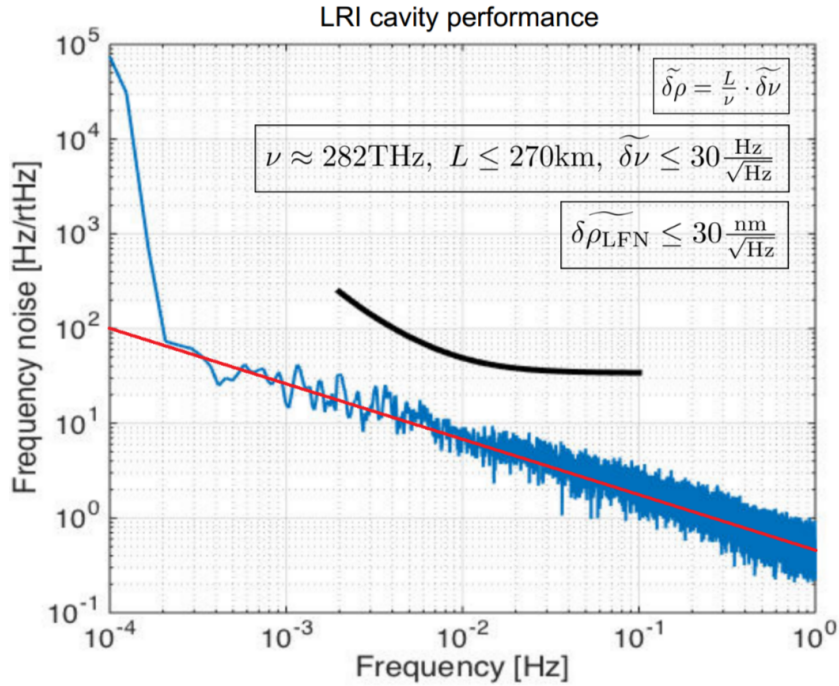
Figure 3.7: LRI cavity performance measured on ground. Image credit: Bill Klipstein, NASA. The image was modified.

when the beatnote amplitude exceeds a threshold. These split-second flashes are seen only if all of the 4 angles, i.e. pitch and yaw for both spacecraft, and laser frequency offset are very close to their optimal values at the same time. Thus, a complicated five-dimensional scan pattern is needed, which is depicted in Fig. 3.8 for the angular domain. The total duration of the scan is approximately 8.5 hours. During this initial acquisition scan there is no transition into science mode. The data is merely recorded and analyzed afterwards. When the optimal set point is determined, a parameter file is uploaded to the S/C.

Figure 3.8: Angular scan pattern of the initial acquisition scan, started on 13 June 2018. Image credit: Alexander Koch [Koc+18]

Once the initial pointing offsets are uploaded, the LRI is commanded into the re-acquisition mode. In this mode, the instrument performs only a short scan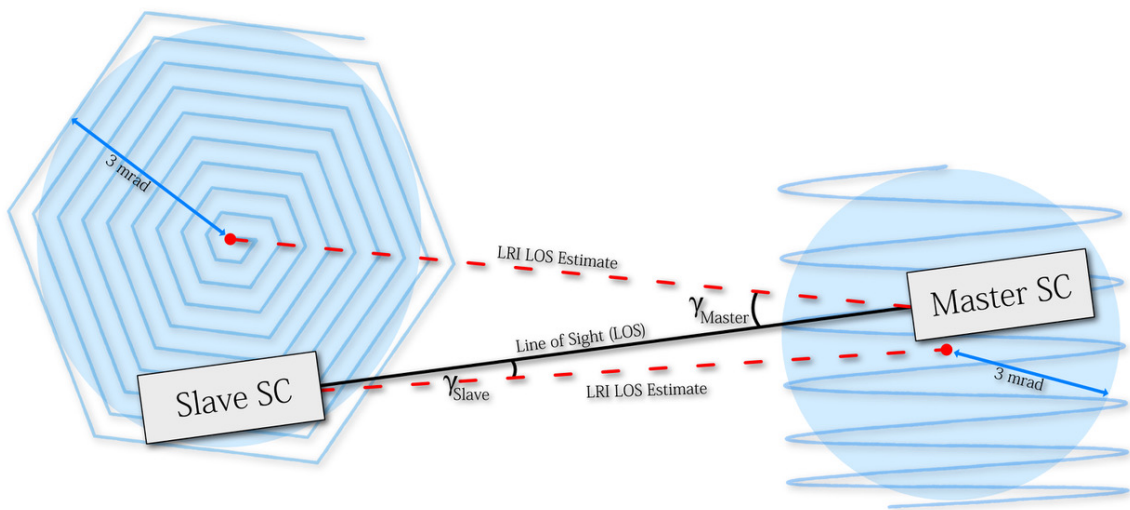 with smaller range, starting with the values that were previously determined by the initial line of sight calibration procedure. These values are already very close to the optimum and the instrument automatically attempts to transition from the re-acquisition mode into the science mode, once a re-acquisition flash is seen.

This initial acquisition scan was started on 13 June 2018, continuing until the following night. The data recorded during the scan was sent to ground and analyzed. The analysis showed that enough flashes were recorded in order to determine the initial offsets for the re-acquisition scan, which include the misalignment of the LRI OBA w.r.t. the SF, as well as the TMA coalignment error and estimation errors in the pointing towards the distant spacecraft. The parameter files containing this information were uploaded shortly afterwards. The same day, the instrument successfully established the interferometer laser link. The following ground-station pass of the satellites confirmed that the LRI was in science mode and taking continuous measurements. The identified initial pointing offset in terms of angles were -913.2 µrad in pitch and -691.1 µrad in yaw, for GF1. For GF2, these values were -446.6 µrad in pitch and -638.2 µrad in yaw [Mis19].

3.2 TTL coupling effects

There may be a number of effects causing TTL coupling. In an environment with small angle variations, it is often useful to approximate a function of the angles by a first or second order. In this thesis, any TTL error in the range ρ will be approximated with a Taylor expansion ignoring all orders larger than 2. In general, a ´TTL error will be written as

$$
\delta\rho_{\text{TTL}} = \begin{pmatrix} a_x & a_y & a_z \end{pmatrix} \cdot \begin{pmatrix} \theta_x \\ \theta_y \\ \theta_z \end{pmatrix} + \begin{pmatrix} \theta_x & \theta_y & \theta_z \end{pmatrix} \cdot \begin{pmatrix} b_{xx} & b_{xy} & b_{xz} \\ 0 & b_{yy} & b_{yz} \\ 0 & 0 & b_{zz} \end{pmatrix} \cdot \begin{pmatrix} \theta_x \\ \theta_y \\ \theta_z \end{pmatrix}, \tag{3.21}
$$

with linear and second order coupling factors a_i and b_{ij}, $i, j = x, y, z$. Note that a Taylor expansion is valid in a neighborhood of some working point, e.g. $\vec{\theta}_0 = (0, 0, 0)^T$. The more the actual pointing angles deviate from that working point, the less accurate is the Taylor expansion. It is assumed here that third and higher order terms are negligible. Further, note that within this thesis, terms called $\delta\rho$ with any subscript refer to errors in the measured one-way inter-satellite range ρ.

In this section, different effects of TTL coupling are analyzed, which may appear in the LRI measurements. This provides a first impression of the magnitude of the coupling factors, that is, the numbers a_i and b_{ij} in Eq. (3.21). To this end, those TTL effects, which may be relevant for the LRI, are described in the following, commencing with the TMA VP offset. Moreover, the TTL coupling via optical components on the OBA, TTL coupling due to TMA misalignments, and other effects are discussed.

3.2.1 TMA vertex point offset

The TMA is a key component of the LRI, described in Sec. 3.1.5. Recall that the three mirror planes are nominally pairwise perfectly perpendicular, and their virtual intersection point is called the VP. The TMA is used because of its advantageous geometrical properties, which suppress TTL coupling to a large extent, if the VP is colocated with the S/C CoM. However, the coupling due to a residual offset is still considered the largest TTL effect affecting the LRI measurements.

As mentioned previously in this chapter, the LRI measures the biased range between the two VPs, one at each S/C. Consequently, the measured range is invariant under small rotations

of either one of the S/C around its VP, which is, to the accuracy of S/C integration, placed in the CoM of the S/C. Due to residual offsets between the VP and CoM of the order of 100 µm, there is a difference between the distance from VP to VP on the one hand, and the distance from CoM to CoM on the other hand. This difference is varying, when the S/C rotates around its CoM, cf. Fig. 3.9. Hence, S/C attitude variations cause an error in the measured biased range, which shall be denoted by $\delta\rho_{\mathrm{VP}}$ in this section.

The principle of the TTL coupling due to the TMA-VP offset is depicted in Fig. 3.9. In this scheme, the black axes show the x and y axes of the LOSF, which is fixed in this picture, i.e. the position of the distant S/C is fixed. Hence, also the distance between the two satellites' CoMs is fixed, which is the quantity one would like to measure. The actual measured range depends on the position of the VP. Since the VP is not colocated with the S/C CoM, its position w.r.t. the other S/C is varying, when the local S/C is rotating around its CoM. In Fig. 3.9, this is illustrated by two different hypothetical VP positions (green and purple), where one is obtained from the other by a yaw rotation of the S/C. It is clearly visible that the measured range is not the same in both scenarios. While a constant offset would not be relevant for the biased range, such S/C pointing variations indeed cause a time-varying error term in the LRI observations. In the following, this error term is computed in dependency of the S/C pointing angles.
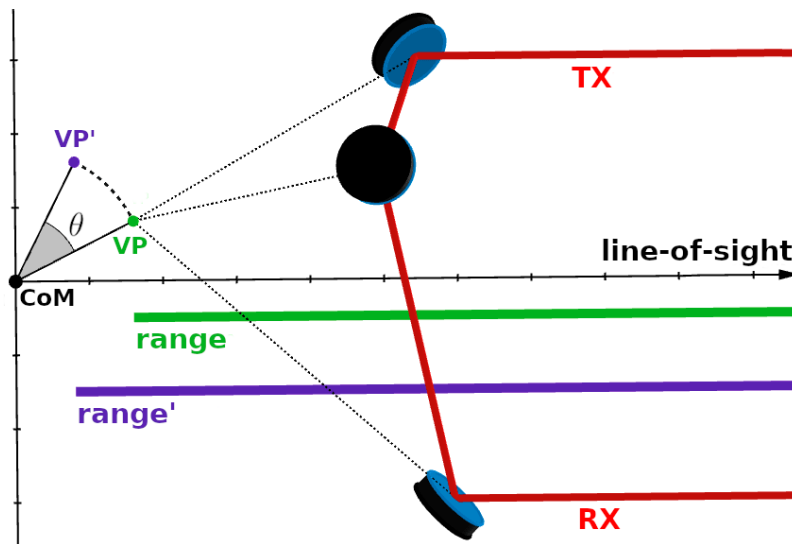

Figure 3.9: Schematic of TTL error due to VP-CoM offset. Rotating the VP around the CoM varies the measured range, approximated by the projection onto the LoS. If the VP was exactly colocated with the CoM, the difference would vanish.

Let the measured one-way range be written as $\bar{\rho} = \rho + \delta\rho_{\mathrm{VP}} + \delta\rho_{\mathrm{other}}$, where ρ is the true distance between the satellite CoMs, $\delta\rho_{\mathrm{VP}}$ is the sum of TTL errors caused by the VP-CoM offsets of both S/C, and $\delta\rho_{\mathrm{other}}$ denotes the contribution from all other error sources, including a bias. Note that this section merely focuses on $\delta\rho_{\mathrm{VP}}$. The term $\delta\rho_{\mathrm{other}}$ plays a role, once it gets to developing parameter estimation algorithms, in Chap. 5.

Using the subscript i $\in \{1, 2\}$ to indicate GF1 or GF2, let $\vec{V}_i$ and $\vec{C}_i$ denote the positions of the TMA vertex points and the S/C CoMs, respectively. As usual, superscripts are used to indicate the frame in which a vector is represented. E.g., $V_i^{\mathrm{SF\text{-}i}}$ is the VP position of satellite i expressed in the SF of satellite i, $i = 1, 2$. Since $\vec{C}_i$ is the origin of SF i, $V_i^{\mathrm{SF\text{-}i}}$ is also the vector pointing from the CoM to the VP. It turns out useful to express the TTL coupling factors

computed in this section via the vector pointing from VP to CoM. Define

$$\vec{C}_i^{\text{SF-i}} - \vec{V}_i^{\text{SF-i}} = -\vec{V}_i^{\text{SF-i}} = \begin{pmatrix} \Delta x_i \\ \Delta y_i \\ \Delta z_i \end{pmatrix} \tag{3.22}$$

with components in the SF. This will be a key quantity in this section. Subsequently, one way of computing $\delta\rho_{\text{VP}}$ is presented. Two alternative ways are shown in App. B.

Let $\vec{e}_{\text{VP, i}}$ be the unit vector pointing from the VP on S/C i towards the VP on the other S/C i, and let $\vec{e}_{\text{LOS, i}}$ be the unit vector pointing from the CoM on S/C i towards the CoM on the other S/C. With this notation, one has

$$\bar{\rho} = |\vec{V}_2 - \vec{V}_1| + \delta\rho_{\text{other}} = \langle \vec{e}_{\text{VP,1}}, \vec{V}_2 - \vec{V}_1 \rangle + \delta\rho_{\text{other}}$$
$$\rho = |\vec{C}_2 - \vec{C}_1| = \langle \vec{e}_{\text{LOS,1}}, \vec{C}_2 - \vec{C}_1 \rangle,$$

where $\langle \cdot, \cdot \rangle$ denotes the standard scalar product of $\mathbb{R}^3$. Since $\rho \gg \|\vec{V}_i - \vec{C}_i\|$, $i = 1, 2$, the approximation $\vec{e}_{\text{VP, i}} \approx \vec{e}_{\text{LOS, i}}$ is valid, which yields

$$\delta\rho_{\text{VP}} = \bar{\rho} - \rho - \delta\rho_{\text{other}} \tag{3.23}$$
$$\approx \langle \vec{e}_{\text{LOS, 1}}, \vec{V}_2 - \vec{V}_1 - \vec{C}_2 + \vec{C}_1 \rangle \tag{3.24}$$
$$= \langle \vec{e}_{\text{LOS, 1}}, \vec{C}_1 - \vec{V}_1 \rangle + \langle \vec{e}_{\text{LOS, 2}}, \vec{C}_2 - \vec{V}_2 \rangle, \tag{3.25}$$

since $\vec{e}_{\text{LOS, 1}} = -\vec{e}_{\text{LOS, 2}}$. The TTL error due to the VP-CoM offset on S/C i is thus approximated by the projection of the negated VP offset, $\vec{C}_i - \vec{V}_i$, onto the LoS. That is, denoting by $\delta\rho_{\text{VP-i}}$ the respective TTL error for S/C i, $i = 1, 2$, one has

$$\delta\rho_{\text{VP-i}} = \langle \vec{e}_{\text{LOS, i}}, \vec{C}_i - \vec{V}_i \rangle. \tag{3.26}$$

Since $\vec{C}_i^{\text{LOSF}} = \vec{0}$, one has $\vec{C}_i^{\text{LOSF}} - \vec{V}_i^{\text{LOSF}} = -\vec{V}_i^{\text{LOSF}}$. Thus, omitting the index i on the right hand side of the following equations, $\delta\rho_{\text{VP-i}}$ can be expressed in the LOSF as

$$\delta\rho_{\text{VP-i}} = \left(\vec{e}_{\text{LOS}}^{\text{LOSF}} \right)^T \cdot \vec{V}^{\text{LOSF}} \tag{3.27}$$
$$= \begin{pmatrix} 1 & 0 & 0 \end{pmatrix} \cdot R_{\text{SF}}^{\text{LOSF}} \cdot \vec{V}^{\text{SF}} \tag{3.28}$$
$$= R_{11}\Delta x + R_{12}\Delta y + R_{13}\Delta z, \tag{3.29}$$

where $R_{\alpha\beta}$ is the entry in row α and column β of the rotation matrix $R_{\text{SF}}^{\text{LOSF}}$, which was introduced in Sec. 2.1.3. In terms of pointing angles, writing $c_x = \cos(\theta_x)$, $s_x = \sin(\theta_x)$, etc., using Eq. (2.28), one has

$$\delta\rho_{\text{VP-i}} \approx c_y c_z \cdot \Delta x + (s_x s_y c_z - c_x s_z) \cdot \Delta y + (c_x s_y c_z + s_x s_z) \cdot \Delta z. \tag{3.30}$$

The second order approximation for small angles is

$$\delta\rho_{\text{VP-i}} \approx \left(1 - \frac{1}{2}\theta_y^2 - \frac{1}{2}\theta_z^2 \right) \cdot \Delta x + (\theta_x \theta_y - \theta_z) \cdot \Delta y + (\theta_y - \theta_x \theta_z) \cdot \Delta z. \tag{3.31}$$

Neglecting the constant error and adding up the terms for both S/C, the first order approximation of the total TTL error due to VP-CoM offsets is

$$\delta\rho_{\text{VP}} = \delta\rho_{\text{VP-1}} + \delta\rho_{\text{VP-2}} \approx \Delta z_1 \theta_{y,1} - \Delta y_1 \theta_{z,1} + \Delta z_2 \theta_{y,2} - \Delta y_2 \theta_{z,2}, \tag{3.32}$$

where $\theta_{y,\text{i}}$ and $\theta_{z,\text{i}}$ stand for pitch and yaw angles of S/C i, respectively. Δy_i and Δz_i denote y and z components of the vector pointing from the TMA VP to the CoM of S/C i, respectively, expressed in the SF.

Note that, in particular, there is no linear coupling of the roll angles expected from this effect. In order to verify this hypothesis, and to monitor possible change, linear roll coupling factors will be estimated nevertheless. This yields in total 6 model parameters for the TMAVP effect. In App. B, two more variants of computing $\delta\rho_{\text{VP}}$ are given.

3.2.2   Misaligned TMA mirrors

There may be misalignments within the TMA itself, i.e. the planes defined by each of the three mirrors may not be pairwise perpendicular. This can be described using the so-called dihedral angles, which are the three angles $\angle(M_i, M_j)$ for each pair of mirrors i and j, $i, j = 1, 2, 3$ with $i \neq j$. The deviations of the dihedral angles from $90°$, denoted by

$$\gamma = \begin{pmatrix} \gamma_1 \\ \gamma_2 \\ \gamma_3 \end{pmatrix} = \begin{pmatrix} \angle(M_1, M_3) - \frac{\pi}{2} \\ \angle(M_1, M_2) - \frac{\pi}{2} \\ \angle(M_2, M_3) - \frac{\pi}{2} \end{pmatrix}, \tag{3.33}$$

can be used to describe the TMA misalignment. According to [Mül17], the additional TTL coupling due to the TMA misalignment described by $\vec{\gamma}$ is approximately

$$\delta\rho_{\mathrm{TMA}} \approx 1 \text{ mm rad}^{-2} \cdot \vec{\gamma}^T \cdot \begin{pmatrix} 266 & -300 & 24 \\ -333 & 300 & -24 \\ 424 & 424 & -34 \end{pmatrix} \cdot \vec{\theta} \tag{3.34}$$

For instance, if $\|\vec{\gamma}\| \approx 10$ µrad, the coupling factors could potentially be in the order of 10 µm rad^{-1} for roll and pitch, and 1 µm rad^{-1} for yaw.

Tables 3.3 and 3.4 summarize the results of in situ measurements of the TMA misalignments in terms of pitch and yaw offsets of the TX beam direction, $\delta\theta_y$ and $\delta\theta_z$. To first order, these offsets are related to γ via

$$\delta\theta_y \approx -\gamma_1 + \gamma_2 - \sqrt{2}\gamma_3 \tag{3.35}$$
$$\delta\theta_z \approx -\sqrt{2}(\gamma_1 + \gamma_2). \tag{3.36}$$

Unfortunately, this relation does not impose a boundary on the individual γ_i, $i = 1, 2, 3$, given the measured $\delta\theta_y$ and $\delta\theta_z$. Therefore, one does not obtain a definitive boundary for the additional TTL coupling that is caused by imperfectly aligned TMA mirrors.

3.2.3   Coupling via beam splitter

The pathlength of a beam passing through a beam splitter (BS) depends on the refractive index of the material and on the incident beam angle. Note that the interesting quantity is the optical pathlength, which differs from the geometrical pathlength inside the BS. An analytical description of the optical pathlength of a beam traveling through a BS and its dependency on the beam angle is given in [Mül13]. The resulting coupling into the LRI range for one BS made of borosilicate glass (BK7) with a thickness of 5 mm is approximately

$$\delta\rho_{\mathrm{BS}} = \frac{1600 \text{ µm}}{\text{rad}} \cdot \theta_z + \frac{800 \text{ µm}}{\text{rad}^2} \cdot \theta_y^2 + \frac{1500 \text{ µm}}{\text{rad}^2} \cdot \theta_z^2. \tag{3.37}$$

The linear term is unacceptably large, since the requirement for the coupling factor of the yaw angle θ_z, from all possible TTL effects combined, was 200 µm rad^{-1}, cf. Sec. 3.1.1. Thus a second BS is used, called the compensation plate (CP). The CP is rotated by $90°$ w.r.t. the original BS, whereas at both of them the nominal incident beam angle is $45°$. This yields a cancellation of the linear term and a doubling of the quadratic terms:

$$\delta\rho_{\mathrm{BS+CP}} = \frac{1600 \text{ µm}}{\text{rad}^2} \cdot \theta_y^2 + \frac{3000 \text{ µm}}{\text{rad}^2} \cdot \theta_z^2, \tag{3.38}$$

This TTL effect is supposedly the one with the largest quadratic terms, cf. Tab. 3.5. Experimental testing of the coupling factors given above is described in [Sch15], confirming to the

measurement uncertainty of $20\ \mu\mathrm{m\,rad}^{-1}$ that linear coupling is indeed suppressed by the use of the CP.

In order to linearize the quadratic coupling from Eq. (3.38), one may pessimistically assume static pitch and yaw pointing offsets of 1 mrad each. That is, let $\theta_y = \theta_{y,0} + \delta\theta_y$ with $\theta_{y,0} = 1$ mrad, and similarly for θ_z. A Taylor expansion around $(\theta_{y,0}, \theta_{z,0}) = (1,1)$ mrad yields

$$\delta\rho_{\mathrm{BS+CP}} = 3.2\ \mu\mathrm{m\,rad}^{-1} \cdot \delta\theta_y + 6\ \mu\mathrm{m\,rad}^{-1} \cdot \delta\theta_z. \qquad (3.39)$$

3.2.4 Phase front curvature

When the transmitted laser beam is tilted, the phase which is measured at the distant S/C changes, if the center of phase front curvature does not coincide with the center of beam rotation. Note that this means not a S/C tilt, but an actual tilt of the direction of beam propagation, which is almost completely compensated by the DWS and FSM control loop. In the case of an inactive control loop, the quadratic pitch and yaw coupling could be as large as $2\ \mathrm{m\,rad}^{-2}$, according to [Mül17]. Such an error would be intolerable. With the control loop, merely a residual pointing error of the FSM itself, say $\psi = (\psi_{\mathrm{pitch}}, \psi_{\mathrm{yaw}})$, would couple into the range with this coupling factor. A potential misalignment of the TMA mirrors would furthermore add a static component to this residual pointing offset. Linearizing potential quadratic coupling of $2\ \mathrm{m\,rad}^{-2}$ around a working point of $\psi_0 = (10,10)\ \mu\mathrm{rad}$ would leave a coupling of

$$\delta\rho_{\mathrm{PC}|\psi_0} \approx 40\ \mu\mathrm{m\,rad}^{-1} \cdot (\delta\psi_{\mathrm{pitch}} + \delta\psi_{\mathrm{yaw}}) \qquad (3.40)$$

for both S/C in the same way. Given that the residual orientation error ψ of the FSM is of the order of a few $\mu\mathrm{rad}/\sqrt{\mathrm{Hz}}$, such an effect is tolerable, in the worst case yielding a ranging error of about $1\ \mathrm{nm}/\sqrt{\mathrm{Hz}}$.

3.2.5 Other TTL coupling effects

Further potential sources of TTL coupling are listed here.

- Nonplanar or contaminated mirror surfaces can also cause a pointing dependent ranging error.

- Beamwalk due to changes of the beam angle is suppressed by the imaging system on the OBA, however, residual beamwalk can potentially introduce a phase error.

- Ghost beams, e.g. due to multiple reflections in the BS or CP, can result in an error in the measured range, which is depending on the beam direction.

- The off-racetrack paths, cf. Fig. 3.2, nominally cancel out, since they are common to both beams, however, the beams could be shaped differently, which could potentially also cause an angle dependent phase error.

Due to the high sensitivity of the LRI, even more potential disturbing sources could certainly exist. However, after more than three years of LRI operation, the hypothesis that the TMAVP effect is the dominating TTL effect still seems to hold.

3.2.6 Angular rate coupling

During the studies for this thesis, it has been discovered that not only the pointing angles couple into the measured LRI range, but so do the time derivatives of the pointing angles. Here this phenomenon is denoted by angular rate coupling (ARC). The effect of this was already seen in the data before the publication of the original LRI TTL estimation results, cf. [Weg+20b], however, it was described as an unexplained phase shift, not as an ARC effect.

The true explanation of the observed artifact was found afterwards. The existence of ARC in the LRI was reported for the first time in [Weg+20a]. ARC is not a function of the pointing angles, but the angular rates, and thus technically not TTL coupling as it was defined in the beginning of Sec. 3.2. Nevertheless, it will be treated in this thesis in a very similar way. In general, let the ARC error $\delta\rho_{\mathrm{ARC}}$ be described with a first order term,

$$\delta\rho_{\mathrm{ARC}} = \begin{pmatrix} c_x & c_y & c_z \end{pmatrix} \cdot \begin{pmatrix} \dot{\theta}_x \\ \dot{\theta}_y \\ \dot{\theta}_z \end{pmatrix}. \tag{3.41}$$

For the case of the LRI, second and higher order terms are entirely negligible, for all that was found during the investigations for this thesis. In fact, it shall be seen that also the first order ARC error is much smaller than the TTL error for the relevant Fourier frequencies. For the most part, the ARC error is negligible for the science data, it merely becomes important for the analysis of CMC maneuvers, when the pointing angles are oscillating with a relatively high frequency of $83.\bar{3}$ mHz.

The effects which are described in this section cannot be explained when neglecting the light travel time, which is the reason why ARC effects in the LRI were actually not anticipated before the launch. Recall that the LRI is the first instrument of its kind ever operated in space, so that now is the first opportunity to gain experience with its measurement data. Surely, one is aware of the necessity to correct the measured range for a light travel time. To this end, a light time correction (LTC) term is defined, which was recently described in detail in [Yan+21]. I.e., the LTC term is the difference between measured range and instantaneous range. However, this issue is different from the effect described in the following.

Simplified explanation of ARC in the LRI

Fig. 3.10 shows a simplified sketch of the LRI roundtrip path, focusing on the transmitter S/C. It must be noted in advance that for the following explanation, the imaging system on the LRI optical bench (OB) was neglected.

For the sake of theoretical considerations, imagine a plane perpendicular to the LoS, depicted as a vertical dashed line in Fig. 3.10, which has a fixed distance f to the CoM of the transmitter S/C. The term s (in purple) denotes the length of the TX beam path from the BS through the TMA, to the point where it passes the aforementioned virtual plane. The term r (in red) denotes the geometrical length from the point where the RX beam passes the virtual plane to the BS on the optical bench. Note that the sum $r(t) + s(t)$ is by construction constant for all times t, that is, in fact not depending on t. This is because, for the analysis of this error source, perfect alignment of the TMA is assumed, as well as perfect colocation of the VP with the CoM of the S/C. I.e., a small rotation of the whole S/C around the CoM neither changes the instantaneous total pathlength, nor the the lateral offset, nor the antiparallelism of received and transmitted beam, cf. Sec. 3.1.5.

Opposed to that, any expression of the form $r(t) + s(t + \Delta t)$, with $\Delta t \neq 0$, cannot be assumed to be constant w.r.t. t. This is a key observation for the following reason. The RX beam, which has just traveled through the entire roundtrip, is recombined with the local beam at the BS on the transmitter S/C. Any changes of the pathlength r that have occurred during the light travel time on the green path in Fig. 3.10 will appear in the measured range. Note that the way the sketch in Fig. 3.10 is constructed, each one of the pathlenghts r and s depends only on the satellite's orientation w.r.t. the LoS. Another way of saying this is that they change if and only if the transmitter satellite rotates, whereas their instantaneous sum remains unchanged.

In order to estimate the magnitude of this effect, consider the following simplified computation. Consider the situation depicted in Fig. 3.10 to be at time $t = t_0$, and the situation in Fig. 3.11 to be at time $t = t_0 - \tau_{\mathrm{rt}}$, where τ_{rt} denotes the roundtrip light travel time. One would
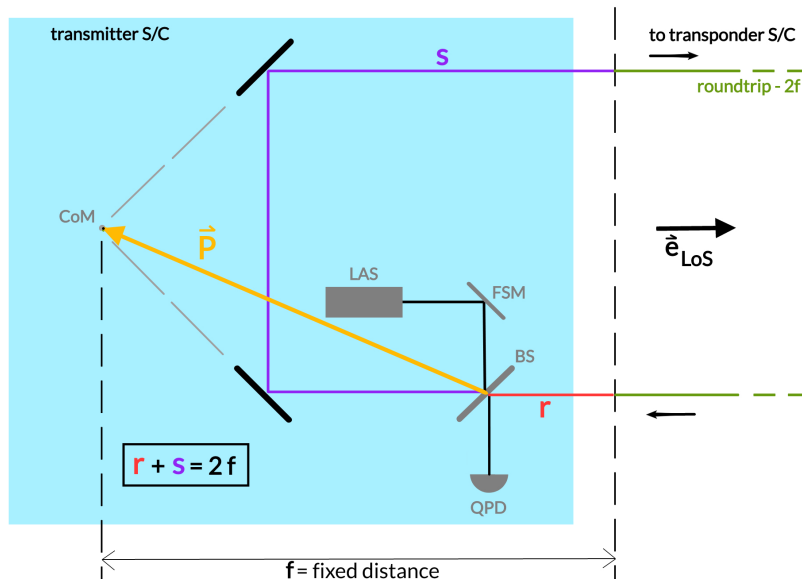
Figure 3.10: Sketch of the LRI roundtrip path. Situation at $t = t_0$.

like to measure the instantaneous range $\rho(t_0)$, which is equal to half the roundtrip pathlength, i.e.

$$2 \cdot \rho_{\text{true}}(t_0) = s(t_0) + r(t_0) + d, \tag{3.42}$$

where d is the rest of the roundtrip pathlength (green path). However, what is in fact measured is $\bar{\rho}(t_0)$:

$$2 \cdot \bar{\rho}(t_0) = s(t_0 - \tau_{\text{rt}}) + r(t_0) + d. \tag{3.43}$$

It is evident that the two quantities are not the same, if there was a nonzero S/C rotation between the two instances of time depicted in Figs. 3.10 and 3.11. Note that d also changes during the light travel time. This is the subject of the light time correction, cf. [Yan+21]. Here the focus lies only on the pathlength changes due to S/C rotation. Therefore, one may consider the length d constant for the considerations in this section.

Thus, the error $\delta\rho_{\text{ARC}}$, which is made by neglecting such rotations, is the difference between the two quantities. One has

$$2 \cdot \delta\rho_{\text{ARC}} = 2 \cdot \bar{\rho}(t_0) - 2 \cdot \rho(t_0) \tag{3.44}$$
$$= s(t_0 - \tau_{\text{rt}}) - s(t_0) \tag{3.45}$$
$$\approx -\tau_{\text{rt}} \cdot \dot{s}(t0) \tag{3.46}$$
$$= \tau_{\text{rt}} \cdot \dot{r}(t0). \tag{3.47}$$

For the time derivative of r, one can write $r(t) = r_0 + \delta r(t)$, for some r_0, and describe the variations of r by

$$\delta r = \vec{e}_{\text{LoS}}^T R_{\text{SF}}^{\text{LOSF}} \vec{P}^{\text{SF}}, \tag{3.48}$$

where $\vec{P}^{\text{SF}} = (P_x, P_y, P_z)^T$ is the vector pointing from the BS to the CoM (depicted in yellow), given in SF. Analogous to the computation that lead to Eqs. (3.31) and (3.32) for the TTL error caused by the VP-CoM offset, one can derive the first order approximation

$$\delta r(t) \approx P_z \theta_y(t) - P_y \theta_z(t), \tag{3.49}$$

where θ_y is the pitch angle and θ_z is the yaw angle of the transmitter S/C. The vector $\vec{P}^{\text{SF}}$ is
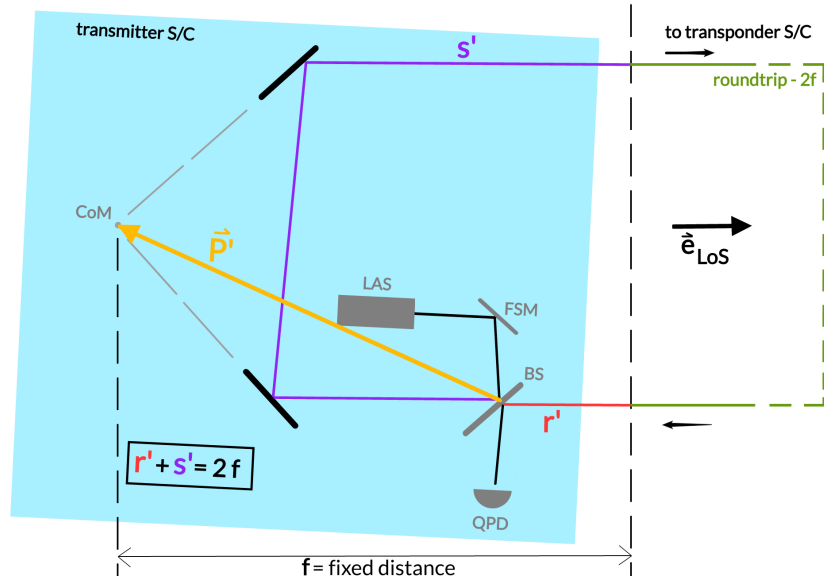
Figure 3.11: Sketch of the LRI roundtrip path. Situation at $t = t_0 - \tau_{\mathrm{rt}}$.

roughly given by $\vec{P}^{\mathrm{SF}} \approx (900, -300, 24)^T$ mm [14]. Hence,

$$\delta\rho_{\mathrm{ARC}} \approx \frac{\tau_{\mathrm{rt}}}{2} \cdot \dot{r}(t) \tag{3.50}$$

$$\approx \frac{\tau_{\mathrm{rt}}}{2} \cdot \frac{d}{dt}\left(e_{\mathrm{LoS}}^T \cdot \vec{P}\right) \tag{3.51}$$

$$\approx \frac{L}{c} \cdot \left(24 \ \mathrm{mm\,rad}^{-1}\dot{\theta}_y(t) + 300 \ \mathrm{mm\,rad}^{-1}\dot{\theta}_z(t)\right) \tag{3.52}$$

Note again that this error only occurs for rotations of the transmitter S/C, not the transponder. Also important to note, the magnitude of the error depends on the absolute S/C separation L. Assuming for instance $L = 175$ km, roughly the mean separation of the GFO S/C during the year 2019, one obtains

$$\delta\rho_{\mathrm{ARC}} \approx 15 \ \mathrm{\mu m\,s\,rad}^{-1}\dot{\theta}_y(t) + 175 \ \mathrm{\mu m\,s\,rad}^{-1}\dot{\theta}_z(t), \tag{3.53}$$

where $\dot{\theta}_y$ and $\dot{\theta}_z$ denote the time derivatives of the transmitter satellite's pitch and yaw angles, respectively. Since faster S/C rotations cause a larger ARC error, ARC is less relevant for low Fourier frequencies. It becomes important when there are relatively fast satellite rotations, e.g. during a rotation maneuver. In fact, as shall be seen later, during a CMC maneuver, the magnitude of the range variations it causes can be close to the magnitude of TTL coupling. The theoretical examination in this section suggests that a significant ARC effect can be expected during yaw maneuvers of the transmitter S/C. This will be confirmed by the data analysis presented in Chap. 5. Figure 3.12 shows exemplarily the ASDs of pitch and yaw rates, $\dot{\theta}_y$ and $\dot{\theta}_z$, based on FSM data from 6 days in April 2019. In the following, TTL and ARC effects are summarized.

3.2.7   Summary of TTL and ARC effects

A summary of some of the expected TTL effects is given in Tab. 3.5, including rough values for their respective linear coupling factors a_i, as well as quadratic coupling factors b_{jj}, given in $\mathrm{\mu m\,rad}^{-1}$ and $\mathrm{\mu m\,rad}^{-2}$, respectively. Note that the values refer to the effect caused on one of the two S/C. The total TTL ranging error is the result of all effects combined, including both S/C.
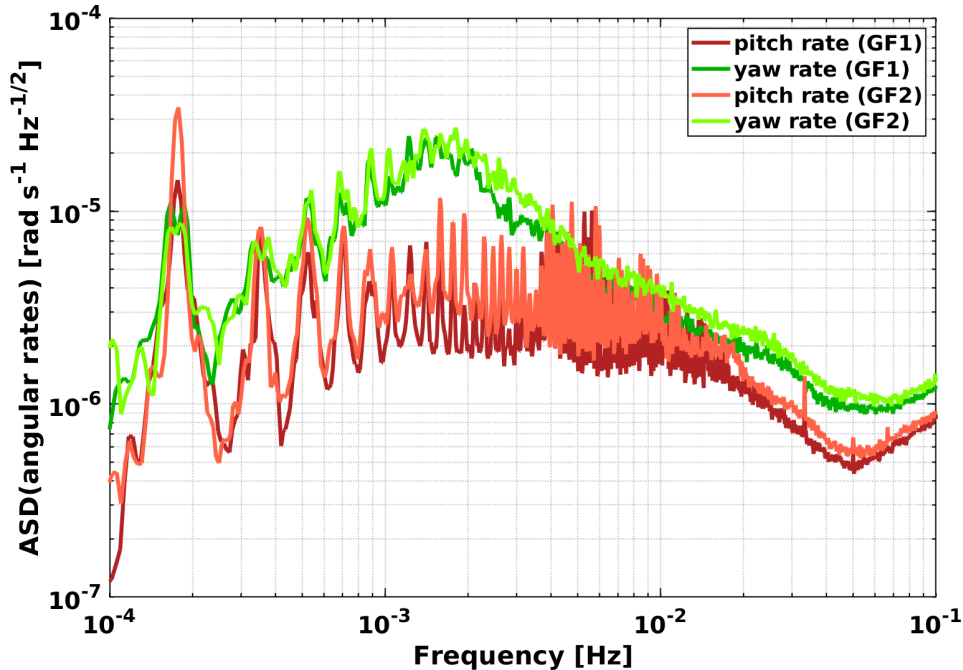
Figure 3.12: Amplitude spectral densities (ASD) of the time derivatives of pitch (red lines) and yaw angles (green lines), for GF1 and GF2. The angles for this plot were derived from LRI FSM data, recorded from 10 to 15 April 2019.

Table 3.5: Overview of LRI TTL effects and rough magnitudes of the respective coupling factors (for one S/C) in $\mu m\,rad^{-1}$ (a_i; linear) and in $\mu m\,rad^{-2}$ (b_{jj}; quadratic).

TTL effect	a_x	a_y	a_z	b_{xx}	b_{yy}	b_{zz}
TMAVP	–	≈ 100	≈ 100		≈ 50	≈ 50
TMA misalignment	≈ 10	≈ 10	≈ 1	–	–	–
BS without CP	–	≈ 1600	–	–	≈ 1500	≈ 800
BS with CP	–	–	–	–	≈ 3000	≈ 1600
phase front curvature	–	–	–	< 1	≈ 5	≈ 5

Figure 3.13 shows a spectrum of the LRI range (purple line), as well as different types of TTL and ARC errors. The shown spectra were computed using FSM angles from a 9-day data segment (9 to 17 April 2019), and with the theoretical coupling factors shown in Tab. 3.5. I.e., for the TMAVP effect (green line), the values 0, 100, and 100 $\mu m\,rad^{-1}$ were assumed for roll, pitch, and yaw, respectively. For the TTL error caused by TMA misalignment (red line), the values 10, 10, and 1 $\mu m\,rad^{-1}$ were assumed for roll, pitch, and yaw coupling. In relation to the other error contributions, the assumed quadratic coupling due to the BS and CP of 2 $mm\,rad^{-2}$ for pitch and 4 $mm\,rad^{-2}$ for yaw is negligible (cyan line), even if an additional bias of 1 mrad is assumed for all pointing angles (orange line). For the ARC, a S/C separation of $L = 175$ km was assumed, cf. Eq. (3.53). The effects due to pitch and yaw rate coupling, labeled *PRC* and *YRC* (pink and blue lines) are plotted separately.

The additional bias for the quadratic coupling was assumed for the following reason. Due to imperfect knowledge of the alignment of different reference frames, it may only be possible to determine the pointing angles up to a constant. In this sense, the pointing angles vary around some constant values, which are called here a static pointing offset. For linear coupling, such a static pointing offset leads to a constant pathlength error, which is irrelevant for the biased range. For quadratic coupling, however, it leads to a nonconstant pathlength error, and thus
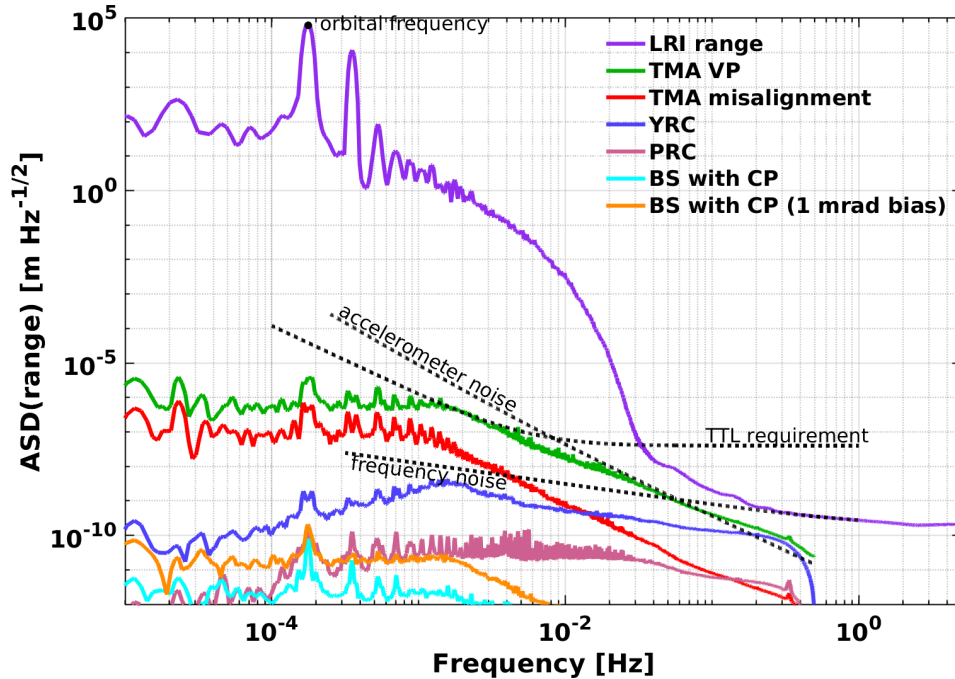
Figure 3.13: Amplitude spectral densities (ASD) of LRI range, and simulated TTL and ARC errors, for a 9-day segment during April 2019. Coupling factors are based on pre-flight expectations. For the orange line, an additional static pointing offset of 1 mrad was assumed for all angles. For the frequency noise, a mean inter-satellite distance of 175 km was assumed. For the ARC, the effects due to pitch and yaw rate coupling, labeled *PRC* and *YRC* (pink and blue lines) are plotted separately.

cannot be ignored in general.

For comparison, Fig. 3.13 also shows the TTL requirement as well as a model of LRI frequency noise (LFN) derived from ground measurements, cf. Eq. (3.20). The model depends on the S/C separation, which was 175 km here. Shown is also accelerometer noise based on a model for GRACE [Dar+17], converted to LoS range. Noise in the accelerometer data is a significant error contributor in GFR. Figure 3.13 illustrates that the TTL error is lower than the contribution to GFR from accelerometer noise. The elevated LRI range spectrum between 40 and 200 mHz is caused by physical range variations from nongravitational forces, which can be partly removed using accelerometer data, see App. E.

To summarize, as the quadratic TTL coupling seems to be negligible, a linear TTL model is assumed from now on in this thesis. Since the TMAVP effect can be expected to be the dominant linear TTL effect, it will be assumed that the total TTL error term is approximately described in Eq. (3.32). The model for the ARC error shall be (3.52). In the following section, different approaches for the TTL estimation are presented.

3.3   LRI TTL estimation strategy

In this section, the approach of estimating LRI TTL coupling is outlined, which is pursued within the study presented in this thesis. Furthermore, a work flow shall be developed for this purpose. Before going into the details of each step, some light may be shed on a more basic decision, which should be made first. In order to estimate the TTL error, the most fundamental requirement is to have a ranging product, i.e. a modification of the raw range measured by the LRI, which contains the TTL error. Five basic concepts of TTL estimation can be identified, depending on which ranging product is used, see also Fig. 3.14. The different
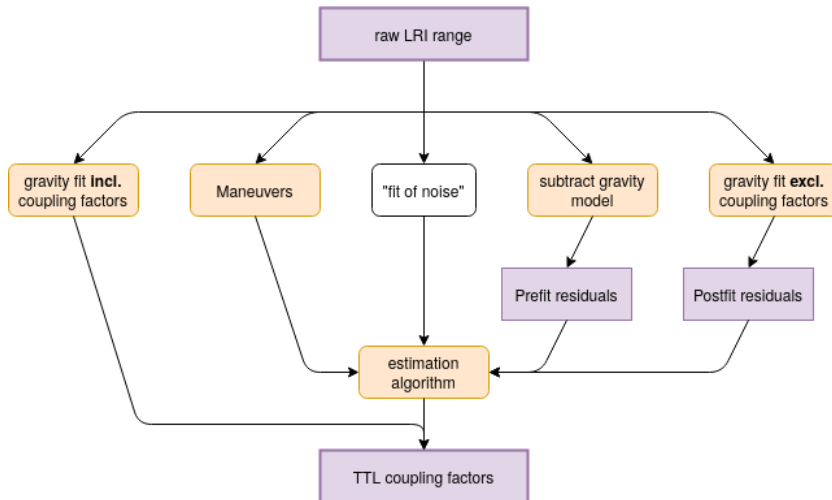
approaches are briefly described below.

Figure 3.14: Five approaches for estimating LRI TTL coupling factors.

3.3.1 TTL estimation approaches

At first, consider the concept of using satellite rotation maneuvers for TTL estimation, since this is the approach that is preferred in this study. The main results presented in this thesis are based on this method.

Using satellite rotation maneuvers

The TTL error is a function of the pointing angles. It can be amplified by deliberately causing excitations of the angles, i.e. by rotating the S/C. Such an excitation is then called a stimulus. This is achieved by utilizing the S/C ACS. Typically, a periodic excitation profile is chosen, such that the TTL error can be isolated well from the range. From the data collected during the maneuver, the TTL estimation is more accurate than from data collected in the absence of a maneuver.

This thesis concentrates on the estimation using such maneuvers. In the GFO mission, so-called CMC maneuvers are performed regularly. Their original purpose is to estimate the offset between the ACC proof mass and the S/C CoM, see Sec. 4.1 for a more detailed description. The CMC maneuvers consist of periodic angular accelerations caused by MTRs. These angular accelerations have a period of 12 seconds, which yields a signal with a frequency of $83.\overline{3}$ mHz. It will be worked out in this thesis that CMC maneuvers are suited for LRI TTL estimation.

An advantage of this concept in general is that the maneuver frequency can be chosen to yield the best estimation results. Further maneuver parameters can be optimized as well, see Sec. 4.3 for more details. The maneuver approach is also less susceptive to attitude measurement noise than other approaches.

The main disadvantage of the concept of estimating TTL using maneuvers is that only very small amount of data can be analyzed, due to the limited duration of the maneuvers. Moreover, planning and performing rotation maneuvers requires effort and time. Possibly, the taking of the main science data of a satellite mission may be partly or fully interrupted during a rotation maneuver. As with any S/C operation, there is also some risk in performing maneuvers, although this risk is rather small.

Fit of noise

In the "fit of noise" approach, the LRI range is used directly for the estimation. The data does not have to be from a certain restricted time span, as is the case if one uses calibration maneuvers. Moreover, there should not have been any advanced processing before the TTL estimation. However, the range and auxiliary data may have undergone some basic processing, e.g. time stamp correction, resampling, or filtering out certain frequency bandwiths.

For estimation methods such as the least squares fit, the standard deviation (STD) of the estimated parameters is anti-proportional to the square root of the length of the time series that was used, as shall be seen later in this thesis. Thus, the fact that this approach is not restricted to a short time span is a direct advantage. In principle, the entire data measured since launch can be used. A drawback of this approach is that unprocessed range can contain a variety of other disturbances as well as gravity signal, which may distort the TTL results. In fact, for instance the activation of attitude control thrusters turns out to be a big hurdle within this approach.

Subtraction of gravity model from the range

Another possible way is to subtract a static gravity model, as well as accelerometer data from the range to obtain so-called pre-fit residuals. Those should in theory still contain the TTL error, and may thus be used for the estimation of coupling factors.

Gravity fit excluding coupling factors

Within this approach, a gravity fit is performed, excluding the estimation of coupling factors, to obtain so-called post-fit residuals. These residuals are then used for the estimation of the TTL error. In theory, the pots-fit residuals could still contain the unchanged TTL error as it was present in the raw range. However, it is uncertain whether it would be partly absorbed by other parameters that are estimated during the gravity fit.

Gravity fit including coupling factors

One possible approach is to include the estimation of LRI TTL coupling factors in the GFR process. The gravity field of the Earth is usually modeled using spherical harmonic (SH) functions. Here gravity fit means to determine the corresponding SH coefficients that yield the best fit of the model to the satellite data. It is common practice to include certain parameters such as ACC bias and scale in the same fitting process. I.e. these parameters are estimated together with the SH coefficients. Thus, it should be technically possible to add the TTL coupling factors to the list of parameters to be determined.

The technique of GFR is a complicated topic on its own and is beyond the scope of this thesis. This approach is thus not pursued in this thesis. A possible drawback of it could be that the coupling factors absorb more of the data than they are supposed to, e.g. due to other effects which are correlated with the inter-satellite pointing angles.

3.3.2   TTL estimation work flow

By the time of writing, the LRI is in operation and a sufficient amount of data is available. A major part of the investigations, which form the basis of this thesis, was carried out before the launch of GFO and thus before the availability of GFO data. This time was used to gain experience and familiarity with GRACE data, study the theory of S/C attitude determination, and the necessary data analysis tools and methods. The LRI TTL effects were studied and a TTL model was derived. Moreover, the simulation of maneuvers and sensor data is a basic prerequisite in order to test the parameter estimation algorithms, as well as for the purpose

of maneuver design. The latter was a necessary task to be carried out before the launch of GFO, in order to be prepared to make a proposal for a dedicated LRI TTL calibration maneuver, should the CMC maneuvers turn out not to be sufficient. Simulations are therefore also incorporated in the overall strategy depicted in Fig. 3.15. These will be treated in the following chapter. The data processing and analysis of real data, carried out after the launch, is discussed in Chap. 5.

Figure 3.15 illustrates the different steps in the TTL calibration work flow. It is applicable for any of the five basic concepts described above, however, the individual steps should be adjusted accordingly. Out of the different basic concepts described above, satellite rotation maneuvers seemed to be the most promising approach. The different steps are briefly addressed individually in the following. For each step, a reference to the respective section in this thesis is given, where it is treated in detail.
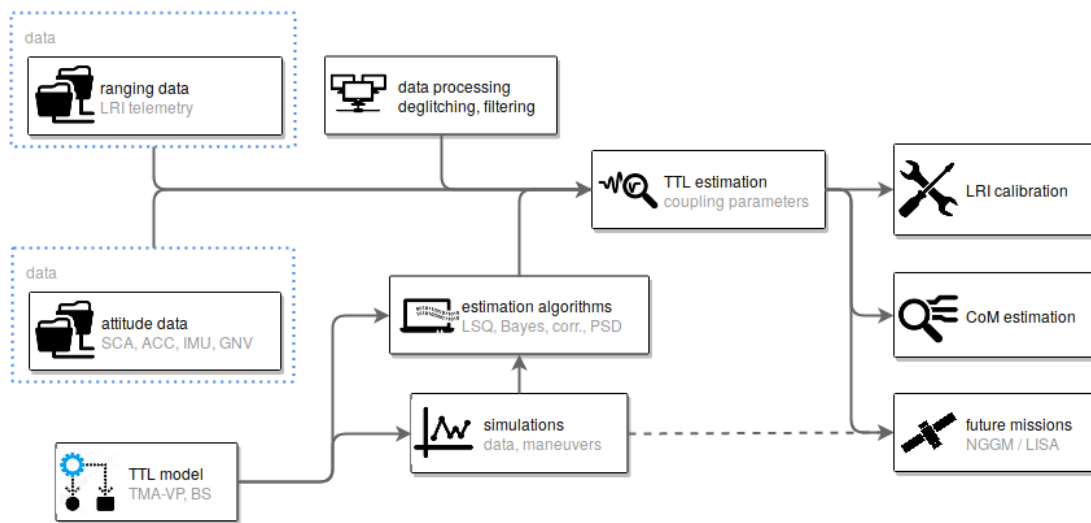

Figure 3.15: Flow chart illustrating the path to LRI TTL calibration.

Data and data processing

Data and data processing for TTL estimation is explained in Sec. 5.1. Attitude data processing in particular is treated in detail in Sec. 2.2.

TTL model

The linear TTL model for the LRI that will be assumed in this thesis has been derived in Sec. 3.2. Considered will be merely linear coupling factors, which are assumed to be related to the components of the VP-CoM offset according to Eq. (3.52). Roll coupling factors are expected to be close to zero. If this expectation can be confirmed, it may be sufficient to estimate pitch and yaw coupling factors from thereon.

The ARC model is given in Eq. (3.52). Since there the coupling factors depend merely on the S/C separation, it may not be necessary to estimate these factors continuously. Once the model is confirmed, the ARC error term can be computed for any time.

Simulations

The simulation of maneuvers is an important step to prepare for TTL estimation before the mission launch. It is treated in Sec. 4.2. It is a useful tool which may also be useful for future missions.

Estimation algorithms

The estimation algorithms which were used in this study are described in depth in Sec. 5.2. Several different approaches will be tested and their performance will be evaluated.

TTL estimation

The key point of TTL and ARC estimation is to determine the coupling factors. This step is where the outputs of the previous steps are combined, which are: processed range and pointing angles, as well as estimation algorithms based on a TTL model. The output of this step are the TTL and ARC coupling factors. The final results are shown in Sec. 5.3.

LRI calibration, CoM estimation, future missions

Once the coupling factors are estimated, the total error term can be computed using pointing angles from any of the mentioned sources. This error term can be subtracted from the LRI range to obtain the calibrated range, see Sec. 5.4. Any insights that were gained can be used to derive lessons learnt for future missions which are utilizing inter-satellite laser interferometry. According to Sec. 3.2, the coupling factors may moreover be used to derive the offsets between S/C CoM and TMA VP. With many subsequent data points available, one can track the CoM movement over time, see also Sec. 5.3.4.

Chapter 4

Satellite rotation maneuvers

For the purpose of this study, a satellite rotation maneuver is a sequence of angular S/C motion, which is evoked by a pre-defined control torque, executed using the onboard attitude control mechanisms. In this thesis, the fact is utilized that rotation maneuvers evoke a magnified TTL error with a periodic profile. As such, it is much easier to be isolated from the measurements than the TTL error which is present in the absence of a rotation maneuver. This chapter is meant to cover all aspects of S/C rotation maneuvers, which are relevant for the analysis presented in this thesis.

As will be seen, the so-called center-of-mass calibration (CMC) maneuvers can be utilized for the LRI TTL estimation, and they will in fact be used to obtain the estimated coupling factors presented in this thesis, cf. Chap. 5. In Sec. 4.1, the CMC maneuvers are described in detail. Their suitability for LRI TTL estimation is examined here, since they are primarily performed for a different purpose. Also, some emphasis is put on how the CMC maneuvers have changed from GRACE to GFO.

Section 4.2 is meant to give a comprehensive description of the maneuver simulation technique, which is restricted to using MTRs or attitude thrusters for attitude actuation. It can be used as a guide for simulating satellite rotation maneuvers, which is also applicable beyond GFO. The most important force and torque models are described, as well as the integration technique. The methods are validated using data from the real GFO mission.

In Sec. 4.3, it is illustrated in much detail how to design a rotation maneuver for the purpose of estimating TTL coupling. When planning a maneuver, some choices can be made and some restrictions have to be respected. The entire procedure of making these decisions is described. In doing so, it is essential to be clear about what the exact purpose of the maneuver is. This will be elaborated on, with a focus on LRI TTL coupling. In the end, some configurations can be derived which are optimal for this specific purpose.

Some simulation results are presented in Sec. 4.4: i) reconstruction of CMC maneuvers in order to validate the simulation technique; ii) simulation test case of 14 maneuvers, utilizing two different frequencies and a phase shift; iii) full simulation test case with optimal parameters; iv) simulation of longer maneuvers with occasional activation of attitude control thrusters.

4.1 Center-of-mass calibration (CMC) maneuver

Two types of maneuver procedures exist for GFO, which have already been common practice for GRACE: center-of-mass calibration (CMC) maneuvers and KBR maneuvers. Both are potentially interesting for LRI TTL estimation, since they consist of periodic pointing angle oscillations. However, it can be seen immediately that the LRI cannot take measurements during KBR maneuvers, since the pointing deviation during a KBR maneuver is with up to 3 °, i.e. about 52.4 mrad, too large for the LRI to take measurements. For the sake of

completeness, the KBR maneuvers are described in App. C. This leaves only CMC maneuvers as a valid option for TTL estimation.

The purpose of the CMC maneuvers for GFO is to determine the offset between the S/C CoM and the ACC RP. This offset is important to know, since it causes a coupling of S/C rotations into the accelerometer measurements, cf. [Wan03]. The mission requires that the offset must not be larger than 0.5 mm, with a stability of 0.1 mm per half year, or better [Kor+19]. If desired, the S/C CoM can be shifted back to the ACC RP, using movable trim masses on the satellite. This procedure is called mass trim maneuver. By the time of writing, such mass trims have been carried out on GF1 on 18 July 2018, as well as on 14 May 2020, not counting mass trims in SF x direction, which do not play a role in this thesis, see also Sec. 5.3.4. After each calibration, the updated offset vector pointing from the ACC RP to the S/C CoM is reported via the VCM1B data product [Wen+19].
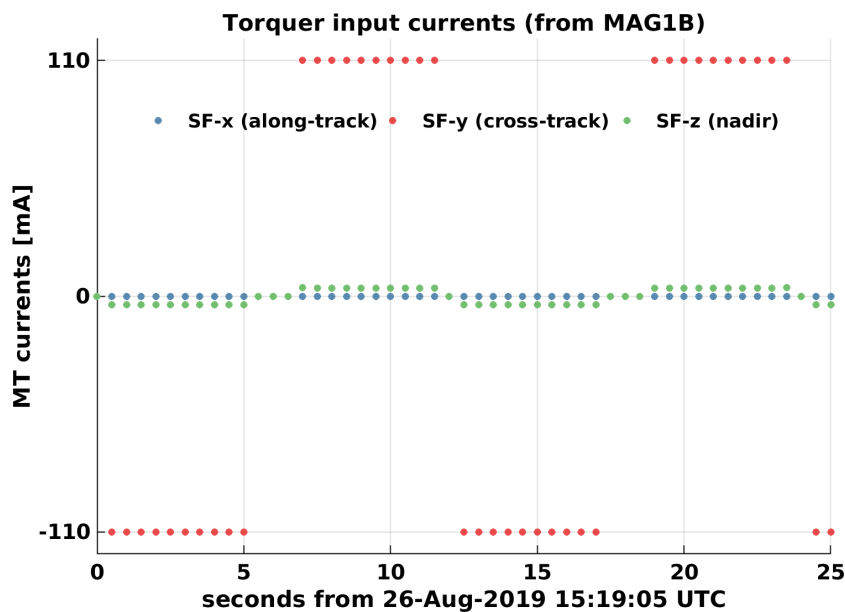

Figure 4.1: First two cycles of GF1 magnetic torque rod currents applied during a CMC roll maneuver on 26 August 2019.

The CMC maneuvers are performed using MTRs, whose primary purpose is to control the S/C attitude in the nominal mission phase [Her+04]. These rods produce a magnetic dipole moment, which causes a torque in combination with the Earth's magnetic field, as described in Sec. 2.3. During a CMC maneuver on GFO, two of the torque rods are activated in such a way that the resulting magnetic dipole moment is aligned perpendicular to the desired rotation axis. Its magnitude profile is rectangular with a period of 12 seconds, yielding a signal with the highest component at the first harmonic, i.e. with a Fourier frequency of $83.\bar{3}$ mHz, besides higher harmonics with smaller amplitudes. Each CMC maneuver consists of 15 cycles of this profile, which results in a maneuver duration of 180 seconds. The nearly square wave pattern allows for larger angle amplitudes compared to a sine wave pattern, cf. Sec. 4.3.2. While the period is pre-defined, the optimized combination of the two torque rods which are activated is computed onboard, using measurements of the Earth's magnetic field [tea19]. The objective of this optimization is that the torque should be aligned with the desired rotation axis. Each maneuver is meant to cause angular motion around one of the S/C axes, i.e. excite either roll, pitch, or yaw. Figure 4.1 shows two cycles of the profile of the MTR currents, as reported in the MAG1B data [Wen+19], during a roll CMC maneuver in August 2019. The currents can

be converted to the resulting magnetic dipole moment $\vec{m}$ by

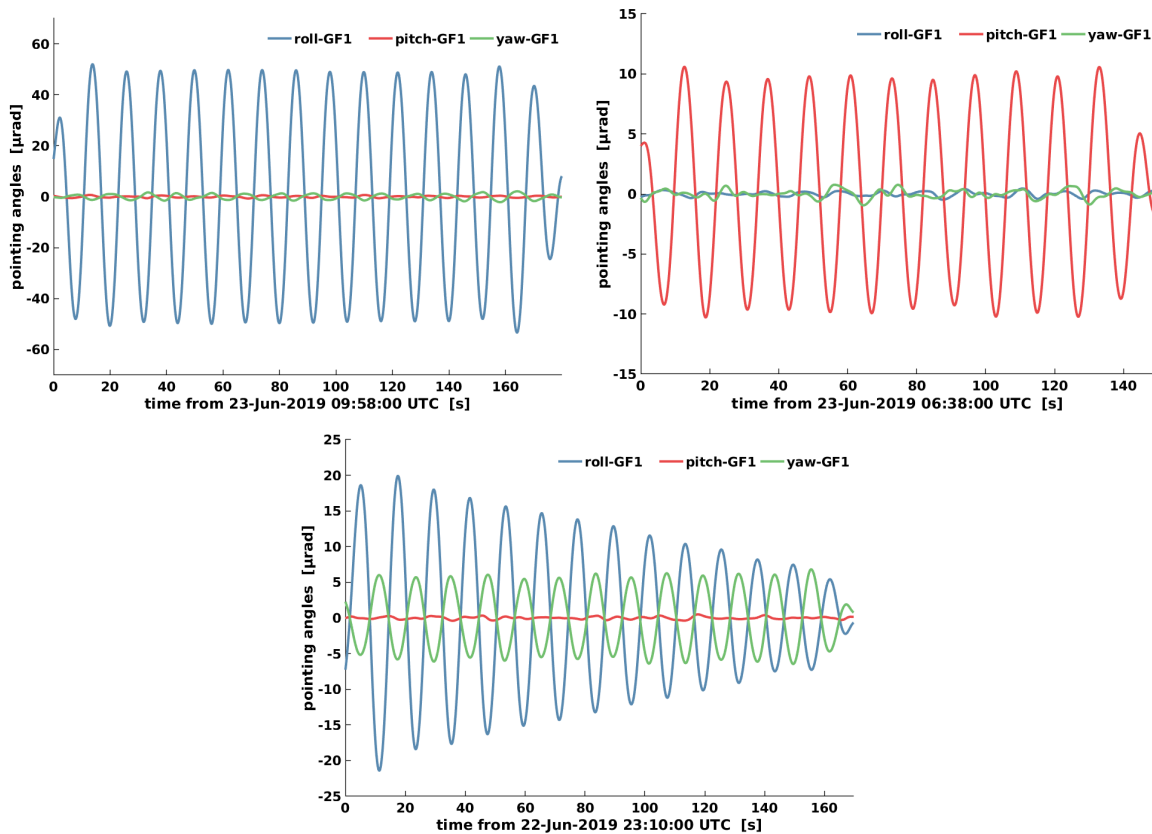$$\vec{m} = \begin{pmatrix} I_x \\ I_y \\ I_z \end{pmatrix} \cdot 250 \text{ m}^2. \tag{4.1}$$

Figure 4.2: Bandpass filtered inter-satellite pointing angles during CMC maneuvers on GF1 in June 2019. Top left: roll maneuver. Top right: pitch maneuver. Bottom: yaw maneuver.

The magnitude of the angular accelerations typically achieved during the CMC maneuvers are about 12.4, 2.3, and 1.4 µrad s^{-2} for roll, pitch, and yaw axes, resulting in pointing angle oscillations with amplitudes about 50, 10, and 6 µrad, respectively. Figure 4.2 shows pointing angles during a roll maneuver (top left), a pitch maneuver (top right), and a yaw maneuver (bottom) performed on GF1 on 22 and 23 June 2019. The pointing angles for this plot were computed from IMU1B RL04 data, cf. Sec. 2.2.1. All angles in these plots were filtered with a pass band from 50 to 120 mHz.

The excitation of the roll angle during the yaw maneuver is not desired, but unavoidable for the following reason. Figure 4.3 shows the SF components of the geomagnetic field, exemplarily for GF1 in October 2019, plotted over the degree of latitude. Although these depend on the longitude and on the S/C orientation as well, they typically stay within the depicted margin. The field lines near the equator have a large component in SF x direction. This x component is used to achieve a torque in z direction, in order to excite the yaw angle, by activating the torque rod in y direction. This activation of the y rod produces also a torque in x direction, exciting the roll angle, due to the magnetic field z component. This z component is rapidly changing its sign at about zero degree latitude. The result is an unavoidable excitation of the roll angle, with rapidly changing amplitude. The yaw maneuvers take place near the equator, but the S/C is not crossing it during the maneuver. With an orbit revolution time of about
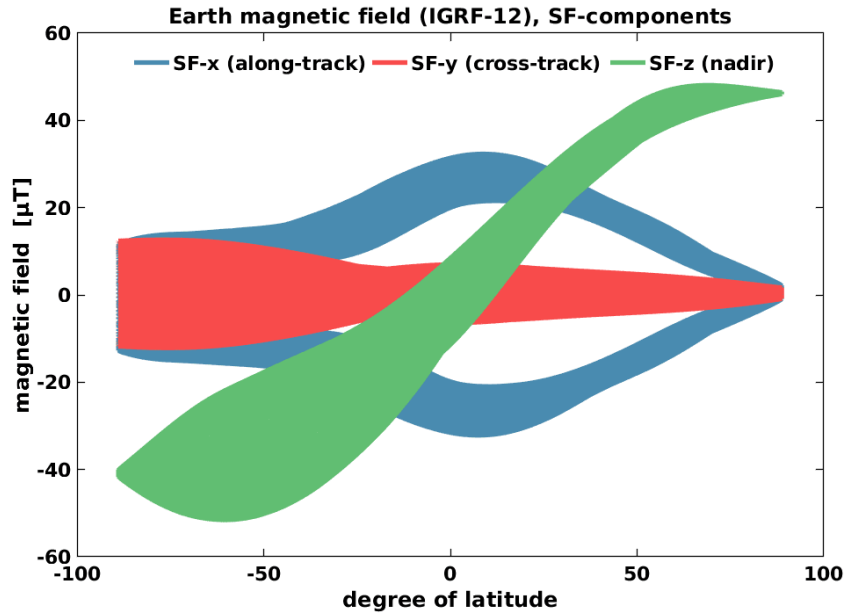
Figure 4.3: Geomagnetic field SF-components from five days in October 2019, from the IGRF12 model.

5600 seconds, in a near-polar orbit, it takes about 15-16 seconds for the S/C to overfly one degree of latitude. With a maneuver duration of 180 seconds, CMC maneuvers thus take place in a latitude band of size 11-12 degrees.

For the GRACE mission, roll and pitch maneuvers were executed near the north pole within the region between 60 and 80 degree latitude, yaw maneuvers were executed near the equator between 10 and 20 degree latitude [Wan+10]. These locations were carefully chosen. One of the main criteria for planning the maneuvers is that the achievable magnitude of the angular acceleration is maximal in one of the S/C axes, while low in the other axes. The optimal maneuver locations for GFO are similar to those for GRACE, since both missions utilize a near-polar orbit. Maneuver locations that would be optimal for a dedicated TTL calibration maneuver are discussed in Sec. 4.3.5.

CMC maneuvers have been performed once per month up to September 2019, and there-after planned to be performed in a half yearly cycle. At each instance, 14 maneuvers in total, i.e. 7 maneuvers per S/C, are spread over two calendar days. For each of the angles roll, pitch, and yaw, two maneuvers are performed. Furthermore, one mixed maneuver per S/C is performed, exciting both roll and pitch angles. The same procedure was used for GRACE, however, with a slightly different magnitude profile of the torque.

As far as the estimation of the offset between ACC and CoM is concerned, the CMC maneuvers can be performed simultaneously on both S/C, since the measurements of one accelerometer are independent of the rotations of the distant S/C. Regarding the LRI, the pointing variations of both S/C couple into the same measurement, the biased range. If both S/C simultaneously perform rotation maneuvers, it may not be possible to disentangle the two effects, which would likely result in less accurate estimation of the LRI TTL coupling factors. For this reason, CMC maneuvers on GFO are planned such that the time spans of any two maneuvers do not overlap. Since the accuracy of TTL estimation from CMC maneuvers seems to be sufficient, no dedicated TTL calibration maneuvers are planned for the GFO LRI. For the sake of completeness, in App. C, the geometric ranging error of the KBR instrument is described, as well as the rotation maneuvers which are performed in order to calibrate this error.

In the following section, 4.2, a technique for simulating individual rotation maneuvers is

developed. Afterwards, in Sec. 4.3, optimal maneuver parameters for the purpose of LRI TTL estimation are derived, which can then be compared to the values of a CMC maneuver.

4.2 Maneuver simulation

The dynamics of rotational motion are given by Eqs. (2.18) to (2.20) in Sec. 2.1.2. According to Eq. (2.20), the S/C angular accelerations are driven by the total torque $\vec{\tau}$ that is acting on the S/C. Thus, in order to carry out a rotation maneuver, one must apply a control torque which is large enough to dominate the environmental torque. Defining the control torque is the goal of planning and simulating S/C rotation maneuvers.

Simulating a rotation maneuver means to integrate the state vector of the S/C attitude, and, if applicable, also that of the S/C position. Besides a suitable initial state, this requires knowledge of the torque and, if applicable, the forces acting on the S/C. Different types of torque will be defined and analyzed in Sec. 4.2.1. Some force models are defined in Sec. 4.2.2, which are later used for orbit integration. Sec. 4.2.3 covers all other aspects of the simulation technique used in this analysis.

4.2.1 Torque

Any force $\vec{F}$ acting on a point of the S/C produces a torque, unless the force vector is exactly parallel or antiparallel to the vector $\vec{r}$ pointing from the S/C CoM to that point. These torques, for each point of the S/C given by

$$\vec{\tau} = \vec{r} \times \vec{F}, \tag{4.2}$$

in general do not sum to zero when accumulated over the whole S/C. The total torque $\vec{\tau}$ can be decomposed into environmental nongravitational, gravitational, and control torque:

$$\vec{\tau} = \vec{\tau}_{\text{ng}} + \vec{\tau}_{\text{grav}} + \vec{\tau}_{\text{ctrl}}. \tag{4.3}$$

In the following, some sources of S/C torque for a low Earth orbit (LEO) satellite such as GFO are defined.

Nongravitational torque

The environmental nongravitational torque can be decomposed further into its components. For the purpose of this thesis, merely aerodynamic torque and solar radiation torque are considered, i.e.

$$\vec{\tau}_{\text{ng}} = \vec{\tau}_{\text{aero}} + \vec{\tau}_{\text{solar}}. \tag{4.4}$$

The aerodynamic torque is the torque caused by atmospheric drag. It can be computed by integrating Eq. (4.2) over the outer surfaces of the S/C , cf. [Wer78],

$$\vec{\tau}_{\text{aero}} = \int \vec{r} \times d\vec{F}_{\text{aero}}. \tag{4.5}$$

The solar radiation torque is caused by solar radiation pressure forces acting on the S/C surfaces. Similar to the aerodynamic torque, it is simply defined by integrating the torques acting on each surface element of the S/C, which can be written as

$$\vec{\tau}_{\text{solar}} = \int \vec{r} \times d\vec{F}_{\text{solar}}. \tag{4.6}$$

In order to compute these torques, the respective force models must be available. The force models are introduced in Sec. 4.2.2 below. For the computation of solar radiation pressure accelerations, merely the forces of each outer S/C surface which is exposed to sunlight

need to be determined and summed up. A larger effort is required to compute the torque, since there the force model should be evaluated for every point of the outer S/C surfaces. A method to approximate this is to consider finite surface elements and use summation instead of integration, i.e. with a so-called finite element model (FEM).

In principle, any force can create a torque. However, atmospheric drag (ATD) and solar radiation pressure (SRP) are the largest sources of nongravitational acceleration for satellites flying at a similar altitude as GFO, i.e. 500 km. Thus, these two types of nongravitational torque are considered the most relevant. Examplarily, Fig. 4.4 shows modeled aerodynamic and solar radiation torques for GF1 given in SF during roughly 3 orbit revolutions in April 2019. Other contributions, such as torque caused by radiation from the Earth, are not investigated for the analysis presented in this thesis. In the following, the gravitational torque is defined.
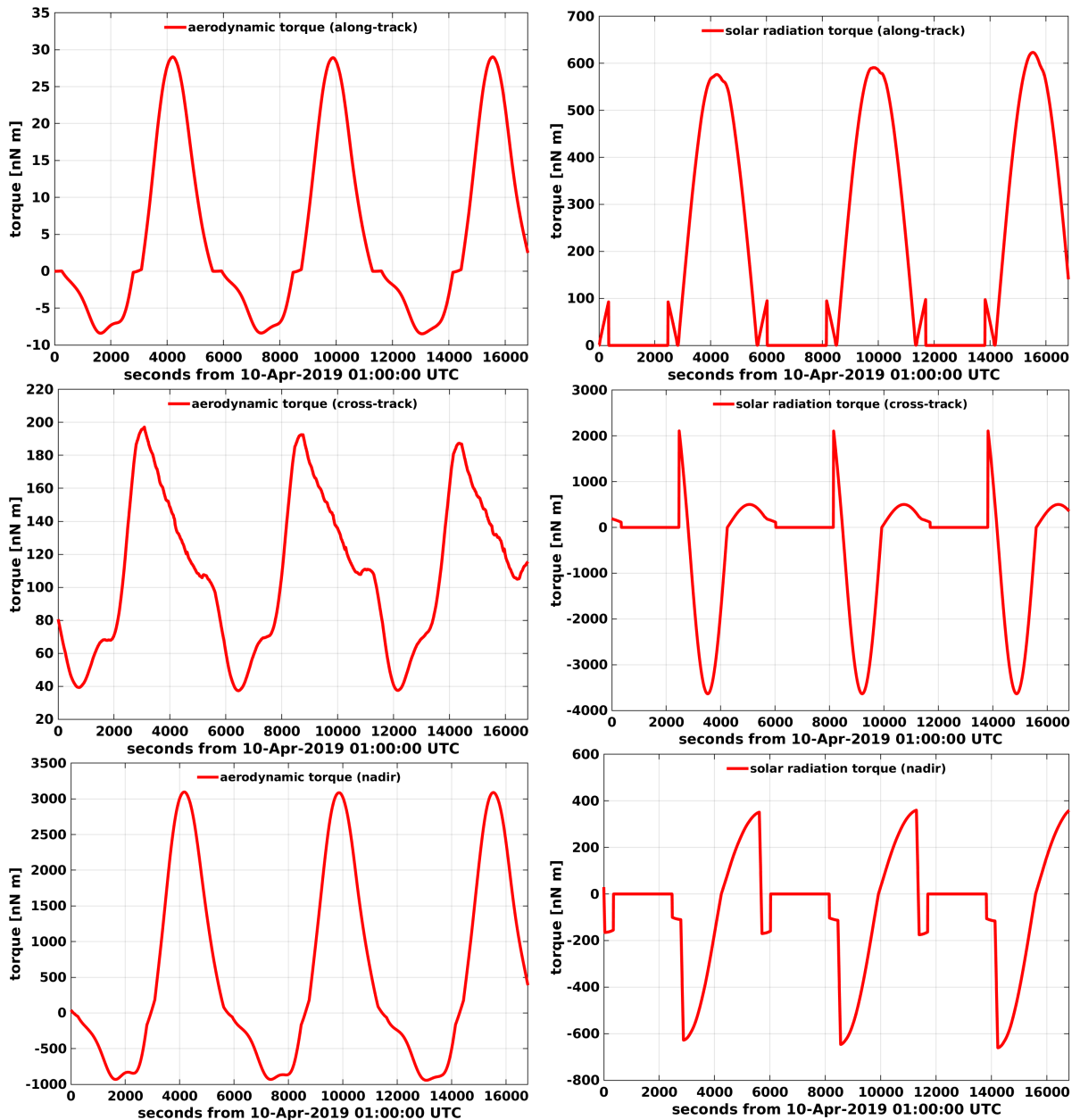

Figure 4.4: Modeled GF1 torques for 16800 seconds during 10 April 2019, given in SF. Left: aerodynamic torque. Right: solar radiation torque.

Gravitational torque

Similar to the nongravitational torque, the gravitational torque, which is caused by the inhomogeneity of the gravitational field, can be obtained by regarding infinitesimal parts of the S/C, and then integrating in order to obtain the total torque. For the purpose here, the Earth's mass distribution can be assumed to be spherical. Then, according to [Wer78], the gravitational force acting on a mass element dm of the S/C is given by

$$d\vec{F} = -\mu \frac{\vec{R}}{R^3} dm, \tag{4.7}$$

where μ is the Earth's gravitational constant, $\vec{R}$ is the vector pointing from the geocenter to the mass element, and $R = |\vec{R}|$. The torque imposed on the S/C by the force $d\vec{F}$ is then

$$d\vec{\tau} = \vec{r} \times d\vec{F}. \tag{4.8}$$

denoting by $\vec{r}$ the vector pointing from the S/C CoM to the mass element dm. The total gravitational torque can thus be computed as

$$\vec{\tau}_{\mathrm{grav}} = \int d\vec{\tau} = -\mu \int \vec{r} \times \frac{\vec{R}}{R^3} dm, \tag{4.9}$$

where the integral is to be taken over the whole S/C body. Because of the dependency on the inverse distance squared, this integral is in general not zero. By reformulating and allowing some approximations, cf. [Wer78], the total gravitational torque can be written in terms of the MoI matrix J,

$$\vec{\tau}_{\mathrm{grav}} = \frac{3\mu}{R_{\mathrm{sat}}^3} \left(\vec{e}_{\mathrm{sat}} \times (J\vec{e}_{\mathrm{sat}}) \right), \tag{4.10}$$

where $\vec{e}_{\mathrm{sat}}$ is the normalized vector pointing from the center of the Earth towards the S/C CoM, and R_{sat} is the distance between the geocenter and the S/C CoM. For GFO, J is given by Eqs. (2.22) and (2.23).

Control torque

The control torque should be governing the total S/C torque during the execution of a rotation maneuver. Means of S/C attitude control have been discussed in Sec. 2.3. For GRACE and GFO, two types of attitude control mechanisms come into consideration for performing rotation maneuvers: cold gas thrusters and MTRs. Thus, the control torque can be written as the sum of magnetic torque and thruster torque:

$$\vec{\tau}_{\mathrm{ctrl}} = \vec{\tau}_{\mathrm{mag}} + \vec{\tau}_{\mathrm{thr}}. \tag{4.11}$$

On GFO, there are 12 attitude control thrusters, cf. Sec. 2.3.1. Using Eq. (2.44), the control torque due to thrusters is thus obtained by summing over all thrusters, i.e.

$$\vec{\tau}_{\mathrm{thr}} = \sum_{i=1}^{12} \vec{r}_i \times \vec{F}_i, \tag{4.12}$$

where each force $\vec{F}_i$ is zero most of the time, when the respective thruster is not firing. In addition to the torque, each thruster i is causing a linear acceleration of the S/C as well, according to the force $\vec{F}_i$. In order to cancel out this linear acceleration, attitude control thrusters are activated in opposite pairs. It is also beneficial to let the second thruster of a pair be placed opposite to the first one, so that they produce the same torque. I.e., for each

thruster with position $\vec{r}$ and force $\vec{F}$, there is another thruster with position $-\vec{r}$ and force $-\vec{F}$. Thus, in an ideal simulation environment, the torque produced by a pair of thrusters is equal to the torque of one thruster multiplied by two. Equation (4.12) then becomes a sum over 6 thrusters.

Since the attitude control thrusters are rigidly connected to the S/C, the torque which is exerted by each one can be assumed to be time independent. Thus, the six torque vectors can be computed once and temporarily added to the total S/C torque in the integration process, in case it is desired to apply a thruster control torque during the maneuver simulation.

The working principle of the MTRs has been sketched in Sec. 2.3.1. Recall that the torque produced by the MTRs is given by Eq. (2.42):

$$\vec{\tau}_{\mathrm{mag}} = \vec{m} \times \vec{B}, \tag{4.13}$$

where $\vec{m}$ denotes the magnetic moment, and $\vec{B}$ the Earth's magnetic field. The right plots in Fig. 4.5 exemplarily show time series of actual magnetic torque for GF1 during 10 April 2019. No rotation maneuvers were performed during this period.

Note that $\vec{m}$ is the sum of the magnetic moments produced by the different torque rods. Those are aligned with the SF axes, so that each component of $\vec{m}$ represents the magnetic moment of one of the torque rods. In reality, the alignment of the rods may slightly deviate from the nominal alignment. Moreover, Eq. (4.13) applies to the total dipole moment of the S/C, which may have other contributors, e.g. due to currents in S/C electronics. These effects could be roughly modeled by adding noise to the control magnetic moment $\vec{m}$, however, it was neglected in the simulations described here, and $\vec{\tau}_m$ given in Eq. (4.13) was considered the total magnetic torque of the S/C. There are sources of undesired magnetic torque, such as Eddy currents or hysteresis, cf. [Wer78], but these are also considered negligible for the purpose of this study.

Earth magnetic field

In order to compute the magnetic torque, a model of the Earth's magnetic field is needed. For the analysis presented in this thesis, a Matlab implementation of the IGRF12 model has been used[3]. For the computation of $\vec{B}$, the NED frame is used, cf. Sec. 2.1.1. The inputs are time and geographic position in terms of latitude, longitude, altitude. The output, that is $\vec{B}$, needs to be rotated from the NED frame to the ECI frame, and subsequently to the SF. The magnetic torque may then be computed by Eq. (4.13), where $\vec{m}$ can be chosen freely. Each GFO satellite also hosts a magnetometer to measure the Earth's magnetic field. This data is provided in the MAG1A and MAG1B data products [Wen+19]. Figure 4.6 compares the IGRF12 model to the measured magnetic field.

4.2.2   Force models

At the altitude of the GFO satellites, i.e. about 500 km, both SRP and ATD accelerations are relevant. At significantly lower altitudes, the ATD is the dominant nongravitational force, whereas at significantly higher altitudes, SRP becomes the dominant nongravitational force. However, the gravitational pull from the Earth is by far the largest contribution to the S/C acceleration. In the following, models for these three acceleration components are described.

Earth gravitational model

The gravity field due to the Earth's mass is described in terms of the gravitational potential at each point in the vicinity of Earth. A useful tool to approximate such a function are the

---

[3]© Drew Compston (2020). International Geomagnetic Reference Field (IGRF) Model (https://www.mathworks.com/matlabcentral/fileexchange/34388-international-geomagnetic-reference-field-igrf-model), MATLAB Central File Exchange. Retrieved November 26, 2020.
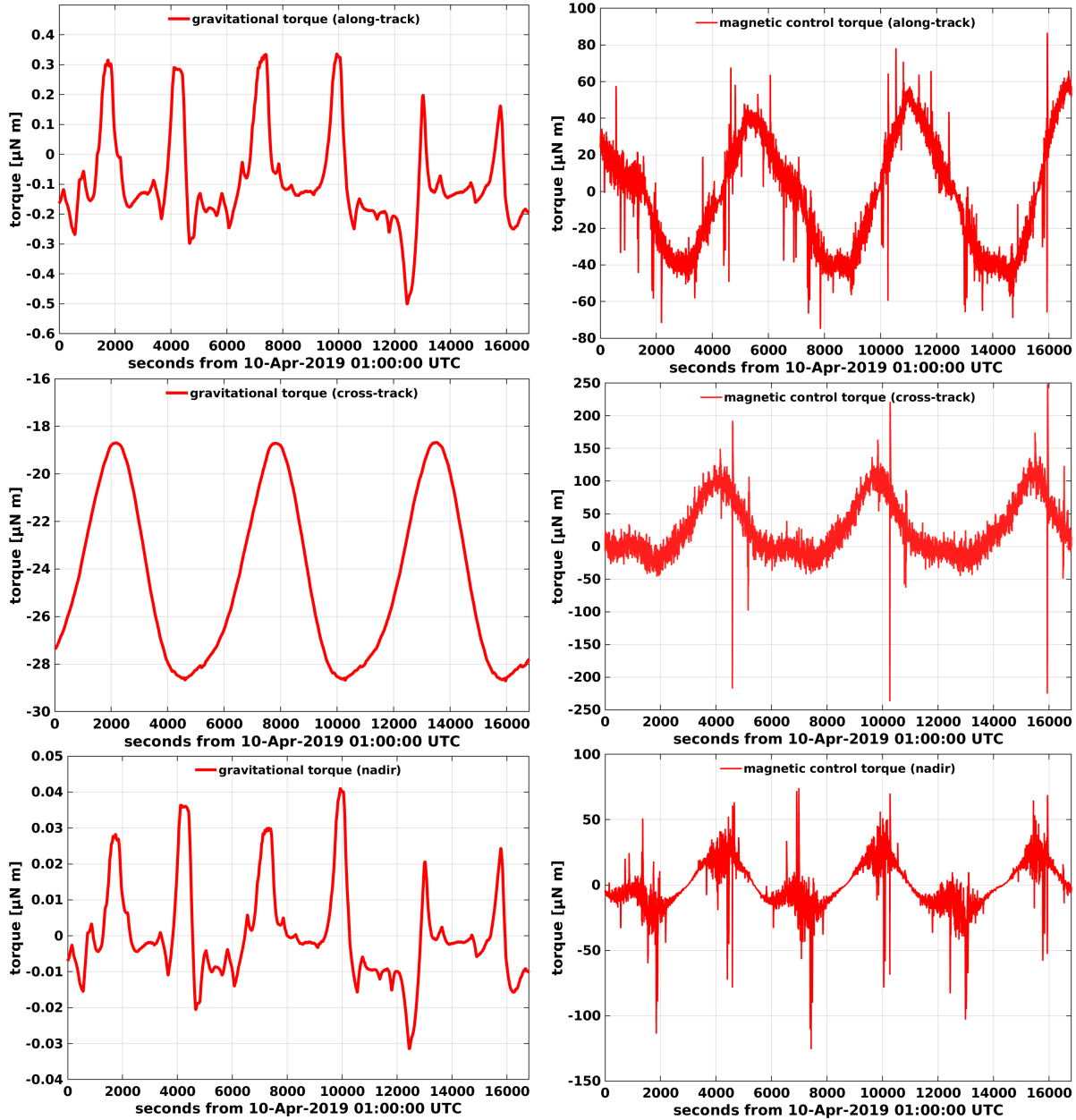
Figure 4.5: GF1 torques in SF, for 16800 seconds during 10 April 2019. Left: gravitational torque. Right: magnetic control torque, derived from MAG1B data.

so-called spherical harmonic (SH) functions. These are an orthogonal set of base functions which are defined on the entire sphere. Similar to the way a function defined on $\mathbb{R}$ can be approximated by a Fourier series, a function f defined on the sphere can be approximated by SH functions as

$$f(\phi, \lambda) = \sum_{n=0}^{\infty} \sum_{m=0}^{n} \left(\bar{a}_{nm} \cos(m\lambda) + \bar{b}_{nm} \sin(m\lambda) \right) \bar{P}_{nm}(\sin \phi), \tag{4.14}$$

where ϕ, λ are spherical coordinates. $\bar{a}_{nm}$ and $\bar{b}_{nm}$ are called SH coefficients of degree n and order m, also called Stokes coefficients. $\bar{P}_{nm}$ are the normalized associated Legendre functions.
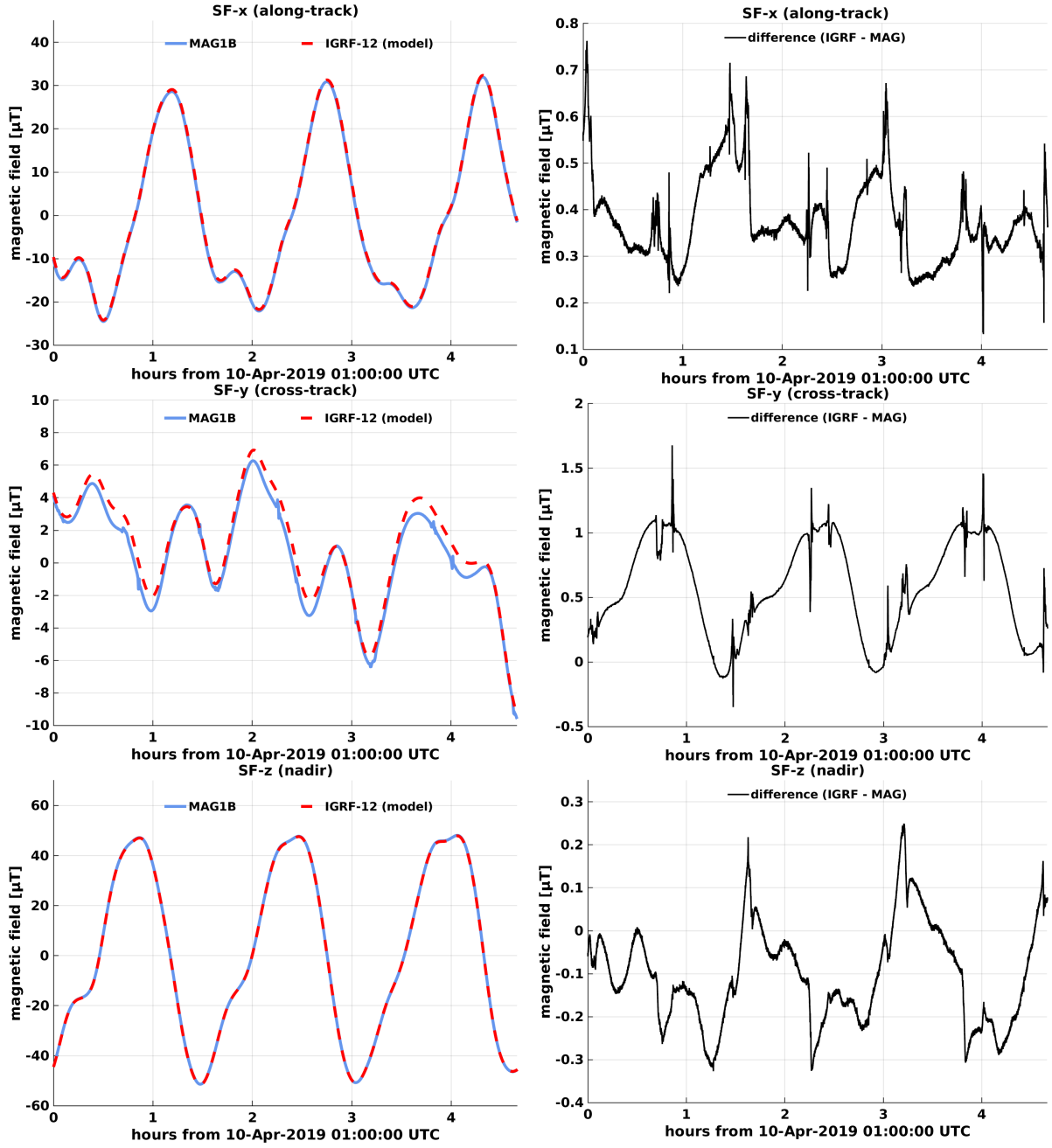
Figure 4.6: Left: Comparison of Earth magnetic field in SF, model (IGRF12) vs. MAG1B data, for 16800 seconds during 10 April 2019. Right: Residuals, model (IGRF12) minus measurement (MAG1B).

The SH base functions are now defined by

$$\bar{Y}_{nm}^c(\phi, \lambda) = \bar{P}_{nm}(\sin \phi) \cos(m\lambda) \tag{4.15}$$

$$\bar{Y}_{nm}^s(\phi, \lambda) = \bar{P}_{nm}(\sin \phi) \sin(m\lambda). \tag{4.16}$$

These can then be used to approximate the function f, which is in this case the Earth's gravitational potential $V = V(r, \phi, \lambda)$:

$$V(r, \phi, \lambda) = \frac{\text{GM}}{R} \sum_{n=0}^{\infty} \left(\frac{R}{r}\right)^{n+1} \sum_{m=0}^{n} \left(\bar{c}_{nm} \bar{Y}_{nm}^c + \bar{s}_{nm} \bar{Y}_{nm}^s\right) \tag{4.17}$$

with

$$\bar{c}_{nm} = \frac{R^{-n}}{\text{GM}} \bar{a}_{nm} \tag{4.18}$$

$$\bar{s}_{nm} = \frac{R^{-n}}{\text{GM}} \bar{b}_{nm} \tag{4.19}$$

being the scaled versions of $\bar{a}_{nm}$ and $\bar{b}_{nm}$.

The technical derivation of this representation is presented in detail in [HM67]. $\bar{c}_{nm}$ and $\bar{s}_{nm}$ are commonly used coefficients to describe a model of the Earth's gravitational potential. The Earth Gravitational Model 2008 (EGM08) is a model of the Earth's gravitational potential given in terms of SH coefficients, which is presented in [Pav+12]. It is complete to degree and order 2159 and publicly accessible. In this thesis, the EGM08 coefficients are used, together with a Matlab code[4] to convert them to linear accelerations acting on the GFO S/C.

Atmospheric drag model

The acceleration due to ATD can be modeled by [Mon00]

$$\vec{a} = -\frac{1}{2} C_D \frac{A_\perp}{m} \rho v^2 \vec{e}_v, \tag{4.20}$$

where C_D is the drag coefficient, A is the cross-sectional area, m is the S/C mass, ρ is the atmospheric density, v is the scalar S/C velocity relative to the atmosphere, and e_v is the normalized velocity vector.

The mass of each GFO satellite is roughly $m = 601$ kg, cf. [Wen+19]. A time series of the mass is also provided in the MAS1B data product. The drag coefficient C_D depends on the material of the outer surfaces of the S/C, as well as on its shape. It is a dimensionless constant, which is not trivial to determine. A value of $C_D = 2$ was used for the simulations presented here, which is a common value for nearly cuboid shaped objects. The S/C velocity can be obtained from GPS positions, provided in the GNV1B data. Note that $\vec{v} = v \cdot \vec{e}_v = \vec{v}^{\text{ECEF}}$ must be considered in ECEF frame, since this is the velocity relative to the atmosphere, when winds are neglected.

The cross-sectional area $A_\perp$ slightly depends on the attitude of the S/C. For GFO, the angle between LoS and velocity vector typically stays in the range between 10 and 15 mrad. Therefore, $A_\perp$ does not vary with time by a large amount. For the simulations discussed here, however, the author has implemented a geometrical model of the S/C body, based on the description given in [Wen+19]. In combination with the S/C attitude, it is then possible to compute a time series of $A_\perp$. Based on such an analysis, it seems to vary by about 15 %, between 1.03 and 1.18 m^2.

In Eq. (4.20), the term whose magnitude varies the most along the orbit trajectory is the atmospheric density ρ, i.e. the total mass density of the atmosphere at the S/C position, given in kg m^{-3}. In order to compute it, the Matlab function *atmosnrlmsise00* was used, which is part of the aerospace toolbox for Matlab. For the altitude of the GFO satellites, modeling ρ requires 10.7 cm solar flux data, as well as the geomagnetic activity indices Kp and Ap, all of which are publicly available [5][6].

For the GFO satellites, the ATD accelerations can be as large as 35-40 nm s^{-2}. The left plots in Fig. 4.7 show the ATD accelerations of GF1 on 10 April 2019, for a time span of 16800 s. The plots show the acceleration components in SF. The largest acceleration due to ATD

---

[4]written by Majid Naeimi, Institut für Erdmessung, Hannover, Germany

[5]The f10.7 data for this analysis has been downloaded from Natural Resources Canada: `ftp://ftp.seismo.nrcan.gc.ca/spaceweather/solar_flux/daily_flux_values/fluxtable.txt`

[6]The Kp and Ap indices for this analysis have been downloaded from the Deutsches GeoForschungsZentrum (GFZ): `http://swe.gfz-potsdam.de/kp/Kp_filelist.html`

is in the x direction, which is the axis pointing towards the distant S/C, or roughly in flight direction, cf. Sec. 2.1.1.

The ATD model, as well as the model for SRP, implemented by the author, have been validated with GFO accelerometer data. Figure 4.8 shows a comparison between linear non-gravitational accelerations provided in the ACT1A data product on the one hand, and the sum of ATD and SRP on the other hand. Plotted are the components of the respective accelerations in SF, covering the same time span as for Figs. 4.4 to 4.7. Here the same model was used, which has already been used to derive the ATD torques shown in Fig. 4.4.

Solar radiation pressure model

The solar radiation pressure (SRP) is the pressure which acts on a surface that is exposed to sunlight, i.e. the pressure which is caused by incident photons hitting the surface and hence applying a force to it. In App. D, a simple SRP model is derived, considering merely radiation pressure from direct sunlight. For more theoretical background, see [Mon00]. The formula that was used for the analysis behind this thesis is given as follows, in terms of the SRP acceleration acting on a GFO S/C:

$$\vec{a} = -\nu \frac{P_\odot}{m} \left(\frac{AU}{x} \right)^2 \sum_i \left[\cos(\theta_i) A_i \cdot \left((1 - \zeta_i) \cdot \vec{e} + 2\zeta_i \cos(\theta_i) \cdot \vec{n}_i \right) \right], \qquad (4.21)$$

where the notation is given in App. D.

For the GFO satellites, the SRP accelerations are of the order of $0 \dots 10\,\mathrm{nm\,s^{-2}}$. Figure 4.7 shows the SRP accelerations of GF1 on 10 April 2019, covering a time span of 16800 seconds, which corresponds roughly to three orbit revolutions. The figure shows the components in SF, cf. Sec. 2.1.1 for the frame definition. Figure 4.8 compares linear nongravitational accelerations provided in the ACT1B data product to the sum of modeled ATD and SRP on the other hand, showing good agreement. Note that some residual between the two time series is expected, since the ACT data also contains additional accelerations such as those caused by attitude control thruster firings.

4.2.3   Simulation technique

In order to simulate a rotation maneuver, it is necessary to integrate the attitude state vector, cf. Eqs. (2.18) to (2.20). This yields the attitude quaternions which describe the satellite's orientation w.r.t. inertial space, cf. Sec. 2.1.2. For all practical purposes, the integration requires knowledge of the S/C positions as well, e.g. for the computation of torque. Also, simulating MTR control requires knowledge of the ambient magnetic field, which again depends on the S/C position and orientation. Furthermore, here the purpose of the simulated maneuvers is to investigate their benefit for estimating TTL coupling. Since the TTL coupling model derived in the previous chapter is expressed in terms of S/C pointing angles, those must be simulated as well. This in fact requires knowledge of the positions of both S/C, in addition to the attitude quaternions.

In principle, the S/C positions may be taken from an existing orbit, e.g. from real GNV1B data in the case of GFO, or from an independently simulated orbit. Then, it is merely needed in order to integrate the attitude state vector of one of the S/C. However, if the goal is to simulate a comprehensive test case including inter-satellite ranging, more precise orbit propagation becomes necessary.

State vector

Two cases are distinguished here, depending on whether the orbit is already given or it needs to be integrated as well. If the orbit, i.e. the S/C positions, are given, merely the 7-dimensional
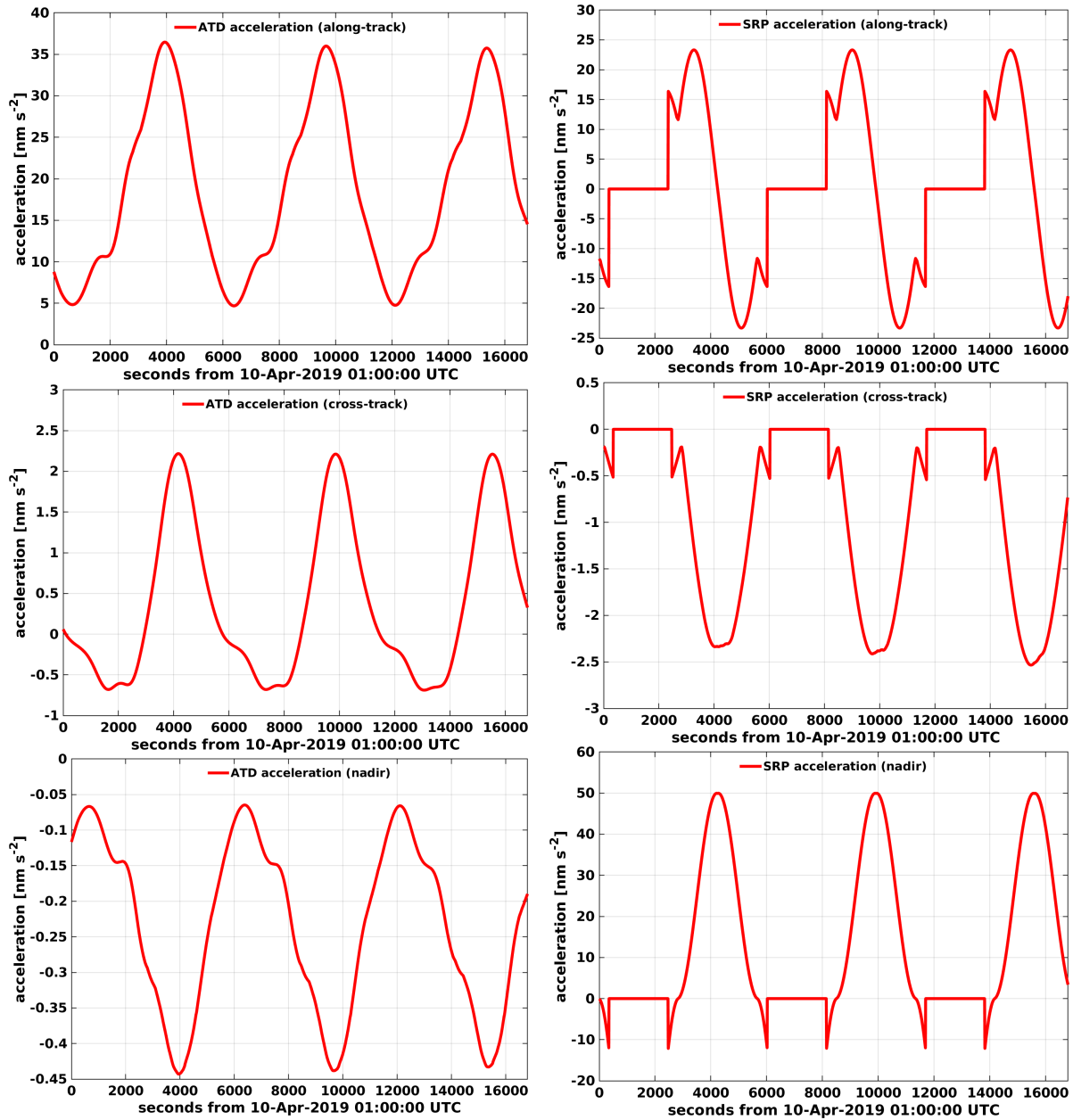
Figure 4.7: GF1 nongravitational accelerations rotated to SF, for 16800 seconds during 10 April 2019. Left: ATD. Right: SRP.

attitude state vector needs to be considered. Recall that it is given by

$$\vec{X}_{\mathrm{att}} = \begin{pmatrix} \vec{q} \\ \vec{\omega} \end{pmatrix}, \tag{4.22}$$

cf. Eq. (2.18). If the orbit must be integrated, the orbit and attitude dynamics equations are used, see also [Wan00]. The 13-dimensional state vector is then given by

$$\vec{X} = \begin{pmatrix} \vec{p} \\ \vec{v} \\ \vec{q} \\ \vec{\omega} \end{pmatrix}, \tag{4.23}$$
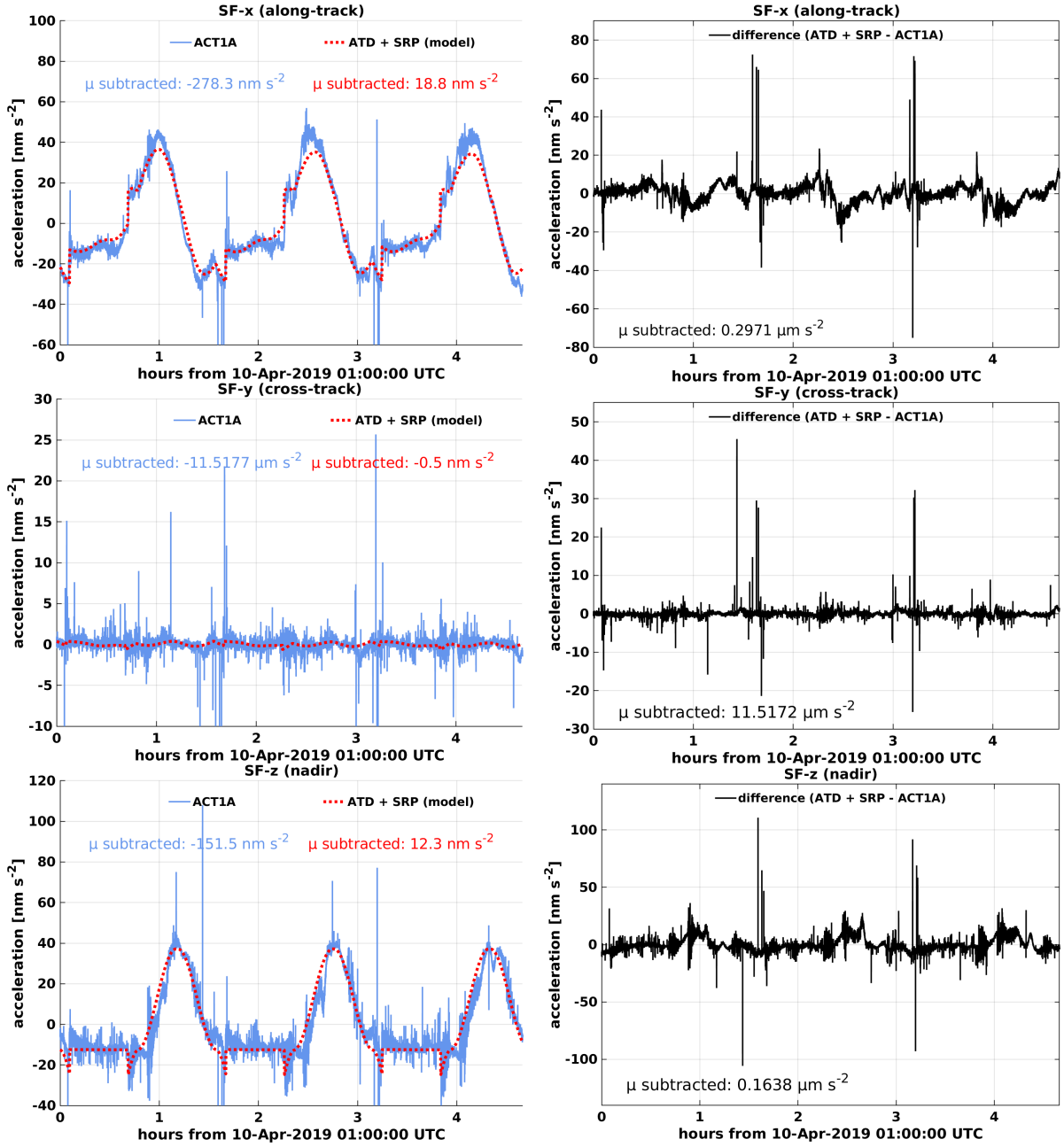
Figure 4.8: Left: Comparison of GF1 nongravitational accelerations rotated to SF, models (ATD + SRP) vs. ACT1A data, for 16800 seconds during 10 April 2019. The mean μ of each time series has been subtracted. Right: Residuals, models (ATD + SRP) minus measurement (ACT1A).

where rows 7 to 13 are just the attitude state vector as before. The derivative of $\vec{X}$ is given by

$$\dot{\vec{X}} = \begin{pmatrix} \vec{v} \\ \vec{a} \\ \frac{1}{2}\Omega(\vec{\omega}) \cdot \vec{q} \\ J^{-1}(\vec{\tau} - \vec{\omega} \times (J\vec{\omega})) \end{pmatrix}, \tag{4.24}$$

with inertial position $\vec{p}$, velocity $\vec{v}$ and acceleration $\vec{a}$ of the satellite. The notation of the attitude part has been defined in Sec. 2.1.2.

In general, the two parts of the state vector $\vec{X}$, i.e. rows 1 to 6 on the one hand and rows 7 to 13 on the other hand, must be integrated simultaneously, since they are interdependent. That is, the S/C orbit depends on the attitude and vice versa. In practice, e.g. for short time periods such as the duration of a CMC maneuver, the orbit of a S/C will be relatively insensitive to small variations of its attitude. In this case, it is possible to integrate the two parts of X separately. In the end, it depends on what level of accuracy is required for both the orbits and the S/C attitude.

Moreover, in some cases, it is desired to simulate an active pointing control. This means that a control torque is not only applied with the goal of performing a rotation maneuver, but an additional control torque is required to keep the absolute pointing deviation below some defined threshold. If this is the case, the integration of the attitude state requires knowledge of the orbits of both S/C, not only of the S/C performing the maneuver, since the pointing angles depend on both S/C positions.

Initial conditions

For the integration, the initial quaternions should be such that the S/C pointing is nearly nominal. Apart from that, they can be chosen freely. For instance, initial quaternions may simply be taken from SCA1B data. Alternatively, it can be assumed that the S/C pointing is perfect at the time of initialization. This means that SF and LOSF coincide, or, equivalently, the three pointing angles are all set to zero. In other words, the matrix $R_{\text{SF}}^{\text{LOSF}}$ is the identity matrix, cf. Sec. 2.1.3. According to the decomposition in Eq. (2.30), this implies that

$$R_{\text{SF}}^{\text{ECI}} = \left(R_{\text{ECI}}^{\text{LOSF}}\right)^{-1} = \left(R_{\text{ECI}}^{\text{LOSF}}\right)^{T}. \tag{4.25}$$

The matrix $R_{\text{ECI}}^{\text{LOSF}}$ can be obtained using Eq. (2.3). Note that this already requires knowledge of the initial positions of both GFO satellites.

The initial angular velocities need to be defined as well, and also may not be chosen arbitrarily, since a drift of the pointing angles during the maneuvers is not desired. Angular velocities in x and z axes of the SF should therefore be close to zero. The initial angular velocity y component corresponds to the pitch angle. If T_{orbit} is the orbit period of the S/C, the y component should be close to 2π rad divided by T_{orbit}, since the satellite undergoes a complete 360 ° turn during the course of a whole orbit. For GFO, $T_{\text{orbit}} \approx 5600$ seconds as of January 2020, and hence the initial angular velocity vector should be close to

$$\vec{\omega}_0 = \begin{pmatrix} 0 \\ -0.00112 \\ 0 \end{pmatrix} \text{rad s}^{-1}, \tag{4.26}$$

expressed in SF, for the S/C which is flying forward. For the S/C which is flying backwards, the y component of ω_0 must have the opposite sign. One way to define initial angular velocities is to derive them from measured Level-1 data. It was explained in Sec. 2.2.1 how the angular velocity vector $\vec{\omega}$ in SF can be derived from IMU data, cf. Eq. (2.35). A further alternative is to determine the derivative of the SCA1B attitude quaternions at the time of initialization t_0, and afterwards determine $\omega(t_0)$ by performing a fit of Eq. (2.19).

In case initial values are taken from the IMU, one needs to estimate the angular velocity bias which is inherent in the data. The same has to be done if IMU data is integrated to obtain pointing angles, as described in Sec. 2.2. The author has estimated the IMU bias by matching IMU-derived pointing angles with those derived from SCA1B data. Figure 4.9 shows estimated angular velocity biases for GF1 during roughly one day in August 2019, estimated every 100 seconds. The estimated biases show large variations at the orbit frequency, in this case approximately 174 µHz, as well as at twice the orbit frequency. The origin of these variations was not investigated further.
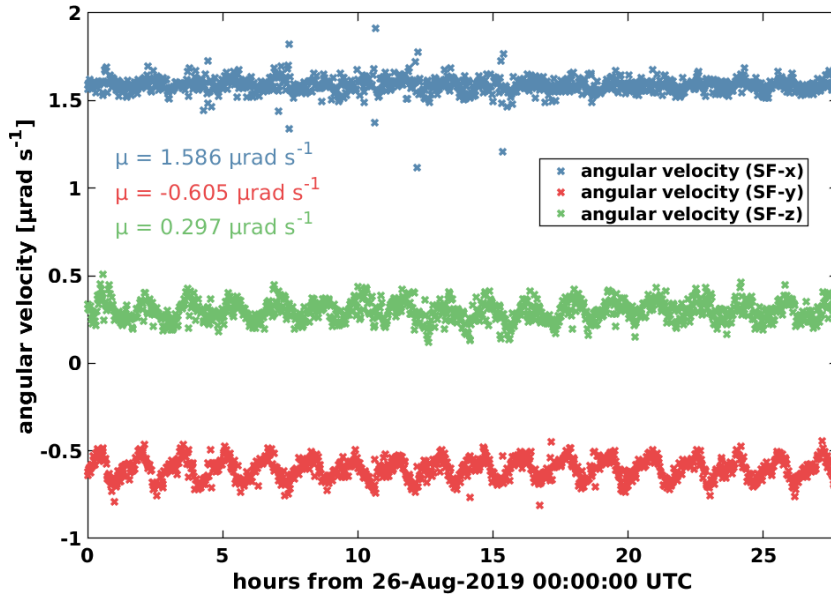
Figure 4.9: Estimated GF1 IMU angular velocity bias; components in SF.

Integration

Before the integration, some more preparation is necessary. As described above, the state vector and the initial conditions have to be defined. The latter means that also the time of initiation t_0 must be chosen, and additionally the duration T of the maneuver, as well as the integration stepsize Δt. Moreover, the framework for the simulation should be set, i.e. which models are included in order to compute S/C torque and acceleration, which integration technique is used, and what type of ACS is implemented.

If MTRs are used to perform the rotation maneuver, it is in principle possible to operate an ACS during the maneuver, which is based on another type of control torque mechanisms, such as thrusters. For this thesis, a scenario has been tested in which the ACS is a simple "bang-bang" controller based on attitude control thrusters. This type of controller acts if and only if at least one of the pointing angles - roll, pitch, yaw - exceeds a certain threshold. If this is the case, the respective thruster is firing, which causes this angle to move into the margin again. The thruster activation time is considered fixed in this analysis. If a single thruster firing is not enough to drive the angle back below the threshold, another thruster firing will be initiated automatically after a minimum waiting time. For the time of activation, the thruster torque τ_{thr} can be computed and added to the control torque.

In order to implement an ACS, the S/C pointing angles must be derived at each step in the integration process. Based on these angles, an algorithm must decide whether and how the controller should react. The derivation of pointing angles requires knowledge of the S/C attitude, as well as the positions of both S/C. This implies that the orbit of the satellite not performing the maneuver must be obtained beforehand. For the purpose of this analysis, it is not necessary to integrate state vectors of both S/C simultaneously.

Most importantly, one must define the control torque which is supposed to produce the desired rotation maneuver. In real satellite missions, it is either pre-defined or computed on board. Note that, if MTRs are used, the actual commanded torquer currents cannot be known beforehand, since they depend on the S/C attitude w.r.t. the ambient geomagnetic field. Hence, the maneuver torque cannot be pre-defined exactly in this case. For GFO, a desired torque profile is programmed, and when the maneuver is initiated, an onboard computer determines how the torque rods must be activated in order to achieve the desired torque [tea19].

This analysis focuses on the GFO mission, however, it is assumed here that the profile of the MDM is pre-defined, instead of a desired torque. Equivalently to defining the MDM profile, the torquer input currents can be defined. The MDM activation profile is represented as a 3-valued function $\vec{m}(t)$. This function, more precisely its values for each instance of time $t_k = t0 + k\Delta t$, $k = 1, \ldots, T/\Delta t$, must be defined before the integration. Considering the geolocation of the satellites at the time of initiation, the resulting torque can be predicted accurately. On this basis, ideal maneuver locations can be identified beforehand, see also Sec. 4.3.

Here, the Runge-Kutta 3 (RK3) method has been used for integration, with an integration step size of $\Delta t = 1$ s. RK5 and RK7 methods have also been tested. For the purpose of this analysis, the results of RK5 and RK7 can be considered equivalent to those of RK3. For theoretical background information on numerical integration, the reader is referred to [MNR12].

In the following section, it is investigated how a rotation maneuver can be designed. When planning a rotation maneuver, some decisions have to be made and some parameters have to be chosen. Those are elaborated on, with a special focus on LRI TTL calibration. Some concepts are also applicable for satellite missions which are similar to GFO. In the end, optimal parameters for the purpose of estimating LRI TTL coupling are derived.

4.3 TTL maneuver design

The goal in this section is to investigate how to design rotation maneuvers, and find the ones which are optimal for the purpose of estimating LRI TTL coupling. For one thing, this requires the capability of simulating realistic rotation maneuvers. In the previous section, it has been described in detail how the simulation can be carried out. Apart from that, three more things are required, which are listed in the following.

Firstly, one needs an objective and efficient way to assess the quality of a rotation maneuver, for the purpose of estimating TTL coupling. More precisely, this must be a quantitative function with the input being the parameters that define an individual maneuver. This way, the respective values for the individual maneuvers can be compared against one another. Such a function will be developed in Sec. 4.3.1.

Secondly, it will be elaborated what the maneuver parameters are. I.e., what are the choices to be made when planning a rotation maneuver? These parameters can be chosen freely with some restrictions. It shall be seen that a maneuver is completely defined by deciding on the following four choices, treated in Secs. 4.3.2 to 4.3.5.

1. How is the control torque defined? ($\to$ Sec. 4.3.2)

2. What should be the maneuver frequency? ($\to$ Sec. 4.3.3)

3. What should be the duration of the maneuver? ($\to$ Sec. 4.3.4)

4. What should be the geographic location? ($\to$ Sec. 4.3.5)

Thirdly, the above mentioned maneuver parameters should be optimized w.r.t. the maneuver quality, as it is defined in Sec. 4.3.1. The results of this optimization will be demonstrated in Sec. 4.3.6.

4.3.1 Maneuver assessment

The purpose of the maneuvers investigated in this thesis is to excite the inter-satellite pointing angles, and thereby cause a TTL error with a corresponding signature in the measured range. Using a coupling model, for the LRI discussed in Chap. 3, the measured pointing angles can then be fitted to the range. An objective and quantitative measure of the success of this

procedure are the standard deviations (STD) of the estimated parameters. The different methods of estimation are discussed in detail in Chap. 5 below. A standard and solid method for a linear coupling model is given by the least squares (LSQ) estimator,

$$\hat{\lambda} = \left(\bar{\theta}^T \bar{\theta}\right)^{-1} \bar{\theta}^T \bar{\rho}. \tag{4.27}$$

Here, $\bar{\theta}$ is an $(N \times M)$-matrix of bandpass filtered pointing angles, with N being the number of samples and M the number of angles to be fitted. See Sec. 5.1.6 for more details on the choice of the bandpass filter. $\hat{\lambda}$ has size $(M \times 1)$ and denotes the estimated linear coupling factors. ρ denotes the filtered range, with size $(N \times 1)$. The STD of the LSQ estimator is given by [HTF09]

$$\sigma(\hat{\lambda}) = \sigma\left(n_\rho\right) \cdot \mathrm{diag}\left(\sqrt{\left|(\bar{\theta}^T \bar{\theta})^{-1}\right|}\right), \tag{4.28}$$

where $\sigma(n_\rho)$ is the STD of the measurement noise which is present in the filtered measured range $\bar{\rho}$. In Eq. (4.28), the operation $\sqrt{|\cdot|}$ applied to a matrix is to be understood elementwise. This formula for $\sigma(\hat{\lambda})$ may be underestimating the uncertainty of the estimated parameters. Note that the LSQ estimation method assumes that the noise n_ρ has a white frequency spectrum, which is not exactly true in reality, but a good approximation. Nevertheless, the formula has informative value for comparing the STD of two maneuvers. Moreover, it is quickly evaluable, and thus the author opted to use it as a basis for defining a maneuver quality indicator.

It is noteworthy that formula (4.28) can in principle also be used when only one of the angles is regarded, i.e. $M = 1$. However, this is only valid if, in relation, the TTL error caused by all other angles of both S/C is negligible, which can rarely be assumed to be the case. Due to this, it may be advisable to estimate at least the three angles of one S/C at the same time. In fact, Eq. (4.28) may be applied to a whole set of maneuvers, by concatenating the time series. Since the STD is to be minimized, the optimal choice of parameters will be a tradeoff between large pointing angle excitation, low inter-angle correlations, low ranging noise, a long maneuver duration, and of course feasibility.

It would be desirable to define an evaluation function by

$$f\left(\text{maneuver parameters}\right) = \sigma(\hat{\lambda}), \tag{4.29}$$

which can be minimized w.r.t. the maneuver parameters. However, f is then a function with M values, the number of angles which are considered. Moreover, f should not be too expensive to evaluate. For instance, it would be undesirable if an entire rotation maneuver had to be simulated in order to evaluate f, for each point in the space of maneuver parameters. Instead, a more efficient way to estimate the pointing angles θ during a rotation maneuver, given a set of parameters, is introduced. The values of f can thus be approximated very quickly. While this develops, it should become clear what these parameters are. In the following, three approximations are made and justified.

The first approximation is, explicitly, not valid in general, but merely for the specific purpose of this analysis. In this thesis, maneuvers of relatively short duration are investigated, where one is only interested in a specific part of the pointing angles, the intended part. This part is typically a signal with a specific frequency, such that it can be separated from the background signals. Before the parameter estimation, the range and the angles are bandpass filtered, and merely signal close to that frequency remains. Equations (4.27) and (4.28) then apply to these filtered time series. In the case of GFO, the lower cutoff frequency of that filter should be above 37 mHz, where there is much less gravity signal. Under these considerations, the statement

$$\theta(t) \approx \int_{t_0}^{t} \omega(s)\, ds = \int_{t_0}^{t} \int_{t_0}^{s} \dot{\omega}(\tilde{s})\, d\tilde{s}\, ds \tag{4.30}$$

holds, where ω and $\dot{\omega}$ are angular velocities and angular accelerations of the S/C w.r.t. the SF. Since θ is considered to be filtered, the line $\theta(t_0) + (t - t_0) \cdot \omega(t_0)$ was also neglected on the right hand side. During this chapter, for integral equations such as (4.30), the short notation

$$\theta \approx \iint \dot{\omega} \tag{4.31}$$

is often used for double time integrals, and similarly for single time integrals. I.e., whenever the integration variable is omitted, the integration is meant w.r.t. time.

Note again that the approximation (4.30) is to be used with care. The nonfiltered pointing angles can drift off, e.g. due to an initial angular velocity, or due to the relative change of positions of the two S/C. This is certainly important for the maneuver planning, since it restricts the maneuver duration. It will therefore be discussed separately in Sec. 4.3.4. Moreover, recall that the TTL coupling model for the LRI is linear. In case there is second or higher order coupling, the absolute pointing deviation is relevant, and not only the high frequency variations.
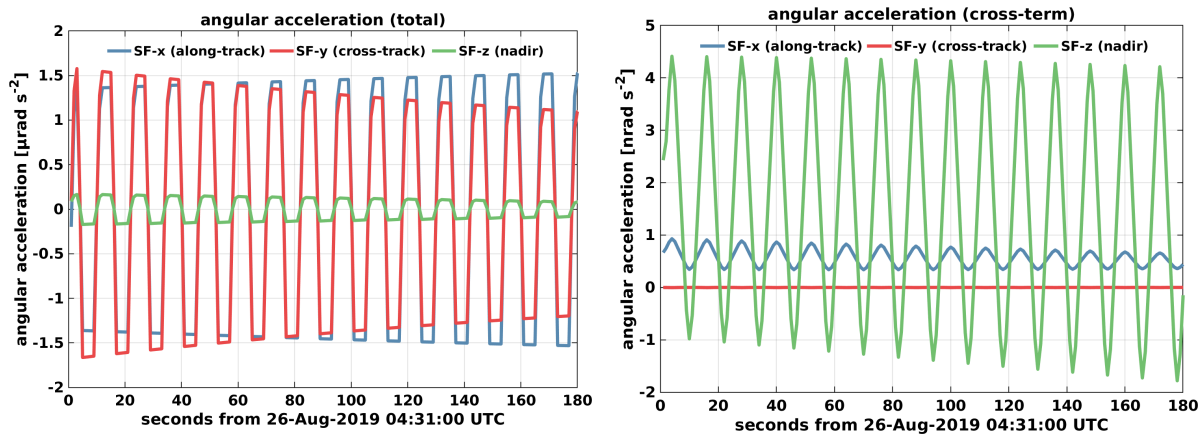

Figure 4.10: Left: total S/C angular acceleration from torques, $J^{-1}(\tau - \omega \times (J\omega))$, during a CMC maneuver on 26 August 2019. Right: cross-term, $J^{-1}(\omega \times (J\omega))$, for the same period.

One can make use of Eq. (4.30), with the help of the second approximation, which reads

$$
\begin{aligned}
\dot{\omega} &= J^{-1} \left(\tau - \omega \times J\omega \right) \\
&\overset{(1)}{\approx} J^{-1} \tau \\
&\overset{(2)}{\approx} \begin{pmatrix} \tau_x / J_{xx} \\ \tau_y / J_{yy} \\ \tau_z / J_{zz} \end{pmatrix} .
\end{aligned}
\tag{4.32}
$$

Here two approximations have been made. (1) holds because the cross-term $\omega \times J\omega$ is very small compared to τ. This is demonstrated in Fig. 4.10, which shows the total angular acceleration (left plot), opposed to the term $J^{-1}(\omega \times J\omega)$ (right plot), during a CMC maneuver performed on GF1 during 26 August 2019. Approximation (2) utilizes the fact that the MoI matrix J given in the SF is almost diagonal in the case of GFO, i.e.

$$J \approx \mathrm{diag}(J_{xx}, J_{yy}, J_{zz}), \tag{4.33}$$

cf. Eqs. (2.22) and (2.23). The physical meaning of this is that the S/C principal axes of rotation, which are the eigenvectors of J, are nearly perfectly aligned with the SF axes. This is an advantageous configuration, which simplifies the S/C attitude control, since wobbling is minimized when rotating around one of the principal axes.

Thirdly, make the approximation that all torques except the control torque are negligible, i.e.

$$\tau \approx \tau_{\text{ctrl}}, \tag{4.34}$$

during the execution of the rotation maneuver. Again, similar to the approximation (4.30) made above, approximation (4.34) is valid because one is, in the end, interested in the bandpass filtered pointing angles.

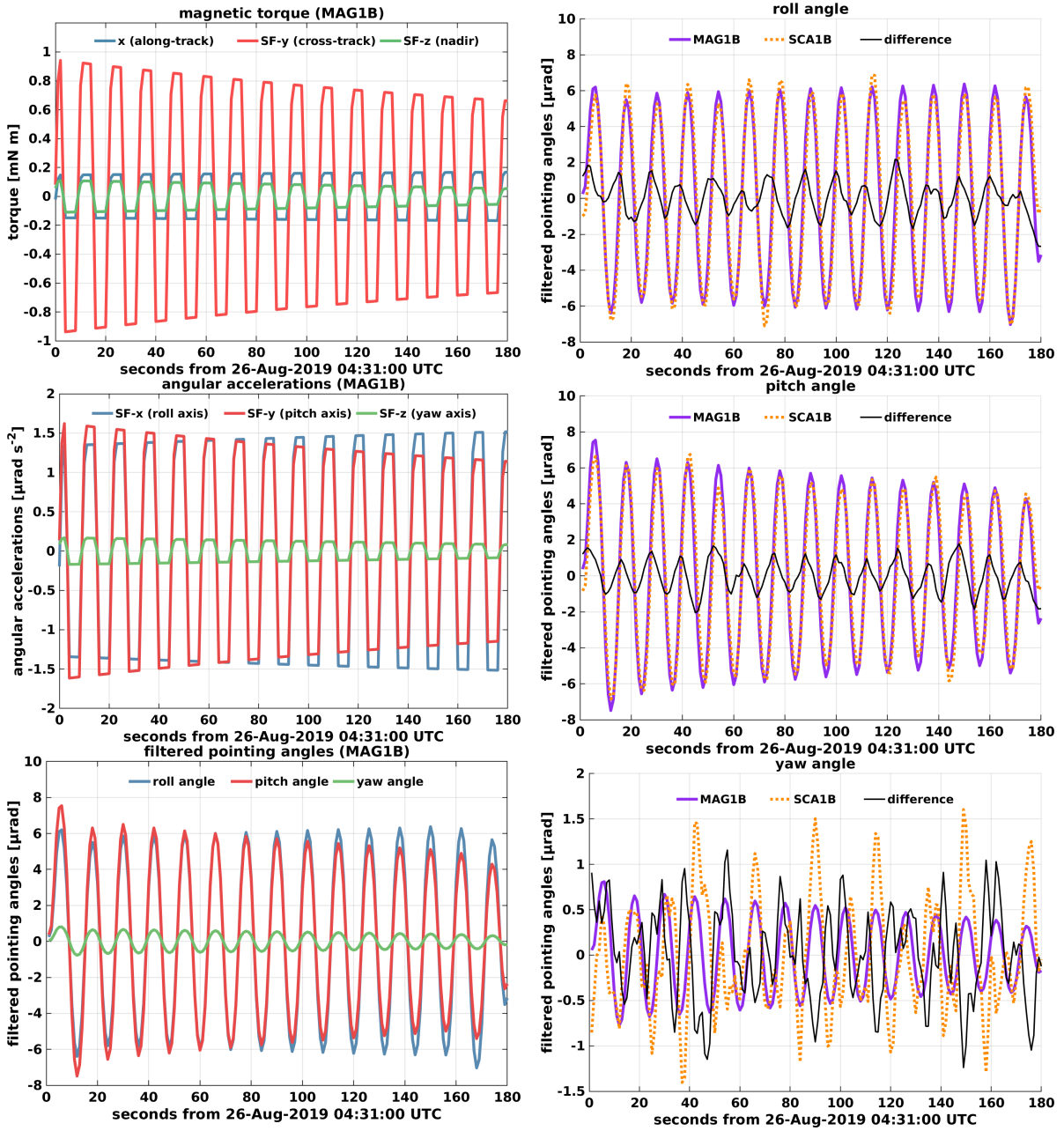Figure 4.11: Left: torques, angular accelerations, and filtered pointing angles derived from MAG1B torquer currents. Approximated using equations (4.30) to (4.34). Right: Comparison of filtered pointing angles derived from MAG1B and SCA1B, difference = MAG1B - SCA1B.

These approximations shall be put to the test with GFO data from CMC maneuvers. To this end, the following steps must be performed.

1. Compute the magnetic torque, using torquer currents from MAG1B data and the IGRF12 model. The measured magnetic field is also provided in the MAG1B data product [Wen+19], however, here one would like to stay independent of measurements, and thus use the model.

2. Use approximation (4.32) to derive the angular accelerations $\dot{\omega}$.

3. Approximate the high frequency part of the S/C pointing angles, by applying (4.30) and bandpass filtering.

These steps are illustrated in Fig. 4.11, on the left, for a CMC maneuver on GF1 on 26 August 2019. One can compare the approximated filtered pointing angles derived from MAG1B data, against filtered pointing angles derived from SCA1B and GNV1B data. This comparison is shown in Fig. 4.11 on the right. They seem to agree well down to the measurement noise of the SCA1B data. Thus, one may proceed and use these approximated angles to compute $\sigma(\hat{\lambda})$. Before, white noise with $\sigma = 0.3$ µrad is added to the approximated angles, as otherwise the matrix in Eq. (4.28) becomes close to singular if one of the angles is identically zero, which is problematic since it must be inverted. Note that this is only an issue for the simulations and does not affect the analysis of the real mission data.

The STD of the ranging noise, $\sigma(n_\rho)$ in Eq. (4.28), may be approximated by generating a time series of simulated LFN, applying the same filter that was used for the pointing angles, and then compute the STD of this time series. The Matlab toolbox LISA Technology Package Data Analysis (LTPDA) provides the function *noisegen1D*, which can be used to simulate noise with a given spectrum. From ground measurements, the author has derived a model of the spectrum of the ranging error caused by LFN, cf. Chap. 3. Here a second order highpass filter with cutoff frequency 40 mHz was used. Then, the term $\sigma(n_\rho)$, which is for now assumed to be constant, takes roughly the value 0.4 nm.

Now all the pieces have been collected to evaluate the maneuver quality function $f = \sigma(\hat{\lambda})$, developed in this section. Note that all the steps can be performed very efficiently for many points in the parameter space. As input for this procedure, the S/C orbit is required, the approximate attitude, and the profile of the control magnetic dipole moment (MDM). Both the orbit and the attitude do not have to be precise, and can be simulated or taken from real mission data, depending on the situation. Given these inputs, the approximated filtered pointing angles can be computed for a time span of practically arbitrary length.

As another test of this method, the author has performed the steps explained above for the entire day of 26 August 2019. For the magnetic dipole moment, a copy of the one from a pitch CMC maneuver performed on that day was used, as it is reported in the MAG1B data. This MDM is plotted on the left of Fig. 4.12. The right plot shows the results of this procedure for a time span of roughly one orbit revolution, centered at the pitch CMC maneuver. The y axis shows the approximated STDs of the estimated TTL coupling factors, which define the maneuver quality. The approximated STD at the time of the CMC maneuver agree well with those computed from measured pointing angles, here derived from SCA1B and GNV1B data. Furthermore, it appears that the location of this maneuver was optimally chosen, given the specific magnetic dipole moment profile. Note that the upper limit that appears to be in the right plot, which is in this case attained by the STDs of the roll and yaw CFs, does not reflect real STDs but is likely an artifact due to measurement noise in the pointing angles. The lower values seem not significantly affected by this, and thus they can be used for the assessment of calibration maneuvers.

Finally, one finds that the choices to be made for defining a maneuver, which are relevant for $f = \sigma(\hat{\lambda})$, are

- the initial time, t_0

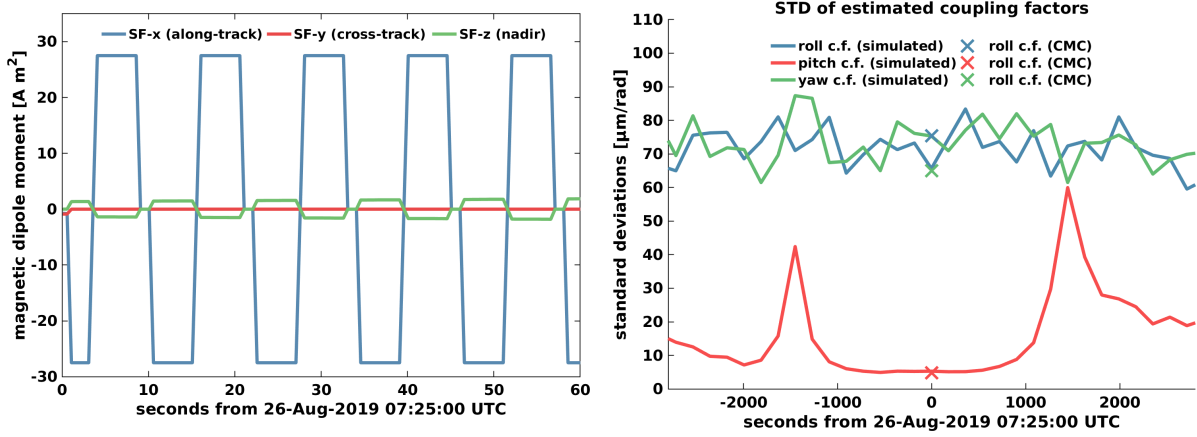- the commanded magnetic dipole moment, $\vec{m}(t)$

Figure 4.12: Left: MDM produced by the torque rods on GF1, during a pitch CMC maneuver on 26 August 2019. Right: STDs of estimated coupling factors, derived from approximated filtered pointing angles, for GF1 during roughly one orbit revolution around a pitch CMC maneuver (solid lines). For comparison, standard deviations derived from filtered pointing angles measured by the star cameras (crosses).

Since the orbit is given, choosing t_0 is equivalent to choosing the location of the maneuver. This shall be discussed in Sec. 4.3.5. Once the basic form of $\vec{m}(t)$ is decided, it merely depends on the duration, the frequency and phase, and which torque rods are activated. In the following section, possible choices of $\vec{m}(t)$ will be discussed.

4.3.2   Magnetic dipole moment

The rotation maneuver is performed by means of MTRs. Here the control torque is not directly chosen, but the MDM $\vec{m}$ which causes the control torque. It is clear that $\vec{m}$ should have a periodic profile, so that it creates a signal with a specific frequency. Here this frequency is called the maneuver frequency, f_m, and the corresponding period is called the maneuver period, $P_m = 1/f_m$. One may concentrate on two basic shapes, sinusoidal and rectangular, which may also be called sine wave and square wave profile, respectively.

Denote by t_k, $k = 1, \ldots, N$, the time tags for which the maneuver shall be simulated. Assume that the time steps are equidistant, and denote by $\Delta t \equiv t_{k+1} - t_k$ the constant time difference between two time steps. The term sinusoidal profile means that the MDM of each of the torque rods has the form

$$m_{\text{sine}}(t_k) = m_0 \cdot \sin\left(2\pi f_m(t_k - t_0) + \varphi_0\right). \tag{4.35}$$

Here, t_0 denotes the initial time, defining the maneuver location, which is discussed in Sec. 4.3.5 below. The strength of the MDM can be chosen by m_0, where $|m_0| \leq 27.5 \,\text{A}\,\text{m}^2$ for GFO, cf. Sec. 2.3. Furthermore, an additional phase shift φ_0 can be introduced.

A rectangular profile means that each of the torque rods produces an MDM of the form

$$m_{\text{rect}}(t_k) = m_0 \cdot \begin{cases} 1, & \text{if } k \bmod 2n = 1, \ldots, n \\ -1, & \text{if } k \bmod 2n = n+1, \ldots, 2n \end{cases}, \tag{4.36}$$

for $k = 1, \ldots, N$, and for some $n \in \mathbb{N}$. The total number of samples, N, must then be a multiple of $2n$. The period of this profile is $P_m = 2n \cdot \Delta t$. Here a phase shift φ_0 can also be applied by shifting the profile by the time $\varphi_0 P_m/(2\pi)$. Note that, in practice, the achievable time shifts are restricted to multiples of Δt.

The MDMs of the three torque rods together define $\vec{m}(t)$. Given t_0, the following decisions regarding $\vec{m}(t)$ have to be made:

- sinusoidal or a rectangular profile

- which torque rods to activate

- for each of the activated rods, choose: m_0, f_m or P_m, φ_0

The torque which results from activating the torque rods depends on the geomagnetic field. It will, however, have almost the same magnitude profile as the MDM by which it is caused, unless the geomagnetic field is rapidly changing. Then, recalling approximations (4.30) to (4.34), one can estimate the amplitude of the resulting pointing angle oscillations. The second integral of the sinusoidal profile is simply

$$\iint m_{\text{sine}} = -\frac{1}{4\pi^2 f_m^2} m_{\text{sine}},\tag{4.37}$$

with amplitude $m_0/(4\pi^2 f_m^2)$. The Fourier series of the rectangular profile, i.e. the square wave, is given by

$$m_{\text{rect}}(t) = \frac{4m_0}{\pi} \sum_{n=1,3,5,\ldots}^{\infty} \frac{1}{n} \sin\left(\frac{2\pi}{P_m}n(t-t_0)\right),\tag{4.38}$$

such that one has

$$\iint m_{\text{rect}} = -\frac{m_0 P_m^2}{\pi^3} \sum_{n=1,3,5,\ldots}^{\infty} \frac{1}{n^3} \sin\left(\frac{2\pi}{P_m}n(t-t_0)\right).\tag{4.39}$$

Hence, for a rectangular profile, the magnitude of the pointing angles at the first frequency, $f_m = 1/P_m$, is by a factor of $4/\pi$ larger than a sinusoidal profile of the same period, which means an increase of about 27 %. This is a clear advantage for a rectangular profile, since it is obvious from Eq. (4.28) that $\sigma(\hat{\lambda})$ will then be reduced by the inverse factor, i.e. by $\pi/4$.

Which torque rods should be activated for a specific maneuver, depends on the location. This question cannot be answered generally. However, since there are not many possible combinations, they may all be investigated, and the optimal one can be picked in the end. This decision is thus postponed to Sec. 4.3.6. Moreover, m_0 includes a sign, which determines the direction of the torque. In the following section, it is discussed what needs to be considered when choosing f_m or P_m, and potentially a phase shift φ_0.

4.3.3   Maneuver frequency and phase

The purpose of this section is to study the influence that the choice of the maneuver frequency has on the STD of the estimated CFs, and hence on the quality of the maneuver. At first, the formula for the STDs of the LSQ estimation is analyzed in general, when the MDM profile is not further specified. A lower bound for the STD of the estimated coupling factors is given. Then, a more specific case is studied, which corresponds to the MDM profile which is used for the GFO CMC maneuvers. From studying this case, the motivation arises to take the comparison with a slightly more general case, namely when different frequencies and phases may be used for the different torque rods. Furthermore, the STD also depends on the ranging noise, which itself is frequency-dependent. This will also be discussed. Finally, further restrictions on the maneuver frequency are discussed.

Lower bound for the STD

The STD of the LSQ CF estimator, cf Eq. (4.28), depends on the inverse of the matrix $A = \theta^T \theta$. Since the highpass filtered pointing angles are used, which have zero mean, A is nothing but

the nonnormalized correlation matrix of the three pointing angles. The elements of A can also be viewed as integrals, i.e.

$$A_{ij} \sim \int\limits_0^T \theta_i(t)\theta_j(t) \, dt, \tag{4.40}$$

where $i, j \in \{1, \ldots, M\}$. Here M stands for the number of pointing angles to be considered in the estimation process. I.e., if merely the pointing angles of one S/C are considered, one has $M = 3$, and then the indices $1, 2, 3$ may correspond to the SF axes x, y, z.

The diagonal elements A_{ii} of the symmetric, positive definite matrix A represent the strength of the excitation of the angles θ_i. Inter-angle correlations are represented by the off-diagonal entries of A. It is intuitively clear that if there are inter-angle correlations, the STD is expected to be larger, since the correlating parts of the TTL error caused by different angles cannot be distinguished from one another. In fact, denoting $B = A^{-1}$, one can show that the diagonal elements B_{ii} of B fulfill

$$B_{ii} \geq \frac{1}{A_{ii}}, \tag{4.41}$$

for all $i = 1, \ldots, M$, with equality if and only if A is diagonal, i.e. if and only if all the inter-angle correlations vanish.

Proof of inequality (4.41). Note that $A = \theta^T\theta$ is obviously symmetric and positive definite, unless one column of θ is the zero vector. The latter can be excluded without loss of generality, since otherwise that particular angle is uninteresting and may be excluded entirely. This implies that there exists a symmetric positive definite matrix C such that $C^2 = A$. One has

$$A_{ii} = e_i^T A e_i = e_i^T C^T C e_i = |C e_i|^2, \tag{4.42}$$

as well as

$$B_{ii} = e_i^T A^{-1} e_i = e_i^T (C^{-1})^T C^{-1} e_i = |C^{-1} e_i|^2, \tag{4.43}$$

since C^{-1} as the inverse of a symmetric matrix is also symmetric. The Cauchy-Schwarz inequality implies

$$\langle C e_i, C^{-1} e_i \rangle^2 \leq |C e_i|^2 \cdot |C^{-1} e_i|^2. \tag{4.44}$$

On the other hand, one has

$$\langle C e_i, C^{-1} e_i \rangle = e_i^T (C^{-1})^T C e_i = e_i^T e_i = 1, \tag{4.45}$$

which proves $1 \leq A_{ii} B_{ii}$ and hence the claim.   *q.e.d.*

Now, in particular, one has $B_{ii} > 0$, since $A_{ii} > 0$, assuming that none of the pointing angles is identically zero for the duration of the maneuver. For the STD of the estimator of the TTL CF of the angle θ_i, denoted by $\sigma(\hat{\lambda}_i)$, it follows that

$$\sigma(\hat{\lambda}_i) \geq \frac{\sigma(n_\rho)}{\sqrt{\int \theta_i^2}}, \tag{4.46}$$

where $\sigma(n_\rho)$ denotes the STD of a white ranging noise. This lower bound for the STD justifies seeking for a way to achieve larger angle excitations, without increasing the inter-angle correlations. In the following, sinusoidal MDM profiles are considered, similar to the ones used for the GFO CMC maneuvers. Subsequently, these maneuvers are adapted slightly, in the attempt to approach equality in Ineq. (4.46).

Using a single frequency and no phase shift

In Sec. 4.3.2, it has been shown that sine wave and square wave profiles of the MDM lead to very similar signals in the pointing angles, however, with a larger amplitude for the square wave profile. In this section, for the simplicity of the following computations, a sine wave profile for the MDM of each torque rod is assumed.

At first, assume that each MDM has the same frequency and zero phase shift. Later, each MDM will be allowed to have its own frequency and its own phase shift. Furthermore, assume and consider only the pointing angles of one S/C. That is, let $M = 3$, where M is the number of considered pointing angles. For now, let

$$\vec{m}(t) = \begin{pmatrix} m_x(t) \\ m_y(t) \\ m_z(t) \end{pmatrix} = \begin{pmatrix} m_{x,0} \\ m_{y,0} \\ m_{z,0} \end{pmatrix} \cdot \sin\left(2\pi f_m t\right), \tag{4.47}$$

while, for this and the following computations, $t_0 = 0$ has been set without loss of generality. Recall that the magnetic torque of the S/C is given by

$$\vec{\tau}_m = \vec{m} \times \vec{B} = \begin{pmatrix} m_y B_z - m_z B_y \\ m_z B_x - m_x B_z \\ m_x B_y - m_y B_x \end{pmatrix}. \tag{4.48}$$

Still under the assumption that Eqs. (4.30) to (4.34) hold, the filtered pointing angles for each axis can be approximated by

$$\theta_x \approx \iint \tau_x/J_{xx} \approx \frac{1}{J_{xx}} \iint m_y B_z - \frac{1}{J_{xx}} \iint m_z B_y \tag{4.49}$$

$$\theta_y \approx \iint \tau_y/J_{yy} \approx \frac{1}{J_{yy}} \iint m_z B_x - \frac{1}{J_{yy}} \iint m_x B_z \tag{4.50}$$

$$\theta_z \approx \iint \tau_z/J_{zz} \approx \frac{1}{J_{zz}} \iint m_x B_y - \frac{1}{J_{zz}} \iint m_y B_x, \tag{4.51}$$

where the double integral is to be taken w.r.t. time. For the purpose of this analysis, assume that the geomagnetic field $\vec{B}$ is constant for the duration of the maneuver, which is approximately true for many locations in the GFO orbit, but needs to be considered again at a more detailed stage of the maneuver planning. With an MDM according to (4.47), for the roll angle θ_x one has

$$\begin{aligned} \theta_x(t) &\approx \frac{m_{y,0} B_z - m_{z,0} B_y}{J_{xx}} \iint \sin\left(2\pi f_m t\right) \\ &= \frac{m_{z,0} B_y - m_{y,0} B_z}{4\pi^2 f_m^2 J_{xx}} \sin\left(2\pi f_m t\right), \end{aligned} \tag{4.52}$$

and accordingly for the pitch angle θ_y,

$$\theta_y(t) \approx \frac{m_{x,0} B_z - m_{z,0} B_x}{4\pi^2 f_m^2 J_{yy}} \sin\left(2\pi f_m t\right), \tag{4.53}$$

and for the yaw angle θ_z,

$$\theta_z(t) \approx \frac{m_{y,0} B_x - m_{x,0} B_y}{4\pi^2 f_m^2 J_{zz}} \sin\left(2\pi f_m t\right). \tag{4.54}$$

Then, the first diagonal entry of A, A_{11}, is approximately given by

$$A_{11} \approx \left(\frac{m_{z,0} B_y - m_{y,0} B_z}{4\pi^2 f_m^2 J_{xx}}\right)^2 \cdot \int_0^T \sin^2(2\pi f_m t) \, dt = \left(\frac{m_{z,0} B_y - m_{y,0} B_z}{4\pi^2 f_m^2 J_{xx}}\right)^2 \cdot \frac{T}{2}, \tag{4.55}$$

if T is a multiple of the period $P_m = 1/f_m$. Similarly,

$$A_{22} \approx \left(\frac{m_{x,0}B_z - m_{z,0}B_x}{4\pi^2 f_m^2 J_{yy}} \right)^2 \cdot \frac{T}{2}, \tag{4.56}$$

and

$$A_{33} \approx \left(\frac{m_{y,0}B_x - m_{x,0}B_y}{4\pi^2 f_m^2 J_{zz}} \right)^2 \cdot \frac{T}{2}. \tag{4.57}$$

If there were no inter-angle correlations, A would be diagonal, and so would A^{-1}, with entries reciprocal to the entries of A. This is the case of equality in (4.46). In particular, this would yield

$$\sigma(\hat{\lambda}_x) \approx \sigma(n_\rho) \cdot \left| \frac{4\sqrt{2}\pi^2 f_m^2 J_{xx}}{(m_{z,0}B_y - m_{y,0}B_z)\sqrt{T}} \right| \tag{4.58}$$

$$\sigma(\hat{\lambda}_y) \approx \sigma(n_\rho) \cdot \left| \frac{4\sqrt{2}\pi^2 f_m^2 J_{yy}}{(m_{x,0}B_z - m_{z,0}B_x)\sqrt{T}} \right| \tag{4.59}$$

$$\sigma(\hat{\lambda}_z) \approx \sigma(n_\rho) \cdot \left| \frac{4\sqrt{2}\pi^2 f_m^2 J_{zz}}{(m_{y,0}B_x - m_{x,0}B_y)\sqrt{T}} \right| \tag{4.60}$$

Regarding the off-diagonal elements of A, as an example, using Eqs. (4.52) and (4.53), for A_{12} one obtains

$$A_{12} = \int_0^T \theta_x(t)\theta_y(t) \, dt \tag{4.61}$$

$$= \left(\frac{m_{z,0}B_y - m_{y,0}B_z}{4\pi^2 f_m^2 J_{xx}} \right) \cdot \left(\frac{m_{x,0}B_z - m_{z,0}B_x}{4\pi^2 f_m^2 J_{yy}} \right) \cdot \int_0^T \sin^2\left(2\pi f_m t\right) \, dt \tag{4.62}$$

$$= \left(\frac{m_{z,0}B_y - m_{y,0}B_z}{4\pi^2 f_m^2 J_{xx}} \right) \cdot \left(\frac{m_{x,0}B_z - m_{z,0}B_x}{4\pi^2 f_m^2 J_{yy}} \right) \cdot \frac{T}{2} \tag{4.63}$$

$$= \frac{T}{32\pi^4 f_m^4} \cdot \left(\frac{m_{z,0}B_y - m_{y,0}B_z}{J_{xx}} \right) \cdot \left(\frac{m_{x,0}B_z - m_{z,0}B_x}{J_{yy}} \right), \tag{4.64}$$

since T is a multiple of $P_m = 1/f_m$. Similar equations hold for A_{13} and A_{23}. In particular, this yields the important observation that

$$A \sim \frac{T}{f_m^4}, \tag{4.65}$$

i.e., all elements of the matrix A are proportional to T/f_m^4. Hence, the STD of each estimated coupling factor, cf. Eq. (4.28), is proportional to f_m^2 and inversely proportional to $\sqrt{T}$. Considering the ranging noise $\sigma(n_\rho)$ as well, one has

$$\sigma(\hat{\lambda}_i) \sim \frac{\sigma(n_\rho)f_m^2}{\sqrt{T}}, \tag{4.66}$$

for $i = 1, 2, 3$, whether there are inter-angle correlations or not.

Nevertheless, inter-angle correlations are indeed almost unavoidable. A close look reveals that $A_{ij} = 0$ if and only if $\theta_i(t) = 0$ or $\theta_j(t) = 0$ for all $t \in [0, T]$. It follows that all correlations are zero if and only if at least two of the three angles vanish entirely, or equivalently, if and only if the magnetic torque $\vec{\tau}_m$ has only one nonzero component in the SF, i.e. is parallel to one of the S/C axes. This, in turn, is only possible if $\vec{B}$ is perpendicular to that axis, since $\vec{\tau}_m$ is always perpendicular to $\vec{B}$.

Using arbitrary frequency and phase

Suppose now that each MDM is allowed to have its own frequency and phase shift, that is,

$$m_x(t) = m_{x,0} \sin\left(2\pi f_{x,0} t + \varphi_{x,0}\right), \tag{4.67}$$
$$m_y(t) = m_{y,0} \sin\left(2\pi f_{y,0} t + \varphi_{y,0}\right), \tag{4.68}$$
$$m_z(t) = m_{z,0} \sin\left(2\pi f_{z,0} t + \varphi_{z,0}\right). \tag{4.69}$$

Additionally, the requirement will be useful that the frequencies and T must be chosen such that T is a multiple of each period, so that each profile has an integer number of cycles. The following abbreviations will be used:

$$s_x = \sin\left(2\pi f_{x,0} t + \varphi_{x,0}\right), \tag{4.70}$$
$$s_y = \sin\left(2\pi f_{y,0} t + \varphi_{y,0}\right), \tag{4.71}$$
$$s_z = \sin\left(2\pi f_{z,0} t + \varphi_{z,0}\right). \tag{4.72}$$

Then, one has

$$\theta_x \approx \frac{m_{y,0} B_z}{J_{xx}} \iint s_y - \frac{m_{z,0} B_y}{J_{xx}} \iint s_z \tag{4.73}$$

$$= \frac{m_{z,0} B_y}{4\pi^2 f_{z,0}^2 J_{xx}} s_z - \frac{m_{y,0} B_z}{4\pi^2 f_{y,0}^2 J_{xx}} s_y, \tag{4.74}$$

and accordingly for θ_y and θ_z:

$$\theta_y \approx \frac{m_{x,0} B_z}{4\pi^2 f_{x,0}^2 J_{yy}} s_x - \frac{m_{z,0} B_x}{4\pi^2 f_{z,0}^2 J_{yy}} s_z, \tag{4.75}$$

$$\theta_z \approx \frac{m_{y,0} B_x}{4\pi^2 f_{y,0}^2 J_{zz}} s_y - \frac{m_{x,0} B_y}{4\pi^2 f_{x,0}^2 J_{zz}} s_x. \tag{4.76}$$

In this more general case, one has

$$\theta_x \theta_y = \ldots$$
$$\frac{1}{16\pi^4 J_{xx} J_{yy}} \cdot \left[\frac{m_{x,0} m_{z,0} B_y B_z}{f_x^2 f_z^2} s_x s_z - \frac{m_{x,0} m_{y,0} B_z^2}{f_x^2 f_y^2} s_x s_y + \frac{m_{y,0} m_{z,0} B_x B_z}{f_y^2 f_z^2} s_y s_z - \frac{m_{z,0}^2 B_x B_y}{f_z^4} s_z^2 \right]. \tag{4.77}$$

Writing $\mathcal{I}_{xy} = \int s_x s_y$, $\mathcal{I}_{xz} = \int s_x s_z$, and $\mathcal{I}_{yz} = \int s_y s_z$, it follows that

$$A_{12} = \frac{1}{16\pi^4 J_{xx} J_{yy}} \cdot \left[\frac{m_{x,0} m_{z,0} B_y B_z}{f_x^2 f_z^2} \mathcal{I}_{xz} - \frac{m_{x,0} m_{y,0} B_z^2}{f_x^2 f_y^2} \mathcal{I}_{xy} + \frac{m_{y,0} m_{z,0} B_x B_z}{f_y^2 f_z^2} \mathcal{I}_{yz} - \frac{T m_{z,0}^2 B_x B_y}{2 f_z^4} \right]. \tag{4.78}$$

Regard the last term in the bracket. Unless all three angles are identically zero, this term, and the corresponding terms in the equations for A_{13} and A_{23}, cannot all be zero at the same time. However, these terms can be minimized by choosing the optimal maneuver parameters. When the frequencies and phases are well chosen, all the other terms vanish. In fact, from

$$\sin(\alpha)\sin(\beta) = \frac{1}{2}\left(\cos(\alpha - \beta) - \cos(\alpha + \beta)\right), \tag{4.79}$$

it follows that

$$\mathcal{I}_{xy} = \int\limits_0^T \sin\left(2\pi f_{x,0} t + \varphi_{x,0}\right) \sin\left(2\pi f_{y,0} t + \varphi_{y,0}\right) dt \tag{4.80}$$

$$= \frac{1}{2} \int\limits_0^T \cos\left(2\pi(f_{x,0} - f_{y,0})t + \varphi_{x,0} - \varphi_{y,0}\right) dt - \frac{1}{2} \int\limits_0^T \cos\left(2\pi(f_{x,0} + f_{y,0})t + \varphi_{x,0} + \varphi_{y,0}\right) dt.$$
$$\tag{4.81}$$

It is easily seen that the second term always vanishes, since T is a multiple of both periods, i.e. $T = n/f_{x,0} = m/f_{y,0}$, for some integers n and m. Moreover, three cases can be distinguished:

1. If $f_{x,0} \neq f_{y,0}$, the first term vanishes as well, independently of $\varphi_{x,0}$ and $\varphi_{y,0}$. Thus, $I_{xy} = 0$.

2. If $f_{x,0} = f_{y,0}$ and $\varphi_{x,0} = \varphi_{y,0}$, the first term in (4.81) equals $T/2$, thus $I_{xy} = T/2$, which is the case in (4.64).

3. If $f_{x,0} = f_{y,0}$ and $\varphi_{x,0} \neq \varphi_{y,0}$,

$$\mathcal{I}_{xy} = \frac{T}{2} \cos\left(\varphi_{x,0} - \varphi_{y,0}\right), \tag{4.82}$$

   which is zero if $\varphi_{x,0} - \varphi_{y,0} = (n + 1/2)\pi$ for some integer n, in particular if there is a 90 degree phase shift between the MDM profiles of the two torque rods.

The same statements made above for the pair x, y also hold for the pairs x, z and y, z. Therefore, if different frequencies are used for the different torque rods, most of the terms in Eq. (4.78) are zero. The same effect is obtained if the activation profile of one of the torque rods is phase shifted by $\pi/2$, compared to the others.

Identifying the optimal combination

Previously, in Sec. 4.3.1, it could be seen that one can adequately predict the STD of the estimated coupling factors, given the MDM profile and the S/C orbits, cf. Fig. 4.11. This allows a quick assessment of the maneuver quality for different locations in orbit, cf. Fig. 4.12. Here the author has performed a similar analysis considering the same time span during a pitch maneuver for GF1 on 26 August 2019, using the same orbit data. This time, consider hypothetical maneuvers with alternative MDM profiles, with the goal of revealing the optimal constellation. Three cases were investigated:

1. Two torque rods were activated with the maximal amplitude, phase shifted against each other by 90 °. The rods in SF x and z direction were activated, since the maneuver is meant to stimulate the pitch angle. Both rods were activated with a frequency of $83.\bar{3}$ mHz.

2. In this case, no phase shift between the two activated rods was applied. Instead, two different frequencies were used: $83.\bar{3}$ mHz for the SF x direction, and 100 mHz for the z direction.

3. Here, all three MTRs were activated. By using 100 mHz for the x axis, as well as a 90 ° phase shift between y and z, the inter-angle correlations were minimized. $83.\bar{3}$ mHz was used for the y and z axes. Among all other possible combinations, by visual comparison, this case was found to be close to the optimal constellation.
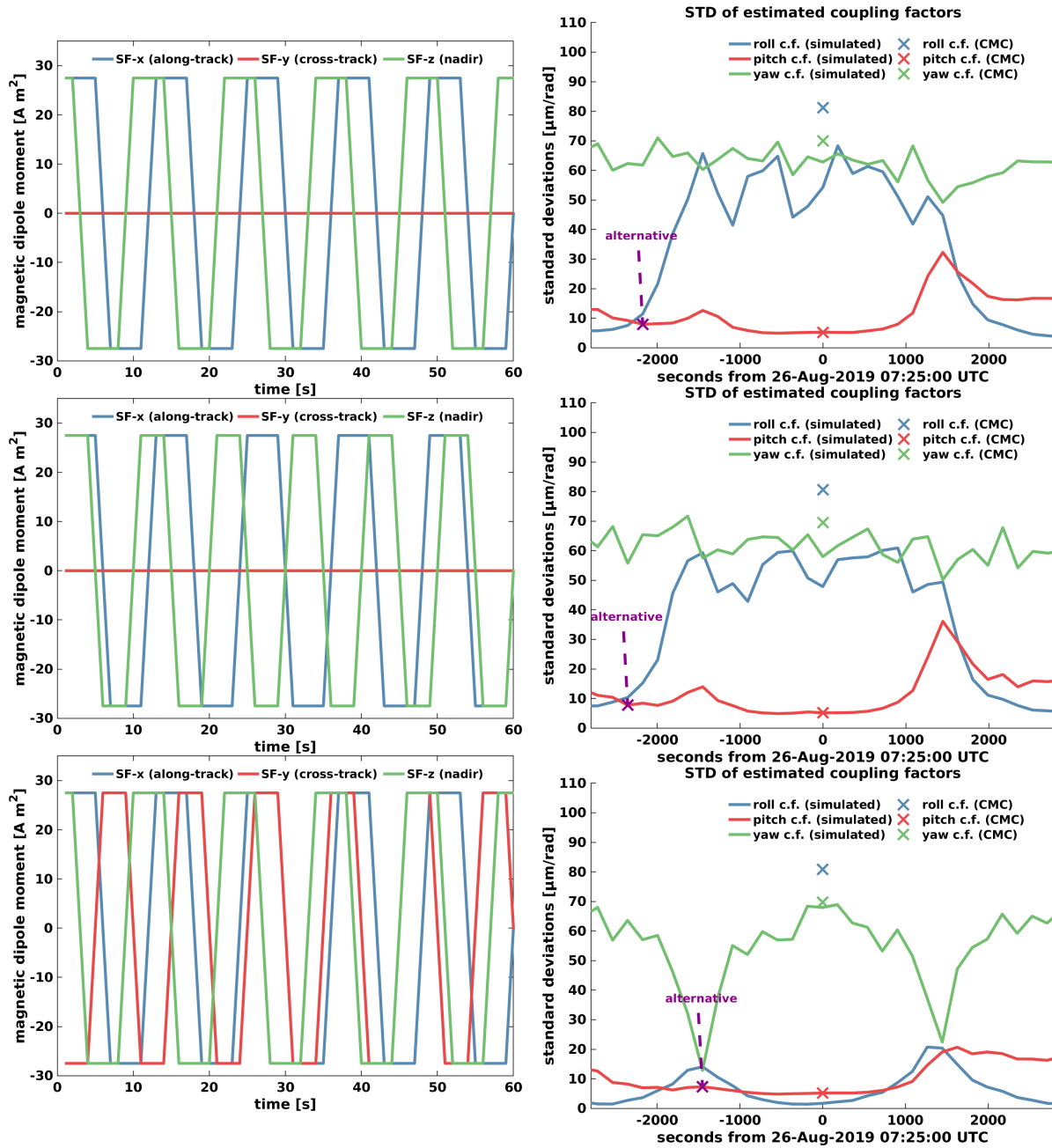
Figure 4.13: Different hypothetical maneuver cases, using a phase shift (top), using different frequencies (middle), and with the optimal combination (bottom). Left: MDM profiles. Right: STDs of estimated CF.

The left plots of Fig. 4.13 show the MDM profiles that were used for these three cases. The right plots show all three STDs, i.e. $\sigma(\hat{\lambda}_i)$ for $i = 1, 2, 3$, over time. For comparison, the location and the STDs from the actual CMC maneuver are marked with crosses. In all cases, the location of the CMC maneuver is optimal with regard to estimating the pitch CF. However, it can be seen that the hypothetical cases provide the opportunity to estimate more than one CF at a time. As illustrated in the plots by purple crosses, alternative locations can be found, where the maneuver time could be used more efficiently, e.g. by estimating the roll CF at the same time. Table 4.1 shows the results when using the indicated alternative maneuver locations for the hypothetical cases, compared to the values from the actual CMC.

Note that in all three hypothetical cases the STDs of the pitch CFs are only slightly larger than in the CMC case, while all achieving better values for the roll angle. In the optimal case, a significantly lowered STD of the yaw CF is attained additionally.

Table 4.1: Results of different simulated maneuvers, each based on the same time span and orbit data, but using alternative MTR profiles.

	frequency [mHz]:			phase [rad]:			STD [µm rad^{-1}]:		
case	f_x	f_y	f_z	φ_x	φ_y	φ_z	roll	pitch	yaw
CMC	$83.\bar{3}$	N/A	$83.\bar{3}$	0	0	0	68.3	5.4	71.8
alt. phase	$83.\bar{3}$	N/A	$83.\bar{3}$	0	0	$\pi/2$	11.3	7.5	68.2
alt. frequency	$83.\bar{3}$	N/A	100	0	0	0	10.4	9.0	64.8
optimal	$83.\bar{3}$	100	$83.\bar{3}$	0	0	$\pi/2$	12.9	6.9	12.7

Summarizing the results of this section, correlations between the MDM of two torque rods imply correlations between the resulting pointing angle variations. In the general case, the STDs of estimated CFs, $\sigma(\hat{\lambda})$, have a lower bound, which is attained if the matrix $A = \theta^T \theta$ is diagonal, i.e. if inter-angle correlations vanish. Two ways for obtaining larger angle excitations while minimizing the inter-angle correlations have been identified. One option is to use different frequencies for the different torque rods. Another option is to use the same frequency for two torque rods, phase shifted against each other by 90 °. When a single frequency and no phase shift is used, $\sigma(\hat{\lambda})$ is proportional to f_m^2. In the general case, $\sigma(\hat{\lambda})$ is inversely proportional to $\sqrt{T}$, and proportional to the STD $\sigma(n_\rho)$ of the ranging noise. The latter is examined in the following.

Optimal frequency considering ranging noise

The STDs of the estimated TTL coupling factors are proportional to the STD of the ranging noise. Thus, it must also be taken into consideration. Not considering the dependency on the maneuver duration here, one has

$$\sigma(\hat{\lambda}) \sim \sigma(n_\rho) f_m^2. \tag{4.83}$$

When planning a rotation maneuver for the purpose of TTL estimation, it is thus important how the amount of instrument noise depends on the considered frequency range. Unfortunately, the in-flight instrument noise spectrum is not perfectly known before the launch of the mission. However, by now there is a good understanding of the noise in the LRI range at high frequencies, cf. App. E. For the purpose of this analysis, consider the following four candidates of defining the noise in terms of ASDs, which are depicted in the left plot of Fig. 4.14.

1. By the time of writing this thesis, real LRI data is already available. One can thus estimate the spectrum of the measured LRI range. In a sense, this spectrum can be considered to be the worst case, since it is an upper bound for the actual ranging noise. The respective curve in the plot is labeled *LRI*.

2. In the frequency region around the maneuver frequency, the LRI range spectrum contains signal caused by nongravitational forces in the LoS direction. Thus, the spectrum can be lowered by removing these contributions, which are called differential linear nongravitational (DLN) range variations in this thesis. They can be derived from ACT1A data, which is described in more detail in App. E.2. In the plot the range reduced with ACT1A data is labeled *LRI - DLN*.

3. A second way of lowering the LRI range spectrum is by subtracting the effects of the attitude control thruster firings, which can make up a large part of the nongravitational

signal. This procedure is described in App. E.1. In the plot the range reduced with THR1B data is labeled *LRI - THR*.

4. In the case of GFO, LFN was the major expected noise source apart from TTL. A model of the LFN ASD is given in Sec. 3.1.6. Since this noise source cannot be removed in post-processing, one may consider this model to be the best possible case, i.e. the lowest possible noise level. In the plot this is labeled *LFN*.

By Parseval's theorem, one has

$$\sigma(n_\rho)^2 = \int\limits_0^\infty \mathrm{PSD}_{n_\rho}(f) \ df = \int\limits_0^\infty \left(\mathrm{ASD}_{n_\rho}(f)\right)^2 \ df. \tag{4.84}$$

Note that since all the data is bandpass filtered, $\sigma(n_\rho) = \sigma_{f_m}(n_\rho)$ actually depends on the maneuver frequency f_m. Making the simplifying assumption that the range, including the noise, is perfectly filtered with a narrow passband around f_m of a given size, within which ASD_{n_ρ} is approximately constant, one obtains the heuristic relation

$$\sigma_{f_m}(n_\rho)^2 = \int\limits_{f_m-\delta}^{f_m+\delta} \left(\mathrm{ASD}_{n_\rho}(f)\right)^2 \ df \propto \left(\mathrm{ASD}_{n_\rho}(f_m)\right)^2. \tag{4.85}$$

Recalling Eq. (4.83), if one seeks to minimize $\sigma(\hat\lambda)$, one ought to minimize $\sigma_{f_m}(n_\rho)\cdot f_m^2$. Hence, it is beneficial to examine $f^2 \cdot \mathrm{ASD}_{n_\rho}(f)$ and define the optimal maneuver frequency $f_{m,\mathrm{opt}}$ as

$$f_{m,\mathrm{opt}} = \arg\min_f \left[f^2 \cdot \mathrm{ASD}_{n_\rho}(f)\right], \tag{4.86}$$

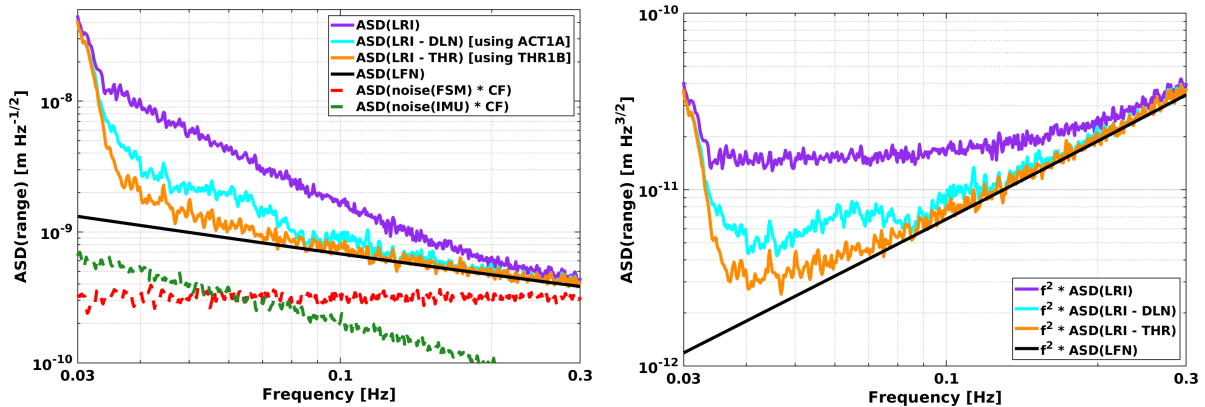i.e. the frequency f for which $f^2 \cdot \mathrm{ASD}_{n_\rho}(f)$ is minimal.

Figure 4.14: Left: ASD of LFN, LRI range, reduced range, and angle noise times CF. Right: ASDs multiplied by f^2.

The amplitude spectral densities of the 4 candidates of $\mathrm{ASD}_{n_\rho}(f)$ are plotted in Fig. 4.14, on the left. The plot on the right shows $f^2 \cdot \mathrm{ASD}_{n_\rho}(f)$, which one desires to minimize w.r.t. f. The plots are based on data from 15 June 2019. In both plots, for frequencies below about 38 mHz, the gravity signal is visible as a steep rise. Frequencies lower than that can be excluded right away. For the case of the LRI, Fig. 4.14 clearly yields a similar conclusion for all 4 curves: the lower the maneuver frequency the better. However, there should be some margin between f_m and 38 mHz, since there are no perfect highpass filters. It can be concluded that

the optimal value for f_m in case of the LRI is close to 50 mHz. According to Eq. (4.83), a maneuver frequency of 50 mHz could reduce $\sigma(\hat{\lambda})$ by a factor of about 2.7, compared to the $83.\bar{3}$ mHz of the CMC maneuvers.

Furthermore, the angle noise should be considered as well, see also Sec. 5.2. The interesting quantity in that regard is the spectrum of $n_\theta \lambda$, i.e. the sum of the measurement noise in each angle scaled by the coupling factors. The red and orange dashed lines in the left plot of Fig. 4.14 show simulations of the ASDs of $n_\theta \lambda$, based on the noise models of FSM and IMU1B angles, respectively. Hypothetical coupling factors of 100 µm rad^{-1} each, for pitch and yaw of both S/C, were assumed. In the case considered here, this term is small compared to the ranging noise, and thus likely to be less important.

Note that the LRI noise is in reality not static. The shown ASDs are estimations and do depend on time, correlated with the satellite location in orbit, among other things. Here the reader is referred to App. E.3, where the LRI range spectrum is analyzed further. The reduced curves (with ACT1A or THR1B) depend further on the accuracy of ACC data or the thruster models, respectively. Additionally, the LFN depends on the inter-satellite separation, cf. Eq. (3.20).

Finally, consider the following aspect. A gravity experiment such as GFO is not equally sensitive to the entire spectrum of gravity variations [Spe21]. As was already illustrated in Fig. 2 of [Wol69], undulations of gravity with a wavelength equal to the S/C separation are undetectable, since these cause both satellites to accelerate and decelerate in step with each other, and the difference vanishes. This is called a resonance of the satellites with spherical harmonics of the geopotential. Using the trigonometric identity

$$\sin(\theta + \varphi) - \sin(\theta - \varphi) = 2\cos\theta \sin\varphi, \tag{4.87}$$

it can immediately be derived that the response to gravity undulations is proportional to $|\sin(\pi f / f_L)|$, where $f_L = \frac{v_0}{L}$, with the S/C separation L and the absolute satellite velocity v_0. This function is depicted in Fig. 4.15. Thus, the frequencies at which GFO cannot detect gravity variations, called the gravity null frequencies, are at $f_k = k \cdot f_L$, $k \in \mathbb{N}$. The first null is at $f_1 \approx 38$ mHz, assuming a satellite velocity of $v_o = 7.6$ km s^{-1} and a S/C separation of $L = 200$ km.
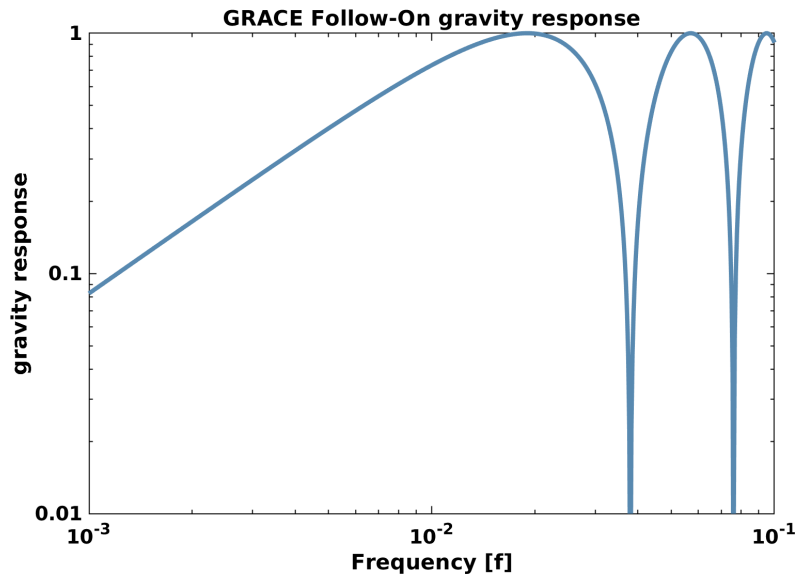

Figure 4.15: The sensitivity to the ranging signal induced by the Earth's gravity field is proportional to this curve. For this plot, an absolute S/C velocity of 7.6 km s^{-1} and a S/C separation of 200 km was assumed.

Maximal gravity response is given e.g. at about 57 and 95 mHz, which would make frequencies close to these values not a good choice for a TTL maneuver, since a large gravity signal at the maneuver frequency would impede the TTL estimation. In the case of GFO, there is no significant gravity signal at these frequencies. This fact is related to the orbit altitude, see [Wol69; Mül17] for more information. Therefore, this consideration is not of further importance for the maneuver design discussed here. However, when TTL maneuvers are planned for future geodesy missions such as NGGM, where the satellite formation may be different, one should keep it in mind.

4.3.4 Maneuver duration

Since the STD of the LSQ estimator is inversely proportional to $\sqrt{T}$, the maneuver should be as long as possible, cf. Eq. (4.66). However, there are certain limits. E.g., the pointing angles drift off during the maneuver, if the ACS is not preventing it. Recall that this is the case for the CMC maneuvers, which are performed by MTRs and during which the control thrusters are not firing. This puts a limit on T, since the LRI requires fine inter-satellite pointing. The LRI can tolerate S/C attitude deviations from the LoS of about 6.5 mrad in pitch and yaw. During the first three years of GFO operation, the largest angle deviations during a CMC maneuver with 180 s duration on GF1 have been 3.2 and 1.6 mrad, for pitch and yaw, respectively. However, on GF2 one observes larger angle deviations during a maneuver, up to about 5.9 and 2.8 mrad. The author did not further investigate the reason for this different behavior. This means that in the current constellation, the maneuver duration of 180 s is already maximal for an LRI TTL maneuver. If the larger deviations as observed on GF2 could be avoided, a duration of about 240 s would also be possible.

A prospect for future missions might be to involve the ACS to a larger extent, which continuously attempts to drive the S/C attitude towards a desired attitude, called ACS set point. Thus, the maneuver stimulus may be injected via a pre-defined time series of ACS set points, instead of commanding the desired torque profile. With this approach, the drifting of the pointing angles during the maneuver would be compensated automatically. The maneuver duration could be prolonged further by allowing attitude control thruster usage during the maneuver. However, it needs to be assured that the ACS can cope with it.

When MTRs are used, there is another reason for a limited maneuver duration. The feasibility of the desired torque depends on the geomagnetic field lines and thus on the location of the satellite in orbit. In the case of GFO, the orbit period is about 90 minutes, which means that - in the SF - the direction of the geomagnetic field vector may already be changing significantly during a few minutes. Further potential restrictions on T may be given by the amount of energy that is consumed by the MTRs in order to perform the maneuvers, or because the taking of main mission science measurements should not be interrupted for too long.

4.3.5 Maneuver location

For the individual maneuver planning, one long time series of simulated STDs $\sigma(\hat{\lambda})$ should be simulated, which covers well the surface of the Earth. Then the optimal locations are chosen by minimizing $\sigma(\hat{\lambda}_i)$, for each coupling factor λ_i. A key aspect is also that the geomagnetic field is ideally not too volatile and should be approximately constant during the course of the maneuver. This criterion is even more significant, the longer the maneuver duration.

Figure 4.16 shows the predicted values for $\sigma(\hat{\lambda}_i)$, for i = roll (top right), pitch (bottom left), and yaw (bottom right). The shown values are based on the real GF1 orbit data from November 10 to 20 in 2019, and on an optimized MDM activation. In particular, three torque rods were activated with rectangular profiles with periods of 20, 16, and 20 s, for the x, y, and z directions, which corresponds to 50, 62.5, and 50 mHz, respectively. The z profile was shifted by 10 s w.r.t. the x profile, and the maneuver duration was $T = 240$ s. The plot shows

only values from descending orbits, i.e. when the satellites were on the trajectory from the most northern to the most southern point of the orbit, since this yields a more homogeneous picture.

Further, one must consider the ranging noise as well as disturbances such as thruster firings, see App. E. Ideally, one should choose a more quiet location. Similarly, it may be worthwhile to check whether there are regions with larger natural pointing variations, respectively with large environmental torque, and avoid those. Moreover, star tracker blindings ought to be avoided, as well as LRI blindings. The latter can occur about twice per year when the solar beta angle is close to zero.

Finally, depending on the mission, it may be beneficial to choose a maneuver location close to a ground station, in order to enable prompt transfer of the maneuver data. There are 5 available ground stations for GFO[9], whose locations are depicted in Fig. 4.16 (top left): Ny-Ålesund/Spitzbergen, Weilheim/Germany, Neustrelitz/Germany, O'Higgings/Antarctica, Inuvik/Canada. Note that this criterion may be relevant for mission operations planning, however, from the pure perspective of TTL analysis it is not important.
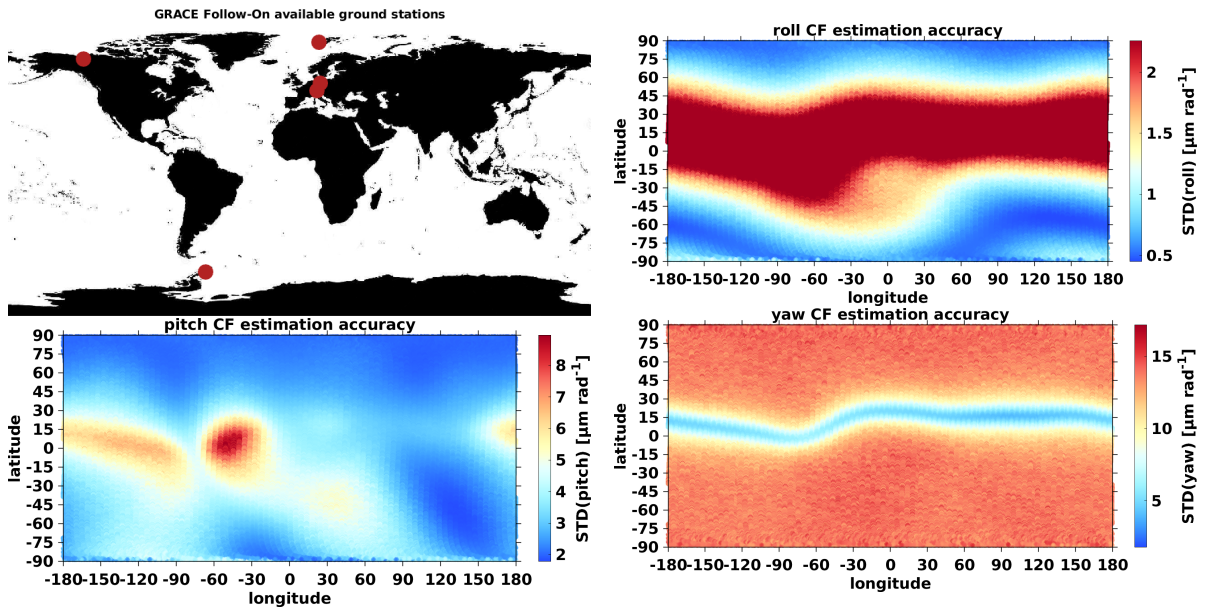

Figure 4.16: Top left: Ground stations in principle available for receiving GFO data. Top right and bottom: predicted STDs of coupling factor estimators, using optimal maneuver parameters.

4.3.6 Optimal parameters for the LRI

Summarizing the results of this section on maneuver design, the optimal parameters for an LRI TTL calibration maneuver are in short:

- optimal MDM profile: use square waves - *by a factor of 1.27 better than sinusoidal*

- torque rod activation: utilize all rods - *depends on the ambient magnetic field*

- optimal maneuver frequency: two different frequencies close to $f_m = 50$ mHz - *lower limit due to gravity signal*

- optimal phase shift: have one rod shifted by $\pi/2$ - *in order to minimize correlation*

---

[9]according to the GFZ website: `https://www.gfz-potsdam.de`

- optimal duration: 240 seconds - *upper limit due to pointing deviation*

- optimal locations: individual choice - *depends on the other parameters*

Compared to the CMC maneuvers, a lower frequency and longer duration could decrease the STD of the CF estimate by a factor of about 3. By activating a third torque rod with a different frequency and by phase shifting one of the MDM profiles, the time spent to perform the maneuvers could be used even more efficiently. The optimal locations in orbit must be determined individually. The geographic locations for the CMC maneuvers of GFO were already well chosen. In the following, some simulation cases are briefly presented.

4.4 Selected simulation cases

In this section, a few examples of rotation maneuvers are presented, which have been simulated by the author. First, some CMC maneuvers have been reconstructed that had already been carried out on GFO, in order to put the simulation technique to the test. Then, some results of simulated maneuvers with optimal parameters for the LRI, as derived in the precedent section, are shown. Finally, the performance of maneuvers that use attitude thrusters to produce the angular stimulus is examined. In the last part of this section, 4.4.5, the results of the different maneuver simulation cases are compared in terms of the predicted STDs of the coupling factor estimators that would result from using the respective set of maneuvers.

4.4.1 CMC reconstruction

In order to validate the maneuver simulation technique, existing CMC maneuvers have been reconstructed. More precisely, for each maneuver GFO Level-1B data at the starting time of the maneuver was used as initial conditions. I.e., initial S/C positions and velocities were taken from GNV1B data, initial quaternions from SCA1B data, and initial angular velocities from IMU1B data, according to Sec. 2.2.1. Then, the full S/C state vector was integrated, cf. Eq. (5.36). For each integration step, the magnetic control torque was derived directly from the MTR input currents as reported in the MAG1B data product. For the computation of the magnetic control torque, the geomagnetic field in SF was needed, which was taken from the IGRF12 model.

The left plots of Fig. 4.17 show comparisons of angular velocities for each SF axis. The angular velocities according to the integrated S/C state vector are plotted against the angular velocities derived from IMU1B data. There are clearly visible differences, which may be due to unmodeled angular accelerations. In the right plots of Fig. 4.17, angular accelerations from integration are compared against angular accelerations i) from ACC1A data, as well as ii) from differentiating angular velocities from IMU1B data. Since the angular accelerations from ACC1A data contain an unknown bias, the mean of the shown ACC1A time series was subtracted. This also means that the ACC data cannot be used to explain the differences that are visible in the angular velocity plots on the left. The periodic variations of the rotation maneuver match well overall, although there are slight differences of the magnitudes, especially in the x direction.

On the left side of Fig. 4.18, the pointing angles derived from the integrated state vector are compared against pointing angles derived from SCA1B and IMU1B data. The angles from integration seem to drift off slower than angles from SCA1B or IMU1B. The order of magnitude of the differences are consistent with the angular velocity differences visible in Fig. 4.17 (left side). The right side of Fig. 4.18 shows the same pointing angles after applying a highpass filter. In that case, the angles from integration agree well with angles derived from SCA1B or IMU1B data, down to the respective measurement noise.

What causes the different pointing angles? Since the angles from SCA1B data agree well with those derived from IMU1B data, it is assumed that these two are accurate. The reason
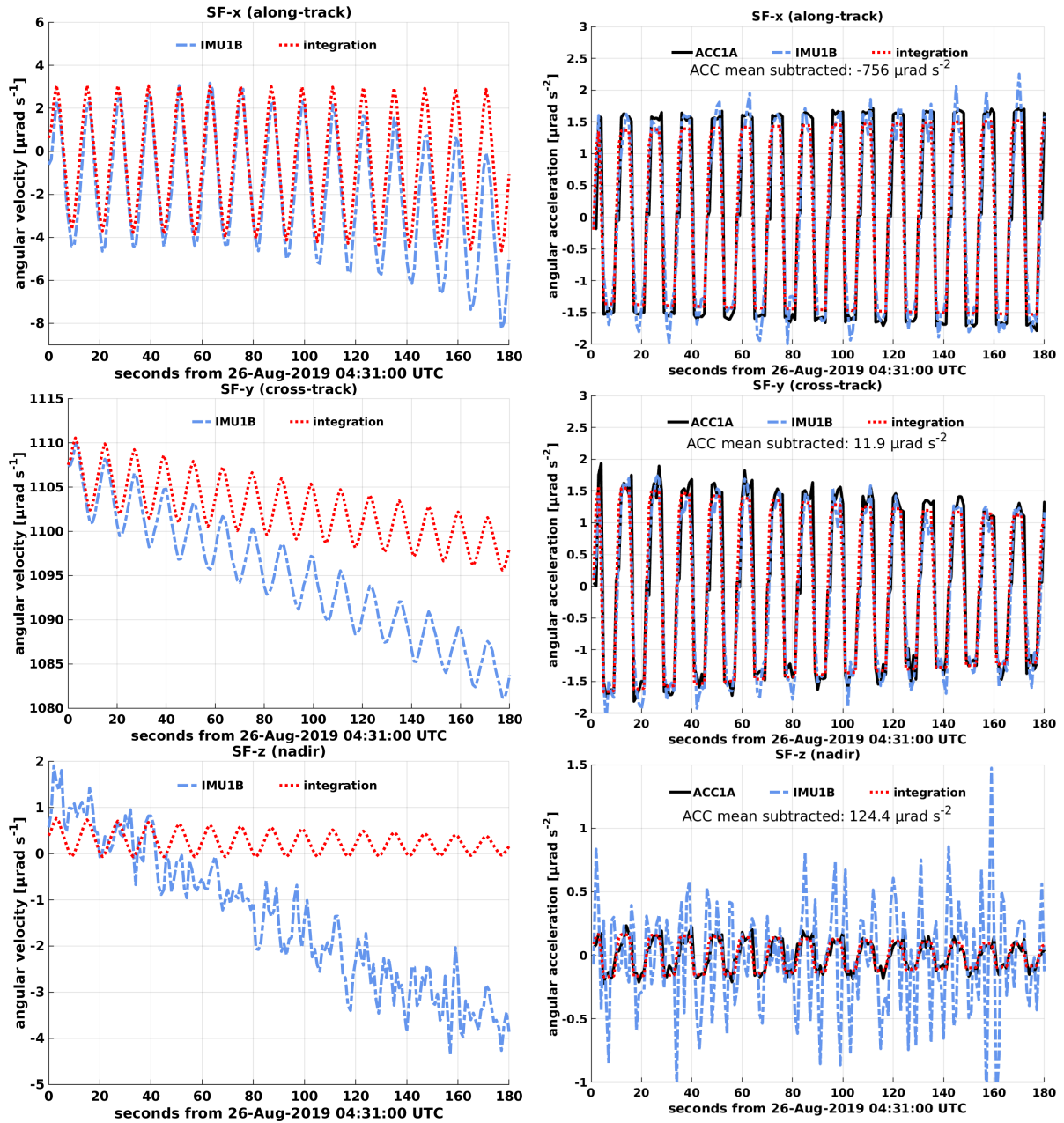
Figure 4.17: Left: Comparison of angular velocities in SF, IMU1B vs. integrated. Right: Comparison of angular accelerations in SF, ACC1A and IMU1B vs. integrated.

for the differences to the angles from integration cannot be inaccurate S/C positions, since the orbit deviation after 180 seconds of integration is of the order of centimeters, as depicted in Fig. 4.19. Such positional errors can explain at most a pointing deviation of the order of 100 nrad, but not the differences visible in Fig. 4.18.

It seems likely that the torque that was used for the integration was not accurate enough, that is, either some environmental torque or the magnetic control torque. To confirm this and in order to exclude a systematic mistake within this integration method, the S/C torque was derived exclusively from IMU1B angular velocities, and afterwards performed the integration again applying exactly this torque. The pointing angles obtained in this way showed no significant discrepancies any more when compared with SCA1B. In Fig. 4.20 the torque derived from IMU1B data is plotted against the torque that was used for the original integration. For
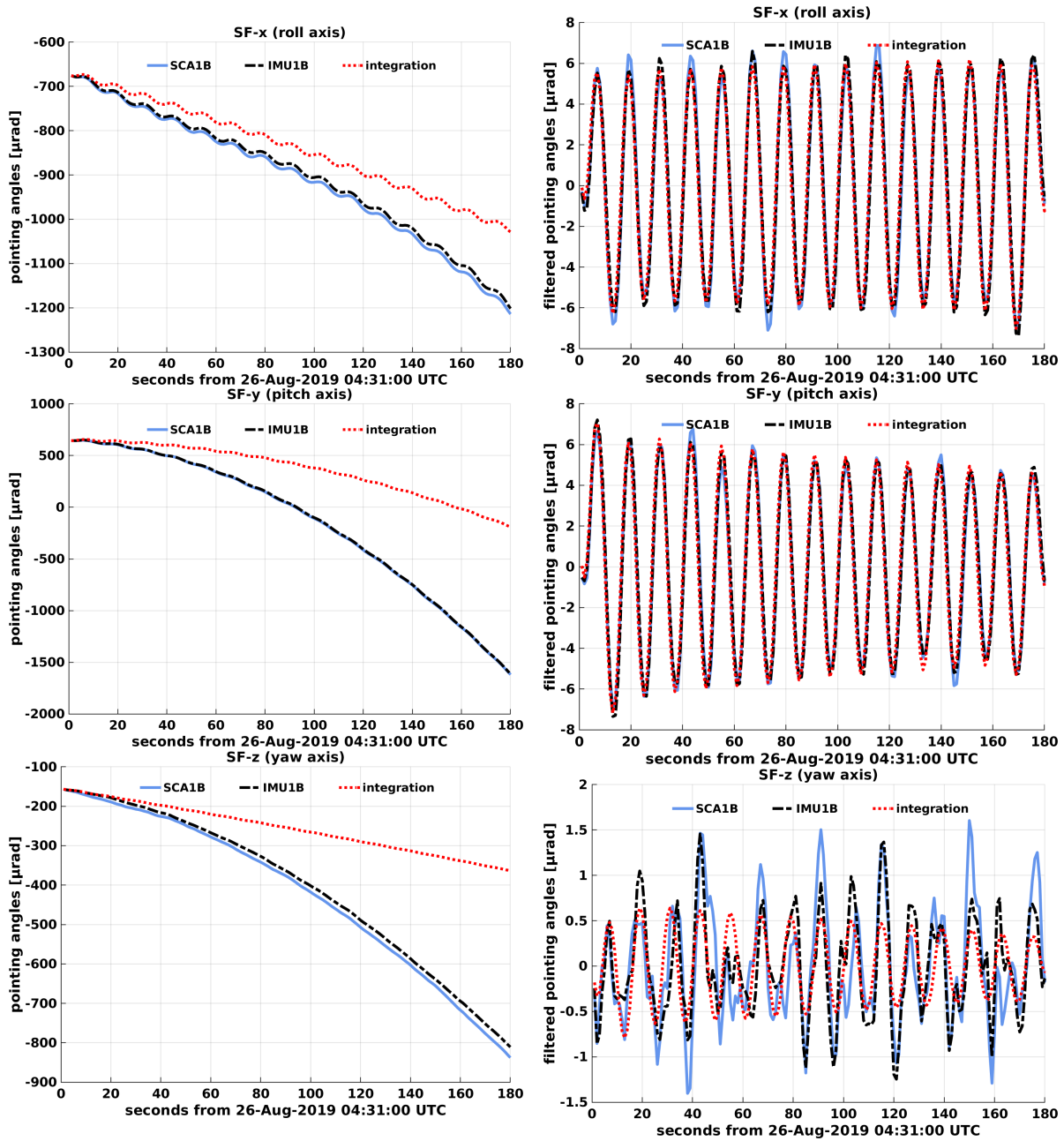
Figure 4.18: Comparison of pointing angles, SCA1B vs. IMU1B vs. integrated. Left: unfiltered. Right: highpass filtered with cutoff frequency 50 mHz.

comparison, the upper left plot shows the sum of the modeled environmental torques, which were used for the integration. The lines labeled *integration* in the remaining plots are the sum of environmental torques and the magnetic control torque derived from MAG1B data. As another possible cause for the torque differences (dotted black lines), one also has to consider that the magnetorquer currents reported in the MAG1B files may not be perfectly accurate, or that the torque rods themselves may be slightly misaligned.

The basis for the estimation of LRI TTL coupling factors via rotation maneuvers is always filtered data. The low frequency components do not influence the results here, since the TTL function is approximately a linear function of the angles. Thus, for the purpose of maneuver assessment, slow angular movement can be ignored. Merely for the discussion about possible
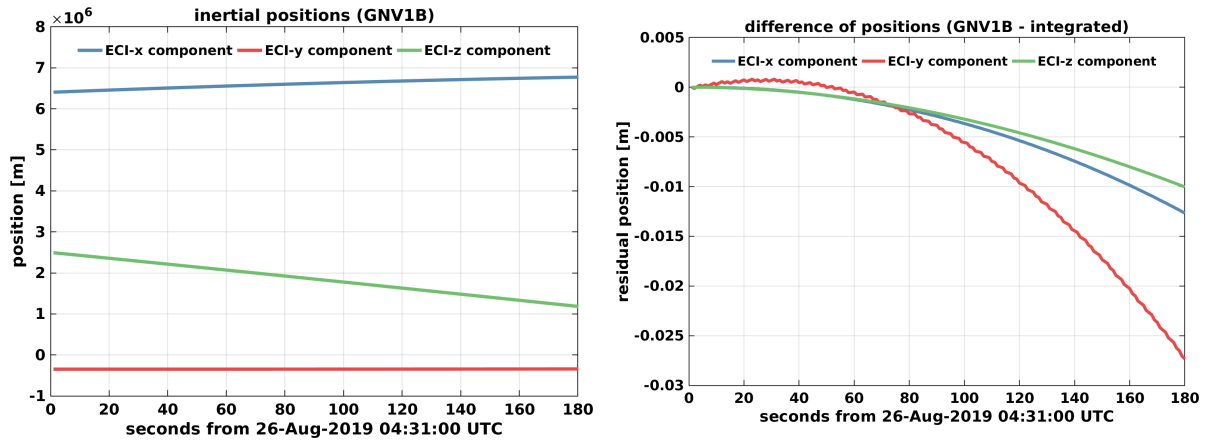
Figure 4.19: Comparison of inertial positions (top) and velocities (bottom), GNV1B vs. integrated. Left: GNV1B only. Right: difference "GNV1B - integrated".
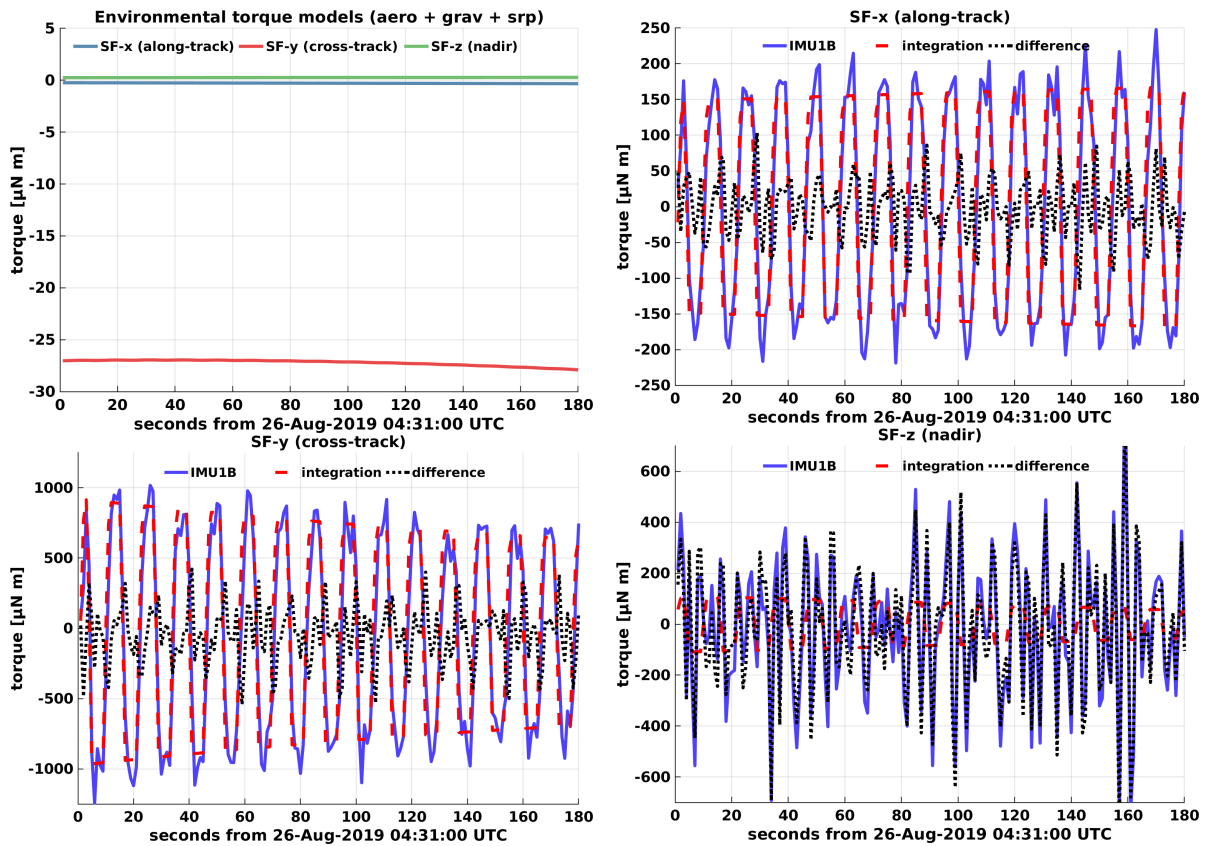

Figure 4.20: Upper left: environmental torque model (aerodynamic + solar radiation + gravitational). Top right and bottom: torques derived from IMU1B data versus torques used for the integration (magnetic + environmental); difference = IMU - integration.

maneuver durations, the absolute pointing deviation is important and needs to be kept in mind. Note however that for an instrument other than the LRI, the TTL function might not be linear in the angles, and then absolute knowledge of the S/C pointing might be crucial.

4.4.2 Adjusted magnetic dipole moment

As indicated in Sec. 4.3.3, the CMC maneuvers can be optimized w.r.t. the accuracy of TTL coupling factor estimation by activating all three MTRs, where one rod is activated with an alternative frequency and one rod is activated with a phase shifted magnitude profile. Here the same MDM profile that is depicted in Fig. 4.13 (bottom left plot) has been used. For the purpose of illustration, the author has simulated a set of 14 maneuvers and compared them to the actual 14 CMC maneuvers. In this example case, the maneuver frequency f_m or the duration T was not optimized. Two different frequencies were used, $83.\bar{3}$ and 100 mHz, and phase shifted one torque rod profile by $\pi/2$. Also, the optimized geographic locations were chosen. The locations are depicted in Fig. 4.21. The results in terms of $\sigma(\hat{\lambda})$ are given in Tab. 4.2, in contrast to the respective values for $\sigma(\hat{\lambda})$ in case of the 14 actually performed CMC maneuvers.
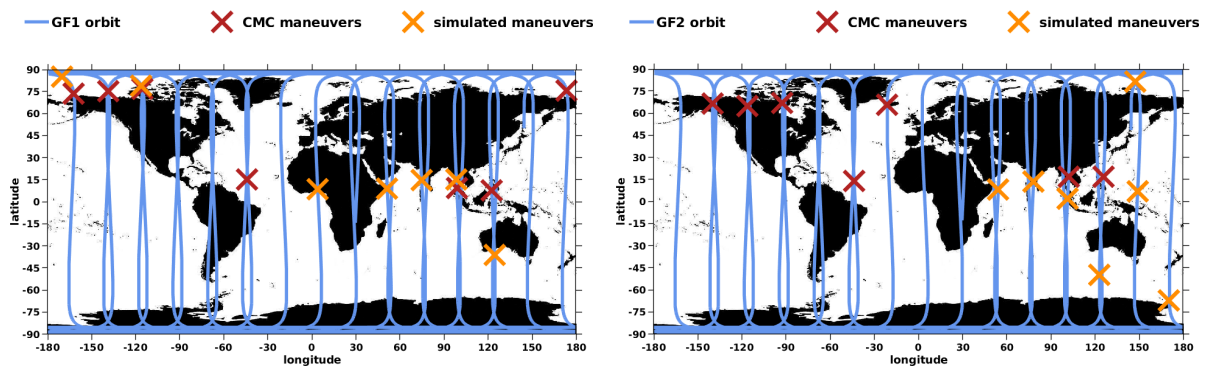

Figure 4.21: Locations of CMC maneuvers (red crosses) and simulated maneuvers (orange crosses) over the orbit trajectory. Left: GF1. Right: GF2.

4.4.3 Optimal LRI TTL calibration maneuvers

As in the previous case, two different frequencies were used, as well as a phase shift of $\pi/2$ for one torque rod profile. Here a maneuver duration of $T = 240$ s was used. In this case, two of the torque rods were activated with a maneuver frequencies of 50 mHz, where the MDM of one rod was shifted by $\pi/2$. A third rod was activated with 62.5 mHz. The second frequency and the maneuver duration T were chosen such that T is a multiple of both periods, which are 20 and 16 seconds. The same locations as in the simulation case before, cf. Fig. 4.21, were used here. Figure 4.22 exemplarily shows MDM and pointing angles for one of the GF1 maneuvers. As in the previous case, a total of 14 maneuvers was simulated.

4.4.4 Maneuvers with activated attitude thruster control

The author implemented an ACS simulator with "bang-bang" type thruster control, and simulated maneuvers with activated ACS. The benefit is that the maneuver can have a much longer duration, since then there is no danger of the inter-satellite pointing drifting too far off. In this example, a maneuver duration of $T = 1940$ s was chosen. The MDM profile is simply an extension of the "optimal LRI" case described above, i.e. in particular $f_m = 50$ mHz was chosen, and 62.5 mHz for the second frequency. Here two maneuvers were simulated, one per S/C, where in both cases all three pointing angles were excited. The angles have varying amplitudes due to a varying geomagnetic field viewed in the SF.

The ACS deadband limits were set to 15, 4 and 4 mrad for roll, pitch and yaw, i.e. the limits were relaxed compared to the respective default values for GFO, which are 2.5 mrad, 250 µrad, and 250 µrad, cf. Sec. 2.3.1. That is, attitude thruster control is activated when one
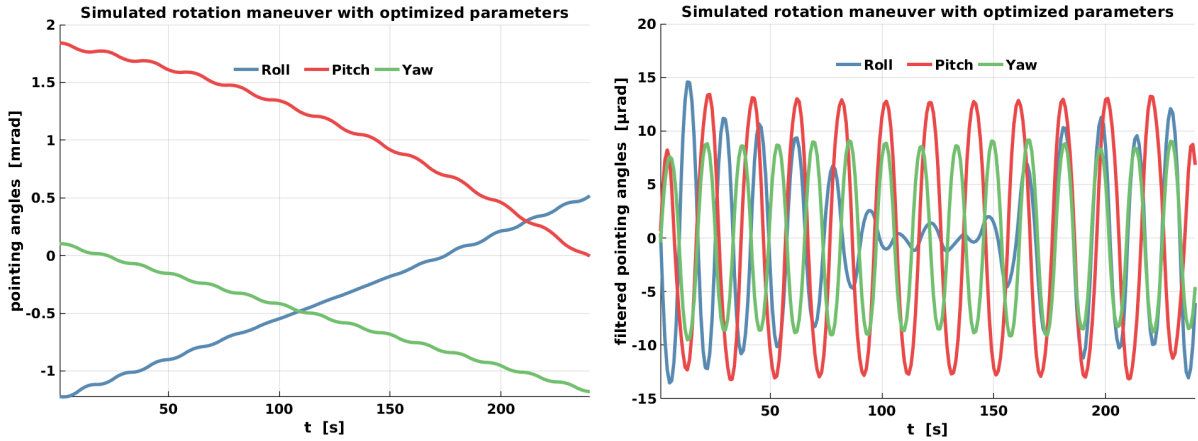
Figure 4.22: Pointing angles during a simulated optimized LRI TTL calibration maneuver. Left: unfiltered angles. Right: filtered angles.

of the pointing angles reaches the respective deadband limit. More precisely, each thruster is commanded to fire if and only if i) the absolute value of the pointing angle is above the deadband limit and ii) the derivative of the absolute value of the pointing angle is positive. This is a much simplified version of the GFO system, however, for the amount of torque produced by each thruster, the exact values from the GFO thrusters were adopted as provided in [Wen+19].

As described earlier, given a fixed MDM profile, one can obtain a good prediction of the STDs of the TTL coupling factors along a given satellite orbit. From a quick assessment of such predictions, the locations were chosen such that the expression

$$\sqrt{\sum_{i=\text{roll, pitch, yaw}} \sigma\left(\hat{\lambda}_i\right)^2}, \tag{4.88}$$

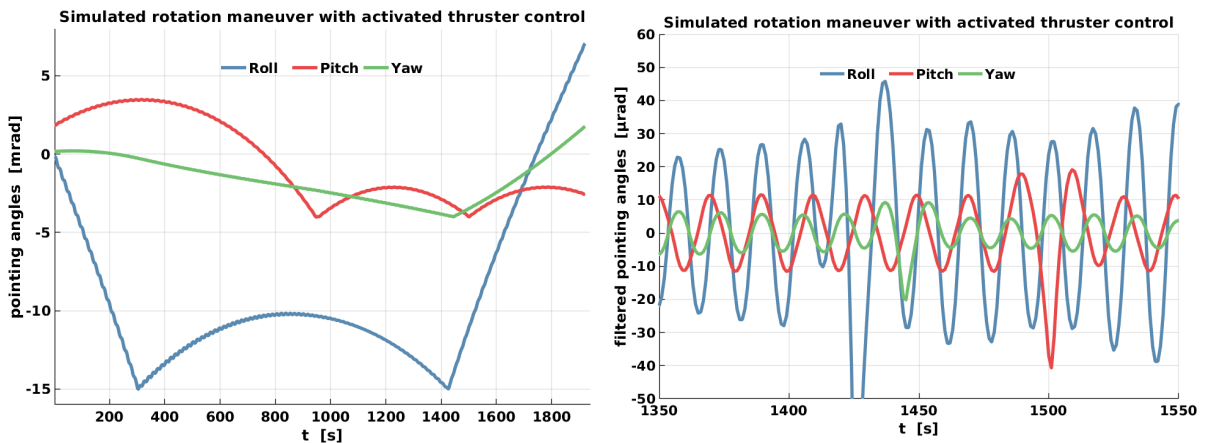i.e. the RMS of the STDs of the three coupling factors, is minimal.

Figure 4.23: Pointing angles during a simulated rotation maneuver with activated attitude thruster control. Left: unfiltered angles. Right: filtered angles (x axis zoomed in).

Figure 4.23 shows the pointing angles that were obtained from this simulation. The left plot shows the unfiltered pointing angles during the entire GF1 maneuver, where the thruster activations are visible. The right plot shows the filtered pointing angles, which were afterwards used for determining the CF STDs. For illustration purposes, the x axis of this plot was

Table 4.2: Summary table of different maneuver simulation test cases. Here K is the number of maneuvers that are needed to achieve the given uncertainties.

case	T [s]	f_m [mHz]	K [ ]	$\sigma(\hat{\lambda})$ (roll, pitch, yaw) [μm rad^{-1}] GF1	GF2
I CMC	180	83.$\bar{3}$	14	(0.7, 3.2, 4.8)	(0.7, 3.1, 4.5)
II optimized MDM	180	83.$\bar{3}$	14	(0.8, 2.1, 3.8)	(0.8, 2.3, 4.3)
III optimized all parameters	240	50	14	(0.3,0.9,1.8)	(0.3,1.0,2.0)
IV with thruster control	1940	50	2	(0.2, 0.7, 2.3)	(0.2, 0.7, 2.6)

restricted to a region where thruster firings in all three axes occurred. If there were no more disturbances caused by thruster firings other than those visible in the plot, the entire time series could likely be used for the coupling factor estimation. However, in the real GFO mission, attitude thruster firings cause undesired linear accelerations of the S/C, which are measured by the LRI and can thus disturb the parameter estimation. These disturbances can either be modeled and subtracted or simply cut out. The thruster modeling is described in detail in App. E.1.

If the entire time series could be used for parameter estimation, the resulting STDs of the LSQ estimator for GF1 are 0.2, 0.7, 2.3 μm rad^{-1}. Note that these uncertainties are even below those reached with 7 combined CMC maneuvers per S/C, cf. Tab. 4.2. Here only about 30 minutes of operation time are used per S/C. Both maneuvers together could be executed within less than 2 hours, instead of more than one day as is necessary for 14 CMC maneuvers. The case presented here is thus a very time efficient type of calibration maneuver.

Note that the author did not simulate maneuvers using only thrusters, i.e. without utilizing MTRs. If a satellite is not in the vicinity of the Earth, there may be no significant ambient magnetic field, such that MTRs cannot be used. For instance, this is the case in the planned LISA mission, which will likely also require rotation maneuvers for the purpose of TTL calibration. If maneuvers shall be simulated for such a mission, the general simulation technique presented in this chapter can still be used. If attitude control mechanisms other than thrusters shall be implemented, their control effect has to be formulated in terms of either torques or angular accelerations in the SF, and can then easily be implemented within the simulation framework.

4.4.5 Summary of maneuver simulations

Table 4.2 summarizes the different simulation cases that were presented in this section, showing the theoretical STDs of the coupling factors estimated using the pointing angles during the respective maneuvers. One insight from this comparison is that optimizing the MDM profile (case II) does already slightly improve the estimation accuracy, compared to the original CMC (case I). Recall that the CMC maneuvers are not optimized for LRI TTL analysis. The main improvement could be achieved by choosing a lower maneuver frequency f_m (case III). Here the longer duration of 240 as opposed to 180 seconds merely contributes a factor of about $\sqrt{240/180} \approx 1.15$.

Another interesting option is to let the attitude thruster control be active during the maneuver (case IV), which allows for a longer maneuver duration. The simulation results suggest that two such maneuvers are sufficient to reach a similar estimation accuracy as in the "optimal" case (III) with 14 maneuvers. Note that the entire procedure in case IV can be executed within a few hours, whereas each of the other cases with 14 maneuvers takes almost two days to complete. However, such maneuvers with activated thruster control are not intended in the GFO mission. Should such maneuvers be considered for future missions, further investigations would be due, concerning their feasibility as well as possible disturbances that the thruster firings may impose on the science instruments. A further potential option,

which is not investigated here, would be to program the ACS in such a way that it performs periodic attitude variations, while still maintaining the S/C pointing within an acceptable margin.

In the following, in Chap. 5, all aspects of the estimation of LRI TTL coupling factors will be illustrated, including the analysis of in-flight mission data.

Chapter 5

Estimation of in-flight LRI TTL coupling factors

This chapter is concerned with the analysis of GFO mission data, with the goal being the estimation of the LRI TTL coupling factors. Estimating the TTL coupling factors requires time series of S/C pointing angles as well as LRI range in a certain form. Section 5.1 describes the different steps of data processing which are necessary to transform the raw instrument data to the desired form. These steps include the derivation of pointing angles from so-called Level-1 data, resampling, filtering, and the mitigation of disturbing signals such as those caused by attitude thruster firings.

In Sec. 5.2, the different methods of parameter estimation are presented that are used for the estimation of LRI TTL coupling factors within this thesis. The theoretical background of each method is described, and a derivation of the respective CF estimators is given. Each method has its strengths and weaknesses, which are compared in the end of the section.

In Sec. 5.3, results from the individual estimation methods and their performance are evaluated. The final product, i.e. one set of LRI TTL coupling factors, is derived by combining the results from different methods. Two versions of such a set are defined, one with and one without considering angular rate coupling (ARC). Moreover, the results for the S/C CoM offsets, which can be derived from the coupling factors, are presented. Finally, the results are interpreted with view of their accuracy, and whether the pre-flight assumptions and requirements have been met.

When the TTL coupling factors are estimated, a time series of the TTL error can be computed and subtracted from the LRI range, in order to show that the instrument noise can be reduced in this way. Since the TTL error of the LRI is small, it is not trivial to demonstrate the positive effect of this subtraction. Some attempts to make this effect visible is described in Sec. 5.4.

5.1 Data processing

This section discusses the steps of data processing which have to be performed prior to the parameter estimation. A number of utility functions such as for time conversion are necessary, but will not be discussed here. Figure 5.1 shows a structural overview of the code that was used for data processing and parameter estimation within this thesis. All data processing and analysis was implemented using the Matlab software. Details of the most important individual processing steps will be discussed thoroughly in this section.

Sec. 5.1.1 lists all the GFO Level-1 data products which were used within the scope of this thesis. In Secs. 5.1.2 and 5.1.3, the data processing related to the LRI range and the pointing angles, respectively, is summarized. A special focus lies on the disturbances caused
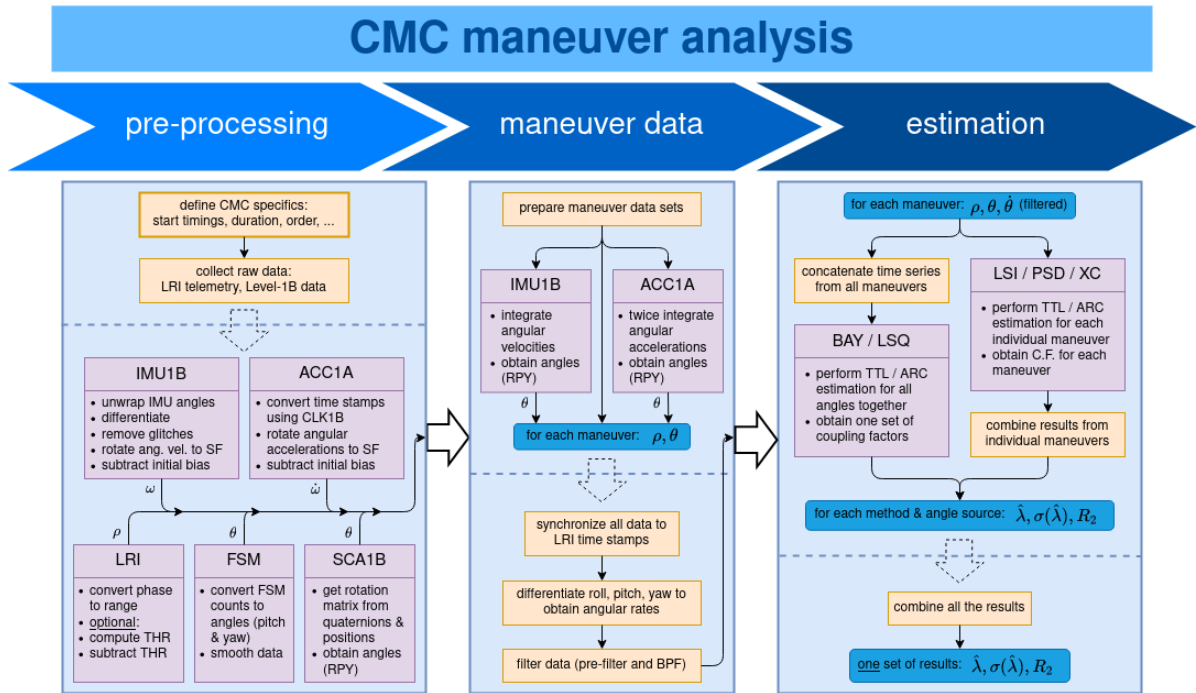
Figure 5.1: Code architecture for the analysis of TTL calibration maneuvers.

by the activations of attitude control thrusters, treated in Sec. 5.1.4. Resampling is discussed in Sec. 5.1.5, and data filtering is discussed in Sec. 5.1.6.

5.1.1   GRACE Follow-On Level-1 data products

For the LRI range, the entire processing from raw telemetry to the biased range was done within the AEI Hannover, cf. Sec. 5.1.2 below. The same is true for the FSM pitch and yaw angles. Apart from that, exclusively the official Level-1 instrument data was used, i.e. Level-1A and 1B data (release RL04), which is provided by the GFO Science Data System (SDS). All data products that were used at any stage during this study are listed below. For a detailed description of each product, the reader is referred to [Wen+19].

- GNV1B: contains S/C positions and velocities given in the ECEF frame.

- SCA1B: contains S/C attitude quaternions, derived from SCA and IMU data using a Kalman filter.

- MAG1B: contains magnetic torquer input currents, as well as measurements of the Earth's magnetic field.

- IMU1B: contains integrated angles from gyroscope measurements.

- ACC1A: contains linear and angular nongravitational accelerations measured by the accelerometer.

- CLK1B: contains timing information, which is used to convert time stamps between Level-1A and 1B data.

- ACT1A: contains linear nongravitational accelerations, for GF2 obtained by data transplant from the GF1 accelerometer.

- THR1B: contains times and durations of activations for all the attitude control thrusters.

- MAS1B: contains a time series of the mass of each S/C.

- KBR1B: contains the biased inter-satellite range derived from KBR measurements.

- IMU1A: contains integrated angles from gyroscope measurements.

Concerning the SCA data, during the analysis presented here, there seemed to be a mismatch of approximately 1 second between the time stamps of the pointing angles derived from SCA1B RL04 data on the one hand, and any of the other main attitude sensor data on the other hand. This observation was already reported in [Weg+20b]. Therefore, 1 second was subtracted from the time stamps of the SCA1B RL04 data, before the TTL estimation.

5.1.2 LRI range

The LRI telemetry data contains the raw beatnote phase measured in cycles. The downlinked data is sampled at 9.664000 Hz for GF1 and 9.664198 Hz for GF2. The phase contains occasional unintended jumps which are correlated to attitude control thruster activations. The jumps are removed and thus do not influence the performance of the LRI [Abi+19]. The time tags of the ranging data have to be corrected for clock errors and additionally for a delay due to onboard decimation filtering [Mis19]. The phase measured on the transponder S/C is subtracted from the master phase, after jumps have been removed from both measurements, and after the two data streams have been synchronized so that they refer to the same time stamps. Subsequently, the combined phase is converted from cycles to biased range in meters.

In the low frequencies, the inter-satellite distance is dominated by the gravity signal, which rapidly drops off above about 37-38 mHz [Abi+19; Mül17]. Therefore, the ASD of the measured range has values from several $\mathrm{m}/\sqrt{\mathrm{Hz}}$ in the low frequencies, down to values below 1 $\mathrm{nm}/\sqrt{\mathrm{Hz}}$ at high frequencies, see e.g. Fig. 3.13. Regarding the time domain, the inter-satellite distance may vary by more than a kilometer within the period of one orbit. On the other hand, the oscillations in the LRI range caused by TTL during the CMC maneuvers have amplitudes of the order of nanometers.

In order to remove the dominating gravity signal from the LRI range, three options may be identified, see also Sec. 3.3. One might use the so-called pre-fit residuals of the range, which can be obtained by removing the known parts of the range, i.e. the static gravity field, the contributions from nongravitational accelerations measured by the accelerometers, and potentially other contributions which can be modeled. A second option is to use the so-called post-fit residuals, which is the residual of the range posterior to the process of gravity field recovery. When estimating TTL coupling factors using rotation maneuvers, the components of the range corresponding to Fourier frequencies away from the maneuver frequency are neglected. This enables a third option for removing the dominating part of the range, i.e. using a highpass or bandpass filter. For the maneuver analysis, a combination of different filters is applied, which are described in Sec. 5.1.6.

5.1.3 Inter-satellite pointing angles

First, the pointing angles are computed according to Sec. 2.2. Afterwards, the pointing angles are resampled to match the time stamps used for the LRI range. The resampling is realized by interpolating the angles to the time stamps given from the LRI data, cf. Sec. 5.1.5. Afterwards, a specifically designed digital filter is applied to the pointing angles, in order to isolate the desired variations at the maneuver frequency from the other frequency components. Here it is important that the exact same filter that is used for the range must be used. This filter is described in Sec. 5.1.6 further below.

5.1.4　Thruster disturbances

During the CMC maneuvers, attitude control thrusters are deactivated on the S/C which is performing the maneuver, since this would disturb the desired angular acceleration profile. However, they can occur on the other S/C. This constitutes no problem concerning the original purpose of the CMC maneuvers, which is the CoM calibration with ACC data, since the measurements of one accelerometer are independent of the distant S/C. For the purpose of estimating LRI TTL, the situation is different, because the thruster firings cause disturbances in the LRI range. There exist two options to cope with this effect. Firstly, the affected data segment can simply be excluded from the TTL analysis. A second option is to remove the variations caused by thruster firings from the LRI range. To this end, the author has derived a model of this effect from data segments without maneuvers. This was done by using thruster activation times and durations provided in the THR1B data product. This procedure is described in App. E.1.

Figure 5.2 illustrates an example of a thruster disturbance that was modeled and subtracted from the LRI range, for a yaw GF2 thruster event during a pitch GF1 CMC maneuver performed on 26 August 2019. Without using these thruster models, simply removing the affected parts before the parameter estimation, about 84 % of the CMC maneuver data could be used, considering all data from the years 2018 and 2019. With the thruster responses removed in the way described above, about 90 % of the maneuver data could be used for TTL estimation. The remaining 10 % could not be used mainly due to thruster activations that occurred just before or after a maneuver period. In theory, the STD of an estimated coupling factor is proportional to $1/\sqrt{T}$, where T is the total length of the time series which is used for the estimation. In this sense, using the thruster models yields an improvement of about 3.5 % in estimation accuracy. Considering that imperfect thruster models may also introduce errors to the TTL CF estimation, it was decided to choose the option of excluding data segments affected by thruster firings.
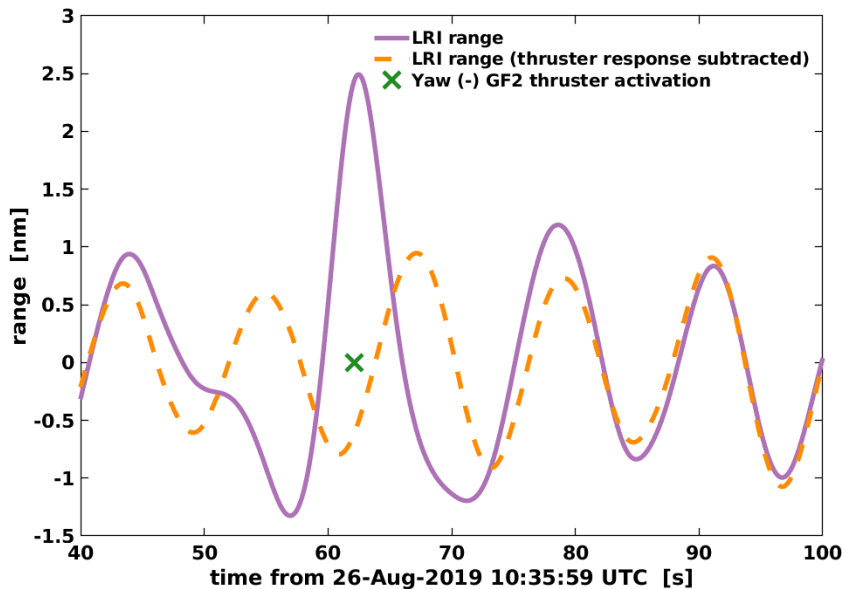

Figure 5.2: Bandpass filtered LRI range during a pitch GF1 maneuver in August 2019. Removing the disturbances due to thruster firings allows to use the full shown time series for TTL estimation.

5.1.5 Resampling

The resampling is realized by interpolation using the piecewise cubic hermite interpolating polynomial (PCHIP) method. That is, the interpolation function is composed of piecewise cubic polynomials. Between each two data points, one cubic function must be computed. Such a cubic has 4 degrees of freedom and is thus uniquely determined by the two data points and two more conditions, which can be chosen as desired. A common choice is to require two adjacent cubics to have identical first and second derivatives at the data points, which yields the famous spline method. The resulting interpolation function has then continuous first and second derivatives. In particular, it has a continuous curvature, which is advantageous for some applications.

In the case of the analysis presented in this thesis, the smoothness of the interpolation function is not as important, so merely a continuous first derivative is required. Instead of using splines, the author opted for a Matlab implementation of the PCHIP interpolation method that preserves the shape of the data. In this method, the two additional degrees of freedom for each cubic are used up by requiring a specific value for the first derivative at each data point. These values are determined to be a weighted harmonic mean of two difference quotients to the adjacent data points. The advantage of this method is that it is monotone in the sense that interpolated values between two given points are between the values of these two points, i.e. it preserves the shape and does not overshoot the data. If the given data has a local extremum, the interpolation function will have a local extremum at that point as well. Thus, the requirement of a continuous second derivative is given up for the sake of monotonicity and preventing overshoot.

5.1.6 Data filtering

For the analysis of S/C rotation maneuvers for TTL calibration, one is interested in a specific frequency. In the case of CMC maneuvers, the maneuver frequency is $83.\bar{3}$ mHz. The way these maneuvers are designed, both inter-satellite range and pointing angles contain a sinusoidal signal with this frequency. In order to extract this signal of interest, the data must be filtered in a way that leaves the maneuver frequency untouched and suppresses other frequencies as good as possible.

At this point, it is important to note that the ASD of the inter-satellite range has values of a few nm/$\sqrt{\text{Hz}}$ at $83.\bar{3}$ mHz, whereas the values at lower frequencies go up to several m/$\sqrt{\text{Hz}}$. A typical ASD of the LRI range is shown for instance in Fig. 5.12 further below. Under these circumstances, designing a filter that suppresses such a large signal, while maintaining the maneuver signal, turned out not to be trivial. In fact, the LRI data showed undesired artifacts when a highpass filter of an order larger than 3 was directly applied to it. Instead, the author analyzed different combinations of cascaded filters and, with some trial and error, settled on the following.

In order to remove a major part of the gravity signal from the LRI range, an order 3 Butterworth highpass filter with a cutoff frequency of 30 mHz was applied. Secondly, a Butterworth highpass filter of order 5 was used, with cutoff frequency 40 mHz, as well as an order 4 Butterworth lowpass filter with a cutoff frequency of 175 mHz, in order to isolate the maneuver signal. This way, the amplitude of the maneuver signal is left almost unchanged, while the undesired part of the data is suppressed. More precisely, the magnitude response is maximal at the maneuver frequency of $83.\bar{3}$ mHz, with a value of about 0.995, or -0.047 dB. The magnitude responses of the individual filters, as well as the cascaded filter, are depicted in Fig. 5.3.

Butterworth type filters were chosen, since their magnitude response is monotonic and designed to be as flat as possible in the passband. Note that the maneuver analysis is done in retrospect, i.e. when the entire time series of the range and pointing angles are available. This allows for zero-phase digital filtering, for which the author used the Matlab *filtfilt* function.
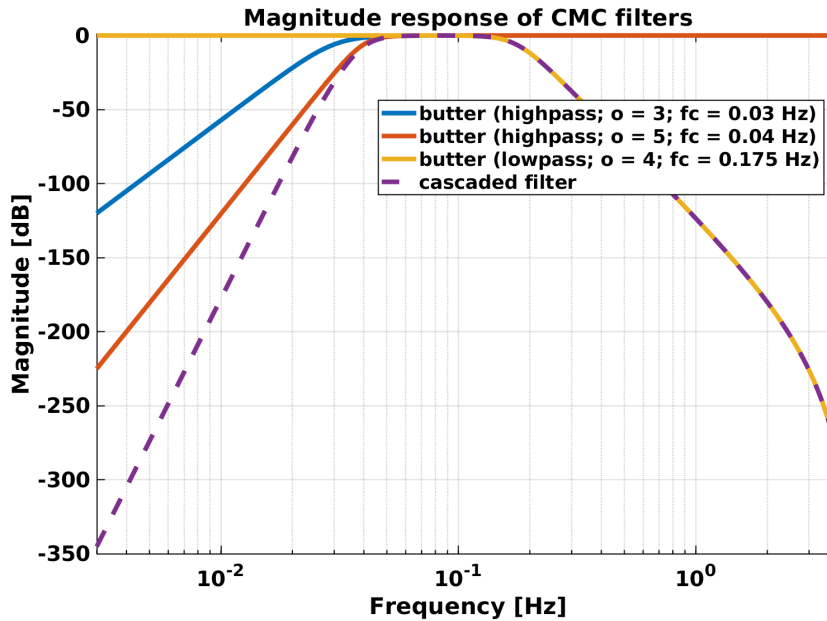
Figure 5.3: Magnitude response function of bandpass filter designed for CMC maneuver data analysis.

That is, each filter is applied two times, forward and reverse, which cancels the phase delay of the filter. This practice negates the property of Butterworth filters to have nonlinear phase response, which would be undesired under other circumstances. Finally, note that the zero-phase filtering has the effect that the magnitude response of each filter is squared, since the same filter is applied twice. The responses shown in Fig. 5.3 are already the final (squared) responses.

Since it is impossible to design a perfect filter, the magnitude response at the maneuver frequency will not be exactly 1, and thus the filter will lower the amplitude of the maneuver signal by some factor < 1. This does not constitute a problem, unless this factor is different for the angles than for the range. The latter case would manipulate the relation between the angle stimulus and the corresponding TTL error in the range, i.e. the coupling factor. Thus, it is important that the same filter is applied to all the involved time series.

5.2   Parameter estimation methods

Here the different methods that were used for estimating the LRI TTL coupling factors are presented. For each method, a formula for the coupling factor estimator will be derived, i.e. the function which assigns a given set of data the respective estimate. Throughout this section, the pointing angles, as well as the LRI range, will be assumed to be already bandpass filtered in the way described previously in Sec. 5.1.6. Although the results, see Sec. 5.3, were all obtained using data from CMC maneuvers, most of the methods shown here can be used in other cases as well, e.g. fit of noise or when using post-fit residuals, either directly or with slight adjustments of the noise models or the filter.

Five different methods will be covered in this section:

1. Sec. 5.2.2 LSQ: Least squares estimation of a collective set of coupling factors

2. Sec. 5.2.3 LSI: Least squares estimation of individual coupling factors

3. Sec. 5.2.4 XC: Estimation using cross-correlation analysis

4. Sec. 5.2.5 BAY: Estimation method based on Bayes' theorem

5. Sec. 5.2.6 PSD: Method using amplitude spectrum analysis

The BAY method yields multiple different estimators, depending on what assumptions are made about the data. The strengths and weaknesses of each of these methods are discussed in Sec. 5.2.7. At first, the mathematical notation and assumptions will be discussed.

5.2.1 Notation and assumptions

The following notation will be used. Let $\rho \in \mathbb{R}^{N \times 1}$ denote the true range, and let $\theta = (\theta^1, \ldots, \theta^M) \in \mathbb{R}^{N \times M}$ denote the true (error-free) pointing angles. Here N is the number of data points, and M is the number of considered angles. E.g., one can consider only one angle at a time ($M = 1$), or roll, pitch, yaw of one S/C ($M = 3$), or all six angles from both S/C ($M = 6$). Further, denote by $\lambda = (\lambda^1, \ldots, \lambda^M)^T$ the respective TTL coupling factors, and denote by $\hat{\lambda} \in \mathbb{R}^{M \times 1}$ the estimate of λ. Bars over the variables shall indicate the measured quantity, i.e. $\bar{\theta}$ denotes the measured pointing angles and $\bar{\rho}$ denotes the range measured by the LRI.

The quantities θ, ρ, etc., can also be viewed as random variables, which will be done in particular in the section on the estimation based on Bayes' theorem, Sec. 5.2.5. Then for example, $\bar{\rho}_i = \bar{\rho}(t_i)$, $i \in \{1, \ldots, N\}$, denotes the ith realization of the random variable $\bar{\rho}$, i.e. the measurement at time t_i. Similarly, $\bar{\theta}_i^j = \bar{\theta}^j(t_i)$, for $i \in \{1, \ldots, N\}$ and $j \in \{1, \ldots, M\}$, denotes the measured angle j at time t_i, and so on.

As mentioned earlier, it is assumed that all measured time series are already bandpass filtered at this stage. Thus, the measured range can be assumed to be free of gravity signal and dominated by the noise which is present within the pass band, or, during a maneuver, by the TTL signal. Denoting by $n_\theta \in \mathbb{R}^{N \times M}$ and $n_\rho \in \mathbb{R}^{N \times 1}$ the measurement noise of pointing angles and range, respectively, it is thereby assumed that

$$\bar{\theta} = \theta + n_\theta \tag{5.1}$$

$$\bar{\rho} = \text{TTL} + n_\rho, \tag{5.2}$$

where

$$\text{TTL} = \theta \cdot \lambda \tag{5.3}$$

is of size $N \times 1$. I.e. it is assumed, for the sake of simplicity, that the true range equals the TTL, and all other parts of the range are considered noise.

The measurement noise can in reality neither be assumed to be white nor to be Gaussian. Both will, however, be assumed as an approximation here, in order to simplify the computations. Gaussian noise is known to be a very good approximation in many cases, which is due to the central limit theorem, which states that the sum of arbitrary independently distributed random variables tends to attain a normal (Gaussian) distribution, if more and more random variables are added. Assume that the values $n_\rho(t_i)$ at the times $t_i, i = 1, \ldots, N$, shall be independent and identically (i.i.d.) distributed, so that $n_\rho(t_i)$ and $n_\rho(t_j)$ are independent for $i \neq j$. The same is assumed for the values $n_\theta^j(t_i)$, for each $j \in \{1, \ldots, M\}$. The distribution of n_ρ is assumed to be Gaussian with zero mean and variance σ_ρ^2, written in short as

$$n_\rho \sim \mathcal{N}(0, \sigma_\rho^2). \tag{5.4}$$

In general, assume that the measurement noise of the angles is M-variate normally distributed with zero mean, i.e.

$$n_\theta \sim \mathcal{N}_M(0, \Sigma_\theta), \tag{5.5}$$

with the angle noise covariance matrix $\Sigma_\theta \in \mathbb{R}^{M \times M}$. Unless stated otherwise, the assumption on n_θ is even strengthened further by requiring

$$\Sigma_\theta = \mathrm{diag}(\sigma_{\theta^1}^2, \ldots, \sigma_{\theta^M}^2) \tag{5.6}$$

i.e. that the noise distributions of the different angles are mutually independent and thus the time series are uncorrelated. This assumption is a simplification, however, to determine the off-diagonal elements is not trivial. If these are not known with sufficient accuracy, including them does not improve the model. Thus, for now Σ_θ is assumed to be a diagonal matrix. For the analysis presented here, the exact distribution of n_θ is only relevant within the Bayesian estimation method. It is further presumed that n_θ and n_ρ are independent of each other.

The whiteness of the measurement noise, which is implied by the i.i.d. condition, is merely assumed in order to simplify the computations. However, the noise variances that should be used for this approximation do depend on the filter that was applied to the data. The values of Σ_θ moreover depend on the attitude sensor which was used to derive the pointing angles. For the results presented in this thesis, the data is assumed to be filtered according to Sec. 5.1.6, and the variances were derived from the ASDs of the measured pointing angles, which can be viewed in Sec. 2.2.1. The numbers are summarized in Tab. 5.1 in terms of the STDs σ_ρ and σ_θ. Here the value for SCA refers not to the fused SCA1B data, but to pointing angles derived from star camera data only. The value given for IMU refers to IMU1A, IMU1B or SCA1B data, since SCA1B data has been fused with IMU data and is assumed to attain the IMU noise level at high frequencies.

Table 5.1: Assumptions on the measurement noise STD of filtered LRI range and pointing angles.

Variable	Sensor	Value
σ_ρ	LRI	0.5 nm
σ_θ	SCA (roll, pitch, yaw)	20 µrad
σ_θ	IMU (roll, pitch, yaw)	1 µrad
σ_θ	ACC (roll, pitch, yaw)	0.1 µrad
σ_θ	FSM (pitch)	1 µrad
σ_θ	FSM (yaw)	2 µrad

In the following, some estimation methods are described, commencing with the least squares approach.

5.2.2   Least squares (collective)

The method described here is denoted by least squares (LSQ) collective, which is meant to indicate that the least squares estimation is applied considering all relevant pointing angles at the same time, i.e. $M > 1$, and hence estimating all M coupling factors at the same time.

With the filtered pointing angles $\bar{\theta} \in \mathbb{R}^{N \times M}$ and the filtered range $\bar{\rho} \in \mathbb{R}^{N \times 1}$, and with the assumption (5.2), the approach of the least squares estimation is to minimize the residual $\bar{\rho} - \bar{\theta}\lambda$ in the least squares sense w.r.t. λ. I.e., the goal is to minimize

$$\sum_i \left(\bar{\rho}(t_i) - \bar{\theta}(t_i)\lambda \right)^2 = (\bar{\rho} - \bar{\theta}\lambda)^T (\bar{\rho} - \bar{\theta}\lambda) \tag{5.7}$$

$$= \bar{\rho}^T \bar{\rho} - 2\lambda^T \bar{\theta}^T \bar{\rho} + \lambda^T \bar{\theta}^T \bar{\theta}\lambda. \tag{5.8}$$

This expression can be minimized by calculating the derivative w.r.t. λ,

$$\frac{\partial}{\partial \lambda} \left(\bar{\rho}^T \bar{\rho} - 2\lambda^T \bar{\theta}^T \bar{\rho} + \lambda^T \bar{\theta}^T \bar{\theta}\lambda \right) = -2\bar{\theta}^T \bar{\rho} + 2\bar{\theta}^T \bar{\theta}\lambda, \tag{5.9}$$

and equating it with the zero vector. Hence, the least squares estimator is defined as

$$\hat{\lambda}_{\text{LSQ}}\left(\bar{\theta}, \bar{\rho}\right) = \left(\bar{\theta}^T \bar{\theta}\right)^{-1} \bar{\theta}^T \bar{\rho}, \tag{5.10}$$

where the subscript LSQ was introduced to indicate the collective least squares method. This is indeed a minimum of Eq. (5.7), since the matrix $\bar{\theta}^T \bar{\theta}$ is positive definite and thus also the Hessian matrix, unless one of the angle time series is identically zero. For some theoretical background, see e.g. [CJ04].

The covariance matrix of $\hat{\lambda}_{\text{LSQ}}$ is given by

$$\text{cov}\left(\hat{\lambda}_{\text{LSQ}}\right) = \sigma_\rho^2 \left(\bar{\theta}^T \bar{\theta}\right)^{-1}. \tag{5.11}$$

Hence, the theoretical formula for the STD of this estimator is computed as

$$\sigma\left(\hat{\lambda}_{\text{LSQ}}\right) = \text{diag}\left(\sqrt{\left|\text{cov}\left(\hat{\lambda}_{\text{LSQ}}\right)\right|}\right) \tag{5.12}$$

$$= \text{diag}\left(\sqrt{\left|\sigma_\rho^2 \left(\bar{\theta}^T \bar{\theta}\right)^{-1}\right|}\right). \tag{5.13}$$

Note that the measurement noise of θ is entirely neglected with this method. Note further that, since n_ρ is assumed to be normally distributed, the least squares estimator is equivalent to the maximum likelihood estimator.

5.2.3 Least squares (individual)

LSI abbreviates the method of estimating each of the considered angles individually, using least squares, and afterwards combine the results to get an estimate of the set of considered coupling factors. This idea is based on the fact that each individual CMC maneuver excites mainly one specific pointing angle, while the other angles have a low or negligible amplitude at the maneuver frequency. During the yaw maneuvers, the roll angle is excited as well, but the roll coupling is small compared to the yaw coupling, so that the TTL error during the maneuvers is still dominantly caused by the yaw angle.

For each maneuver, the respective pointing angle is fitted to the range using linear least squares. The LSQ formula, Eq. (5.10), holds also in the case where $\bar{\theta}$ denotes only one pointing angle. Here $\bar{\theta}$ is interpreted as a time series of size $N \times 1$. Thus, each estimation is following the same process as with the LSQ method, except the estimand is one CF. Since usually two CMC maneuvers are performed per angle, one thus obtains two estimates for each angle. Finally, the estimate $\hat{\lambda}_{\text{LSI}} \in \mathbb{R}^{M \times 1}$ is obtained by taking the mean of the two individual estimates for each of the considered angles.

5.2.4 Cross-correlation estimation

As in the LSI approach, here one angle at a time is considered. This requires for the TTL error to be caused almost exclusively by the excitation of one pointing angle. At first, the cross-correlation of the range with this angle, say $\bar{\theta}$, is computed. With the notation given above, the nonnormalized cross-correlation of $\bar{\theta}$ and $\bar{\rho}$ is defined as

$$\chi(\bar{\theta}, \bar{\rho})(m) = \begin{cases} \sum\limits_{k=1}^{N-m} \bar{\theta}(t_{k+m}) \cdot \bar{\rho}(t_k), & m \geq 0 \\ \chi(\bar{\rho}, \bar{\theta})(-m), & m < 0 \end{cases} \tag{5.14}$$

for $m = -(N-1), \ldots, (N-1)$.

After computing $\chi(\bar{\theta}, \bar{\rho})$, the cross-correlation $\chi_{\max}$ with maximal absolute value is determined. For the results presented in this thesis, the search was restricted to a maximal time shift of 2.5 seconds, which means $|m| \leq \text{fs} \cdot 2.5 \text{ s}$, where fs is the sampling frequency of the time series. The estimated CF $\hat{\lambda}$ is then computed by

$$\hat{\lambda} = \frac{\chi_{\max}}{\sum_i \bar{\theta}(t_i)^2}, \tag{5.15}$$

where $\bar{\theta}(t_i)$ denotes the pointing angle measured at time t_i, and the sum is taken over all values recorded during the maneuver. The estimated time shift δt between the two time series is a byproduct of this method and is calculated as

$$\delta t = \frac{m_{\max}}{\text{fs}} \tag{5.16}$$

where $m_{\max}$ is the value of m for which $\chi(\bar{\theta}, \bar{\rho})(m)$ attains its maximal absolute value, i.e.

$$\chi(\bar{\theta}, \bar{\rho})(m_{\max}) = \chi_{\max}. \tag{5.17}$$

If $m_{\max} \neq 0$, a possible explanation is that the time stamps of at least one of the time series could be incorrect. Under this hypothesis, one obtains an estimate of the relative time shift between the two time series. The sign of δt is to be interpreted as follows. If for example $m_{\max} > 0$, i.e. $\delta t > 0$, the correlation between $\bar{\theta}$ and $\bar{\rho}$ is maximal if the time stamps of $\bar{\theta}$ are reduced w.r.t. $\bar{\rho}$ by δt, i.e. the reported time stamps in the $\bar{\theta}$ data are too large.

So far, the estimated CF and time shift obtained in this way can only assume certain discrete values, which are determined by the sampling rate. A more precise estimate can be obtained by interpolating $\chi(\bar{\theta}, \bar{\rho})$ in a small neighborhood around $m_{\max}$, and searching once more for the maximum. Here the property of the piecewise cubic hermite interpolating polynomial (PCHIP) method not to overshoot is not desired, so a different interpolation method should be chosen. Again, as with the LSI method, the final estimate $\hat{\lambda}_{\text{XC}}$ is determined by taking the mean of the individual estimates.

5.2.5   Bayesian estimation

The Bayesian approach can be sketched as follows. For the theoretical background, see e.g. [Koc07] or [Koc99]. As usual, $\lambda = (\lambda_1, \ldots, \lambda_M)^T$ denotes the TTL CFs, with M being the number of angles to be considered. One is interested in the probability density function (PDF) of λ, given all the data that are available, i.e. the processed LRI range and the pointing angles. Bayes' theorem for random variables A, B reads

$$P(A|B) = \frac{P(B|A)P(A)}{P(B)}. \tag{5.18}$$

Here P denotes the PDF. Now, by Bayes' theorem, with $A = \lambda$ and $B = \text{data}$, it follows that

$$P(\lambda|\text{data}) \propto P(\lambda) \cdot P(\text{data}|\lambda), \tag{5.19}$$

where $\propto$ means proportionality w.r.t. λ, i.e. the proportionality constant does not depend on λ. In this context, $P(\lambda)$ is called the prior of λ, and $P(\text{data}|\lambda)$ is called the likelihood of the data given λ. The desired quantity $P(\lambda|\text{data})$, called the posterior of λ, is unknown. However, the relation (5.19) allows to compute the right hand side instead of the posterior. Based on this, one can then define an estimator of λ, e.g. by maximizing this expression w.r.t. λ. This is the goal of the Bayesian estimation approach. More precisely, a Bayesian estimator is defined by choosing a loss function $L(\hat{\lambda}, \lambda)$ and then minimizing the expected loss

$$E\left[L(\hat{\lambda}, \lambda)\right] = \int_{\mathbb{R}^M} L(\hat{\lambda}, \lambda)P(\lambda|\text{data}) \, d\lambda. \tag{5.20}$$

Since it is based on the posterior density of λ, $E[L(\hat{\lambda}, \lambda)]$ is called the posterior expected loss. The purpose of the loss function L is to evaluate how good an estimate $\hat{\lambda}$ is, depending on the true value λ. L should be zero for $\hat{\lambda} = \lambda$, i.e. $L(\lambda, \lambda) = 0 \ \forall \lambda \in \mathbb{R}^M$.

A common choice for the loss function is the quadratic estimation error, i.e. $(\hat{\lambda} - \lambda)^T (\hat{\lambda} - \lambda)$, which leads (cf. [Koc07]) to the estimator

$$\hat{\lambda} = \int_{\mathbb{R}^M} \lambda \cdot P(\lambda|\text{data}) \ d\lambda, \tag{5.21}$$

i.e. the estimated value is the expected value of λ, where λ is interpreted as a random variable distributed according to the posterior density $P(\lambda|\text{data})$. Another common choice for the loss function is the absolute error, i.e. one defines $L(\hat{\lambda}^j, \lambda^j) = |\hat{\lambda}^j - \lambda^j|$ for $j = 1, \ldots, M$. It is shown in [Koc07] that each loss is minimized when the estimator $\hat{\lambda}$ is defined as the median of the posterior $P(\lambda|\text{data})$, i.e. such that the cumulative distribution function $\text{CDF}_{\lambda|\text{data}}(\hat{\lambda}) = 1/2$. A third common choice for the loss function is the so-called zero-one loss

$$L\left(\hat{\lambda}^j, \lambda^j\right) = \begin{cases} 0, & |\hat{\lambda}^j - \lambda^j| < b \\ 1, & |\hat{\lambda}^j - \lambda^j| \geq b \end{cases} \tag{5.22}$$

with some $b > 0$. One can show [Koc07] that, when letting $b \to 0$, the posterior expected loss is minimized if

$$\hat{\lambda} = \arg\max_{\lambda} P(\lambda|\text{data}). \tag{5.23}$$

That is, the estimate is obtained by maximizing the posterior. Thus, this estimator is called the maximum a posteriori (MAP) estimator. All results shown within this thesis are obtained using the MAP estimator, since it is the least complicated to implement in code.

In practice, if one wants to compute the posterior density $P(\lambda|\text{data})$ in a meaningful way, it quickly becomes clear that some additional information is needed, apart from the data. In particular, this may be information on the noise in the data. Let the collection of additional information be denoted by $\mathcal{I}$, and define

$$\mathcal{X}(\lambda) = P(\lambda|\text{ data}, \mathcal{I}) \tag{5.24}$$
$$= P\left(\lambda|\ \bar{\theta}, \bar{\rho}, \Sigma_\theta, \sigma_\rho^2\right), \tag{5.25}$$

with data $= (\bar{\theta}, \bar{\rho})$ and $\mathcal{I} = (\Sigma_\theta, \sigma_\rho^2)$. The Bayesian approach can be modified such that it considers any information that may be relevant. The goal here is to compute $\mathcal{X}(\lambda)$, for which there are several ways how to proceed in detail. Which way is used is decided by choosing models of

1. the prior $P(\lambda)$

2. the PDF of the ranging noise $P(n_\rho)$

3. the PDF of the angle noise $P(n_\theta)$

In the following, several ways of calculating the posterior are described. In the beginning, the most simple assumptions for these three choices are made, and then the sophistication is built up step by step.

Derivation without angle noise

For now, assume that the measured pointing angles are free of errors, i.e. $\bar{\theta} = \theta$. At first, it must be remarked that the equality

$$P(A, B|C) = P(A|C) \cdot P(B|A, C) \tag{5.26}$$

holds in general for random variables A, B, C. This can be seen by conditioning the equation $P(B|A) = P(A, B)/P(A)$ with C. Now, since $\bar{\theta} = \theta$, one has $\mathcal{X}(\lambda) = P(\lambda|\theta, \bar{\rho}, \sigma_\rho^2)$. For the following computations, define

$$\mathcal{Y}(\lambda) = P\left(\lambda|\theta, \bar{\rho}, \sigma_\rho^2\right), \tag{5.27}$$

the posterior in the absence of angle noise. By Bayes' theorem, one has

$$\mathcal{Y}(\lambda) = P\left(\theta, \bar{\rho}, \sigma_\rho^2|\lambda\right) \cdot \frac{P(\lambda)}{P\left(\theta, \bar{\rho}, \sigma_\rho^2\right)} \tag{5.28}$$

$$= P\left(\theta, \sigma_\rho^2|\lambda\right) \cdot P\left(\bar{\rho}|\theta, \sigma_\rho^2, \lambda\right) \cdot \frac{P(\lambda)}{P\left(\theta, \bar{\rho}, \sigma_\rho^2\right)}. \tag{5.29}$$

Here, the second equality follows from (5.26). Note that θ and σ_ρ^2 are given, and hence one has $P(\theta, \sigma_\rho^2|\lambda) = 1$. Since $P(\theta, \bar{\rho}, \sigma_\rho^2)$ is independent of λ, one obtains

$$\mathcal{Y}(\lambda) \propto P\left(\bar{\rho}|\theta, \sigma_\rho^2, \lambda\right) \cdot P(\lambda), \tag{5.30}$$

so the desired quantity is proportional to the product of the prior and the likelihood of the ranging data, given λ and the available information.

If nothing is known about the prior, one can set $P(\lambda) = 1$. Note that in that case the posterior is proportional to the likelihood. This is the simplest way to calculate the posterior. If the Bayesian MAP estimator is used, i.e. the estimate is obtained by maximizing the posterior, the Bayesian estimator in this simple case is thus equivalent to the maximum likelihood estimator. With n_ρ being Gaussian noise, it is equivalent to the LSQ estimator as well.

Derivation with angle noise

Now, assume that there is nonzero angle noise. In this case, $\mathcal{X}$ must be marginalized over θ. To this end, note that

$$P(A|C) = \int P(A, B|C) \, dB = \int P(A|B, C) \cdot P(B|C) \, dB, \tag{5.31}$$

where the first step is called marginalization over B, and the second step follows from (5.26). From (5.31), one obtains

$$\mathcal{X}(\lambda) = \int P\left(\lambda|\, \theta, \bar{\theta}, \bar{\rho}, \Sigma_\theta, \sigma_\rho^2\right) \cdot P\left(\theta|\, \bar{\theta}, \Sigma_\theta\right) \, d\theta \tag{5.32}$$

$$= \int P\left(\lambda|\, \theta, \bar{\rho}, \sigma_\rho^2\right) \cdot P\left(\theta|\, \bar{\theta}, \Sigma_\theta\right) \, d\theta \tag{5.33}$$

$$= \int P\left(\lambda|\, \theta, \bar{\rho}, \sigma_\rho^2\right) \cdot P\left(\bar{\theta}|\, \theta, \Sigma_\theta\right) \cdot \frac{P(\theta)}{P(\bar{\theta})} \, d\theta \tag{5.34}$$

$$\propto \int P\left(\lambda|\, \theta, \bar{\rho}, \sigma_\rho^2\right) \cdot P\left(\bar{\theta}|\, \theta, \Sigma_\theta\right) \cdot P(\theta) \, d\theta, \tag{5.35}$$

where $P\left(\lambda|\, \theta, \bar{\rho}, \sigma_\rho^2\right) = \mathcal{Y}(\lambda)$ has been computed above, cf. Eq. (5.30). If there is no meaningful way to determine $P(\theta)$, it can be assumed to be constant. Then,

$$\mathcal{X}(\lambda) \propto P(\lambda) \int P\left(\bar{\rho}|\, \theta, \sigma_\rho^2, \lambda\right) \cdot P(\bar{\theta}|\, \theta, \Sigma_\theta) \, d\theta. \tag{5.36}$$

Concrete formulas

In order to implement a Bayesian estimator, one must write down the concrete equations for the terms that appear in Eqs. (5.30) and (5.36). First, note that Eq. (5.36) can be used in different ways. One could think of the integral as an $(N \times M)$-dimensional integral, however, that would be impractical. Instead, define $\mathcal{X}_0(\lambda) = P(\lambda)$, and recursively

$$\mathcal{X}_i(\lambda) = \mathcal{X}_{i-1}(\lambda) \int_{\mathbb{R}^M} P\left(\bar{\rho}_i \mid \theta_i, \sigma_\rho^2, \lambda\right) \cdot P(\bar{\theta}_i \mid \theta_i, \Sigma_\theta) \, d^M \theta_i, \tag{5.37}$$

for $i = 1, \ldots, N$, where $\bar{\theta}_i = (\bar{\theta}_i^1, \ldots, \bar{\theta}_i^M) \in \mathbb{R}^{1 \times M}$ and $\bar{\rho}_i \in \mathbb{R}$ are the data measured at time t_i. The idea behind this is to first interpret Eq. (5.36) in the sense of Eq. (5.37) for $i = 1$, i.e. as the posterior after the first data point. Subsequently, this posterior is used as an updated prior. The next data point can then be viewed as an independent event, with a new posterior derived with the updated prior. Recursively, this yields another equation for the posterior density:

$$P(\lambda \mid \bar{\theta}, \bar{\rho}, \Sigma_\theta, \sigma_\rho^2) \propto \mathcal{X}_N(\lambda) \tag{5.38}$$

$$= P(\lambda) \cdot \prod_{i=1}^N \int_{\mathbb{R}^M} P\left(\bar{\rho}_i \mid \theta_i, \sigma_\rho^2, \lambda\right) \cdot P(\bar{\theta}_i \mid \theta_i, \Sigma_\theta) \, d^M \theta_i. \tag{5.39}$$

Now, the pointing angle error for one data point is described by

$$P\left(\bar{\theta}_i \mid \theta_i, \Sigma_\theta\right) \propto \exp\left[-\frac{1}{2}(\bar{\theta}_i - \theta_i)\Sigma_\theta^{-1}(\bar{\theta}_i - \theta_i)^T\right]. \tag{5.40}$$

In case Σ_θ is assumed to be diagonal, Eq. (5.40) becomes

$$P\left(\bar{\theta}_i \mid \theta_i, \Sigma_\theta\right) \propto \exp\left[-\frac{1}{2}\sum_{j=1}^M \frac{1}{\sigma_{\theta^j}^2}\left(\bar{\theta}_i^j - \theta_i^j\right)^2\right]. \tag{5.41}$$

Recalling Eqs. (5.2), (5.3), and (5.4), one has

$$\bar{\rho}_i \mid \theta_i, \sigma_\rho^2, \lambda \sim \mathcal{N}(\theta_i \lambda, \sigma_\rho^2). \tag{5.42}$$

That is,

$$P\left(\bar{\rho}_i \mid \theta_i, \sigma_\rho^2, \lambda\right) \propto \exp\left[-\frac{1}{2\sigma_\rho^2}(\bar{\rho}_i - \theta_i\lambda)^2\right]. \tag{5.43}$$

For the prior of λ, assume a normal distribution as well. Let the λ^j be independently distributed, i.e.

$$\lambda^j \sim \mathcal{N}(\tilde{\lambda}^j, \sigma_{\lambda^j}^2), \tag{5.44}$$

for each $j = 1, \ldots, M$, so that

$$P(\lambda) \propto \exp\left[-\frac{1}{2}\sum_{j=1}^M \frac{1}{\sigma_{\lambda^j}^2}\left(\lambda^j - \tilde{\lambda}^j\right)^2\right], \tag{5.45}$$

where the mean $\tilde{\lambda}^j$ and STD σ_{λ^j} describe the a priori guess of λ^j. In the case discussed here, the mean values $\tilde{\lambda}^j$ were set to zero. In case of doubt, the STD values of the prior should be chosen rather large, in order not to restrict the estimates too much. One can assign a lower value for σ_{λ^j} in case of the roll CF than for the pitch or yaw CF, if one is more confident that the roll CF is rather small. For the STDs, the values 10, 250, and 250 $\mu\text{m}\,\text{rad}^{-1}$ were assumed for the roll, pitch, and yaw CF, respectively. Below, 5 different formulas of the final CF estimator are given, named BAY1 to BAY5.

BAY1   In the simplest case, without angle noise and assuming $P(\lambda) = \text{const.}$, one has

$$P\left(\lambda \mid \theta, \bar{\rho}, \sigma_\rho^2\right) \propto \prod_{i=1}^{N} \exp\left[-\frac{1}{2\sigma_\rho^2}(\bar{\rho}_i - \theta_i \lambda)^2\right] \tag{5.46}$$

$$= \exp\left[-\frac{1}{2\sigma_\rho^2}\sum_{i=1}^{N}(\bar{\rho}_i - \theta_i \lambda)^2\right]. \tag{5.47}$$

The MAP estimator in this case is

$$\hat{\lambda}_{\text{BAY1}} = \arg\min_\lambda\left[\sum_{i=1}^{N}(\bar{\rho}_i - \theta_i \lambda)^2\right], \tag{5.48}$$

which is identical to the LSQ estimator, and also the maximum likelihood estimator, in this simple case, as mentioned above.

BAY2   Still without angle noise, but with nonconstant prior, one obtains

$$P\left(\lambda \mid \theta, \bar{\rho}, \sigma_\rho^2\right) \propto \exp\left[-\frac{1}{2}\sum_{j=1}^{M}\frac{1}{\sigma_{\lambda^j}^2}\left(\lambda^j - \tilde{\lambda}^j\right)^2\right] \cdot \prod_{i=1}^{N} \exp\left[-\frac{1}{2\sigma_\rho^2}(\bar{\rho}_i - \theta_i \lambda)^2\right] \tag{5.49}$$

$$= \exp\left[-\frac{1}{2}\sum_{j=1}^{M}\frac{1}{\sigma_{\lambda^j}^2}\left(\lambda^j - \tilde{\lambda}^j\right)^2 - \frac{1}{2\sigma_\rho^2}\sum_{i=1}^{N}(\bar{\rho}_i - \theta_i \lambda)^2\right]. \tag{5.50}$$

The MAP estimator is then given by

$$\hat{\lambda}_{\text{BAY2}} = \arg\min_\lambda\left[\sum_{j=1}^{M}\frac{1}{\sigma_{\lambda^j}^2}\left(\lambda^j - \tilde{\lambda}^j\right)^2 + \frac{1}{\sigma_\rho^2}\sum_{i=1}^{N}(\bar{\rho}_i - \theta_i \lambda)^2\right]. \tag{5.51}$$

BAY3   When including angle noise, one cannot avoid computing M-dimensional integrals. For the BAY3 estimator, assume a constant prior, $P(\lambda) = \text{const.}$ With Eq. (5.39), one obtains

$$\hat{\lambda}_{\text{BAY3}} = \arg\max_\lambda\left[\prod_{i=1}^{N}\int_{\mathbb{R}^M} \exp\left(-\frac{1}{2\sigma_\rho^2}(\bar{\rho}_i - \theta_i \lambda)^2 - \frac{1}{2}\sum_{j=1}^{M}\frac{1}{\sigma_{\theta^j}^2}\left(\bar{\theta}_i^j - \theta_i^j\right)^2\right) d^M\theta_i\right]. \tag{5.52}$$

BAY4   Including angle noise as well as a nonconstant prior, one obtains the formula for the BAY4 estimator:

$$\hat{\lambda}_{\text{BAY4}} = \arg\max_\lambda\left[\exp\left(-\frac{1}{2}\sum_{j=1}^{M}\frac{1}{\sigma_{\lambda^j}^2}\left(\lambda^j - \tilde{\lambda}^j\right)^2\right) \ldots\right.$$

$$\left. \cdot\prod_{i=1}^{N}\int_{\mathbb{R}^M} \exp\left(-\frac{1}{2\sigma_\rho^2}(\bar{\rho}_i - \theta_i \lambda)^2 - \frac{1}{2}\sum_{j=1}^{M}\frac{1}{\sigma_{\theta^j}^2}\left(\bar{\theta}_i^j - \theta_i^j\right)^2\right) d^M\theta_i\right]. \tag{5.53}$$

BAY5 As an additional option, one can derive another estimator with the following heuristic approach. Observe that Eq. (5.2) for the filtered measured range can be transformed as

$$\bar{\rho} = \text{TTL} + n_\rho \tag{5.54}$$

$$= \theta\lambda + n_\rho \tag{5.55}$$

$$= (\bar{\theta} - n_\theta)\lambda + n_\rho \tag{5.56}$$

$$= \bar{\theta}\lambda + n_{\text{new}}, \tag{5.57}$$

with $n_{\text{new}} = n_\rho - n_\theta\lambda$. In this sense, one could interpret $\bar{\theta}$ as error-free angles, and n_{new} as the ranging noise. Then, assuming Σ_θ to be diagonal, one has

$$n_{\text{new}} \sim \mathcal{N}\left(0, \sigma_{\text{new}}^2(\lambda)\right), \tag{5.58}$$

with

$$\sigma_{\text{new}}^2(\lambda) = \sigma_\rho^2 + \sum_{j=1}^{M} (\lambda^j)^2 \sigma_{\theta^j}^2. \tag{5.59}$$

The posterior PDF of λ can then be derived similar to Eqs. (5.30) and (5.51). However, note that σ_{new}^2 now depends on λ, as opposed to σ_ρ^2. Hence,

$$P(\lambda|\,\bar{\theta}, \bar{\rho}, \sigma_{\text{new}}^2) \propto P(\lambda) \cdot P\left(\bar{\rho}|\,\bar{\theta}, \sigma_{\text{new}}^2, \lambda\right) \tag{5.60}$$

$$\propto \left(\frac{1}{\sigma_{\text{new}}^2(\lambda)}\right)^{\frac{N}{2}} \exp\left[-\frac{1}{2}\sum_{j=1}^{M}\frac{1}{\sigma_{\lambda^j}^2}(\lambda^j - \tilde{\lambda}^j)^2 - \frac{1}{2\sigma_{\text{new}}^2}\sum_{i=1}^{N}(\bar{\rho}_i - \bar{\theta}_i\lambda)^2\right] \tag{5.61}$$

$$\propto \exp\left[-\frac{N}{2}\ln(\sigma_{\text{new}}^2(\lambda)) - \frac{1}{2}\sum_{j=1}^{M}\frac{1}{\sigma_{\lambda^j}^2}(\lambda^j - \tilde{\lambda}^j)^2 - \frac{1}{2\sigma_{\text{new}}^2}\sum_{i=1}^{N}(\bar{\rho}_i - \bar{\theta}_i\lambda)^2\right]. \tag{5.62}$$

For the last step, note that $a^b = (e^{\ln(a)})^b = e^{b \cdot \ln(a)}$. Since the exponential function is monotone, this yields the MAP estimator

$$\hat{\lambda}_{\text{BAY5}} = \arg\min_\lambda \left[N \cdot \ln(\sigma_{\text{new}}^2(\lambda)) + \sum_{j=1}^{M}\frac{1}{\sigma_{\lambda^j}^2}\left(\lambda^j - \tilde{\lambda}^j\right)^2 + \frac{1}{\sigma_{\text{new}}^2(\lambda)}\sum_{i=1}^{N}(\bar{\rho}_i - \bar{\theta}_i\lambda)^2\right]. \tag{5.63}$$

Note that in case $n_\theta = 0$, one has $\sigma_{\text{new}} = \sigma_\rho$ and the BAY5 formula reduces to BAY2, Eq. (5.51), or to BAY1, Eq. (5.48), in case $P(\lambda) = \text{const.}$

Confidence regions

A $1 - \alpha$ confidence region, $\alpha \in (0, 1)$, is a subset S of the parameter space Ω, such that

$$\int_S P(\lambda|\,\text{data}, \mathcal{I})\, d\lambda = 1 - \alpha \tag{5.64}$$

and

$$P(\lambda_1|\,\text{data}, \mathcal{I}) \leq P(\lambda_2|\,\text{data}, \mathcal{I}) \quad \forall \lambda_1 \notin S, \lambda_2 \in S. \tag{5.65}$$

The second condition ensures that an arbitrary region outside S cannot have a higher probability than a region of the same measure inside S. Here the parameter space is $\Omega = \mathbb{R}^M$, where M is the number of considered pointing angles. Common choices for α are 0.32, 0.05, or 0.003.

In the case where $P(\lambda_1| \text{ data}, \mathcal{I})$ is a Gaussian distribution, these values approximately yield the 1-, 2-, and 3-sigma confidence regions. E.g., if $M = 1$, $\alpha = 0.32$ then yields the confidence interval $\{\lambda : |\hat{\lambda} - \lambda| \leq \sigma(\hat{\lambda})\}$.

Recall that so far the posterior has always been computed up to a factor which does not depend on λ, say computed was $Q(\lambda) = \mathcal{I} \cdot P(\lambda| \text{ data}, \mathcal{I})$. The proportionality constant $\mathcal{I}$ must be determined, in order to obtain confidence regions. Since

$$\int_{\Omega} P(\lambda| \text{ data}, \mathcal{I}) \ d\lambda = 1, \tag{5.66}$$

the proportionality constant must be given by

$$\mathcal{I} := \int_{\Omega} Q(\lambda) \ d\lambda. \tag{5.67}$$

Hence, the probability that λ lies in a certain region $S \subset \mathbb{R}^M$ is given by

$$P(\lambda \in S) = \int_{S} P(\lambda| \text{ data}, \mathcal{I}) \ d\lambda = \frac{1}{\mathcal{I}} \int_{S} Q(\lambda) \ d\lambda. \tag{5.68}$$

The value of $\mathcal{I}$, as well as the confidence region, must usually be determined numerically, since generally the equations do not have an analytic solution.

Implementation of Bayes estimators

Above, five different BAY estimators were derived. Their implementation requires a bit more effort than is necessary for the other methods. One does not need to implement BAY1, since it is equivalent to the LSQ estimator. BAY2 is not expected to deviate a lot from BAY1 in this case. BAY3 is the same as BAY4, but without considering a prior. Thus, the author decided to implement BAY4, which is the most sophisticated and most interesting of the BAY estimators, as well as BAY5, which requires less implementation effort due to the heuristic approach, while still considering the pointing angle noise. During the implementation of the Bayesian estimation methods, one may face a few practical challenges, especially with BAY4. Therefore, some words on how one might proceed in the case of BAY4 and BAY5 is given in the following.

Recalling Eq. (5.39), the posterior PDF $P(\lambda| \bar{\theta}, \bar{\rho}, \Sigma_\theta, \sigma_\rho^2)$ can be described in the form

$$P(\lambda| \bar{\theta}, \bar{\rho}, \Sigma_\theta, \sigma_\rho^2) \propto \prod_{i=1}^{N} f_i(\lambda, \bar{\theta}, \bar{\rho}, \Sigma_\theta, \sigma_\rho^2), \tag{5.69}$$

where N is the number of data points, for suitable functions f_i. In the case of BAY4, these functions may be derived from Eq. (5.53):

$$f_i(\lambda, \bar{\theta}, \bar{\rho}, \Sigma_\theta, \sigma_\rho^2) = \exp\left(-\frac{1}{2N} \sum_{j=1}^{M} \frac{1}{\sigma_{\lambda^j}^2} \left(\lambda^j - \tilde{\lambda}^j\right)^2\right) \dots$$

$$\cdot \int_{\mathbb{R}^M} \exp\left(-\frac{1}{2\sigma_\rho^2}(\bar{\rho}_i - \theta_i \lambda)^2 - \frac{1}{2} \sum_{j=1}^{M} \frac{1}{\sigma_{\theta^j}^2} \left(\bar{\theta}_i^j - \theta_i^j\right)^2\right) \ d^M \theta_i. \tag{5.70}$$

Recall that the $\tilde{\lambda}^j$, $j = 1, \dots, M$, are the mean values of the prior distribution of the λ^j, cf. Eq. (5.44), which were set to zero here. The functions f_i can be implemented easily, however,

there are two aspects that require a bit of care. Firstly, computing the values of f_i involves solving an M-dimensional integral, where M is the number of considered angles. Since these integrals typically must be evaluated numerically, the computation time rapidly increases with M. Moreover, a single evaluation of the posterior requires calculating N of such integrals, where N is the number of data samples. Secondly, the values of the functions f_i may become very small or, depending on the units in which the input data is given, very large. Thus, the computer may not return a useful result when performing the product over $i = 1, \ldots, N$. In order to mitigate this problem, define

$$F(\lambda) := \prod_{i=1}^{N} f_i(\lambda)^{\frac{1}{N}}. \tag{5.71}$$

Here F and f_i are written as a functions of only λ, as the other parts are assumed to be known at this point. Abbreviating the posterior PDF by $P(\lambda) := P(\lambda|\ \bar{\theta}, \bar{\rho}, \Sigma_\theta, \sigma_\rho^2)$, one has

$$P(\lambda) \propto F^N(\lambda), \tag{5.72}$$

and the function F can be evaluated accurately. Since the Nth power is a monotone function, the MAP estimator is equal to

$$\hat{\lambda} = \arg\max_\lambda F(\lambda). \tag{5.73}$$

For the computation of the actual posterior PDF for many points in the parameter space, it is beneficial to define

$$\tilde{F}(\lambda) = \left(\frac{F(\lambda)}{F_{\max}}\right)^N, \tag{5.74}$$

where $F_{\max} = F(\hat{\lambda})$ is the maximum value of F, so that $P(\lambda) \propto \tilde{F}(\lambda)$ as well. Then one has $\tilde{F}(\hat{\lambda}) = 1$, as well as $\tilde{F}(\lambda) \leq 1\ \forall \lambda$. Note that the normalization in Eq. (5.74) has the effect that the values of $\tilde{F}$ become neither impractically large, nor small, at least in the vicinity of $\hat{\lambda}$. Finally, the posterior can be obtained by computing

$$\mathcal{I} = \int_{\mathbb{R}^M} \tilde{F}(\lambda)\ d\lambda, \tag{5.75}$$

and then

$$P(\lambda|\ \bar{\theta}, \bar{\rho}, \Sigma_\theta, \sigma_\rho^2) = \frac{1}{\mathcal{I}} \tilde{F}(\lambda). \tag{5.76}$$

In the case of BAY5, the situation is less complicated and the required computation time is far less than for BAY4. Note that the expression in square brackets in Eq. (5.63) is equal to $-2\ln(c \cdot P)$, for some constant c, where P denotes the posterior PDF. Define the function $G := \ln(c \cdot P)$. Then, denoting by $G_{\max}$ the maximum value of G, the proportionality

$$P \propto \exp(G - G_{\max}) =: \tilde{G} \tag{5.77}$$

holds and the function $\tilde{G}$ on the right hand side has a maximum value of 1. Using this intermediate function ensures that the computer does not run into problems with extremely large numbers. The PDF can be obtained in the usual way by dividing by the integral of $\tilde{G}$ over $\mathbb{R}^M$.

Finally, note that once the PDF, or a function monotonely related to the PDF, is implemented, the estimation can be performed very quickly by a numerical minimization or maximization. Computing the PDF values for many points, which is necessary for instance for the determination of confidence regions, requires much more computation time. For this, investing some time into the optimization of code efficiency can be worth the effort.

5.2.6   Amplitude spectrum analysis

With the approach abbreviated here by PSD, only one CF at a time can be estimated, as for the LSI and XC methods. First, the amplitude spectra (AS) of the range and the respective pointing angle are computed from the time series, denoted $\text{AS}(\bar{\rho})$ and $\text{AS}(\bar{\theta})$, respectively. Both amplitude spectra should show peaks at the maneuver frequency of $83.\bar{3}$ mHz. With f_0 being the frequency value which is closest to $83.\bar{3}$ mHz, the heights H_ρ, H_θ of the peaks are simply estimated by

$$\hat{H}_\rho = \text{AS}_\rho(f_0), \tag{5.78}$$

$$\hat{H}_\theta = \text{AS}_\theta(f_0). \tag{5.79}$$

If the time series are relatively short so that the AS does not have a good frequency resolution, one may consider to cut off a few data points from the time series in order for f_0 to be as close to $83.\bar{3}$ mHz as possible. Here the AS were computed with the Matlab software, using the LTPDA toolbox. A flattop window (HFT90D) was chosen, which has a good amplitude accuracy, cf. [HRS02]. No averaging was applied, since the frequency resolution of the AS is already relatively low due to the short duration of the maneuvers.

The magnitude of the CF is then estimated by the quotient of the peak heights:

$$|\hat{\lambda}| = \frac{\hat{H}_\rho}{\hat{H}_\theta}. \tag{5.80}$$

In the end, the sign of the CF is determined by minimizing the residual, that is

$$\text{sign}(\hat{\lambda}) = \begin{cases} 1, & \text{if } \text{AS}_{\bar{\rho}-|\hat{\lambda}|\theta}(f_0) \leq \text{AS}_{\bar{\rho}+|\hat{\lambda}|\theta}(f_0) \\ -1, & \text{otherwise} \end{cases}, \tag{5.81}$$

thus

$$\hat{\lambda}_{\text{PSD}} = \text{sign}(\hat{\lambda}) \cdot |\hat{\lambda}|. \tag{5.82}$$

The uncertainty of $\hat{H}_\rho$ and $\hat{H}_\theta$ can be determined by estimating the value that the AS would have at f_0 without the peak. This value was estimated here by the mean of the adjacent values of the AS, taking three values from each side. Other possibilities would be to analyze the models of the error terms n_ρ and n_θ, or by computing spectra of measurement time series in the absence of a maneuver. By error propagation, one can compute the uncertainty of $\hat{\lambda}_{\text{psd}}$ as

$$\delta\hat{\lambda}_{\text{psd}} = \frac{\delta\hat{H}_\rho}{\hat{H}_\theta} + \frac{\hat{H}_\rho}{\hat{H}_\theta^2} \cdot \delta\hat{H}_\theta = \frac{1}{\hat{H}_\theta}\left(\delta\hat{H}_\rho + |\hat{\lambda}| \cdot \delta\hat{H}_\theta\right). \tag{5.83}$$

Finally, note that the PSD method requires a stimulus with a periodic profile, such as from a CMC maneuver.

5.2.7   Summary of estimation methods

Table 5.2 summarizes all estimators which have been derived in this section. For each method, it is indicated in the table, whether i) a prior of λ is considered, ii) pointing angle noise is considered, iii) a posterior PDF is obtained, iv) more than one angle can be considered ($M > 1$), and v) how large the implementation effort is. Note that the methods BAY1-3 have not been used for the results presented in this thesis. For the evaluation of the actual performance of individual estimation methods, confer Sec. 5.3.5.

Table 5.2: Summarizing table of parameter estimation methods.

Method	$P(\lambda) \neq const.$	$n_\theta \neq 0$	PDF	$M > 1$	effort (1-4)	remarks
LSQ	✗	✗	✗	✓	1	-
LSI	✗	✗	✗	✗	1	-
XC	✗	✗	✗	✗	2	yields estimate of time stamp mismatch
PSD	✗	✗	✗	✗	2	independent of time stamp mismatches
BAY1	✗	✗	✓	✓	2	equivalent to LSQ
BAY2	✓	✗	✓	✓	2	(not implemented here)
BAY3	✗	✓	✓	✓	4	(not implemented here)
BAY4	✓	✓	✓	✓	4	-
BAY5	✓	✓	✓	✓	3	heuristic derivation

5.3 Results

CMC maneuvers are performed in "bundles", that is, a number of maneuvers is carried out in succession, usually over the course of two calendar days. These maneuvers can be analyzed together, since the parameters are assumed to be constant during such a short time period. The number of maneuvers per bundle is usually 7 per S/C, consisting of two maneuvers per angle - roll, pitch, yaw - and one mixed maneuver, which is exciting both the roll and the pitch angle. Typically, maneuvers are performed on both S/C, so there are in total 14 maneuvers per bundle. However, at some instances in 2020, maneuvers were carried out merely on GF1. One set of results is obtained for each such bundle. In June 2018, one "wiggle test" per angle per S/C has been performed, which are short CMC maneuvers with a duration of 24 instead of 180 seconds. In total, by the time of writing, there are 16 different sets of results for GF1, and 12 for GF2.

In the following, in Sec. 5.3.1, a first version of combined results is presented, which is derived from different methods. These results, published in [Weg+20b], were obtained before the effect of angular rate coupling (ARC) in the LRI was known, cf. Sec. 3.2.6. Therefore, a second version of combined results is presented in Sec. 5.3.2, which does account for both TTL and ARC. Afterwards, in Sec. 5.3.4 the estimation results of the CoM positions w.r.t. LRI RP will be presented as well, which are derived from the second version of combined coupling factors. In Sec. 5.3.5, the individual estimation methods are evaluated by comparing their results. Finally, the results are interpreted and conclusions are drawn in Sec. 5.3.6.

5.3.1 Combined results, version 1

The version 1 results, published in [Weg+20b], are summarized in Tabs. 5.3 and 5.4, in terms of linear TTL coupling factors (CF) with the unit $\mu m\,rad^{-1}$. The CFs are given in the form *value ± uncertainty*. The values are averages over a set of estimated values, obtained using different methods and different sources for the pointing angles. The uncertainties given here are computed as the STD of this set of estimated values, since the individual uncertainties obtained via the different methods are not necessarily inter-comparable.

The values for pitch and yaw CFs are averages over the estimates from 5 different methods: LSQ, LSI, XC, PSD, BAY5. BAY4 has been implemented at a later stage and was hence not used here. Mixed maneuvers, as well as wiggle maneuvers, were only considered by the methods LSQ and BAY5. Moreover, roll coupling factors were only estimated with the methods LSQ and BAY5. The given values are also averages over the estimates obtained using different pointing angle sources: FSM, SCA1B (RL04), IMU1B (RL04). Angles derived from

accelerometers have not been used for the results shown here, since the quality of the GF2 ACC data was not sufficient.

Table 5.3: Estimated linear TTL coupling factors (version 1; for historical reference), for GF1.

| date | LRI linear TTL coupling factors [$\mu m\,rad^{-1}$]: | | |
	roll GF1	pitch GF1 $= \Delta z_1 \cdot rad^{-1}$	yaw GF1 $= -\Delta y_1 \cdot rad^{-1}$
wiggle:			
2018-06-21	0.4 ± 7.1	116.5 ± 14.5	154.1 ± 23.0
CMC:			
2019-01-16	0.2 ± 1.0	90.8 ± 9.6	62.6 ± 44.5
2019-03-26	1.0 ± 1.1	83.3 ± 8.2	70.6 ± 58.1
2019-04-24	0.8 ± 1.6	90.9 ± 10.0	82.8 ± 33.6
2019-05-23	1.0 ± 0.9	82.9 ± 9.2	90.3 ± 32.2
2019-06-22	-0.4 ± 1.2	91.5 ± 8.6	98.8 ± 31.3
2019-07-24	2.2 ± 1.5	99.2 ± 11.3	94.9 ± 33.0
2019-08-26	1.3 ± 0.8	94.9 ± 14.0	94.5 ± 36.4
2019-09-28	0.4 ± 1.4	100.7 ± 10.8	86.0 ± 30.3

Table 5.4: Estimated linear TTL coupling factors (version 1; for historical reference), for GF2.

| date | LRI linear TTL coupling factors [$\mu m\,rad^{-1}$]: | | |
	roll GF2	pitch GF2 $= \Delta z_2 \cdot rad^{-1}$	yaw GF2 $= -\Delta y_2 \cdot rad^{-1}$
wiggle:			
2018-06-21	-5.9 ± 7.7	68.7 ± 12.0	82.8 ± 37.5
CMC:			
2019-01-16	-0.1 ± 1.7	74.9 ± 9.9	142.7 ± 17.6
2019-03-26	-0.4 ± 1.2	74.4 ± 8.9	138.3 ± 22.2
2019-04-24	-1.1 ± 1.5	83.9 ± 9.8	132.5 ± 16.5
2019-05-23	-1.0 ± 1.1	46.6 ± 7.5	103.2 ± 22.5
2019-06-22	0.4 ± 1.0	61.0 ± 54.7	97.1 ± 13.9
2019-07-24	2.5 ± 1.2	73.7 ± 9.0	133.4 ± 17.0
2019-08-26	1.1 ± 0.9	98.7 ± 11.2	133.9 ± 19.6
2019-09-28	1.3 ± 0.9	93.5 ± 11.1	155.9 ± 32.0

It is important to note that the ARC effect was not understood at the time of publishing [Weg+20b], and it was reported as an unexplained artifact in the data. If ARC is not considered, the fitted TTL curves for the yaw angle of the transmitter S/C appear as if they were time shifted w.r.t. the signal in the range. This disturbs the CF estimation and is thus relevant for interpreting these results. This phenomenon is visible in Fig. 5.4, which shows a yaw GF1 maneuver in January 2019. The left plot illustrates the estimated TTL error when not considering ARC. The angles for this plot were derived from IMU1B data. The right plot shows a fit of the same maneuver when ARC is considered.

Furthermore, note that the data shown in the plots of [Weg+20b] have been filtered with a different filter than described in Sec. 5.1.6. This filter had a lower magnitude response at the CMC maneuver frequency, and hence the plotted time series show lowered amplitudes. This did not affect the accuracy of the CF estimation, since both the range and the angle amplitudes were lowered by the same factor. The filter has been updated for version 2 of combined results, which is presented in the following section.
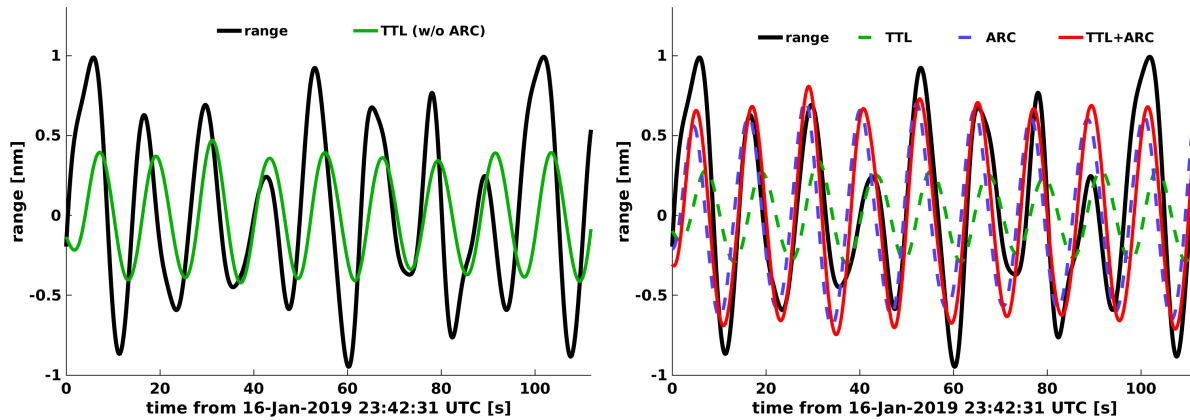
Figure 5.4: TTL fit for a CMC yaw GF1 maneuver in January 2019: bandpass filtered range and estimated TTL error. Left: without considering ARC. Right: including ARC.

5.3.2   Combined results, version 2

As pointed out above, producing a second version of TTL estimation results was necessary after the discovery of ARC. Recall that the ARC error can be computed via Eq. (3.52), given the pitch and yaw rates of the transmitter S/C. In order to confirm the parameters that arise from the theory, the ARC factors were at first estimated along with the TTL coupling factors. The results for the ARC factors are listed in Tab. 5.5, with the unit of μm/(rad/s). The values and uncertainties are the averages and STDs of a set of values obtained from different methods and angle sources. The methods LSI, PSD, and XC are not defined for estimating two parameters at once, and hence they were not used here. Note that ARC only applies to the transmitter S/C, which has been GF2 until December 2018 and GF1 thereafter. The only values for GF2 are not very reliable, since they were obtained from "wiggle" maneuvers with a duration of 24 s instead of 180 s.

The right plot in Fig. 5.4 shows a data fit for the same maneuver as in the left plot, a yaw GF1 maneuver in January 2019. Here considering both TTL and ARC, the data fits well, which confirms that introducing ARC resolves the issue with yaw GF1 maneuvers encountered in [Weg+20b]. Figure 5.5 shows all estimated ARC factors for pitch and yaw of GF1, compared to the theoretical values. Since the ARC estimations are in most instances compatible with the theory, henceforth, the ARC is computed and subtracted from the LRI range in advance of the TTL estimation. For this, the theoretical values from Eq. (3.52) were used. Note further that in the version 1 results, all of the estimated roll CFs are expectedly close to zero. Thus, the roll coupling has been neglected, i.e. assumed to be zero, for the version 2 of combined results.

The combined results of version 2 are given in Tab. 5.6 in terms of CFs with unit $\mu m\,rad^{-1}$. The values are obtained by combining the individual estimations from different methods and angle sources, in a similar way as in version 1. The same angle sources were used as in version 1: FSM, SCA1B (RL04), IMU1B (RL04). Here the PSD method has been excluded, since it exhibits a large uncertainty due to the short maneuver duration. Instead, the BAY4 method has been included this time. For LSQ and BAY5, all maneuvers except roll and mixed were concatenated, then all CFs were estimated together. For BAY4, in order to reduce computation time, each TTL CF was estimated individually. Note that two reasons for the significantly lower uncertainties given in the version 2 results are the consideration of ARC and the fact that some methods, in particular the PSD method, were excluded this time. Figure 5.6 shows exemplary TTL fits for CMC maneuvers performed in August 2019.

Table 5.5: Estimated ARC factors for GF1 and GF2.

date	S/C	ARC factors [μm rad^{-1} s]:			
		pitch		yaw	
		theory	estimated	theory	estimated
wiggle:					
2018-06-21	2	16.2	-10.1 $\pm$ 8.0	202.9	130.8 $\pm$ 23.8
CMC:					
2019-01-16	1	15.4	16.2 $\pm$ 2.6	192.2	167.9 $\pm$ 17.0
2019-03-26	1	13.7	0.8 $\pm$ 3.1	171.4	185.3 $\pm$ 12.1
2019-04-24	1	13.9	16.9 $\pm$ 5.1	173.4	163.0 $\pm$ 14.7
2019-05-23	1	14.0	17.8 $\pm$ 2.6	174.6	133.0 $\pm$ 13.3
2019-06-22	1	14.1	-3.2 $\pm$ 3.5	175.9	175.7 $\pm$ 5.5
2019-07-24	1	14.2	-5.9 $\pm$ 5.3	177.8	181.7 $\pm$ 16.7
2019-08-26	1	14.4	6.3 $\pm$ 4.3	180.0	193.7 $\pm$ 12.0
2019-09-28	1	14.5	-7.2 $\pm$ 4.2	181.2	170.1 $\pm$ 12.4
2020-02-01	1	14.6	21.6 $\pm$ 4.1	183.0	176.1 $\pm$ 5.1
2020-02-14	1	14.6	-0.9 $\pm$ 2.4	182.0	182.9 $\pm$ 12.3
2020-05-09	1	14.1	25.7 $\pm$ 3.2	176.7	180.8 $\pm$ 10.9
2020-05-15	1	14.1	7.6 $\pm$ 4.2	176.4	186.4 $\pm$ 8.1
2020-10-20	1	13.9	11.9 $\pm$ 3.5	174.1	173.6 $\pm$ 14.1
2021-03-28	1	15.6	42.2 $\pm$ 6.7	194.7	185.4 $\pm$ 6.7
2021-09-05	1	16.7	17.1 $\pm$ 5.7	208.3	179.1 $\pm$ 6.7
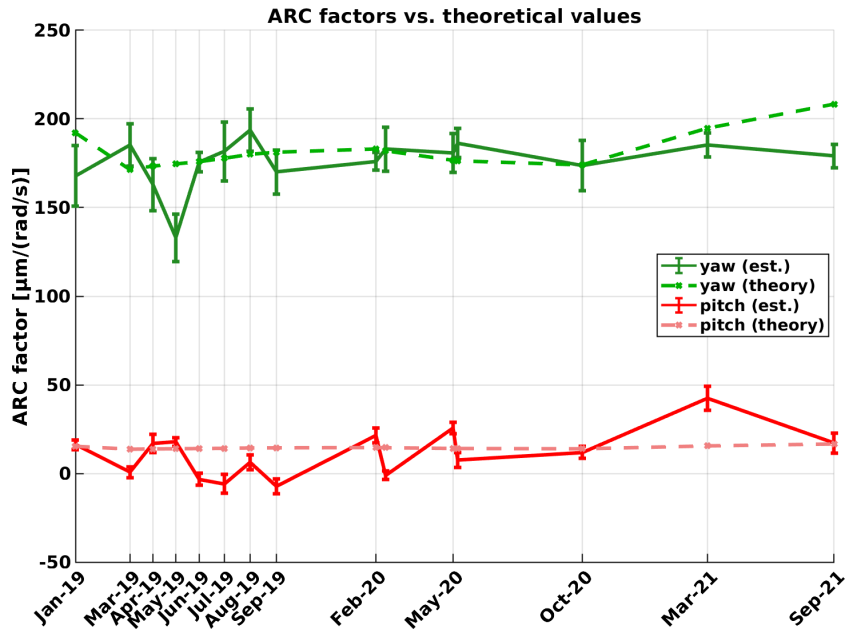
Figure 5.5: Estimated ARC factors for GF1 pitch and yaw compared to theoretical values derived from Eq. (3.52).

5.3.3   Note on the combination of results

The version 1 and 2 results presented above are combinations of the individual results using different angle sources and different estimation methods. For each coefficient, the value and its uncertainty were obtained by simply taking the average and standard deviation of a set of considered values for the same coefficient from different methods.

Table 5.6: Estimated linear TTL CFs version 2.

| | TTL CFs [µm rad^{-1}]: | | | |
| | GF1 | | GF2 | |
date	pitch	yaw	pitch	yaw
wiggle:				
2018-06-21	133.0 ± 4.3	166.0 ± 14.0	67.9 ± 6.6	90.1 ± 15.9
CMC:				
2019-01-16	96.5 ± 3.2	46.0 ± 5.0	77.2 ± 4.5	149.3 ± 8.6
2019-03-26	88.0 ± 1.6	52.4 ± 2.3	82.1 ± 7.0	139.6 ± 8.9
2019-04-24	101.2 ± 2.3	69.5 ± 4.5	84.6 ± 4.1	131.6 ± 6.5
2019-05-23	89.8 ± 2.0	71.0 ± 5.1	49.6 ± 4.7	100.9 ± 7.5
2019-06-22	97.0 ± 2.4	91.0 ± 7.3	33.7 ± 3.9	92.4 ± 8.5
2019-07-24	104.4 ± 2.5	82.8 ± 4.6	77.8 ± 4.0	129.9 ± 8.0
2019-08-26	104.5 ± 2.0	82.4 ± 3.7	97.8 ± 5.1	139.9 ± 8.1
2019-09-28	111.6 ± 2.3	62.1 ± 3.2	100.4 ± 6.0	131.0 ± 8.2
2020-02-01	93.9 ± 2.7	62.4 ± 3.6	-	-
2020-02-14	100.7 ± 3.5	74.2 ± 3.7	-	-
2020-05-09	107.7 ± 3.6	72.6 ± 2.6	-	-
2020-05-15	87.7 ± 2.3	93.8 ± 2.8	-	-
2020-10-20	63.9 ± 3.1	87.3 ± 9.1	86.7 ± 3.2	119.2 ± 5.2
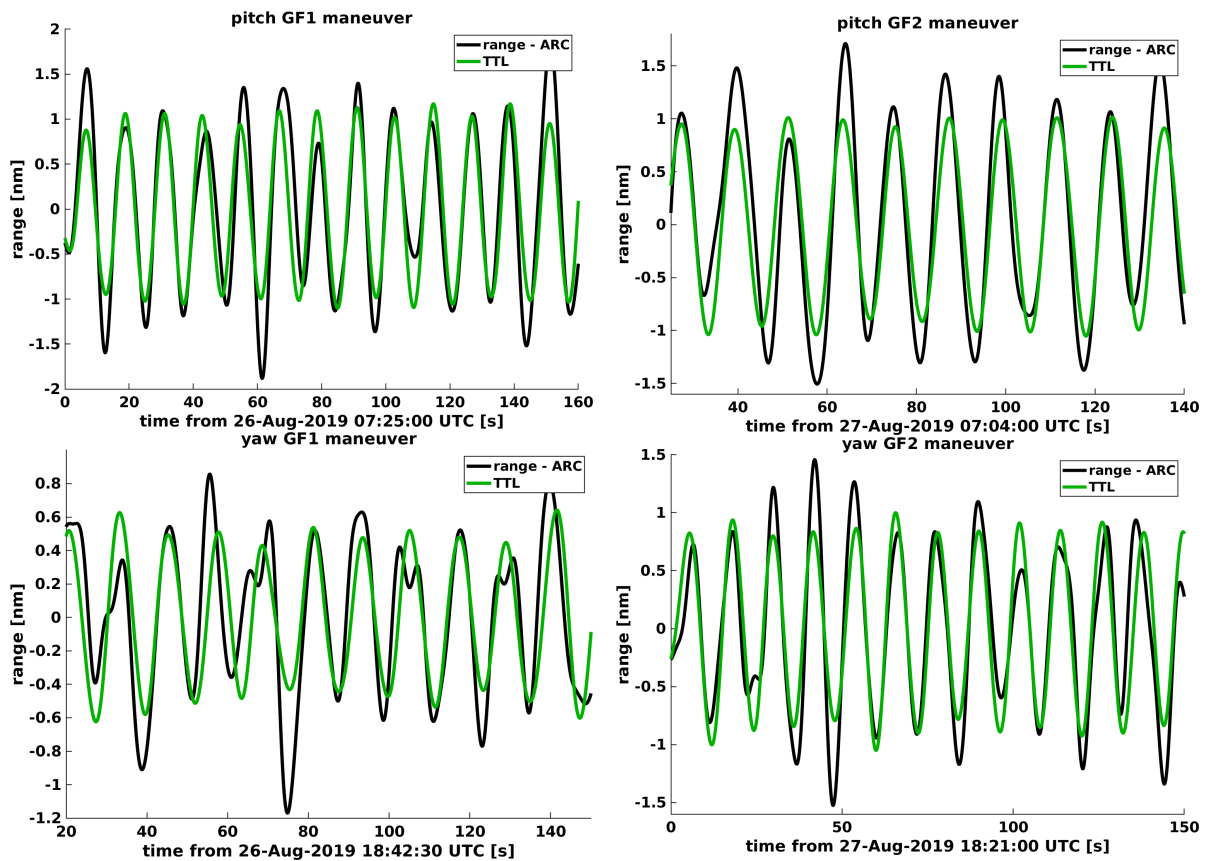
Figure 5.6: TTL fits during CMC maneuvers on GF1 (left) and GF2 (right) in August 2019, bandpass filtered. Range versus fitted TTL and ARC errors. Top: pitch maneuvers. Bottom: yaw maneuvers.

This way of combining results is rather heuristic, but was chosen for practical reasons. For one thing, at the time, some artifacts in the data were not understood, and whether there was a time stamp mismatch between the ranging data and attitude data. As a consequence, it was not clear which estimation method should be preferred, since they all make different assumptions. The estimation uncertainties of different methods could also not be assumed to be well comparable. Moreover, the uncertainty of the LSQ method, see e.g. Eq. (4.28), may underestimate the true uncertainty, as briefly discussed in Sec. 4.3.1.

In order to avoid confusion, this method of combining results has been retained, and a third version has not been created. However, with many available data points by now, the methods have been tested well, and the confidence in the correctness of the time stamps has grown. Therefore, in retrospect, the author would preferrably suggest to settle on one angle source and one estimation method. Since the roll coupling has been found to be negligible, the FSM angles can be used, which brings the advantage that the LRI TTL can be calibrated independently of other instruments. If a low computation time is preferred and knowledge of the uncertainty is not particularly important, the LSQ method may be used. If the computational effort is not as crucial, but a more accurate uncertainty value is desired, then the BAY4 or BAY5 estimators are suggested here.

5.3.4   Center-of-mass positions

According to Eq. (3.32), estimations of the satellite frame (SF) y and z vertex point (VP)-CoM offsets, denoted Δy and Δz, can be obtained from the pitch and yaw TTL CFs. I.e., Δy and Δz are the y and z components of the vector pointing from the LRI VP to the S/C CoM, given in the SF. Precisely, for each S/C, one has

$$\Delta y = -\lambda_{\text{yaw}} \cdot 1 \text{ rad}, \tag{5.84}$$

$$\Delta z = \lambda_{\text{pitch}} \cdot 1 \text{ rad}, \tag{5.85}$$

where λ_{pitch} and λ_{yaw} denote the pitch and yaw TTL CFs, respectively. The estimated CoM positions are plotted in Fig. 5.7. The values are based on the version 2 combined TTL results presented in the previous section, i.e. on the CFs given in Tab. 5.6.

Mass trims were performed on GF1 on 18 July 2018 (y and z), and on 14 May 2020 (z) [tea21]. I.e., the CoM of GF1 was intentionally shifted, using movable trim masses on the S/C, with the goal of colocating the CoM with the ACC RP. A mass trim in x direction has been performed on 6 February 2020, however, note that the LRI is insensitive to the x offset. In Fig. 5.7, the SF y and z (cross-track and nadir) components of these mass shifts are shown as arrows. No mass trims have been performed on GF2, due to the degradation of GF2 accelerometer data. Figure 5.8 compares the results presented here to estimates of the ACC RP-CoM offset, estimated at the Jet Propulsion Laboratory (JPL) as well as the Center for Space Research (CSR, University of Texas). The difference between ACC RP-CoM offset on the one hand and VP-CoM offset on the other hand is expected to be stable, i.e. not varying significantly with time. For GF1, the results are in good agreement, which is a confirmation of the results and provides confidence that the observed changes of estimated CFs from one CMC to the next reflect actual changes of the S/C CoMs. For GF2, not many data points are available for the ACC-CoM offset, due to the degraded GF2 ACC data. As it is nonetheless of interest to monitor the S/C CoM variations over time, the results from the LRI analysis constitute a valuable input for the mission.

5.3.5   Evaluation of the estimation methods

The plots in Fig. 5.9 show a comparison of CFs estimated using different sources for the pointing angles. Here the depicted values were estimated using the BAY4 method. For GF1, nearly all values show very good agreement. For GF2, it is noteworthy that the yaw CFs
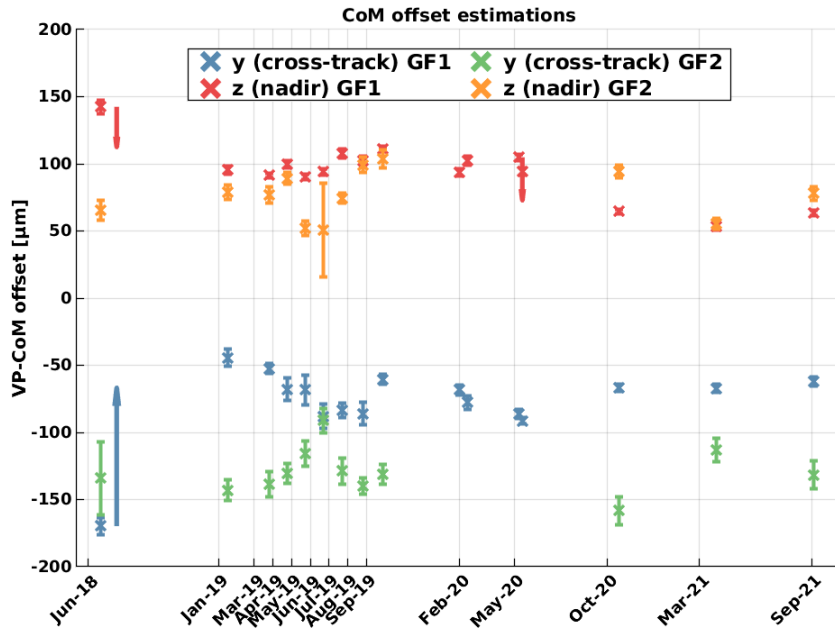
Figure 5.7: Estimated y and z components of CoM positions for GF1 (blue, red) and GF2 (green, orange) w.r.t. LRI RP, given in the SF. Arrows indicate mass trims performed on 18 July 2018 (y and z), as well as on 14 May 2020 (z).
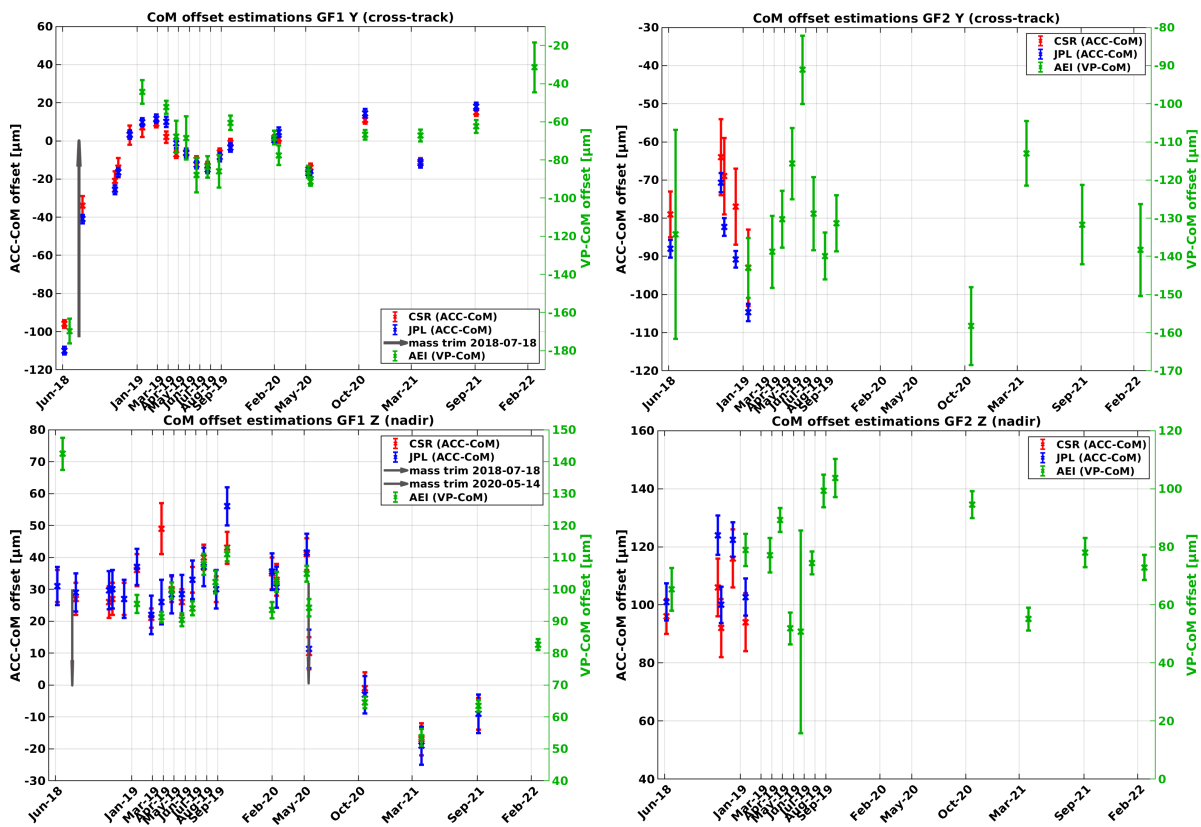

Figure 5.8: Estimated SF y (top plots) and z (bottom plots) CoM offsets for GF1 (left plots) and GF2 (right plots), comparing values from JPL and CSR (ACC-CoM estimation), and AEI (VP-CoM estimation). Arrows indicate mass trims.

obtained using FSM pointing angles seem to be commonly lower than for the other angle sources. The reason for this observation is under investigation.
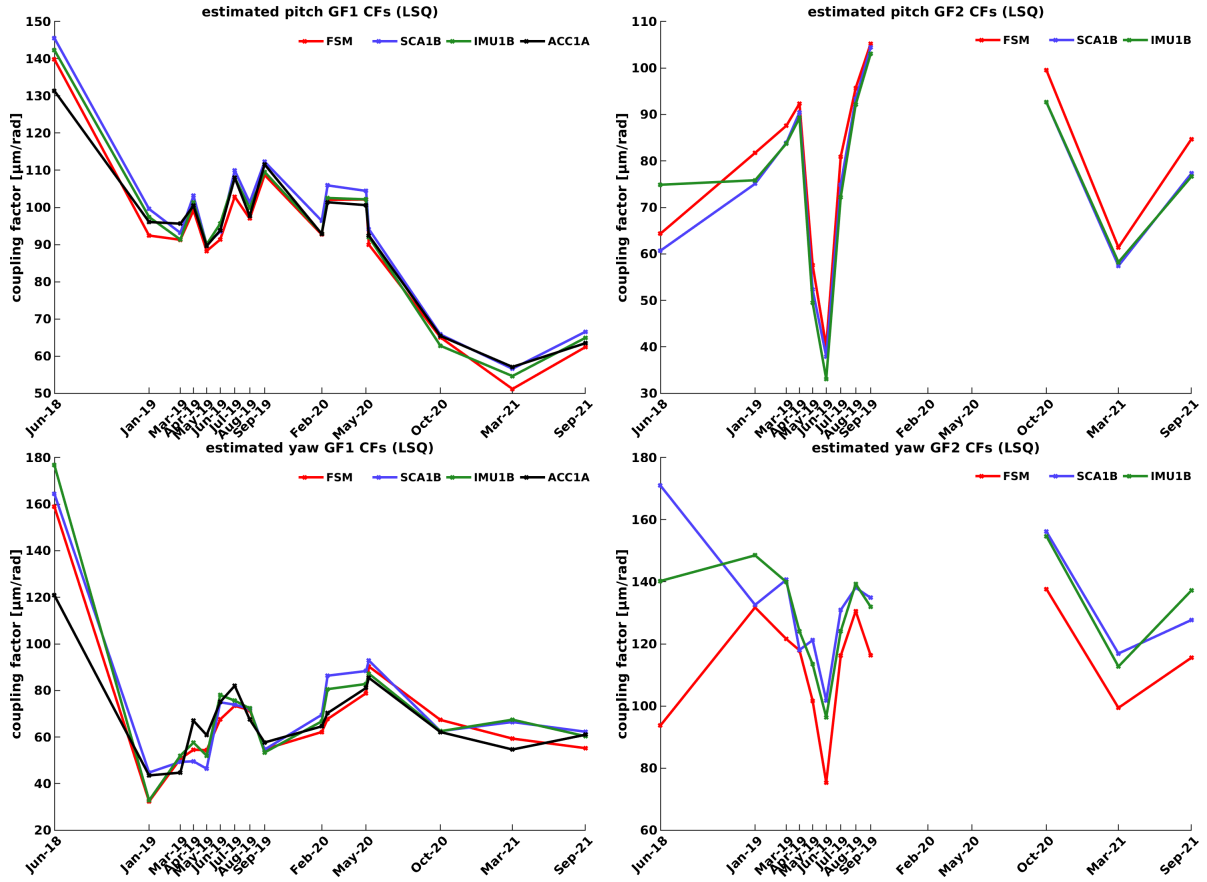
Figure 5.9: Estimated TTL CFs for GF1 (left) and GF2 (right) for pitch (top) and yaw (bottom), estimated with the BAY4 method, comparing different angle sources.

For the sake of comparison, Tab. 5.7 lists all the individual estimated values for the pitch GF1 CF, based on the CMC maneuvers performed on 28 September 2019, for all combinations of available angle sources and estimation methods. For each method, the CFs from different angle sources seem to agree within the estimation uncertainty. For GF1, this is also true for the pointing angles obtained from integrating ACC1A angular accelerations, however, the estimates derived using ACC data are not considered for the final results, since the GF2 ACC data is degraded [McC+19; BMK21], and the calibrated accelerometer data (ACT) provides merely linear accelerations, no angular accelerations.

Table 5.7: Estimated pitch GF1 CFs for 28 March 2021. All values are in µm rad^{-1}. Uncertainties are given in the form of $\pm 1\sigma$.

	FSM	SCA1B	IMU1B	ACC1A
LSQ	51.2 ± 4.1	56.6 ± 4.4	54.6 ± 4.2	57.1 ± 4.2
LSI	49.5 ± 6.4	55.6 ± 6.8	53.1 ± 6.8	52.6 ± 6.3
PSD	59.1 ± 24.9	62.7 ± 25.9	61.0 ± 24.9	60.8 ± 24.8
XC	53.3 ± 6.5	56.8 ± 6.9	54.8 ± 6.7	54.9 ± 6.7
BAY4	49.9 ± 4.6	55.6 ± 4.8	53.1 ± 4.7	51.4 ± 4.6
BAY5	50.3 ± 3.3	57.5 ± 3.4	53.5 ± 3.3	51.7 ± 3.3

Figure 5.10 shows the pitch and yaw TTL CFs for both S/C estimated with the different

methods: LSQ, LSI, PSD, XC, BAY4, BAY5. IMU1B angles were used to create this plot, and ARC was subtracted before the TTL estimation. For each plot, the y axis refers to the CFs measured in $\mu m \, rad^{-1}$, which are depicted by crosses in different colors. The large change for GF1 between June 2018 and January 2019 is mainly due to a mass trim, cf. Sec. 4.1, carried out on 18 July 2018.
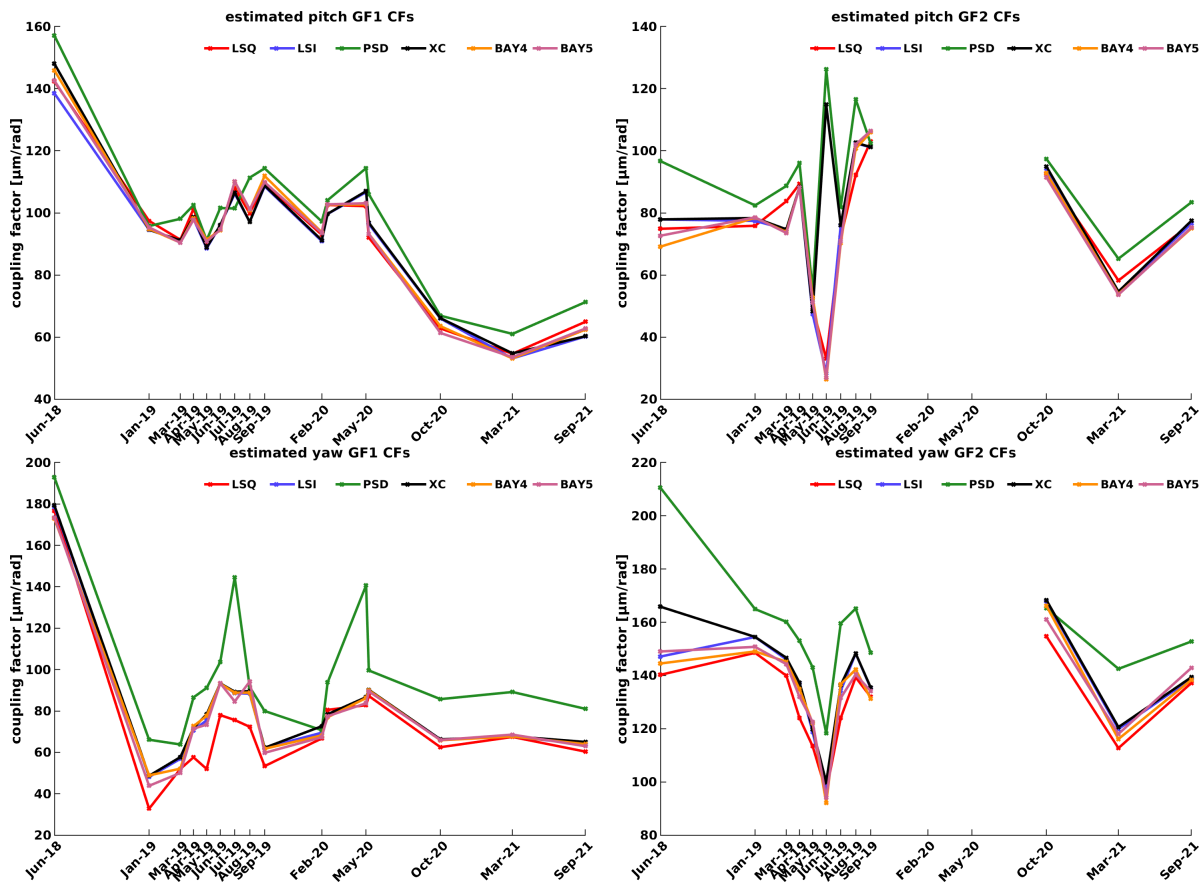
Figure 5.10: Estimated TTL CFs for GF1 (left) and GF2 (right) for pitch (top) and yaw (bottom), based on pointing angles derived from IMU1B data, comparing different methods.

The overall agreement in Fig. 5.10 appears to be good, except for the pitch GF2 CFs (top right plot) estimated in June 2019. For the affected pitch GF2 maneuvers on 22 June 2019, a large timing mismatch was estimated. In such cases, both the XC and PSD methods tend to yield larger values than the other methods, since the PSD method is insensitive to time stamp mismatches, and the XC method accounts for the time shift and estimates it along with the CF. The cause of this artifact is still unknown, and it appeared merely this one time so far, in June 2019. Thus, it may be interpreted as an outlier.

Another noteworthy observation is an apparent tendency of the PSD method to overestimate the CFs. This may be due to noise in the range, which leaks into the AS value for the frequency bin containing the maneuver frequency. The PSD method seems to produce less certain results in general, which may be explained by the fact that the time series for a single CMC maneuver has a duration of at most 180 seconds. Often, such a time series is even significantly shorter because of data segments that have to be excluded, e.g. due to attitude thruster firings, cf. Sec. 5.1.4. The shorter the time series is, the less certain is the estimated peak height in the AS.

The PSD and XC methods by design have the property that they still yield the correct result in the presence of possible timing mismatches between pointing angles and LRI range.

If there are such mismatches, PSD and XC thus have an advantage over the other methods. However, also other artifacts such as ARC, are possibly misinterpreted as time stamp errors. Therefore, PSD and XC are useful tools, but care needs to be taken w.r.t. the assumptions that these methods make, and whether other explanations of an apparent time shift are possible. In any case, a large timing mismatch estimated by the XC method can be interpreted as a warning that there may be an issue with the data.

The BAY methods have the advantage that they yield, in addition to the estimated CF, a reasonable probability density of it. Figure 5.11 shows PDFs of estimated CFs, based on the CMC maneuvers performed on 28 March 2021, obtained with the BAY4 method. The left plots show results for GF1, which was the transmitter S/C at the time. The top left plot shows the posterior PDF for the pitch and pitch rate CFs, the bottom left plot shows the posterior PDF for yaw and yaw rate, so in both cases the dimension is $M = 2$. The right plots show the results for GF2, which was the transponder S/C at the time, and as such has no angular rate coupling, so here the dimension is $M = 1$. Each PDF has been multiplied by a factor, such that the maximum value is 1. Note further that, in particular, the PDFs may be used to derive uncertainties for the estimated parameters.
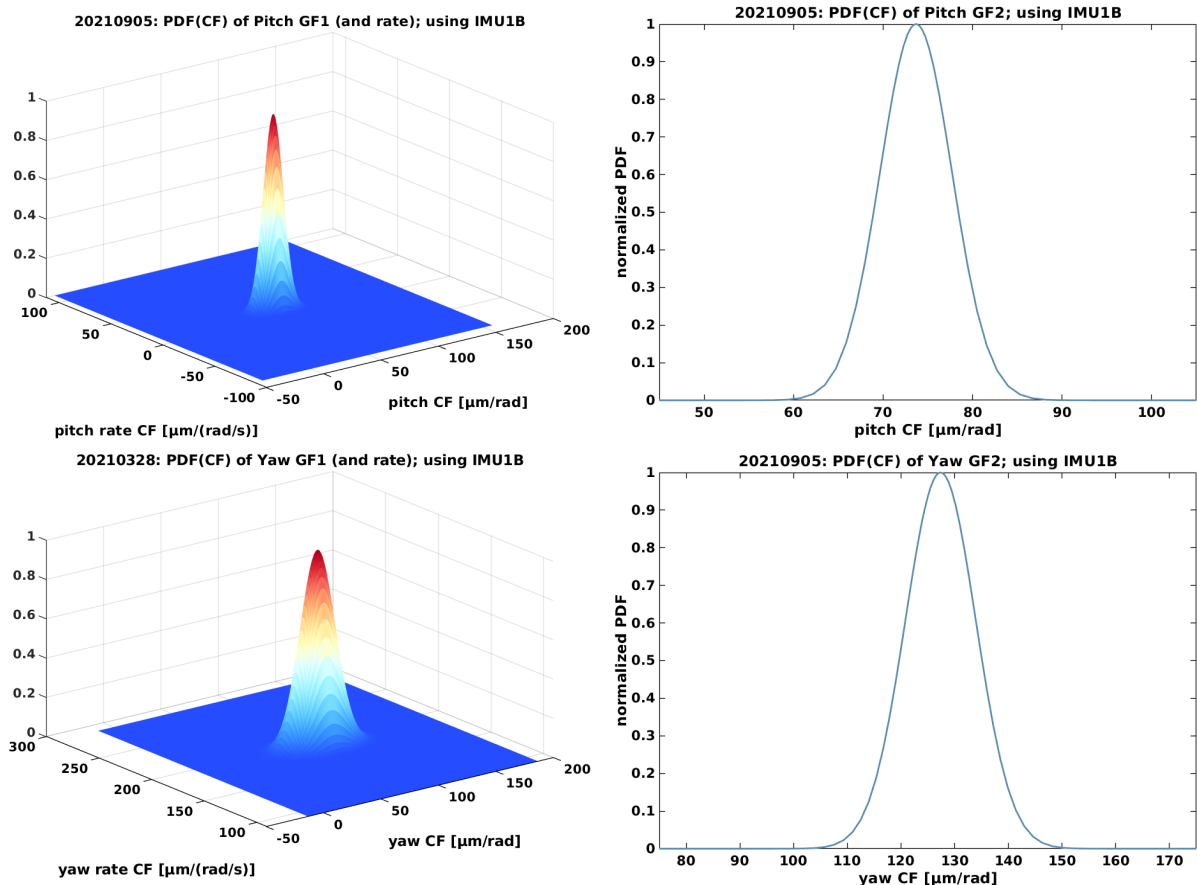
Figure 5.11: Probability density functions (PDF) of CF estimations derived with BAY4, from CMC maneuvers performed on 28 March 2021. Left: GF1 (transmitter S/C) CFs for pitch and pitch rate (top), yaw and yaw rate (bottom) ($M = 2$). Right: GF2 (transponder S/C) CFs for pitch (top) and yaw (bottom) ($M = 1$). Each PDF has been multiplied by a factor such that the maximum value is 1.

5.3.6 Interpretation of the results and conclusions

The ASD of measured TTL and ARC errors is shown in Fig. 5.12. The ARC curve is below the laser frequency noise (LFN) curve for all frequencies. The TTL is within the requirement and everywhere below the ACC noise converted to LoS range, based on the model presented in [Dar+17]. At high frequencies, TTL coupling is below the LFN. The pre-flight requirements on the linear TTL CFs for each S/C were 20, 200, and 200 $\mu m\,rad^{-1}$ for roll, pitch, and yaw, respectively. All of these requirements are met.
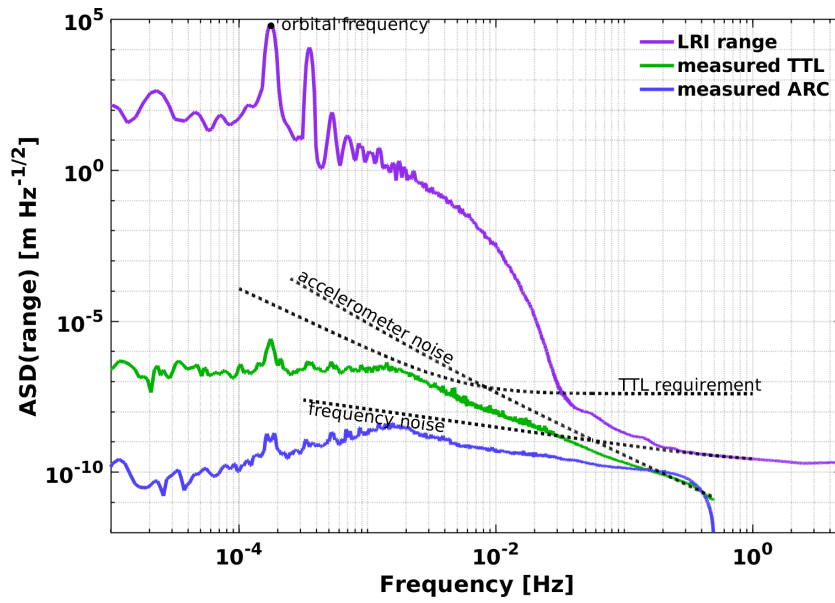
Figure 5.12: Amplitude spectral density of LRI range and measured TTL and ARC errors, for a 9-day segment during April 2019.

It can be concluded that the TTL model derived in this thesis, cf. Sec. 3.2, in particular the linearity and Eq. (3.32), are confirmed to the estimation accuracy. Note that for the potential TTL error caused by TMA misalignment, the conservative values 10, 10, and 1 $\mu m\,rad^{-1}$ for roll, pitch, and yaw coupling were assumed pre-flight, cf. Tab. 3.5 in Sec. 3.2.7. The analysis of in-flight LRI data, however, has shown that a roll coupling as large as 10 $\mu m\,rad^{-1}$ can be excluded for both satellites. In fact, both measured roll CFs are zero to the estimation accuracy. The ARC model, cf. Sec. 3.2.6, could be confirmed as well. In particular, Eq. (3.52) is confirmed to the estimation accuracy. Moreover, note that the good compatibility of LRI VP-CoM offsets with ACC RP-CoM offsets from other processing centers confirms the relation between CoMs and the TTL CFs, which arises from the theory. I.e., it confirms once more the relation given in Eq. (3.32).

5.4 Subtraction of TTL

After estimating the TTL CFs, the LRI TTL model is complete. Using the measured pointing angles, a time series of the TTL error can be computed and subtracted from the range. In principle, the subtraction is viewed as the mitigation of a ranging error. For GFO, the accuracy of gravity field determination is not limited by the ranging noise, and thus the subtraction of TTL is not expected to improve the quality of gravity fields. Nevertheless, it is valuable to demonstrate that the noise level in the data can be reduced. In future missions using inter-satellite laser interferometry, this will likely be important.

During maneuvers, the model fits the data very well and the effect of the TTL subtraction

is clearly visible in the time series as well as in the ASD. Ideally, one would also like to see an effect in the ASD of the range recorded apart from CMC maneuvers, in order to demonstrate that TTL subtraction improves the instrument performance also during the nominal science phase. However, this demonstration is challenging, since the TTL ASD is well below the range ASD, cf. Fig. 5.12. In Sec. 5.4.1, the effect of subtracting TTL on the range ASD above $\sim$40 mHz is analyzed. Section 5.4.2 describes an investigation of post-fit residuals, where two sets of residuals are compared, one with and one without subtracting TTL from the range prior to the gravity field recovery (GFR).

5.4.1   ASD analysis at high frequencies

Above 40 mHz, TTL is even below the LFN. Additionally, there are responses to nongravitational forces in the range, which disturb the attempt to accentuate the TTL part of the LRI range spectrum. The linear accelerations caused by attitude thruster firings account for a major part of the range ASD above $\sim$40 mHz, cf. App. E. Unfortunately, the response of these accelerations in the range is correlated to the TTL error. The responses can be modeled and subtracted, however, the models are not perfect and the TTL error still turns out to be too small to be properly distinguished.

Furthermore, at high frequencies, the measurement noise in the pointing angles becomes significant, and hence subtracting TTL from the range means also adding noise. More precisely, the estimated TTL time series are computed as $\hat{\text{TTL}} = \bar{\theta} \cdot \hat{\lambda}$, using the measured angles $\bar{\theta}$. Even if the TTL model and the CFs are assumed to be perfect, so that $\hat{\lambda} = \lambda$, the estimated TTL is the sum of the true TTL and a term due to pointing angle noise, here written as $n_{\text{TTL}} = n_\theta \cdot \lambda$:

$$\hat{\text{TTL}} = \bar{\theta} \cdot \lambda = \theta \cdot \lambda + n_\theta \cdot \lambda = \text{TTL} + n_{\text{TTL}}. \tag{5.86}$$

It is quickly seen that, if measurement noise is dominating the angles, then the subtraction of TTL can be expected to elevate the range spectrum, instead of lowering it. Unfortunately, this can in fact be observed when regarding Fourier frequencies above $\sim$40 mHz. However, consider the idea of adding TTL instead of subtracting it. Both adding and subtracting TTL should add the same amount of noise. Hence, even if subtraction elevates the range ASD, addition should elevate it by at least the same amount. In the following, two approaches to test this hypothesis are described.

Time segments excluding thruster firings

In this approach, time intervals between January 2019 and May 2021 were studied during which no thruster firings occurred, with a minimum segment length of 800 seconds. For each of these time intervals, 520 in total, ASDs were computed for i) the unchanged LRI range, ii) range minus TTL, and iii) range plus TTL. This was done three times, using FSM, SCA1B, and IMU1B data to derive the pointing angles and thus the TTL. Additionally, all of the above was repeated after removing nongravitational variations from the LRI range using ACT1A data, cf. App. E.2. The coupling factors for computing the TTL were interpolated from the values given in Tab. 5.6 (version 2 results), in particular zero coupling of the roll angles was assumed. ARC was not considered in this analysis, since it is significantly smaller than TTL while also containing measurement noise. Each ASD was then divided into frequency bins of equal size, and for each bin the RMS value was computed. Here the RMS ASD value for a frequency bin of size $2\delta = 5$ mHz, centered at $f_0 = (37.5, 42.5, \ldots, 77.5)$ mHz, was obtained as

$$\text{RMS(ASD)}(f_0) = \sqrt{\frac{1}{2\delta} \int\limits_{f_0-\delta}^{f_0+\delta} \text{ASD}(f)^2 \, df}, \tag{5.87}$$
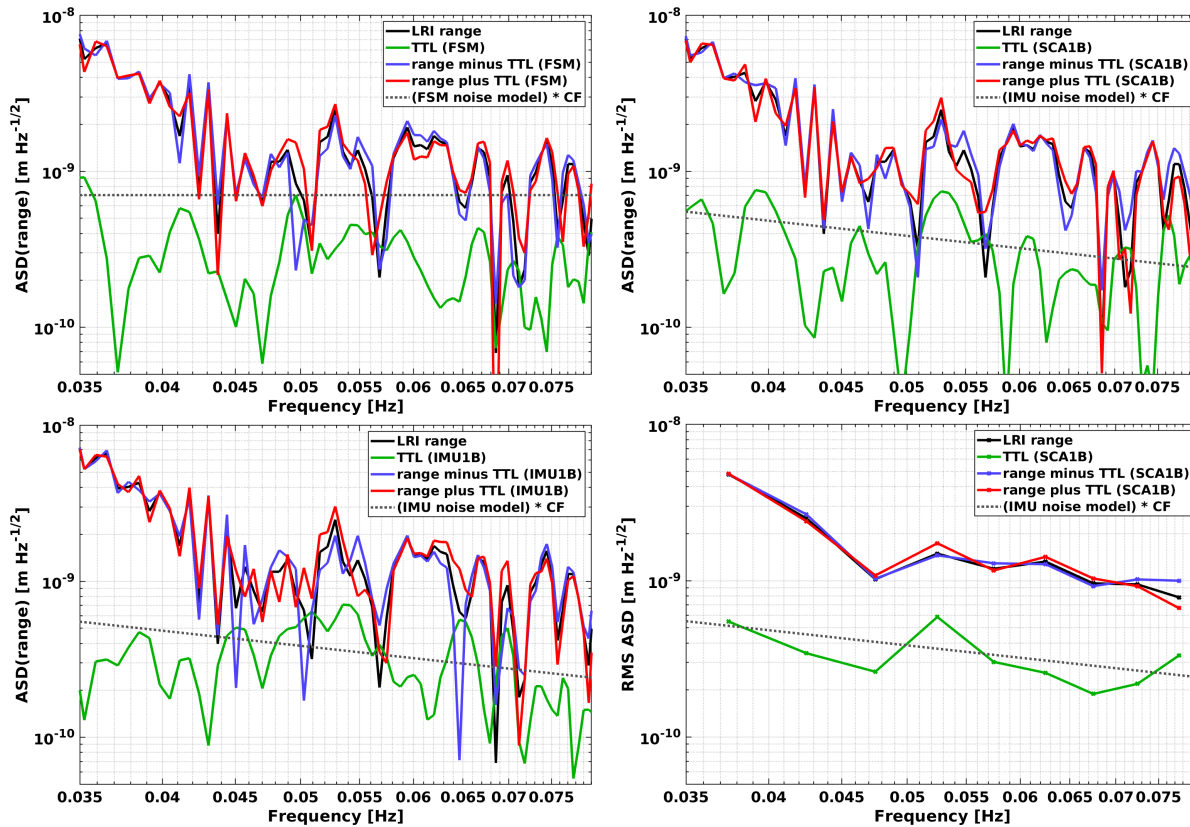
Figure 5.13: Top and bottom left: exemplary ASDs from one of the data segments without thruster firings, based on FSM, SCA1B, IMU1B data, respectively. Bottom right: RMS ASD values of the top right plot (SCA1B).

as is also done very similarly in App. E.

The top plots and the bottom left plot of Fig. 5.13 exemplarily show ASDs of one of the 520 data segments, where the range spectrum is comparatively low, and the effect of the TTL subtraction is visible. The bottom right plot shows the RMS ASD values of the ASD shown in the top right, for which SCA1B data was used. For comparison, each plot shows the ASD of the noise term n_{TTL} (dotted gray lines) that is added due to pointing angle noise. The ASDs of the estimated TTL (green lines) indeed seem to be noise dominated, according to the models of n_{TTL}, even though the models appear to be slightly overestimating the noise in some cases. To compute the IMU noise term, the IMU noise model given in Eq. (2.36) was used. Since the fused SCA1B data is assumed to attain the IMU noise level at high frequencies, the same model was used for the SCA1B data. The FSM angle noise in this analysis was assumed to be white noise with levels of 1.3 µrad/$\sqrt{\mathrm{Hz}}$ and 1.85 µrad/$\sqrt{\mathrm{Hz}}$ for pitch and yaw, respectively, according to Sec. 2.2.1. Note again that the roll coupling was assumed to be zero in all of this analysis.

The goal here is to compare the overall performance of the unchanged range product to the range products with subtracted or added TTL. To this end, for each frequency bin, again the RMS sum was taken over all 520 RMS ASD values. In these final RMS values, the effect of either addition or subtraction of TTL is barely visible. Thus, Fig. 5.14 shows ratios of such final RMS values. These ratios are labeled for better readability as defined in Tab. 5.8, where LRI stands for the unchanged LRI range (RL50), and DLN stands for range variations due to differential linear nongravitational accelerations obtained via ACT1A data. For each entry in the legend, it is indicated in brackets which sensor data was used to compute the TTL. Moreover, when the range reduced by ACT1A data (*LRI - DLN*) was used in place of the

Table 5.8: Abbreviations used in the plot legends of Figs. 5.14 and 5.15 for different ratios of RMS ASD values.

label	definition
-/o (sensor)	$\dfrac{\text{RMS(ASD(LRI - TTL(sensor)))}}{\text{RMS(ASD(LRI))}}$
+/o (sensor)	$\dfrac{\text{RMS(ASD(LRI + TTL(sensor)))}}{\text{RMS(ASD(LRI))}}$
-/+ (sensor)	$\dfrac{\text{RMS(ASD(LRI - TTL(sensor)))}}{\text{RMS(ASD(LRI + TTL(sensor)))}}$
-/o (sensor; ACT1A)	$\dfrac{\text{RMS(ASD(LRI - DLN - TTL(sensor)))}}{\text{RMS(ASD(LRI - DLN))}}$
+/o (sensor; ACT1A)	$\dfrac{\text{RMS(ASD(LRI - DLN + TTL(sensor)))}}{\text{RMS(ASD(LRI - DLN))}}$
-/+ (sensor; ACT1A)	$\dfrac{\text{RMS(ASD(LRI - DLN - TTL(sensor)))}}{\text{RMS(ASD(LRI - DLN + TTL(sensor)))}}$

original range (LRI), this is indicated by $ACT1A$ in the brackets.
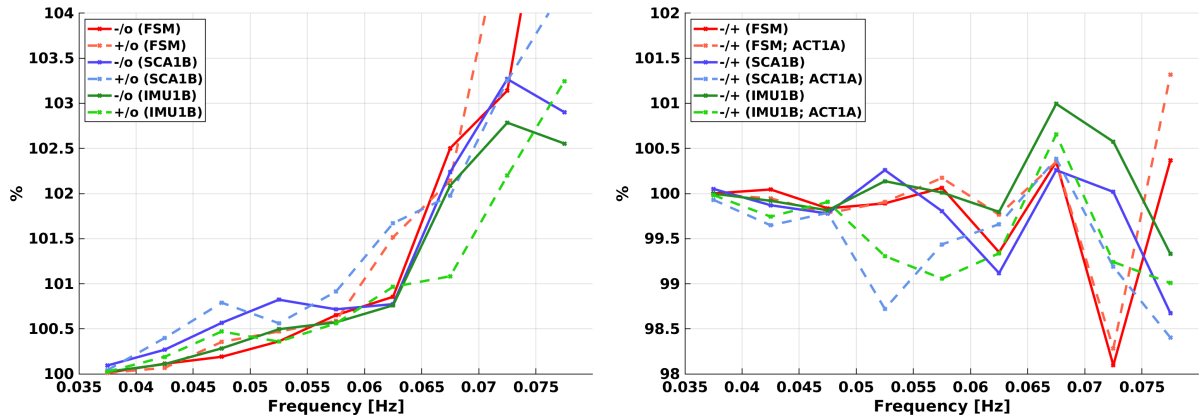
Figure 5.14: RMS ASD values taken over frequency bin centered at specified points on the x axis. From segments without thruster firings.

The left plot of Fig. 5.14 shows the ratios labeled *-/o* and *+/o*. All ratios are larger than 1, which means that subtracting as well as adding TTL both elevates the LRI range spectrum, no matter which attitude sensor was used. This is likely due to dominating measurement noise in the pointing angles. In the right of Fig. 5.14 the ratios *-/+* are plotted. Many values are smaller than 1, which indicates a better performance of the range with subtracted TTL, compared to the range with added TTL. All values are very close to 1, however, in order to obtain a rough estimate of what values can be expected for *-/+*, note that for uncorrelated data x and y one has $\text{ASD}(x+y) \approx \sqrt{\text{ASD}(x)^2 + \text{ASD}(y)^2}$. Since $\text{ASD}(TTL)$ is unknown, one can only speculate here. If $\text{ASD}(LRI)/\text{ASD}(TTL) \approx 10$, one can derive the rough estimate 0.98 for *-/+*, also depending on n_{TTL}. If $\text{ASD}(LRI)/\text{ASD}(TTL) \approx 20$, one obtains about 0.995. Since the plots are based on data from segments excluding thruster firings, one may argue that there is less pointing jitter than normal, and hence the true TTL is smaller than normal as well, so that the factor of 20 might even be realistic.

Long term analysis using ACT1A data

The analysis discussed above is based on relatively small time segments, due to the dismissal of all data affected by thruster firings. Such time segments are scarce and, moreover, barely long enough to estimate a spectrum for the interesting frequency band. An alternative way is to not dismiss this data, but attempt to remove the thruster responses. Since the thruster model parameters used in this thesis have been estimated with LRI data, it is here preferable to use the ACT1A data, which contains thruster responses modeled independently of the LRI. The procedure of reducing LRI range variations with ACT1A data is described in App. E.2. Ideally, the ACT1A data removes other range variations in addition to the thruster responses. Based on the same data set that is discussed in App. E, Fig. 5.15 shows ratios (cf. Tab. 5.8) of RMS ASD values for the frequency interval between 35 and 80 mHz. Each RMS value was computed from one ASD that was obtained from one day of data. The top plot shows the results based on the original LRI range, whereas the bottom plot shows the results of the same process when DLN range variations computed from ACT1A data are subtracted from the range beforehand.
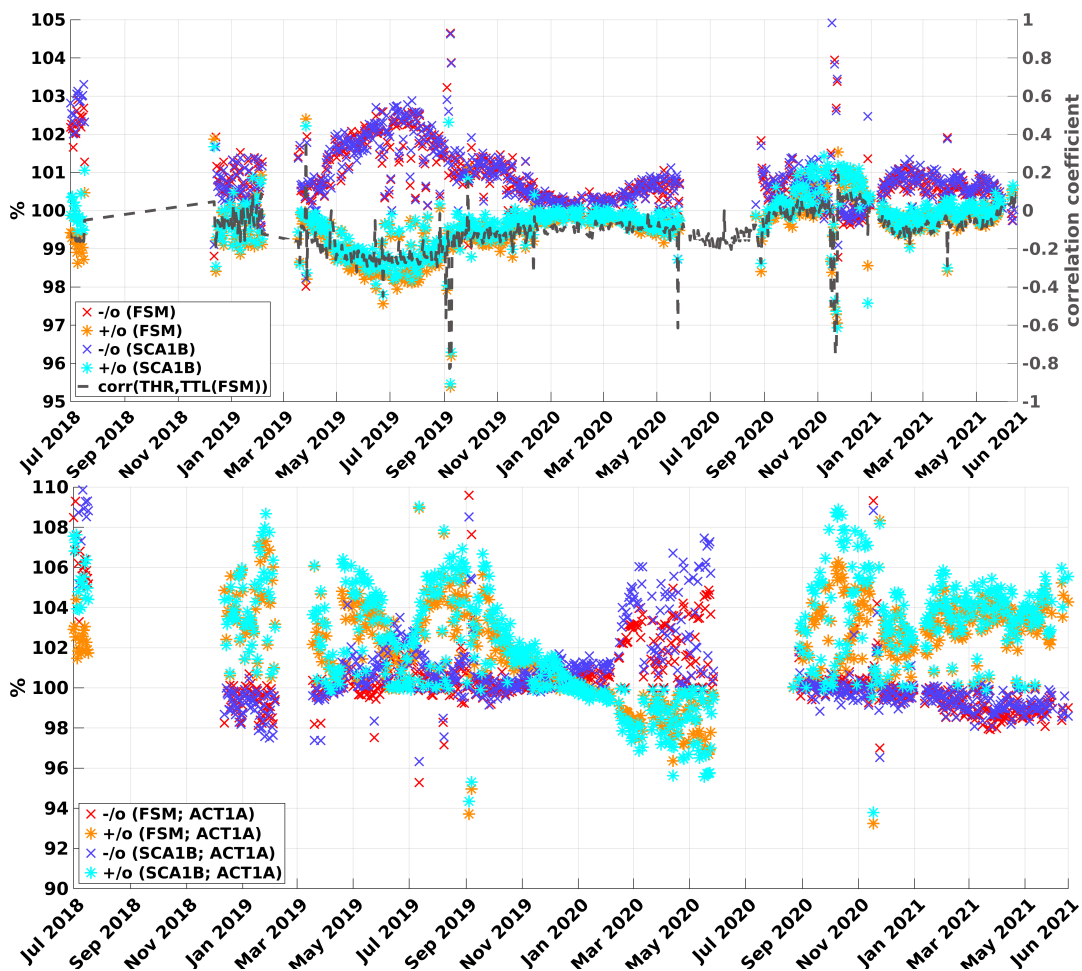
Figure 5.15: RMS ASD ratios for frequencies between 35 and 80 mHz. Each value is based on one day of data.

When ACT1A data is not used (top plot of Fig. 5.15), the ratios -/o (red and blue) are mostly above 1, and the ratios +/o (orange and cyan) are mostly below 1, which means that adding TTL even lowers the range spectrum here. This seems counterintuitive, however, recall that TTL correlates with the thruster responses, which have not been removed in these cases.

Since the correlation happens to be negative most of the time, adding TTL has the effect of removing a part of the thruster responses. The correlation coefficient between *THR* and *TTL(FSM)* is therefore plotted on the right y axis. Here *THR* denotes the time series of modeled thruster responses, and shown as the dashed gray line is Pearson's linear correlation coefficient, which is defined as

$$\text{corr}(X, Y) = \frac{\text{E}\left[(X - \mu_X)(Y - \mu_Y)\right]}{\sigma_X \sigma_Y},$$ (5.88)

for random variables X and Y with means μ_X and μ_Y, respectively. Before computing the correlation coefficients *corr(THR,TTL(FSM))*, both time series were filtered with an order 4 Butterworth bandpass filter with cutoff frequencies 35 and 80 mHz.

On the other hand, when ACT1A data is used to reduce the LRI range in advance (bottom plot of Fig. 5.15), the performance of range minus TTL appears to be significantly better than range plus TTL in many cases. There are some exceptions, which are currently under investigation. In the recent results from the year 2021, most of the ratios -/o are even below 1, which means that subtracting TTL in fact reduces the range variations in these cases.

In conclusion, although the TTL subtraction adds noise to the range via the measured pointing angles, so far nothing could be found that would contradict any of the results presented in this thesis. In lower frequencies, the range with subtracted TTL is still expected to perform better. If a range product with subtracted TTL shall be used for GFR, it may be advantageous to filter out the high frequency part of the angles, where measurement noise might be dominating, before computing the TTL. Further investigations and similar analyses are ongoing. In the following, post-fit residuals from the unchanged LRI range are compared to residuals obtained from corrected LRI range.

5.4.2   Analysis of post-fit residuals

Below 35 mHz, the gravity signal is dominating the LRI range ASD. Thus, without performing a gravity fit, it is not possible to see any effect of the TTL subtraction in the ASD there. However, in the process of GFR, other error contributors, such as accelerometer noise or aliasing, are the limiting factors, even when the KBR range is used. Hence, not much improvement of the gravity fit, if any, can be expected from subtracting TTL.

Here it shall be reported on an attempt to show an improved LRI instrument performance after subtracting TTL. It has been made with the help of the GROOPS software developed by the group of Torsten Mayer-Gürr at TU Graz [May+21]. GROOPS can process both KBR and LRI range simultaneously, which yields the possibility to distinguish between the noise contributions from KBR, LRI, and common noise (CMN). Here the CMN is the part of the noise that can neither be attributed to the KBR nor the LRI. As a result, one obtains three different time series of post-fit residuals, and so the part of the residuals that is attributed to the LRI range can be studied separately. Note that this method has been presented in [BKM21], however, it is still under development and no detailed documentation has been made public yet. The gravity fits have been done by Saniya Behzadpour[10].

Three sets of LRI range data for the entire month of July 2019 were prepared: i) the unchanged LRI range (RL50), ii) range minus TTL, and iii) range plus TTL. The range was taken from the LRI1B RL50 data product, which is computed at the AEI. The TTL was computed using FSM angles and CFs interpolated from the version 2 results given in Sec. 5.3.2. For each set, a gravity field for the month July 2019 was computed with GROOPS.

The results of the GROOPS processing are shown in Fig. 5.16 in terms of ASDs of range-rate post-fit residuals. In the legend, the type of disentangled residuals is indicated in brackets, i.e. whether it is the part attributed to CMN, KBR, or LRI. In the low frequencies, the LRI

---

[10]Institut für Geodäsie, Technische Universität Graz, Austria

part of the residuals from the corrected range, labeled *RL50 minus TTL (LRI)* (blue line), is clearly lower than the LRI part in the the original range, labeled *RL50 (LRI)* (orange line). The amount of reduction is in the order of the subtracted TTL range-rate error (green line) that had been subtracted, however, it seems not to explain the reduction in the low frequencies. The reason for the reduction in the low frequencies remains to be investigated. For high frequencies, the TTL error is too small to make a visible difference. It is evident that the subtraction of TTL cannot yield a significantly improved gravity field, since the common noise (CMN) term (black line) is much larger than TTL. However, it is unexpected that the difference between the CMN terms of original and corrected range, labeled Δ *CMN* (dashed gray line) has a much higher ASD than the TTL. For comparison, note the KBR part of the residuals (light pink line), which is above the LRI part for all frequencies.
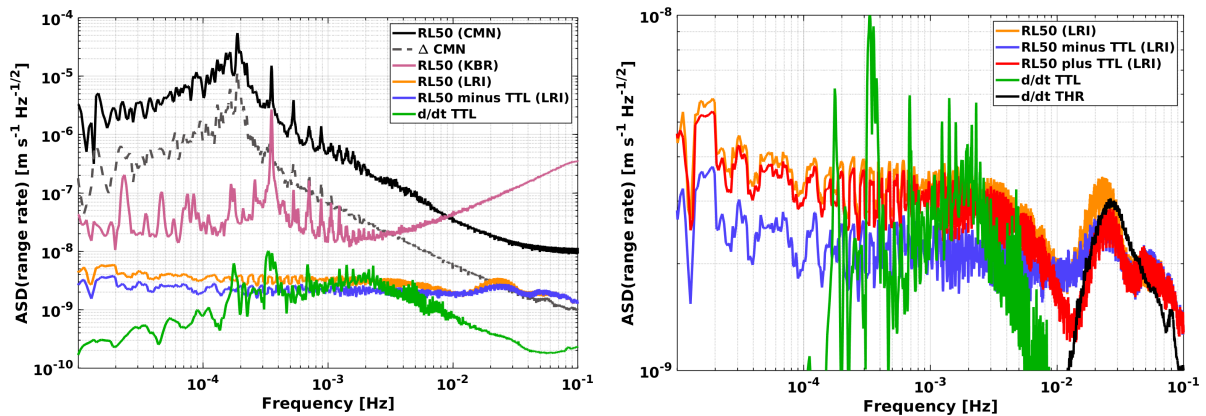
Figure 5.16: Post-fit residuals, different contributions. Obtained using the GROOPS software.

The plot on the right of Fig. 5.16 is a zoom-in of the left plot, but furthermore shows the LRI part of the residuals from the range with added TTL error (red line). Unexpectedly, adding TTL seems not to be elevating the residual ASD, however, it does not lower it as significantly as the subtraction. This indicates that the range data with subtracted TTL is superior to both of the other tested range data sets, original or with added TTL. The elevated LRI residuals near 25 mHz are likely due to linear accelerations caused by attitude thruster firings converted to range-rate (black line).
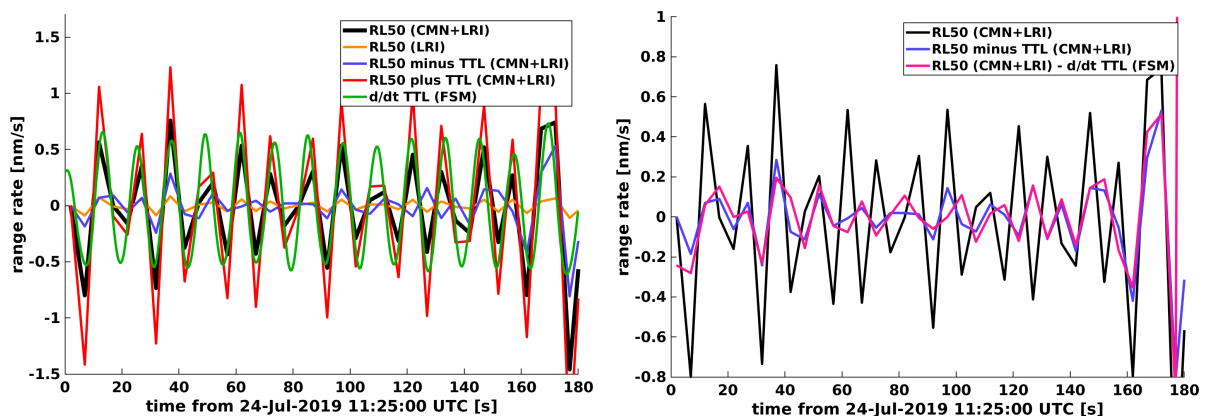
Figure 5.17: Post-fit residuals in the time domain, during a pitch GF1 CMC maneuver on 24 July 2019.

Figure 5.17 shows the post-fit residuals in the time domain, for the time span of a pitch GF1 CMC maneuver performed on 24 July 2019. Note that here the time series are highpass

filtered with a cutoff frequency of 40 mHz, and the residuals are sampled with 0.2 Hz. When examining the combined residuals, i.e. the sum CMN+LRI (black line), the TTL error seems to be contained in the residuals from the unchanged *RL50* range, mostly untouched by the gravity recovery process, as can be seen in the left plot. However, the TTL error (green line) seems to be mainly attributed to the CMN term, merely a small part is contained in the disentangled LRI term (orange line). The TTL seems to be largely suppressed in the time series from the corrected range, *RL50 minus TTL (CMN+LRI)* (blue line). The *RL50 plus TTL (CMN+LRI)* residuals (red line) contain the TTL with roughly doubled amplitudes. The right plot of Fig. 5.17 confirms the observation that the TTL error is left almost untouched by the GFR. Whether TTL is subtracted before the GFR (blue line), or after the GFR (pink line), the resulting time series coincide to a large extent.

In conclusion, some aspects of the results appear to contradict expectations, and a large part of the TTL error seems to be attributed to the disentangled CMN term instead of the LRI term. Nevertheless, there is some indication that the TTL subtraction is indeed improving the LRI instrument performance, and that the corrected LRI range performs slightly better than the uncorrected range. When regarding the combined residuals during CMC maneuvers, the data is behaving in accordance with the expectations.

Chapter 6

Conclusion and outlook

6.1 Summary and conclusion

This thesis provides a comprehensive documentation of the analysis of tilt-to-length (TTL) coupling in inter-satellite laser interferometers on the basis of the GRACE Follow-On (GFO) laser ranging interferometer (LRI). The mitigation of the range error due to TTL coupling requires certain steps, which have been enumerated and described in detail. A mathematical formalism for describing satellite attitude and inter-satellite pointing has been given in Chap. 2. Attitude sensors as well as control mechanisms have been discussed with emphasis on the GFO mission. The theoretical assessment of TTL effects in the LRI has been done in Chap. 3, and a model for the range error has been derived. Satellite rotation maneuvers, which have proven to be useful for the TTL calibration, have been discussed in Chap. 4. In particular, a technique to simulate such maneuvers and design the optimal calibration maneuver has been provided. Different methods to estimate the TTL coupling factors (CF) have been presented and evaluated in Chap. 5. Finally, the CFs have been estimated with in-flight data, and the results have been used to obtain a corrected LRI range product. Where possible throughout the thesis, the matters have been embedded in a more general context, such that they are readily adaptable to other mission scenarios.

The relevant attitude sensors for GFO are the fast steering mirror (FSM), the star camera assembly (SCA), the inertial measurement unit (IMU), and the accelerometer (ACC), where each measures a slightly different observable. The mathematical link between these observables, the spacecraft (S/C) attitude w.r.t. inertial space, and the inter-satellite pointing angles has been established and utilized successfully. The performance of the above mentioned sensors has been analyzed, revealing no significant deviations from the noise specifications, except for the GFO satellite 2 (GF2) ACC. It has been shown that either of the sensors can in principle be used to estimate TTL CFs, with a few restrictions. The data of the GF2 ACC showed unexpected artifacts and an elevated noise level shortly after launch, with the consequence that it can currently not be utilized to the full extent. Since the derivation of pointing angles from ACC data involves double integration w.r.t. time, the potential of this data predominantly lies in its low noise at high frequencies. Pointing angles derived from SCA data on its own have been found to be too noisy for the TTL calibration. The quality of the SCA1B data product, which is obtained by fusing SCA and IMU data, however, has turned out to be sufficiently high. The results of the parameter estimation using either FSM, SCA1B, or IMU1B data, are comparable. Notably, it can be concluded that the TTL coupling of the LRI can be calibrated using exclusively its own instrument data, i.e. the LRI range and FSM angles. Put into prospect, the best approach to obtain the optimal attitude solution is likely to fuse the data of all healthy attitude sensors into one product.

This thesis contains a detailed enumeration of all known TTL effects in the case of the LRI, gathered from different pre-flight studies. Their impact in terms of the levels of the resulting

range errors has been analyzed, confirming that the largest error is likely caused by the offset between the LRI reference points (RP) and the S/C centers-of-mass (CoM). Based on this, a linear model for the LRI TTL coupling has been formulated, which connects the CFs to nadir and cross-track components of the aforementioned offsets. Moreover, during the study presented here, another pointing related coupling effect in the LRI was discovered, denoted angular rate coupling (ARC). While the TTL error is a function of the pointing angles, the ARC error is a function of the angular rates. The physical reason for this effect has been illustrated, and a model for the respective error term has been derived as well. An assessment of this model has revealed that ARC is highly relevant for the analysis of the LRI range during rotation maneuvers, despite being almost negligible for the performance of the LRI in the nominal measurement phase.

A special focus of this study has been laid on satellite rotation maneuvers. The so-called center-of-mass calibration (CMC) maneuvers have proven useful for the LRI TTL calibration, although they originally serve a different purpose. In order to investigate alternative types of rotation maneuvers, a maneuver simulation technique has been developed. The parameters that determine such a maneuver have been identified and optimized w.r.t. the maneuver's suitability for TTL calibration. To this end, a function has been derived that assigns to a set of maneuver parameters the respective uncertainties of estimated CFs. By exploiting some approximations, this assessment function could be implemented in a way that requires minimal computation time. This allows for an efficient search within a large parameter space, given the approximate orbits of the two S/C. Based on all this, selected sets of simulated alternative maneuvers have been presented, and their performance is compared to the performance of the CMC maneuvers. Finally, the optimal maneuver parameters for the case of the LRI have been determined, which might decrease the uncertainty of the estimated CFs by a factor of 2-3, compared to the CMC maneuvers.

A main objective of this work has been to estimate the LRI TTL CFs with in-flight data, which could be achieved by utilizing the data recorded during the CMC maneuvers. For this purpose, several parameter estimation methods have been described in this thesis. Variations of four different approaches have been examined, either based on least squares (LSQ), cross-correlation, amplitude spectrum analysis, or Bayesian stochastics. The advantage and disadvantage of each method has been elaborated. The amplitude spectrum analysis seems to produce deviating results in some cases, and is thus not recommended. This circumstance is likely owed to the shortness of the CMC maneuvers, and might change if the duration of the maneuvers could be increased. In most cases, all of the remaining methods yield comparable results. If there is reason to believe in a timing mismatch between the range and the pointing angles, the cross-correlation approach might be beneficial, since it estimates the timing mismatch along with the CFs. Overall, the standard LSQ estimation as well as the Bayesian methods appear to reliably yield good results. The methods based on the Bayesian approach provide the opportunity to take into account additional information such as the characteristics of the measurement noise. In the simplest case, when all information is neglected, the Bayesian estimator is equivalent to the LSQ estimator. The Bayesian estimation methods always yield probability density functions (PDF) of the estimated values, from which confidence regions can be derived.

With 16 data points after the LRI has been in operation for about 3 1/2 years, the linear TTL model that has been stated in this thesis could be confirmed to the accuracy of parameter estimation. In particular, the supposed relation between CFs and CoM offsets is compatible with the parameter estimation results, and with the CMC analysis results of the Science Data System (SDS) using ACC data. This relation enables the tracking of CoM movement over long time periods, which has proven to be a useful contribution to the GFO mission, especially since the GF2 ACC data yields no more CoM estimates due to its degradation shortly after launch. All of the concrete values of the estimated TTL CFs are within the pre-flight requirements of 20, 200, and 200 $\mu m\,rad^{-1}$ for roll, pitch, and yaw, respectively. In total, it can be concluded

that the TTL range error should be at least one order of magnitude below any error source that would currently limit the accuracy of gravity field recovery (GFR). Finally, the ARC model has been tested by estimating the ARC factors from CMC data. Considering the estimation accuracy, the estimation results seem to be compatible with the model.

Based on the results presented in this thesis, the LRI range precision is likely limited by the sum of TTL error and laser frequency noise (LFN). TTL is larger for Fourier frequencies below about 30 mHz, the LFN is larger for higher frequencies. ARC is negligible for the lower frequencies, but important for the analysis of CMC maneuvers. Thus far, the LRI meets all requirements. Confirming an improved instrument performance after subtracting TTL has turned out challenging. One attempt was to analyze root mean square (RMS) values of range amplitude spectral densities (ASD) in the upper frequency range over a long time span. A second attempt was to perform a gravity fit for one month of data, using the GROOPS software, and analyze the post-fit residuals. Both approaches have revealed some unexpected artifacts. Nevertheless, no observations have been made that would contradict the results of this thesis. Certainly a fair conclusion is that the LRI was designed, built, accomodated, and operated extremely well and is measuring the inter-satellite range with high precision. Recalling that the LRI is a technology demonstrator, in this regard, the science community is well prepared for future missions utilizing high precision inter-satellite laser interferometry.

A few tasks still have to be carried out regularly during the remaining part of the GFO mission. The CMC maneuvers are currently repeated every 6 months. The maneuver data needs to be analyzed in order to update the TTL CFs, which are needed to compute the TTL correction term for the LRI range. The TTL results are also used to derive nadir and cross-track components of the offset between LRI vertex points (VP) and S/C CoMs on both S/C. It is important to continue these measurements, in order to keep track of the S/C CoMs, especially for GF2, where currently the ACC data cannot be used to derive CoM estimates. Also, the triple mirror assembly (TMA) coalignment tests may be repeated sporadically, in order to be informed in case the mirror misalignments become larger again, although the latest tests have not shown any more drastic changes. Other tests of the LRI instrument, not directly related to this thesis, are still occasionally carried out as well. Below, some lessons shall be formulated that can be learned from this study.

6.2 Lessons learnt

The work that is summarized in this thesis has revealed number of artifacts in the data, which were to some extent unexpected, and which can be challenging to mitigate. A few of these shall be listed here briefly:

- Jumps in the LRI phase measurements, cf. [Abi+19].

- Physical range variations caused by attitude thruster firings, cf. App. E.1.

- Coupling of S/C angular rates into the LRI range, cf. Sec. 3.2.6.

- Degraded GF2 ACC data shortly after launch, cf. [McC+19].

Unexpected problems comparable to those encountered within this study may also occur in future missions. When pursuing a similar goal as in this analysis, it is therefore recommended to carry out as many tasks as possible in advance of the mission launch. Based on the experience gained from the LRI TTL analysis, the following framework may be helpful in building a TTL estimation strategy for a future scenario involving inter-satellite laser interferometry. The components of a successful TTL calibration may be divided into tasks that can be fulfilled before the launch, and tasks that must be done afterwards, as follows.

Things that can be done prior to the launch include:

- Gain information on the ranging instrument and other available science instruments, data, and noise specifics.

- Study the mathematical framework of S/C attitude, inter-satellite pointing angles, and general data processing methods.

- Build a TTL model.

- Develop a TTL estimation strategy.

- Study and implement parameter estimation methods.

- If maneuvers shall be used, design an optimal TTL calibration maneuver.

- Perform simulations, test the methods.

Other tasks either require in-flight data or arise not until the data is available, and hence must be done after the launch:

- Establish the actual implementation of data handling and processing, e.g. since not all the data formats may be known beforehand.

- Gain experience with the data (attitude, range, auxiliary). For GFO, this was to an extent possible before the launch, due to the similar and already available Gravity Recovery and Climate Experiment (GRACE) data (except for LRI and IMU data, for example).

- Find and mitigate unexpected artifacts in the data.

- Optimize data processing and estimation algorithms, and obtain estimation results, once maneuver data is available.

- Compute a TTL correction term and subtract it from the range to obtain a corrected range data product.

The experience gained from this study allows to draw some further conclusions and ideas for improvement in view of future satellite missions, which shall be mentioned below.

6.3   Prospect

The main goals of this thesis for have been achieved. Although parts of this study have been performed and described in some detail, there are many interesting open questions and potential tasks left, in particular for the planning of future satellite missions. Some of these that are related to the content of this thesis shall be formulated in the following.

The CMC data from both pitch GF2 maneuvers performed on 22 June 2019 showed some unexpected behavior. The periodic angle oscillations seemed to be time shifted w.r.t. their response in the LRI range. By the time of writing this thesis, no explanation for this observation has been found. So far, this phenomenon occurred merely this one time, in June 2019. However, it should be investigated, since understanding the reason for it may be important, at least for the purpose of mitigating it in future missions. Since it occurred merely one time, a time stamp error is unlikely to be the true cause of this observation. Nevertheless, to exclude this possibility entirely, the question can be raised, whether it could be beneficial for future missions to utilize one and the same clock for time stamping the data from LRI, attitude sensors, and potentially also other instruments.

The model of the ARC error discovered during this study seems to work well, however, it is also rather heuristic. A more sophisticated model might not yield a noticeably advantage in the case of the LRI, since ARC is insignificant for the nominal science measurements in

any case. However, in view of the next generation of gravimetry missions, or beyond that, where more and more precise laser ranging is likely to become crucial, it may be beneficial to investigate this type of range error in more detail. An interesting event with regard to ARC in the LRI, which is not planned yet but may be performed at some point, is the swap of LRI roles. Recall that ARC depends merely on the pitch and yaw rates of the transmitter S/C. The only data point where GF2 was in transmitter mode is not very reliable, since it is based on a wiggle test (24 s) instead of two full CMC maneuvers (each 180 s). Should GF2 be put into transmitter mode, according to the theory, ARC is expected to occur for GF2 and not any more for GF1. This would be another confirmation of the theory. To the knowledge of the author, the possible encounter of ARC in inter-satellite laser interferometry has never been comprehensively studied for any of the missions currently being planned.

The activation of attitude control thrusters causes disturbances in the LRI range. The models for these disturbances that were used in this thesis are very coarse. In the end, these models did not influence the TTL estimation, since it was opted for simply excluding the data affected by thruster firings from the CMC analysis. However, such thruster disturbances posed a big challenge when attempting to show an improved performance of the LRI range after subtracting TTL. Moreover, if the disturbances could be removed almost completely, e.g. with an improved model, this might open up the possibility of estimating the TTL coupling factors directly from the LRI range, without using rotation maneuvers, i.e. with the "fit of noise" approach described in Sec. 3.3.2. For the planning of future missions, it shall be remarked that an interesting idea is to use a linear thruster control system instead of the "bang-bang" control utilized in GRACE and GFO. Should this be feasible, one might be able to get rid of several issues at once, including the phase jumps, certain disturbances in the ACC data, and the high frequency range variations caused by thruster firings. Note that linearly controlled attitude thrusters might still evoke residual linear accelerations, which would also be correlated to the TTL error, however, these would potentially be much easier to handle than the abrupt disturbances that are seen in GFO. Moreover, the TTL error itself could be minimized in the first place by minimizing pointing jitter, e.g. via an improved attitude control system (ACS). Finally, another potential improvement for the ACS could be to implement the option of programming a pre-defined time series of ACS set points, i.e. target attitudes. As mentioned in Sec. 4.3.4, then the rotation maneuver could be injected via this set point, instead of defining the control torque, which would allow in particular longer maneuver durations.

The overall quality of attitude data for GFO has proven to be sufficient for most applications. In fact, the situation has improved significantly compared to GRACE, due to the availability of IMU and FSM data, as well as the additional star camera head. Nevertheless, especially at high frequencies, there is still room for improvement of the attitude solutions, which may yield further improvements in some aspects. For the purpose of the study presented in this thesis, less noise in the attitude data would likely yield more accurate CF estimation. It would mean less noise in the TTL correction term as well. Moreover, it might become feasible to estimate TTL utilizing very high frequencies, at which the current attitude data is quite noisy. This would be another way of enabling the "fit of noise" approach. In view of future missions, improved attitude solutions might also serve as input to an improved ACS. Besides, numerous studies have shown that the quality of attitude determination as well as control do play a role in GFR, see [Gos18] as one example. Thus, there is ample motivation for increasing the capabilities of attitude sensing for future missions. The precision of LRI steering mirror data, for instance, could likely be considerably enhanced with relatively low effort by using electronics with higher resolution.

The analysis presented in this thesis furthermore opens new research paths beyond GFO and the LRI. For one thing, several future satellite geodesy missions such as Next Generation Gravity Mission (NGGM) are currently in the planning process, many of which will most likely utilize laser interferometry. Each such mission requires a similar analysis as the one presented here. In some cases, this work might contribute to these efforts, e.g. regarding the simulation

and estimation techniques, or the maneuver design. Nevertheless, the methods have to be adapted due to the different specifics of each individual mission. Although the main steps are described in this thesis with a lot of detail, being kept as general as possible, this adaptation may still require considerable effort.

TTL coupling is a well known issue in any laser interferometer, especially in space missions. A detailed study of TTL in satellite interferometers has been given in [Sch17]. For the LISA Pathfinder (LPF) mission, the TTL could be mitigated to a large extent in post-processing, by intentionally tilting the test mass and analyzing the interferometric readout [Wa17; Arm+18]. TTL can also be partly prevented or reduced from the outset, e.g. via the careful design of imaging systems, which has also been done in the case of GFO. TTL suppression via imaging systems was experimentally investigated for instance in [Chw+16; Sch+16; Trö+18] with regard to the Laser Interferometer Space Antenna (LISA) mission, which is a spaceborne gravitational wave detector currently planned for launch in the 2030's [DT+96]. Geometric TTL coupling effects have recently been discussed in [HSW22]. For the sake of completeness, the Chinese Taiji mission [Luo+20; HW17] shall be mentioned, which is currently being planned and based on a concept similar to that of LISA, and the TianQin mission [Luo+16], which is another gravitational wave detector planned to consist of three satellites in Earth orbits.

LISA is a particularly challenging application case of TTL analysis. Being based on laser interferometry, TTL is a natural error source expected to affect the science data of the mission. LISA is in many aspects different from GFO. The mission is planned to consist of three S/C in a triangular formation, where the separation between each pair is much larger than for GFO, in the order of 1 million km. This in itself makes it more susceptible to S/C pointing deviations, e.g. due to wavefront tilt [Sch17], or due to the already very low amount of received light power. Moreover, LISA comprises not one but several interferometers, which measure not only the separation between each satellite pair. Each S/C hosts a free-floating test mass that is shielded from external forces and acts as a gravitational reference sensor. The S/C separations are measured by the so-called long arm interferometers, and the separations between the S/C and their test masses are measured by the test mass interferometers. Thus, two types of TTL effects in LISA may be distinguished, those caused by S/C tilt and those caused by test mass tilt [Sch17]. The phase measurements of all interferometers must be combined in order to gain interesting science results, and, due to the different arm lengths, so-called time delay interferometry (TDI) must be utilized to suppress the noise originating from laser frequency jitter [TD20].

A TTL model for LISA must therefore be more complicated than for GFO. It will comprise different TTL effects, more model parameters, possible nonlinearities, and the TTL error must be estimated from the TDI output. For these reasons, investigating the applicability of the methods presented in this thesis to LISA is a challenging and extensive task. Nevertheless, many techniques are in principle adaptable, e.g. estimation algorithms, maneuver simulation, and maneuver design. Especially due to the complexity and high sensitivity of the LISA measurements, rotation maneuvers are presumptively going to be necessary. In this case, basic principles and insights regarding maneuver design may be derived from this study. Since the LISA satellites will be too far away from the Earth to utilize its magnetic field, potential maneuvers should be based on attitude thruster control, which is also covered in this thesis. In spite of the fact that LISA satellites will to the current planning be equipped with μN thrusters instead of mN thrusters like GFO, the insight of this study that thruster firings may cause significant disturbances may be helpful. Likewise, the awareness of possible ARC effects may prove beneficial.

Most importantly, this study has for the first time demonstrated the feasability of mitigating TTL coupling in inter-satellite laser interferometers in post-processing, and thus marks an important step. This thesis has shown that the theoretical considerations made during the mission planning and derived expectations have been proven to be accurate.

Appendix A

Further notes on pointing angles and rotations

Some further issues concerning rotations and inter-satellite pointing angles, defined in Sec. 2.1.3, are discussed in this appendix. App. A.1 investigates the influence on the pointing angles, when a different convention on the order of rotation is chosen. Appendix A.2 discusses the pointing angle bias which is introduced when there is an uncertainty about the absolute S/C attitude in form of a constant rotation, e.g. due to an uncertainty of the alignment of the star cameras.

A.1 Order of rotation

A single rotation can be described by the composition of three rotations around three different axes, e.g. each of the coordinate axes. For example, one can decompose a rotation R into rotations around the x, y, and z axes in that order. Call this the *x-y-z-convention*, because of the order of rotation.

$$R = R_z R_y R_x = R_z(\theta_z) R_y(\theta_y) R_x(\theta_x). \tag{A.1}$$

The corresponding rotation angles $\theta_x, \theta_y, \theta_z$ are called *Euler angles*. However, there are 12 possible ways to define these angles, depending on the order of rotation:

1. involving all three axes: x-y-z, y-z-x, z-x-y, x-z-y, z-y-x, y-x-z; and

2. involving two axes: x-y-x, x-z-x, y-x-y, y-z-y, z-x-z, z-y-z.

In Sec. 2.1.3, the Euler angles were computed with x-y-z convention. If the convention z-y-x is chosen instead, for instance, one obtains

$$R = \begin{pmatrix} R_{11} & R_{12} & R_{13} \\ R_{21} & R_{22} & R_{23} \\ R_{31} & R_{32} & R_{33} \end{pmatrix} = R_x R_y R_z$$

$$= \begin{pmatrix} c_y c_z & c_y s_z & s_y \\ c_x s_z + s_x s_y c_z & c_x c_z - s_x s_y s_z & -s_x c_y \\ s_x s_z - c_x s_y c_z & s_x c_z + c_x s_y s_z & c_x c_y \end{pmatrix}, \tag{A.2}$$

writing $s_x = \sin(\theta_x)$, $c_y = \cos(\theta_y)$, etc. Similar to the x-y-z convention, one obtains

$$\theta_x = \arctan\left(-\frac{R_{23}}{R_{33}}\right),$$

$$\theta_y = \arcsin\left(R_{13}\right), \tag{A.3}$$

$$\theta_z = \arctan\left(\frac{R_{12}}{R_{11}}\right).$$

It is noteworthy that R^T is a rotation around the same axis as for R, but with the opposite angle. If one examines a rotation matrix R with x-y-z convention, and R^T with z-y-x-convention, i.e. with reversed order, then one observes that also the particular angles of the decomposition have opposite sign, e.g.

$$\theta_y^{x-y-z,\text{forward}} = -\arcsin(R_{31}) = -\arcsin(R_{13}^T) = -\theta_y^{z-y-x,\text{backward}}. \tag{A.4}$$

This is intuitively clear, but also evident from

$$R^T = (R_z R_y R_x)^T = R_x^T R_y^T R_z^T. \tag{A.5}$$

Nevertheless, it is also clear that in general the angles depend on the order of rotation. As an example, let θ_y denote the Euler angle computed with z-y-x convention. I.e., denote

$$\theta_y^{z-y-x} = \theta_y. \tag{A.6}$$

On the other hand, one has

$$\theta_y^{x-y-z} = -\arcsin\left(R_{31}\right) = -\arcsin\left(\sin(\theta_x)\sin(\theta_z) - c_x \sin(\theta_y)\cos(\theta_z)\right). \tag{A.7}$$

A Taylor series expansion around $(0, 0, 0)$ now yields

$$\theta_y^{x-y-z} = \theta_y - \frac{1}{2}\theta_x \theta_z + \mathcal{O}(\theta^3). \tag{A.8}$$

Thus, the angles for different orders of rotation do not coincide in general, but they do to first order. The same is true for all other combinations. For small angles, differences between each two conventions of second and larger order are likely to be small as well. E.g., for angles of the order of 1 mrad, the deviations are roughly of the order of microradian.

A.2 Angle bias introduced by constant rotations

In Sec. 2.1.3, the pointing angles are defined as the Euler angles of the rotation $R_{\text{SF}}^{\text{LOSF}}$. Suppose this rotation is slightly manipulated by multiplication with a constant rotation which is close to the identity, and the product matrix is used in place of $R_{\text{SF}}^{\text{LOSF}}$. Certainly, the pointing angles defined by the alternative matrix should be different. In fact, some authors define the pointing angles as the Euler angles of the matrix $R_{\text{KF}}^{\text{LOSF}}$ instead of $R_{\text{SF}}^{\text{LOSF}}$, referring to the K-frame (KF) instead of the satellite frame (SF). Another case where this consideration may be useful is when there is an uncertainty in the star camera alignment, i.e. if the axes the SCA measurements refer to are not perfectly known.

Here it is shown that the differences in the pointing angles obtained from the two definitions are constant to first order. Although the following is true for any rotation matrices and their Euler angles, denote exemplarily $N = R_{\text{SF}}^{\text{LOSF}}$, and $M = R_{\text{KF}}^{\text{SF}}$, the latter of which is assumed

to be constant and close to the identity. Fix a coordinate system (x, y, z) and write these matrices in terms of Euler angles:

$$M = M_z(\psi_z)M_y(\psi_y)M_x(\psi_x), \tag{A.9}$$

$$N = N_z(\theta_z)N_y(\theta_y)N_x(\theta_x). \tag{A.10}$$

Let now $R = N \cdot M = R_{\mathrm{KF}}^{\mathrm{LOSF}}$ be the combined rotation matrix. Euler angles can also be assigned to R:

$$R = R_z(\theta_z')R_y(\theta_y')R_x(\theta_x'). \tag{A.11}$$

It has been derived in Sec. 2.1.3 that the Euler angles can be recovered from the matrix via

$$\theta_x' = \arctan\left(\frac{R_{32}}{R_{33}}\right) \tag{A.12}$$

$$\theta_y' = \arcsin\left(-R_{31}\right) \tag{A.13}$$

$$\theta_z' = \arctan\left(\frac{R_{21}}{R_{11}}\right) \tag{A.14}$$

Recalling Eq. (2.28) and multiplying out $R = N \cdot M$, one can compute the angles θ' in dependency of θ and ψ. Performing a Taylor expansion yields the second order approximations

$$\theta_x' \approx \theta_x + \psi_x + \theta_y\psi_z, \tag{A.15}$$

$$\theta_y' \approx \theta_y + \psi_y + \theta_x\psi_z, \tag{A.16}$$

$$\theta_z' \approx \theta_z + \psi_z + \theta_x\psi_y. \tag{A.17}$$

Recall that in the example considered here, θ_x etc. are the pointing angles as defined in this thesis, θ_x' etc. are pointing angles defined via $R_{\mathrm{KF}}^{\mathrm{LOSF}}$, and ψ_x etc. are the Euler angles of $R_{\mathrm{KF}}^{\mathrm{SF}}$. Very coarsely, each of these quantities are of the order of mrad, and thus the higher order terms are likely to be negligible most of the time.

Appendix B

Alternative derivation of the TMAVP error

Below, two alternative ways of computing the TMAVP error are described, in addition to the first variant that was given in Sec. 3.2.1.

B.1 Variant 2

Here the measured range shall be computed as the length of the vector pointing from one VP to the other VP. To this end, the two VPs, denoted by $\vec{V}_1$ and $\vec{V}_2$, are expressed in the same frame, which is here the line-of-sight frame (LOSF) of GFO satellite 1 (GF1), denoted by LOSF-1. Recall that $\vec{V}_i^{\text{SF-i}} = -(\Delta x_i, \Delta y_i, \Delta z_i)^T$ denotes the vector pointing from the CoM of S/C i to the VP, given in the SF of S/C i, cf. Eq. (3.22). $\vec{V}_1$ in LOSF-1 can be computed as

$$\vec{V}_1^{\text{LOSF-1}} = R_{\text{SF-1}}^{\text{LOSF-1}} \cdot \vec{V}_1^{\text{SF-1}}. \tag{B.1}$$

$\vec{V}_2$ in LOSF-1 is given by

$$\vec{V}_2^{\text{LOSF-1}} = \begin{pmatrix} \rho \\ 0 \\ 0 \end{pmatrix} + R_{\text{LOSF-2}}^{\text{LOSF-1}} \cdot R_{\text{SF-2}}^{\text{LOSF-2}} \cdot \vec{V}_2^{\text{SF-2}}, \tag{B.2}$$

where ρ is the true inter-satellite distance. The matrices $R_{\text{SF-1}}^{\text{LOSF-1}}$ and $R_{\text{SF-2}}^{\text{LOSF-2}}$ are depending on the inter-satellite pointing angles, see Eq. (2.28). The matrix $R_{\text{LOSF-2}}^{\text{LOSF-1}}$ is given by

$$R_{\text{LOSF-2}}^{\text{LOSF-1}} = \begin{pmatrix} -1 & 0 & 0 \\ 0 & -1 & 0 \\ 0 & 0 & 1 \end{pmatrix}, \tag{B.3}$$

i.e. it reverses the signs of the x and y axes. With this, the measured range $\bar{\rho}$ is given by

$$\bar{\rho} = \left\| \vec{V}_1^{\text{LOSF-1}} - \vec{V}_2^{\text{LOSF-1}} \right\|. \tag{B.4}$$

After some computation, a Taylor series expansion yields a lengthy approximation for the error $\delta\rho_{\text{VP}} = \bar{\rho} - \rho$, which converges to

$$\delta\rho_{\text{VP}} = \Delta x_1 + \Delta x_2 \tag{B.5}$$

$$+ \Delta z_1 \cdot \theta_{y,1} - \Delta y_1 \cdot \theta_{z,1} \tag{B.6}$$

$$+ \Delta y_1 \cdot \theta_{x,1}\theta_{y,1} + \Delta z_1 \cdot \theta_{x,1}\theta_{z,1} \tag{B.7}$$

$$- \frac{\Delta x_1}{2} \cdot (\theta_{y,1}^2 + \theta_{z,1}^2), \tag{B.8}$$

$$+ \Delta z_2 \cdot \theta_{y,2} - \Delta y_2 \cdot \theta_{z,2} \tag{B.9}$$

$$+ \Delta y_2 \cdot \theta_{x,2}\theta_{y,2} + \Delta z_2 \cdot \theta_{x,2}\theta_{z,2} \tag{B.10}$$

$$- \frac{\Delta x_2}{2} \cdot (\theta_{y,2}^2 + \theta_{z,2}^2), \tag{B.11}$$

as $\rho \to \infty$. Note furthermore that other error terms were ignored here. The first order approximation coincides with Eq. (3.32):

$$\delta\rho_{\text{VP}} \approx \delta\rho_{\text{VP-1}} + \delta\rho_{\text{VP-2}} \approx \Delta z_1\theta_{y,1} - \Delta y_1\theta_{z,1} + \Delta z_2\theta_{y,2} - \Delta y_2\theta_{z,2}, \tag{B.12}$$

B.2   Variant 3

A third way of computing $\delta\rho_{\text{VP}}$, which is described in [Mül17], uses analytical raytracing. That is, the geometric mirror positions and their orientations are described by position and normal vectors. The measured range can then be computed analytically in terms of pointing angles. This yields a first order approximation of the TTL error, which is compatible with Eqs. (3.32) and (B.12). Furthermore, static misalignments of the TMA mirrors can be introduced, which has an impact on the TTL coupling factors, as described in Sec. 3.2.2.

Appendix C

KBR calibration

C.1 Geometric ranging error of the KBR

The LRI TTL coupling is dominated by geometrical pathlength variations due to the offsets between VPs and S/C CoMs. A similar error occurs in the K/Ka-band ranging (KBR) measurements, due to the fact that it measures the distance between the two antenna phase centers (APC) of the microwave antennas on both S/C, the RPs for the KBR. The nominal APC position is not in the S/C CoM, but on the SF x axis, almost 1.5 m away from the CoM in the direction of the distant S/C. Thus, the offset vector is this x displacement plus a small unintended displacement, which may be as large as 1 mm.

This error may be modeled in the same way as the TMAVP error in the LRI. However, for the KBR, due to the much larger x component of the offset, the dominating part of the error is quadratic in the pointing angles, namely in pitch and yaw. In the notation of Eq. (3.21), the parameters b_{22} and b_{33} are very large in the case of the KBR. This can be seen by applying the derivation given in App. B. The critical terms are clearly (B.8) and (B.11). Denoting by $\vec{Q} = (\Delta x, \Delta y, \Delta z)^T$ the APC position w.r.t. the S/C CoM, given in SF, one has

$$b_{11} = b_{22} = \frac{\Delta x}{2} \cdot \text{ rad}^{-2}. \tag{C.1}$$

Note that here Δx appears with a different sign compared to (B.8) or (B.11), since in App. B the offset vector was defined with a different sign.

Another way of approximating the ranging error is by the negative projection of the vector $\vec{Q}$ pointing from CoM to APC, onto the line-of-sight (LoS), which is a valid approach for small angles. Denote by $\delta\rho_{\text{APC}}$ the error due to the APC offset, and by ψ the angle between LoS and $\vec{Q}$. Then

$$\delta\rho_{\text{APC}} \approx -\langle \vec{e}_{\text{LOS}}, \vec{Q} \rangle = -|\vec{Q}| \cdot \cos(\psi). \tag{C.2}$$

Note that it is appropriate to describe the rotation by angle ψ between the LoS and $\vec{Q}$ as the composition of two rotations. One of them rotates the LoS to the SF x axis, describing the actual pointing deviation. The second rotation is due to the angle ψ_0 between the SF x axis and $\vec{Q}$, which can be as large as 1 mrad and is assumed to be constant for short time spans. For illustration purposes, write this as $\psi = \psi_0 + \delta\psi$, where ψ_0 is constant and $\delta\psi$ describes the pointing jitter.

In the nominal case, the SF x axis and $\vec{Q}$ are parallel, i.e. $\psi_0 = 0$. In that case, the law of cosines implies that $\cos(\psi) \approx \cos(\theta_y)\cos(\theta_z)$, where θ_y and θ_z denote pitch and yaw angles according to the definition given in Sec. 2.1.3. Then, one has

$$\delta\rho_{\text{APC}} \approx -|\vec{Q}| \cdot \cos(\theta_y)\cos(\theta_z) \tag{C.3}$$

$$\approx |\vec{Q}| \cdot \left(\frac{\theta_y^2}{2} + \frac{\theta_z^2}{2} - 1 \right), \tag{C.4}$$

which is compatible with Eq. (C.1). Once again, one may neglect the constant term, since one is interested in the biased range. This case is illustrated in Fig. C.1 a). In contrast, regard case b) of Fig. C.1, where the SF x axis is not aligned with $\vec{Q}$, i.e. $\psi_0 \neq 0$. The same pointing jitter $\delta\psi$ as in case a) then causes a different ranging error.
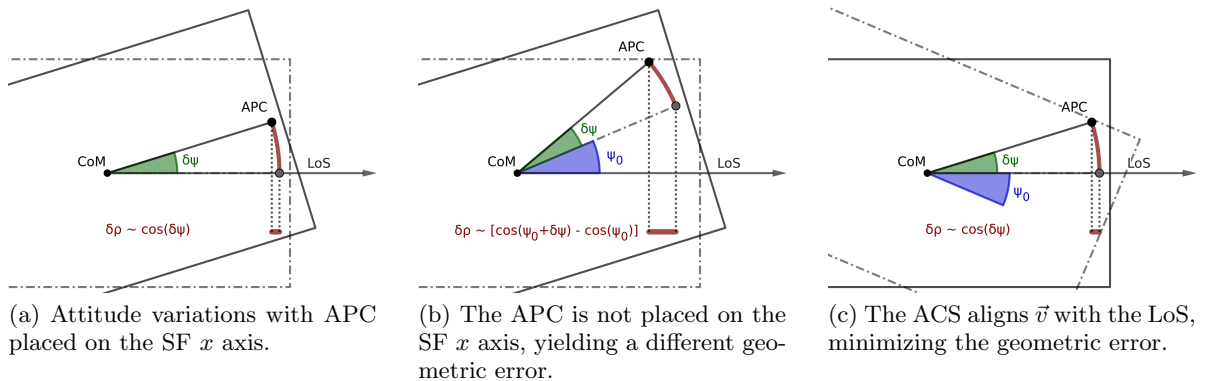

(a) Attitude variations with APC placed on the SF x axis.

(b) The APC is not placed on the SF x axis, yielding a different geometric error.

(c) The ACS aligns $\vec{v}$ with the LoS, minimizing the geometric error.

Figure C.1: KBR geometric error in different constellations.

In order to minimize the ranging error, it is beneficial to choose the target orientation of the ACS such that it attempts to align $\vec{Q}$ with the LoS, as depicted in case c) of Fig. C.1. To this end, the so-called K-frame (KF) is defined, with $\vec{Q}/|\vec{Q}|$ as the x axis, see Sec. 2.1.1. The pointing angles can then actually be defined by a rotation between KF and LOSF as done e.g. in [BFK12], rather than between SF and LOSF as done in this thesis. Denote these slightly different angles by θ'_y and θ'_z, for pitch and yaw, respectively [2]. Then, a correction term called antenna offset correction (AOC) is computed by

$$\text{AOC} = -\frac{|\vec{Q}|}{2}(\theta'^2_y + \theta'^2_z), \qquad (C.5)$$

which is reported in the KBR1B data product. The range can then be corrected by adding this term to the KBR range [Wen+19].

Computation of the AOC term obviously requires knowledge of the APC position and the pointing angles. The pointing angles are derived from SCA1B data, whereas the APC position has to be estimated. This is the objective of the KBR calibration maneuvers, which are described in the following.

C.2   KBR calibration maneuver

The APC positions are predetermined before the launch, however, they have to be estimated again in orbit, in case they have changed during launch or in space. This is achieved by the use of the so-called KBR calibration maneuvers. The algorithms for estimating the APC positions are explained in detail in [Wan03]. Here merely the rotation maneuvers are described.

The KBR calibration maneuvers are fundamentally different from the CMC maneuvers. For instance, they are performed at different ACS set points. That is, the satellite is first brought to a certain angular offset, before the rotational sequence begins. Then, the respective angle oscillates around that value. The angular offsets are $\pm 2° \approx \pm 35$mrad, and the targeted amplitude of the angle oscillation is $1° \approx 17.5$mrad. Since the KBR range is insensitive to roll variations, only pitch and yaw maneuvers need to be performed. Thus, there are 4 different

---

[2]Note that, to first order, $\theta'_y = \theta_y + const.$, where θ_y is the pitch angle as defined in Sec. 2.1.3 of this thesis. The same holds for roll and yaw, as is pointed out in App. A.2.

types of KBR maneuvers: pitch (+), pitch (-), yaw (+), yaw (-). E.g., the sign (+) indicates an angular offset of $+2°$. Each maneuver consists of 15 cycles with a period of $1/f_0 = 250$ s, thus the duration is $T = 3750$ s. Taking pitch (+) as an example, the pitch angle during the maneuver can be described as

$$\theta_y(t) = 2° + 1° \cdot \sin\left(2\pi f_0 t\right). \tag{C.6}$$

The large angular offset and amplitude of the KBR maneuvers are chosen in order to increase the effect in the KBR range, which increases the estimation accuracy. Unfortunately, the consequence is that KBR maneuvers are not suited for LRI TTL calibration, since the LRI can tolerate merely a few mrad of pointing deviation. Moreover, in order to achieve such large angle oscillations, attitude control thrusters are used. Experience with the LRI data has shown that the use of attitude control thrusters for calibration maneuvers is questionable, since their activation causes undesired linear accelerations, which are measured by the LRI and thus can be harmful for the parameter estimation.

The results of the KBR calibrations for GRACE have been reported in [Wan03]. The APC offsets that were found are in the order of a few millimeters. Moreover, the algorithms that were applied also yield estimations of the misalignments between the SF and SCA frames, which were found to be in the order of a few milliradians. It was later reported, e.g. in [Hor+11], that the computation of the correction term still seemed to introduce some error to the range. This is discussed in the following.

C.3 Errors introduced by the AOC term

It has become clear that static angle offsets matter for the correction of the geometric error, which is due to the nonlinear dependency. Therefore, applying the AOC also introduces an error to the KBR range, by not using the correct angles. This is happening for two reasons. Firstly, the angles themselves may be biased, e.g. due to the fact that the star camera frames are not known exactly. I.e.,

$$\hat{\theta}_y = \theta'_y + \delta\theta'_y, \tag{C.7}$$
$$\hat{\theta}_z = \theta'_z + \delta\theta'_z, \tag{C.8}$$

where θ'_y is the true pitch angle and $\delta\theta'_y$ the measurement bias, and accordingly for yaw. Recall that the AOC is computed using the angles θ'_y and θ'_z, defined via $R_{\mathrm{KF}}^{\mathrm{LOSF}}$, cf. Eq. (C.5). In App. C.4, it is derived that the error introduced by such angle biases is approximately

$$\delta\mathrm{AOC} \approx -|\vec{Q}|\left(\delta\theta'_y\theta'_y + \delta\theta'_z\theta'_z\right), \tag{C.9}$$

for one S/C, where $\vec{Q}$ denotes the APC position. If $|\vec{Q}|$ and the angle biases are viewed as invariant, this is simply a type of TTL error, which is of the order of $\delta\theta'$ m rad^{-2}, i.e. of the order of 1 mm rad^{-1} linear coupling for an angle bias of 1 mrad.

Secondly, the estimation of the APC may not be accurate. Let $\hat{\vec{Q}}$ denote the estimated APC position. If the difference between estimated and true APC position is

$$\delta\vec{Q} = \hat{\vec{Q}} - \vec{Q}, \tag{C.10}$$

then, as derived in App. C.5, this results in pitch and yaw biases of

$$\delta\theta_y \approx \frac{1}{|\vec{Q}|} \cdot \delta Q_z, \tag{C.11}$$

$$\delta\theta_z \approx \frac{1}{|\vec{Q}|} \cdot \delta Q_y, \tag{C.12}$$

where $\delta\vec{Q} = (\delta Q_x, \delta Q_y, \delta Q_z)^T$ is the APC estimation error with components in the SF. This introduces further linear pitch and yaw coupling terms of the order of $1\,\mathrm{mm\,rad^{-1}}$, assuming that $\delta Q_y \approx \delta Q_z \approx 1$ mm.

In [Hor+11], it has been pointed out that such errors in the AOC yields a significant reduction of the quality of gravity fields. Thus, techniques have been developed to re-estimate the angle biases, as well as the APC position, in order to mitigate this problem. The angle biases that were found were up to a few milliradian, and the newly determined APC position differed from the previous by up to a few millimeters. According to computations of the author, such mistakes yield an additional error of the order of some $\mathrm{mm\,rad^{-1}} \cdot \theta_{y,z}$, which is introduced by applying the AOC.

Significant biases of SCA-derived angles were also found in [BFK12], as well as a strong dependency of the S/C attitude control on the different quality of SCA heads. In general, SCA instrument noise or degraded attitude solutions due to SCA blindings yield an additional AOC error. The performance of the GRACE SCA quaternions and its influence on gravity field solutions has been studied extensively, cf. [BF14; Iná+15; Har16; HS19; Gos18], and many issues have been discovered. E.g., for GRACE, the alignment of individual SCA heads may have drifted by up to 500 µrad during the mission life time of about 15 years [Iná+15], which is likely due to thermal effects. In terms of the measurement noise of pointing angles, the situation has obviously improved a lot for GFO, since gyroscopes and LRI FSM provide high quality attitude information.

C.4   Influence of angle bias on the KBR AOC term

If biased angles are used to compute the AOC term for correcting the KBR range, a nonconstant error is added to the range. This error shall be quantified here. Let $\hat{\theta}_i$, $i = x, y, z$ denote the biased angles, i.e.

$$\hat{\theta}_i = \theta_i + \delta\theta_i, \tag{C.13}$$

where θ_i are the true angles. Furthermore, denote by $\hat{\mathrm{AOC}}$ the AOC term computed from biased angles, and denote by AOC the AOC term computed using the correct angles, i.e.

$$\hat{\mathrm{AOC}} = -\frac{|\vec{Q}|}{2} \cdot \left(\hat{\theta}_y^2 + \hat{\theta}_z^2 \right), \tag{C.14}$$

$$\mathrm{AOC} = -\frac{|\vec{Q}|}{2} \cdot \left(\theta_y^2 + \theta_z^2 \right), \tag{C.15}$$

where $\vec{Q}$ is the APC position w.r.t. the S/C CoM. Here the fact that the above term needs to be computed and added up for both S/C is omitted. After a quick computation, one obtains

$$\hat{\mathrm{AOC}} - \mathrm{AOC} = -|\vec{Q}| \left(\delta\theta_y \theta_y + \delta\theta_z \theta_z + 0.5 \cdot (\delta\theta_y^2 + \delta\theta_z^2) \right) \tag{C.16}$$

$$\overset{(*)}{=} -|\vec{Q}| \left(\delta\theta_y \theta_y + \delta\theta_z \theta_z \right), \tag{C.17}$$

where $(*)$ is assuming that $\delta\theta_y$, $\delta\theta_z$ and $\vec{Q}$ are time invariant. Recall that constants are irrelevant for the biased range. Then, the error that is introduced by applying an AOC term computed with biased angles, is behaving like a TTL coupling error, with linear pitch and yaw coupling of about $1.5 \cdot \delta\theta_{y,z} \,\mathrm{m\,rad^{-2}}$.

C.5   Angle bias introduced by APC estimation error

The goal of this section is to quantify the angle bias that is introduced by using an estimated APC position, which differs from the true APC position. Nominally, the KF is defined using

the APC position $\vec{Q}$, cf. Sec. 2.1.1. For $\vec{Q} = (Q_x, Q_y, Q_z)$, with components in the SF, one can write

$$X_{\mathrm{KF}} = \frac{P}{|\vec{Q}|}, \tag{C.18}$$

$$Y_{\mathrm{KF}} = \frac{1}{|\vec{Q}|^2} \begin{pmatrix} -Q_x Q_y \\ Q_x^2 + Q_z^2 \\ -Q_y Q_z \end{pmatrix}, \tag{C.19}$$

$$Z_{\mathrm{KF}} = \frac{1}{|\vec{Q}|} \begin{pmatrix} -Q_z \\ 0 \\ Q_x \end{pmatrix}. \tag{C.20}$$

From the axes, the rotation $R = R_{\mathrm{KF}}^{\mathrm{SF}}$ can be computed via

$$R_{\mathrm{KF}}^{\mathrm{SF}} = \begin{pmatrix} X_{\mathrm{KF}}^T \\ Y_{\mathrm{KF}}^T \\ Z_{\mathrm{KF}}^T \end{pmatrix}. \tag{C.21}$$

Applying Eqs. (2.29), one can compute the Euler angles of R. One obtains

$$\psi_x = \arctan\left(\frac{R_{32}}{R_{33}}\right) \approx 0, \tag{C.22}$$

$$\psi_y = -\arcsin(R_{31}) \approx \frac{1}{|\vec{Q}|} \cdot Q_z, \tag{C.23}$$

$$\psi_z = -\arctan\left(\frac{R_{21}}{R_{11}}\right) \approx \frac{1}{|\vec{Q}|} \cdot Q_y, \tag{C.24}$$

for roll, pitch, and yaw axes, respectively.

Recall that the KBR APC position is estimated using the KBR calibration maneuvers. Denote this estimated position by $\hat{\vec{Q}}$, such that

$$\hat{\vec{Q}} = \vec{Q} + \delta\vec{Q}, \tag{C.25}$$

with an estimation error $\delta\vec{Q}$. The angle biases which result from using $\hat{\vec{Q}}$ instead of $\vec{Q}$ can then be written as

$$\delta\psi_x \approx 0, \tag{C.26}$$

$$\delta\psi_y \approx \frac{1}{|\vec{Q}|} \left(\frac{|\vec{Q}|}{|\hat{\vec{Q}}|} \hat{Q}_z - Q_z \right) \approx \frac{1}{|\vec{Q}|} \delta Q_z, \tag{C.27}$$

$$\delta\psi_z \approx \frac{1}{|\vec{Q}|} \left(\frac{|\vec{Q}|}{|\hat{\vec{Q}}|} \hat{Q}_y - Q_y \right) \approx \frac{1}{|\vec{Q}|} \delta Q_y. \tag{C.28}$$

In other words, the APC estimation error has the effect that the KF is not correctly defined. The resulting angle biases derived above will couple into the KBR range, when the AOC term is computed and applied. The biases for pitch and yaw are of the order of $|\delta\vec{Q}|/|\vec{Q}|$ rad, whereas the bias for the roll angle is zero in the first order approximation.

Appendix D

Solar radiation pressure model

In the following, a simple model is developed to compute the solar radiation pressure (SRP) force and acceleration acting on a S/C. Here merely the direct SRP shall be computed, which means that no pressure is considered which is caused by any solar radiation that has been reflected before, e.g. by the Earth, which is called Earth albedo pressure, or any other radiation that is not coming directly from the sun. For more theoretical background, cf. [Mon00].

D.1 SRP force model

The solar flux

$$\phi = \frac{\dot{E}}{A} \tag{D.1}$$

is the rate at which energy E of electromagnetic radiation originating from the sun passes through an area A. For now, the solar flux is assumed not to depend on time, but only on the satellite's distance to the Sun. In fact, suppose here that

$$\phi_\odot = 1361 \ \mathrm{W\,m^{-2}}, \tag{D.2}$$

at a distance of 1 AU (astronomical unit). Since the solar flux decreases with the square of the distance, say x, the solar flux at this distance is given by

$$\phi(x) = 1361 \left(\frac{AU}{x} \right)^2 \ \mathrm{W\,m^{-2}}. \tag{D.3}$$

Note that the momentum p of a photon with energy E is given by

$$p_{\mathrm{photon}} = \frac{E}{c}. \tag{D.4}$$

If the photon is fully absorbed by a planar object with normal vector pointing towards the sun, then the whole momentum passes on to the momentum[7] of this object (e.g. the S/C). I.e.,

$$\dot{p}_{\mathrm{S/C}} = \dot{p}_{\mathrm{photon}} = \frac{\dot{E}}{c}. \tag{D.5}$$

Hence, the force acting on the S/C is

$$F = ma = \dot{p}_{\mathrm{S/C}} = \frac{\phi}{c} \cdot A, \tag{D.6}$$

with m being the S/C total mass, and with A denoting the surface area. This corresponds to a pressure

$$P = \frac{F}{A} = \frac{\phi}{c}. \tag{D.7}$$

Denote by

$$P_\odot = \frac{\phi_\odot}{c} = 4.54 \cdot 10^{-6} \text{ Pa} \qquad (D.8)$$

the solar radiation pressure (SRP) at 1 AU distance. Finally, this yields the resulting acceleration:

$$a = \frac{F}{m} = \frac{P_\odot}{m} \cdot \left(\frac{AU}{x}\right)^2 \cdot A. \qquad (D.9)$$
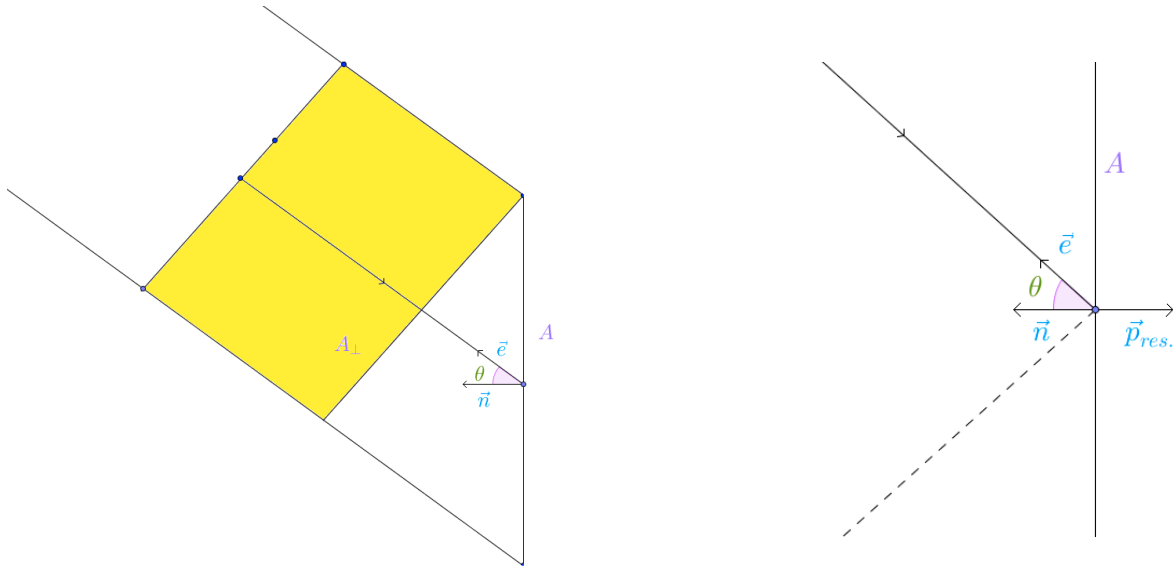
Figure D.1: Left: Illustration of the cross-sectional area. Right: Reflecting photon.

Suppose now that the surface is not perpendicular to the incident photon. In order to account for the smaller amount of sunlight that reaches the surface in this case, A must be replaced by its perpendicular part,

$$A_\perp = \cos(\theta) \cdot A,$$

where θ is the angle between surface normal $\vec{n}$ and the normalized vector $\vec{e}$ that points towards the sun:

$$\cos(\theta) = \langle \vec{n}, \vec{e} \rangle.$$

Further, not all of the photons are being absorbed. When a photon is being reflected from the surface, by momentum conservation, the resulting momentum passing on to the satellite is

$$\vec{p}_{res.} = -2p_{\text{photon}} \cdot \cos(\theta) \cdot \vec{n},$$

cf. Fig. D.1. Hence, the resulting acceleration acting on a surface with normal vector $\vec{n}$ and reflection coefficient ϵ, at an angle θ, is

$$\vec{a} = -\frac{P_\odot}{m} \left(\frac{AU}{x}\right)^2 \cos(\theta) A \cdot ((1 - \epsilon) \cdot \vec{e} + 2\epsilon \cos(\theta) \cdot \vec{n}). \qquad (D.10)$$

---

[7]Note that the relativistic momentum is $p = \gamma m_0 v$, where $\gamma = 1/\sqrt{1 - v^2/c^2}$ is the Lorentz factor, m_0 is the rest mass, and the product γm_0 is the inertial mass of the S/C. For a satellite moving at a speed v close to $8 km/s$, however, the inertial mass coincides with the rest mass up to a deviation in the order of 10^{-10}, which is negligible.

Each of the GFO satellites has 8 surfaces that can be exposed to the sunlight. The surface specifications are given in [Wen+19]. The values which are considered by this model can be summarized in a 6×8 matrix with columns

$$\Pi = \begin{pmatrix} \vec{n}_1 & \cdots & \vec{n}_8 \\ A_1 & \cdots & A_8 \\ \epsilon_1 & \cdots & \epsilon_8 \\ \eta_1 & \cdots & \eta_8 \end{pmatrix}, \tag{D.11}$$

where, for $i = 1, \ldots, 8$, $\vec{n}_i$ is the normal vector of the surface i, A_i is its area, and ϵ_i and η_i are the reflection coefficients for visible light and infrared (IR) light, respectively. The normal vectors are given in SF and must be rotated to Earth-centered inertial (ECI) before being used for computations. Of course, the model can be adapted to satellites other than GFO, by replacing the surface specifications.

The contribution of each surface has to be computed and they have to be added up. In total, one obtains the following formula for visible light.

$$\vec{a} = -\frac{P_\odot}{m} \left(\frac{AU}{x} \right)^2 \sum_i \left[\cos(\theta_i) A_i \cdot ((1 - \epsilon_i) \cdot \vec{e} + 2\epsilon_i \cos(\theta_i) \cdot \vec{n}_i) \right], \tag{D.12}$$

where the sum is to be taken over all those surfaces i which are exposed to sunlight, i.e. over all surfaces i such that

$$\langle \vec{n}_i, \vec{e} \rangle > 0, \tag{D.13}$$

where $\langle \cdot, \cdot \rangle$ denotes the scalar product. It is assumed here that, in terms of energy flux, the sunlight consists by 44% of visible light and by 56% of IR light, neglecting ultraviolet (UV) light. Under this assumption, the combined formula reads

$$\vec{a} = -\frac{P_\odot}{m} \left(\frac{AU}{x} \right)^2 \sum_{i=1}^{8} \left[\cos(\theta_i) A_i \cdot ((1 - \zeta_i) \cdot \vec{e} + 2\zeta_i \cos(\theta_i) \cdot \vec{n}_i) \right], \tag{D.14}$$

where

$$\zeta_i = 0.44 \cdot \epsilon_i + 0.56 \cdot \eta_i$$

is the combined reflection coefficient, for $i = 1, \ldots, 8$.

Furthermore, this formula holds only if the spacecraft is in full sunlight. This equation must hence be multiplied by a shadow function, which equals 1 in the case of full sunlight, 0 in shadow (umbra) and between 0 and 1 in halfshadow (penumbra). A model for the shadow function is presented below, in App. D.2. In total, this yields the following model for the acceleration acting on a GFO S/C, which is caused by SRP:

$$\vec{a} = -\nu \frac{P_\odot}{m} \left(\frac{AU}{x} \right)^2 \sum_i \left[\cos(\theta_i) A_i \cdot ((1 - \zeta_i) \cdot \vec{e} + 2\zeta_i \cos(\theta_i) \cdot \vec{n}_i) \right] \tag{D.15}$$

Computing SRP accelerations requires knowledge of satellite positions and attitudes, in the case of GFO available via the Level-1B data, as well as Earth and Sun positions, which are provided in the Development Ephemerides by National Aeronautics and Space Administration (NASA)'s Jet Propulsion Laboratory (JPL), e.g. JPL DE430. The solar flux data for the analysis performed for this thesis has been downloaded from the homepage of the University of Colorado Boulder:
http://lasp.colorado.edu/home/sorce/data/tsi-data/

D.2 Model of the shadow function

Here, a shadow function ν depending on Sun and S/C positions shall be derived, which is 1 if the satellite is in full sunlight, 0 if it is in full shadow, and between 0 and 1 if it is in penumbra. Neglecting the Earth's oblateness and atmosphere, consider the following sketch, which is furthermore assumed to be rotationally symmetric w.r.t. the horizontal axis.
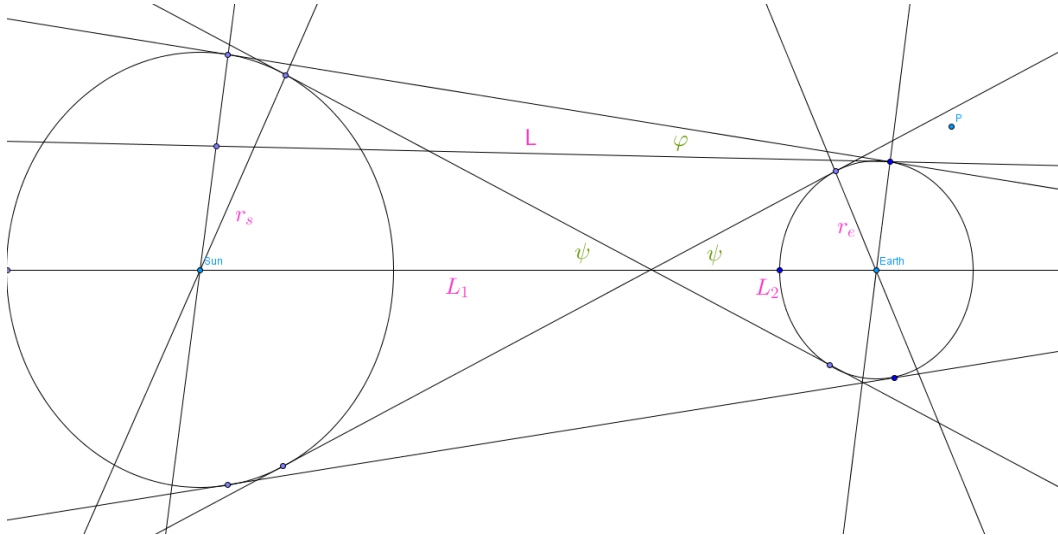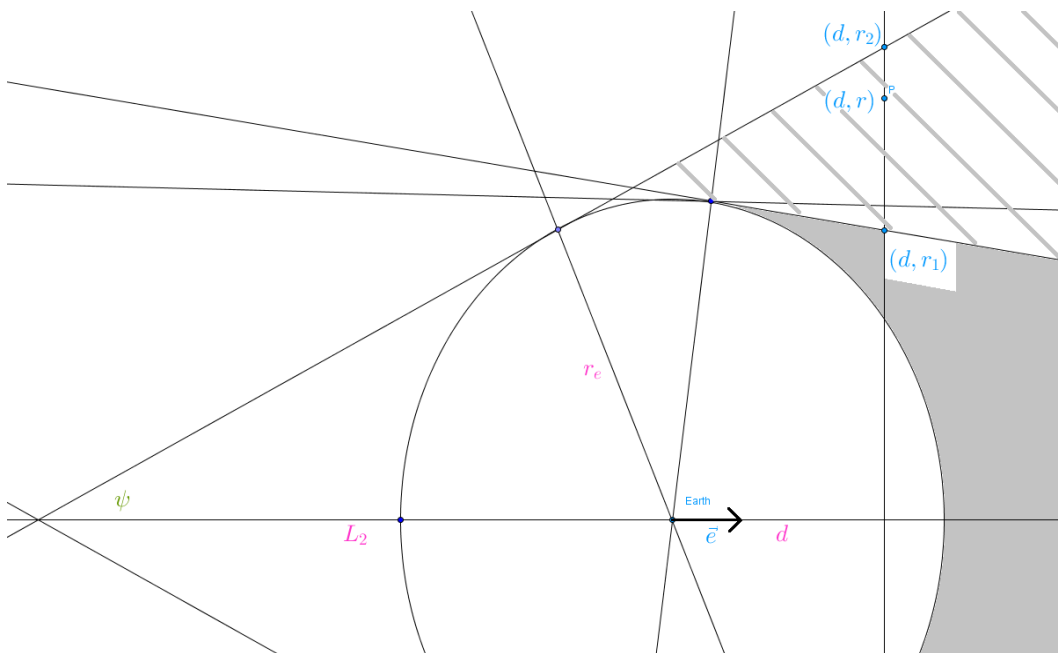

Let L be the distance between Sun and Earth, such that $L = L1 + L2$ as illustrated, and denote by r_s and r_e the radii of Sun and Earth, respectively. Then the angles are given by

$$\sin(\psi) = \frac{r_s}{L_1} = \frac{r_e}{L_2}$$

$$\Rightarrow \qquad L \cdot \sin(\psi) = r_s + r_e,$$

$$\text{and} \qquad L \cdot \sin(\varphi) = r_s - r_e.$$

In the following figure, the gray area indicates umbra (full shadow), whereas the shaded area indicates penumbra.

With the Earth centered at $(0,0)$, let $P = (d,r)$ be the position of the satellite and $S = (-L, 0)$ the position of the sun. Then one has

$$\vec{e} = -\frac{\vec{S}}{L},$$
$$d = \langle \vec{e}, \vec{P} \rangle,$$
$$r_2 = (L_2 + d) \cdot \tan(\psi),$$
$$r = \|\vec{P} - d \cdot \vec{e}\|,$$
$$r_1 = \frac{r_e}{\cos(\varphi)} - d \cdot \tan(\varphi),$$

where the last equation can be seen as follows.
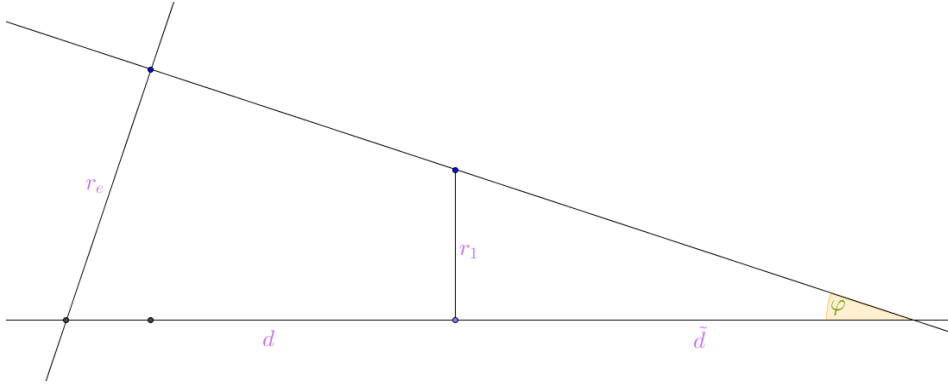
In the above sketch,

$$\sin(\varphi) = \frac{r_e}{d + \tilde{d}}$$
$$\Rightarrow \qquad \tilde{d} = \frac{r_e}{\sin(\varphi)} - d,$$
$$\tilde{d} = \frac{r_1}{\tan(\varphi)}$$
$$\Rightarrow \qquad r_1 = \left(\frac{r_e}{\sin(\varphi)} - d \right) \cdot \tan(\varphi)$$
$$= \frac{r_e}{\cos(\varphi)} - d \cdot \tan(\varphi).$$

With this, one has

$$
\begin{aligned}
\langle \vec{P}, \vec{e} \rangle \leq 0 \quad &\Rightarrow \quad \nu = 1, \\
\langle \vec{P}, \vec{e} \rangle > 0 \ \& \ r \geq r_2 \quad &\Rightarrow \quad \nu = 1, \\
\langle \vec{P}, \vec{e} \rangle > 0 \ \& \ r \leq r_1 \quad &\Rightarrow \quad \nu = 0, \\
\langle \vec{P}, \vec{e} \rangle > 0 \ \& \ r_1 < r < r_2 \quad &\Rightarrow \quad 0 < \nu < 1.
\end{aligned}
\tag{D.16}
$$

The last case is the penumbra case. The fraction of the sunlight that reaches the spacecraft in penumbra is modeled as

$$\nu = \frac{r - r_1}{r_2 - r_1}.$$

This is an approximation, but the error is very small since $r_s/L \ll 1$. This completes the shadow model.

To summarize, the following formula was derived for the acceleration caused by solar radiation pressure, cf. Sec. 4.2.2.

$$\vec{a} = -\nu \frac{P_\odot}{m} \left(\frac{AU}{x} \right)^2 \sum_i \left[\cos(\theta_i) A_i \cdot ((1 - \zeta_i) \cdot \vec{e} + 2\zeta_i \cos(\theta_i) \cdot \vec{n}_i) \right]. \qquad \text{(D.17)}$$

Here the following simplifications (in descending order of urgency) were made:

1. The solar flux was assumed not to depend on time (i.e. no irradiance fluctuation or solar flare etc.).

2. The Earth's oblateness as well as the Earth's atmosphere were ignored, resulting in a simplified penumbra transition.

3. It was assumed that the sunlight consists of visible and infrared light only. In terms of energy, sunlight consists only by about 47% of visible light and by 46% of IR (and 7% UV, roughly); it was assumed that it consists by 54% of visible and by 46% of IR light. Since the surfaces' reflection coefficients for IR (or UV) light differ from those for visible light, the formula for the SRP acceleration needs to be adjusted accordingly.

4. For the penumbra model a circle shaped sun was assumed for the determination of the fraction of the sunlight that reaches the spacecraft.

5. In the photon reflection case, diffuse reflection was ignored, as well as energy conservation considerations (reflected photons gain a Doppler shift because of S/C velocity; freqeuncies (& hence energy & hence momentum) of photons change depending on S/C velocity w.r.t photons, special relativistic effect).

All of these details may be integrated at a later stage, however, the latter is negligible for nonrelativistic spacecraft velocities.

Appendix E

LRI range spectrum at high frequencies

As mentioned in this thesis, the LRI range spectrum at frequencies above ∼40 mHz is dominated by range variations due to nongravitational forces, caused by attitude thruster firings or external forces such as solar radiation pressure (SRP). Since these are physical range variations, not measurement noise, this raises the question what the true LRI noise level at these frequencies is. It will be shown in this appendix that these variations can be removed from the range to some extent, which enables a more detailed analysis of the LRI noise spectrum. One way of achieving this is to model the variations due to attitude control thruster firings using THR1B data, which is described in App. E.1. Since the nongravitational accelerations are measured by the ACCs, another way is to use ACT1A data, which is described in App. E.2. In App. E.3, the LRI range ASD at high frequencies is analyzed, and the results of the two methods are compared.

E.1 Reducing range variations using THR1B data

The GFO attitude control thrusters are described in Sec. 2.3 of this thesis. A sample of the geographic locations of attitude control thruster firings is depicted in Fig. E.1, for the time from 1 to 8 December 2019. Notably, the roll thruster firings appear to be clustering around the geomagnetic equator in a certain pattern, and in another pattern for the yaw thruster firings. This is a consequence of the fact that the GFO satellite attitudes are controlled preferentially by magnetic torque rods (MTR). Attitude thrusters are used when MTRs are not able to produce the required torque, which depends on the geomagnetic field. Note further that the near-polar orbits of the satellites favor pitch axis control with MTRs, which is the reason why pitch thruster firings (marked in blue and red) are scarce for both satellites.
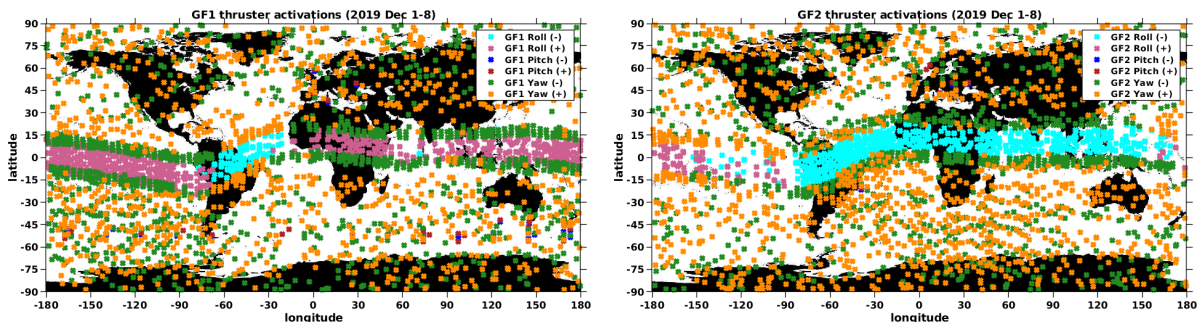
Figure E.1: Geographic locations of thruster firings between 1 and 8 December 2019. Left: GF1. Right: GF2.

Figure E.2 shows all firing durations of the GFO attitude control thrusters, i.e. "on-times" according to THR1B data, cf. [Wen+19], until November 2021. Most firings that occur have a standard on-time that can also be changed, which has been done for instance in the end of 2018. There are exceptions to the standard on-times when necessary. For example, longer on-times are sometimes required before a CMC, in order to minimize the absolute pointing deviation at the maneuver start, since during the maneuver the thruster control is switched off for 180 seconds.

The linear acceleration caused by a thruster firing is given by the force vector of that thruster divided by the satellite mass. In particular, it is independent of the position of the thruster, as opposed to the torque, cf. Eq. (2.44). Attitude control thrusters are therefore activated in pairs with opposite directions, cf. Sec. 2.3.1. If the two force vectors do not sum to zero, the resulting force causes unintended linear accelerations of the satellite. Since these cause physical movement of the satellites, they also vary the inter-satellite range, which is measured by the LRI. Note that these residual linear accelerations ought not to be confused with the phase jumps reported in [Abi+19], which are related to thruster firings in a different way.

The variations in the LRI range caused by such linear accelerations can disturb the analysis of CMC maneuvers, cf. Sec. 5.1.4. In fact, the linear accelerations caused by the thruster firings are correlated to the angular accelerations caused by it. Linear accelerations in LoS direction accumulate to range variations in a similar way as the angular accelerations accumulate to S/C pointing variations. As a consequence, the resulting variations in the range are correlated to the resulting variations in the S/C pointing angles as well. Due to this, it is challenging to distinguish between these range variations and TTL, cf. Sec. 5.4. In the following, an approach to derive models of these range variations is described.

On each GFO satellite there are two types of thrusters per axis: roll (+), roll (-), pitch (+), pitch (-), yaw (+), yaw (-), where +/- indicates the direction of rotation. For each of the six types, there is one pair of thrusters, accomodated in a symmetric pattern around the S/C CoM. The attitude thruster accomodation for GFO is depicted in Fig. 2.10 in Sec. 2.3.1. Here it is assumed that those two thrusters are activated exactly simultaneously, at the times reported in the THR1B data. For simplicity, it is also assumed here that the SF x axis coincides with the LoS axis, which is in the nominal fine-pointing mode true up to a rotation of a few mrad. This assumption implies that the effect of a given thruster pair on the range depends merely on the firing duration, and does otherwise not change with time. Now the linear acceleration in SF x direction caused by a fixed type of thruster is modeled by a rectangular pulse, i.e. by a function which has a constant value during the time of activation, and is zero before and after the activation. This function is then integrated twice and a filter is applied which imitates the onboard decimation filtering of the laser ranging processor (LRP), in order to obtain a model for the resulting change in the measured LRI range. With a least squares fit, for each S/C, one obtains a model for each thruster type, in the form of one parameter, which represents the pulse amplitude of the linear acceleration in LoS direction caused by that thruster pair. For six thruster pairs per S/C, this yields 12 parameters in total.

As mentioned above, these thruster responses correlate with the pointing angles and also with the TTL error. It is thus important to note that the TTL error was subtracted from the range before estimating the thruster model parameters. This was possible, since the TTL CFs were estimated exclusively from CMC maneuver data without any thruster firings. It shall further be remarked that, for both S/C, positive linear acceleration in SF x direction yields negative range acceleration. Finally, it is noteworthy that the models presented here were kept as simple as possible and more dedicated models are possible. E.g., in [Stu20], a model was developed where the two thrusters can be activated at slightly different times.

The derived models of these linear accelerations are shown in Tab. E.1. The results are mostly consistent with the models that were used to compute the ACT1B data product [McC+19]. The Albert Einstein Institute (AEI) values in the table are averaged over
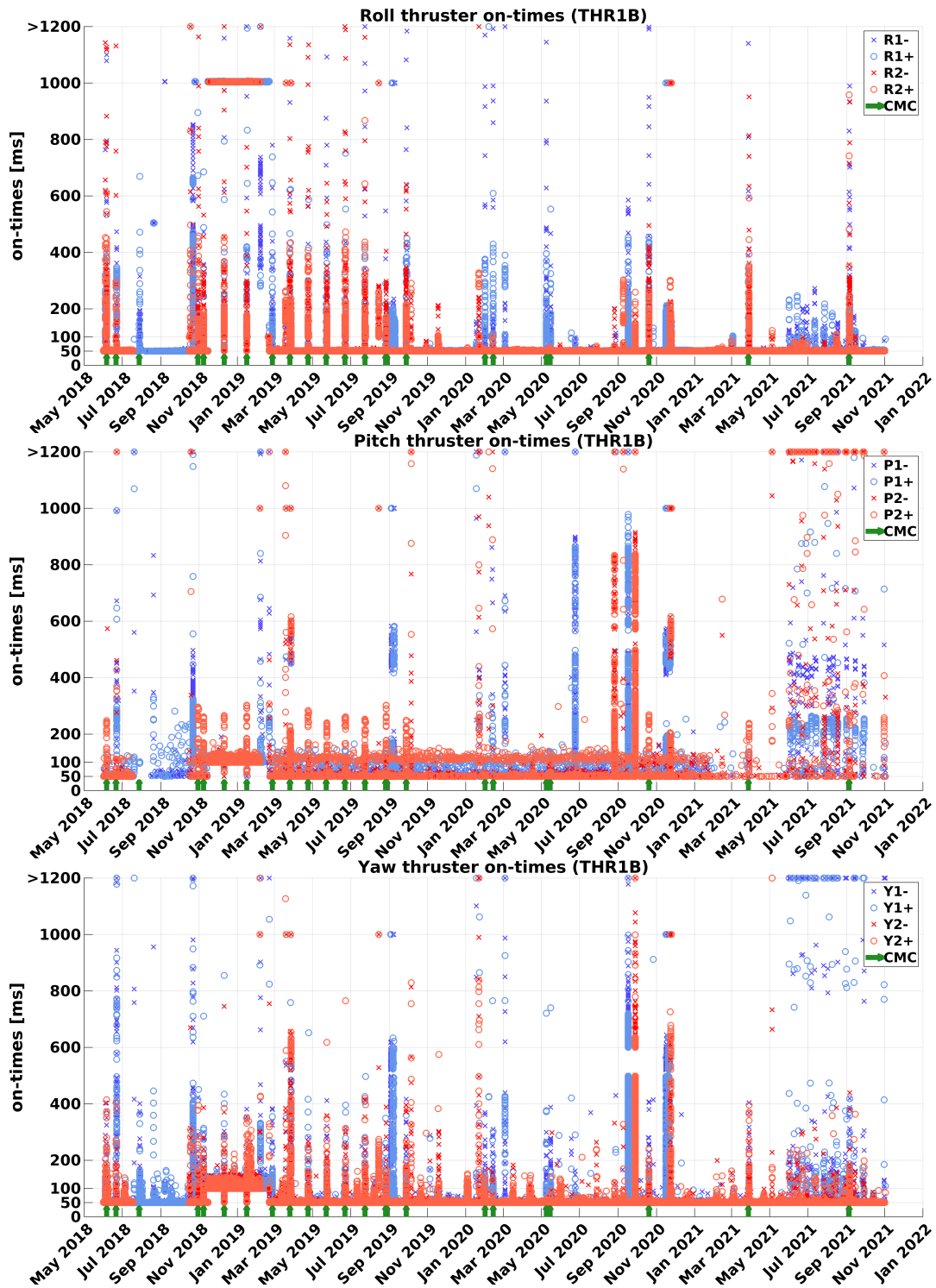
Figure E.2: All attitude thruster firing durations until November 2021 (on-times according to the THR1B data, cf. [Wen+19]) over time.

all estimates, where each estimate is obtained from one day of data. Estimates were derived separately for every day with the LRI switched on, until September 2019. Note that pitch thruster firings are scarce, see Fig. E.1, and are hence modeled with less certainty. The estimates are plotted in Fig. E.3 on the left. Once the models of all thrusters are available, time

Table E.1: Models of linear acceleration in SF x direction caused by different thruster types.

| thruster type | SRF X acceleration | | [nm s^{-2}] | |
| | GF1 | | GF2 | |
	AEI	JPL/CSR	AEI	JPL/CSR
Positive Roll	3.2	15	-24.1	-30
Negative Roll	-22.0	-20	-34.1	-40
Positive Pitch	1.1	0	61.3	55
Negative Pitch	-108.4	-109	-132.8	-119
Positive Yaw	9.9	-7	141.9	141
Negative Yaw	-28.4	-22	144.0	123

series of thruster responses in the range can be produced for any given interval, using merely THR1B data. Afterwards, this time series can be subtracted from the range, if desired. The right plot of Fig. E.3 exemplarily shows a time series of LRI range with modeled thruster responses. The dotted red line labeled *THR* shows the sum of the twelve time series of range variations caused by each thruster type. The range and thruster responses for this plot have been highpass filtered for better visibility.
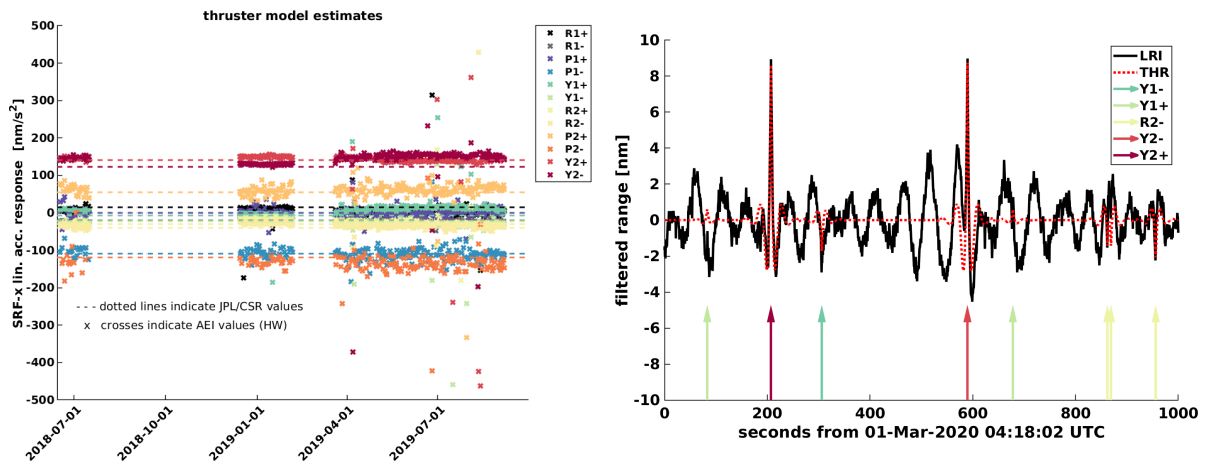
Figure E.3: Left: thruster model parameters over time. Right: example time series of modeled attitude control thruster responses in the LRI range.

The results of each individual thruster pair are shown in Figs. E.4 and E.5. In each plot, the dotted line represents the value given in [McC+19], which overall shows good agreement with the estimated values. For some thruster pairs, changes are visible in the period around January 2019 compared to the other periods. Although the model takes into account the thruster firing duration, this change may be connected to the fact that the standard firing durations have been changed for that period, see Fig. E.2. Note further that the values reported in [McC+19] have been estimated using merely long thruster firings, greater than approximately 750 ms, that occurred before May 2019, whereas the values reported here are based on all thruster firings until September 2019.
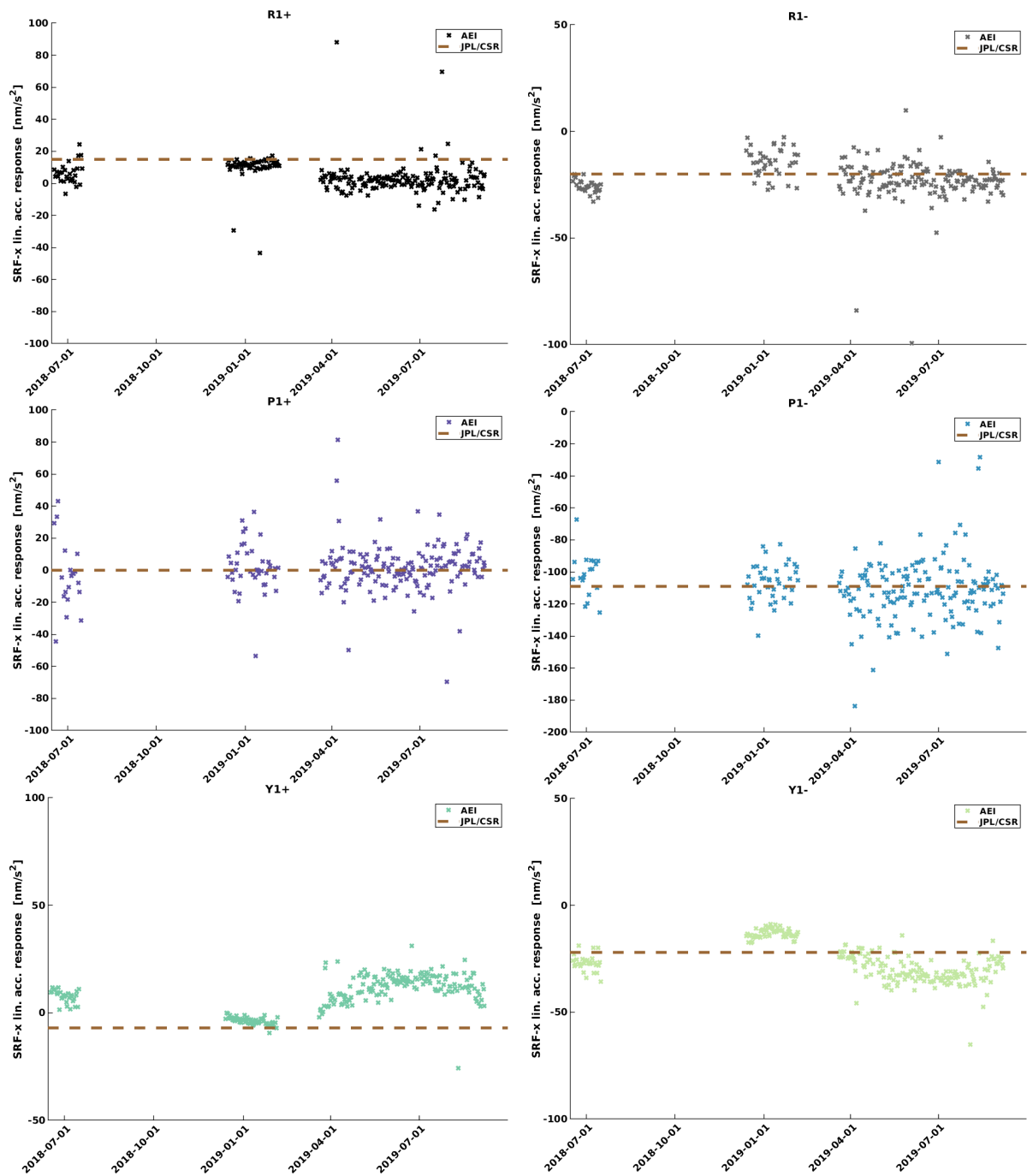
Figure E.4: Linear acceleration thruster models for GF1. Top: roll thrusters (left: positive; right: negative). Middle: pitch thrusters (left: positive; right: negative). Bottom: yaw thrusters (left: positive; right: negative).
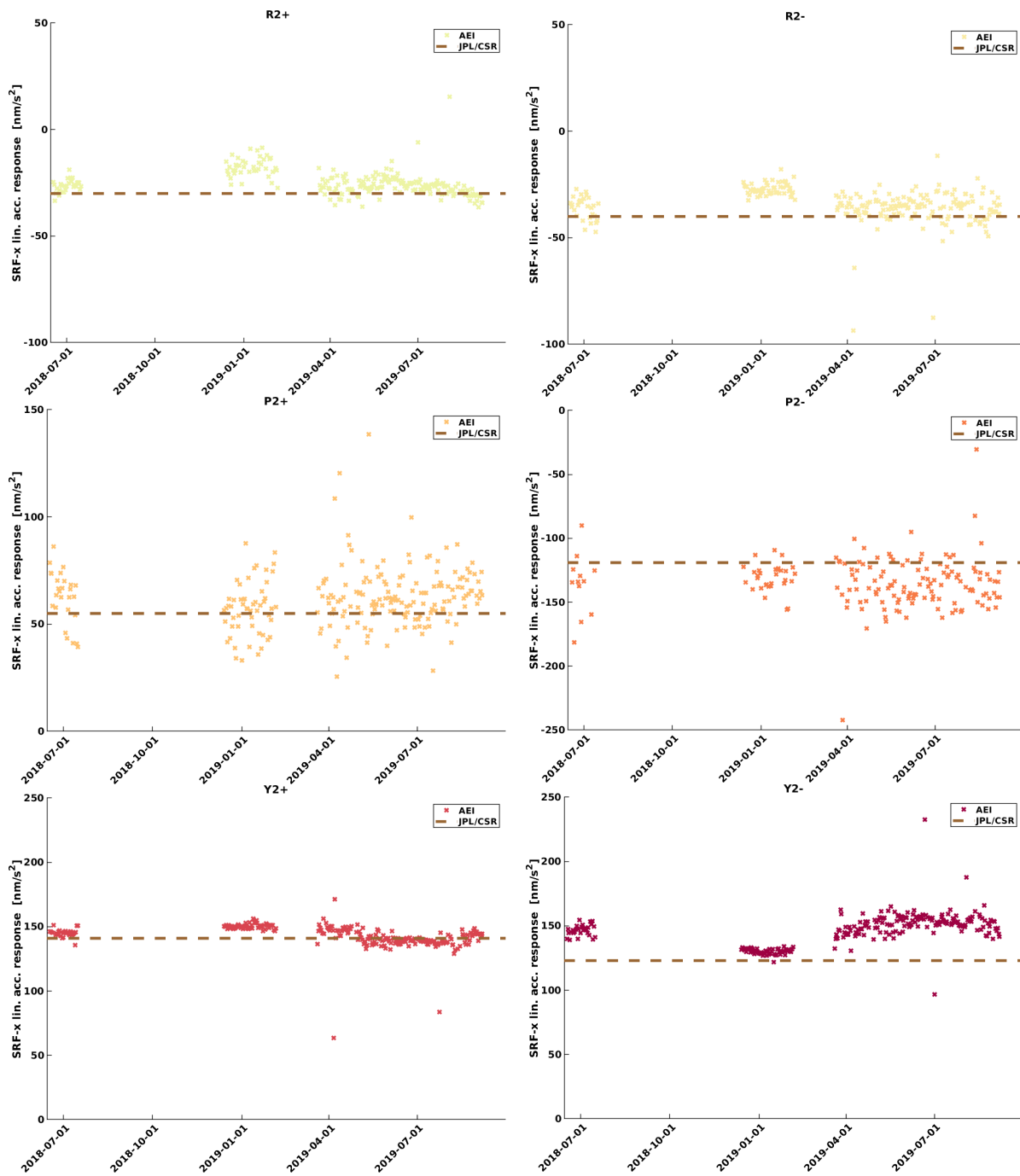
Figure E.5: Linear acceleration thruster models for GF2. Top: roll thrusters (left: positive; right: negative). Middle: pitch thrusters (left: positive; right: negative). Bottom: yaw thrusters (left: positive; right: negative).

E.2 Reducing range variations using ACT1A data

The nongravitational accelerations acting on the GFO satellites are measured by the onboard accelerometers. Below it is described how ACC data can be used to remove the nongravitational range variations from the LRI range. Since the GF2 ACC data is degraded, the calibrated accelerometer data product ACT1A was used here. Note that for the ACT data, the GF2 measurements were replaced by the transplanted GF1 measurements, and the measured accelerations during thruster firings were replaced by models, cf. [McC+19]. For further reading, the reader is also referred to [Ban+19], where the accelerometer data transplant is described for GRACE.

In order to compute the change in the inter-satellite range that is caused by linear nongravitational accelerations, these need to be integrated twice and projected onto the LoS. These two steps can be carried out in arbitrary order. Thus, the straightforward way to proceed is to rotate the ACT1A data from the accelerometer frame (AF) to the LOSF and integrate merely the LOSF x component. Denote by $a_{x,i}$, $i = 1, 2$, the component of the linear acceleration of S/C i in the x direction of the LOSF-i frame, i.e. towards the other S/C. These components from both S/C can be combined to obtain the resulting range acceleration, in this thesis called differential linear nongravitational (DLN) range acceleration $\ddot{\rho}_{\mathrm{DLN}}$:

$$\ddot{\rho}_{\mathrm{DLN}} = -a_{x,1} - a_{x,2}. \tag{E.1}$$

Subsequently, the DLN range variations ρ_{DLN} are computed by

$$\rho_{\mathrm{DLN}} = \iint \ddot{\rho}_{\mathrm{DLN}}. \tag{E.2}$$

The integration constants as well as the error propagation due to the integration do not constitute a problem, since long wavelength variations are not studied here and can be filtered out. In order to subtract the so-obtained time series from the range, the time stamps of the involved data products must be synchronized. For the rotation between the AF and LOSF frames, the S/C attitude quaternions are needed, cf. Sec. 2.1.1, which were taken from SCA1B data here. An alternative would be to neglect the pointing jitter and simply use the SF x component of the acceleration, which coincides with the AF z component.

E.3 Spectrum analysis

As the nongravitational contributions in the LRI range are not measurement noise but signal from physical range variations, the question that was raised in the beginning of this appendix is: *what is the true noise level of the LRI at Fourier frequencies above 40 mHz?* To answer this question, it is useful that time series of THR and DLN range variations can be obtained as described in the previous sections, from THR1B or ACT1A data, respectively, and subtracted from the LRI range. Example ASDs of LRI range, as well as the range reduced by THR or DLN, have been given in the left plot of Fig. 4.14. In that example, subtraction of THR lowers the ASD more than subtraction of DLN. However, this seems to vary with time, as well as the ASD of the unchanged LRI range itself. In order to analyze the behavior of the LRI range spectrum over a long time, ASDs of different combinations of range variations were computed for each day with the LRI switched on between the launch and June 2021. For each ASD, an RMS value for a frequency interval (a, b) can then be computed as

$$\mathrm{RMS(ASD)} = \sqrt{\frac{1}{b-a} \int\limits_a^b \mathrm{ASD}(f)^2 \, df}. \tag{E.3}$$

In Fig. E.6, such RMS ASD values for the frequency interval between 35 and 80 mHz are shown. Here a period around July 2020 was excluded due to a large number of outliers in the ASDs of the LRI range, which was not investigated further. Each cross represents the RMS ASD for one day of data, computed for different range terms as indicated in the legend. These range terms are abbreviated as follows.

- *LRI*: measured LRI range (AEI data product)

- *DLN*: DLN range variations (ACT1A and Level-1B data)

- *LRI - DLN*: difference LRI - DLN

- *SRP*: range variations caused by SRP (model and Level-1B data and JPL DE430)

- *THR*: THR range variations (model and THR1B data)

- *LRI - THR*: difference LRI - THR

- *TTL*: tilt-to-length coupling (model and FSM data)

- *LFN*: laser frequency noise term (model and Level-1B data)

- *ACC noise*: ACC noise converted to range (model)

The range variations caused by SRP were obtained by computing SRP accelerations for both satellites, cf. App. D, and then proceeding in the same way as with ACT1A data. Furthermore, the solar beta angles are plotted on the right y axis, which were computed using GPS-derived S/C positions and JPL's Development Ephemerides JPL DE430. The solar beta angle for a low Earth orbit (LEO) satellite is defined as the smaller of the two angles between the orbital plane and the line connecting the Earth and the Sun. It is also sometimes called Sun beta angle or β' (beta prime).
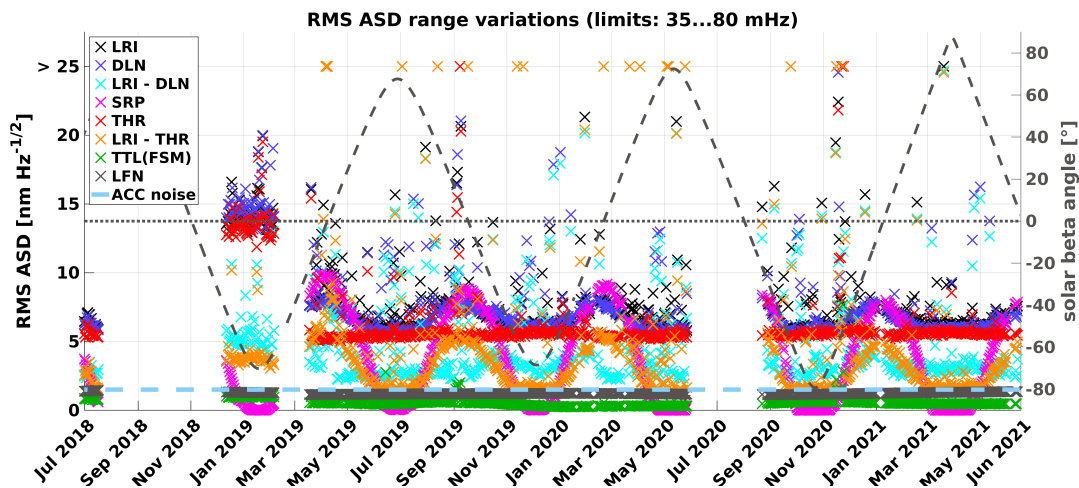
Figure E.6: RMS LASDs for frequencies between 35 and 80 mHz.

Some observations that can be made from Fig. E.6 shall be mentioned here. Always referring to RMS ASD range variations for the frequency range from 35 to 80 mHz here, the first observation is that the *LRI* values (black crosses) appear to be dominated by *DLN* (blue). DLN range variations computed with ACT1A data, notably obtained independently of the LRI, coincide to a large extend with LRI range variations, and subtraction of *DLN* from *LRI* yields significant reduction, see *LRI - DLN* (cyan). The level of DLN range variations undulates with a period of slightly more than 5 months, which seems to be related to the

periodic variations of the solar beta angle. *DLN* appears to be smallest during periods with large beta angles, positive or negative, and largest when the beta angle is close to zero. The *DLN* undulations seem to be in step with the modeled range variations due to SRP (pink), and both are on a similar level during the peaks. During the lows, where the contribution of SRP is almost negligible, *DLN* draws almost down to the level of the thruster responses, *THR* (red). This level is quite steady most of the time, except during a period with increased thruster firing durations around January 2019, cf. Fig. E.2. The contribution of *THR* to *LRI* is significant, to the point of being dominating during those periods that seem to coincide with periods of large solar beta angles. During such periods, *THR* is very close to *DLN*, and subtraction of *THR* from *LRI* yields even better reduction than subtraction of *DLN*. In fact, the difference *LRI - THR* (orange) then nearly approaches the level of the laser frequency noise *LFN* (gray). *TTL* (green) computed with FSM pointing angles is likely to contain a significant amount of measurement noise, cf. Sec. 5.4.1, but stays below *LFN* almost everywhere.

The most immediate interpretation of these observations is that, in the considered frequency interval between 35 and 80 mHz, the LRI seems to measure mainly and very accurately physical range variations caused by nongravitational forces. Periods where these variations are dominated by thruster responses alternate with periods where environmental forces cause even larger range variations. The latter seem to be driven by large SRP forces in the LoS direction, which are related to small solar beta angles, which is likely because the LoS lies in the orbital plane and SRP forces act mainly in the direction of the incident Sun light. The fact that the difference *LRI - THR* is often close to the level of *LFN* suggests that the true LRI performance is indeed limited by the sum of *LFN* and *TTL*, during these periods and in the considered frequency band. It furthermore indicates that the LFN model is accurate or at least not underestimating the true LFN during these periods. During other periods, the LRI performance is most likely as good as or better than indicated by the difference *LRI - DLN*. Elevated *LRI - DLN* values seem to occur when the beta angle is close to zero. This may be due to the LRI itself or due to the ACT1A data. Note that any noise in the ACT1A data also propagates to *DLN*, a simulation of which is plotted as a light blue dashed line, based on the noise model presented in [Dar+17]. Finally, it is also worthwhile to mention again that the ACT1A data for GF2, except for the thruster responses, is transplanted data from GF1, so that this level of accuracy is already impressive.

Bibliography

[03]   *Optimal combination of quaternions from multiple star cameras.* Tech. rep. Jet
            Propulsion Laboratory, May 2003.

[14]   *LRI-STI-RP-007.* Tech. rep. SpaceTech GmbH, Feb. 2014.

[Abi+15]   Klaus Abich et al. "GRACE-Follow On Laser Ranging Interferometer: German
            contribution". In: *Journal of Physics: Conference Series* 610 (May 2015), p. 012010.
            DOI: 10.1088/1742-6596/610/1/012010.

[Abi+19]   K Abich et al. "In-Orbit Performance of the GRACE Follow-On Laser Ranging
            Interferometer". In: *Phys. Rev. Lett.* 123.3 (July 2019), p. 031101. DOI: 10.1103/
            PhysRevLett.123.031101.

[Alt+16]   Zuheir Altamimi et al. "ITRF2014: A new release of the International Terrestrial
            Reference Frame modeling nonlinear station motions". In: *Journal of Geophysical
            Research: Solid Earth* 121.8 (2016), pp. 6109–6131. DOI: https://doi.org/10.
            1002/2016JB013098.

[Alv+21]   Anthony Davila Alvarez et al. *A Simplified Gravitational Reference Sensor for
            Satellite Geodesy.* 2021. DOI: 10.48550/ARXIV.2107.08545.

[Ama+17]   Pau Amaro-Seoane et al. *Laser Interferometer Space Antenna.* 2017. DOI: 10.
            48550/ARXIV.1702.00786.

[And84]   Dana Z. Anderson. "Alignment of resonant optical cavities". In: *Appl. Opt.* 23.17
            (Sept. 1984), pp. 2944–2949. DOI: 10.1364/AO.23.002944.

[Arm+18]   M. Armano et al. "Calibrating the system dynamics of LISA Pathfinder". In:
            Phys. Rev. D 97 (12 June 2018), p. 122002. DOI: 10.1103/PhysRevD.97.122002.

[Arm16]   M Armano. "Sub-Femto-g Free Fall for Space-Based Gravitational Wave Obser-
            vatories: LISA Pathfinder Results". In: *Physical Review Letters* (2016).

[AW96]   Penina Axelrad and L. Monique Ward. "Spacecraft attitude estimation using the
            Global Positioning System - Methodology and results for RADCAL". In: 1996.
            DOI: 10.2514/3.21772.

[Bac+17]   B Bachman et al. "Flight phasemeter on the Laser Ranging Interferometer on
            the GRACE Follow-On mission". In: *Journal of Physics: Conference Series* 840
            (May 2017), p. 012011. DOI: 10.1088/1742-6596/840/1/012011.

[Ban+19]   Tamara Bandikova et al. "GRACE accelerometer data transplant". In: *Advances
            in Space Research* 64.3 (2019), pp. 623–644. ISSN: 0273-1177. DOI: https://doi.
            org/10.1016/j.asr.2019.05.021.

[Bar00]   I Y Bar-Itzhack. "New Method for Extracting the Quaternion from a Rotation
            Matrix". In: *Journal of Guidance, Control, and Dynamics* 23.6 (2000), pp. 1085–
            1087. DOI: 10.2514/2.4654.

[Bar92]   I Y Bar-Itzhack. "Polar Decomposition for Attitude Determination from Vector
            Observations". In: *AIAA Guidance, Navigation, and Control Conference.* 1992,
            pp. 1097–1107.

[Bet12]   S Bettadpur. *Gravity Recovery and Climate Experiment Product Specification Document (Rev 4.6)*. Tech. rep. The University of Texas at Austin Center for Space Research (UTCSR), May 2012.

[BF14]   Tamara Bandikova and Jakob Flury. "Improvement of the GRACE star camera data based on the revision of the combination method". In: *Advances in Space Research* 54.9 (2014), pp. 1818–1827. ISSN: 0273-1177. DOI: https://doi.org/10.1016/j.asr.2014.07.004.

[BFK12]   Tamara Bandikova, Jakob Flury, and Ung-Dai Ko. "Characteristics and accuracies of the GRACE inter-satellite pointing". In: *Advances in Space Research* 50.1 (2012), pp. 123–135. ISSN: 0273-1177. DOI: https://doi.org/10.1016/j.asr.2012.03.011.

[BKM21]   Saniya Behzadpour, Andreas Kvas, and Torsten Mayer-Gürr. *GRACE Follow-On Gravity Field Recovery from Combined Laser Ranging Interferometer and Microwave Ranging System Measurements*. Apr. 30, 2021. URL: https://doi.org/10.5194/egusphere-egu21-9415.

[BMK21]   Saniya Behzadpour, Torsten Mayer-Gürr, and Sandro Krauss. "GRACE Follow-On Accelerometer Data Recovery". In: *Journal of Geophysical Research: Solid Earth* 126.5 (2021). DOI: https://doi.org/10.1029/2020JB021297.

[Bra+04]   Claus Braxmaier et al. "LISA pathfinder optical interferometry". In: *Gravitational Wave and Particle Astrophysics Detectors*. Ed. by James Hough and Gary H. Sanders. Vol. 5500. International Society for Optics and Photonics. SPIE, 2004, pp. 164–173. DOI: 10.1117/12.555266.

[BWN08]   P L Bender, D N Wiese, and R S Nerem. "A possible dual-GRACE mission with 90 degree and 63 degree inclination orbits". In: *Proceedings of the Third International Symposium on Formation Flying. Missions and Technologies*. Noordwijk, NL: ESA / ESTEC, 2008, pp. 1–6. ISBN: 978-92-9221-218-6.

[CBO04]   D Choukroun, I Y Bar-Itzhack, and Y Oshman. "Optimal-REQUEST Algorithm for Attitude Determination". In: *Journal of Guidance, Control, and Dynamics* 27.3 (2004), pp. 418–425.

[Ces+10]   Stefano Cesare et al. "Satellite Formation for a Next Generation Gravimetry Mission". In: *Small Satellite Missions for Earth Observation*. Ed. by Rainer Sandau, Hans-Peter Roeser, and Arnoldo Valenzuela. Berlin, Heidelberg: Springer Berlin Heidelberg, 2010, pp. 125–133. ISBN: 978-3-642-03501-2.

[Che+21]   Jianli Chen et al. "Error Assessment of GRACE and GRACE Follow-On Mass Change". In: *Journal of Geophysical Research: Solid Earth* 126.9 (2021). DOI: https://doi.org/10.1029/2021JB022124.

[Chr+15]   B. Christophe et al. "A new generation of ultra-sensitive electrostatic accelerometers for GRACE Follow-on and towards the next generation gravity missions". In: *Acta Astronautica* 117 (2015), pp. 1–7. ISSN: 0094-5765. DOI: https://doi.org/10.1016/j.actaastro.2015.06.021.

[Chr+19]   B. Christophe et al. "Status of Development of the Future Accelerometers for Next Generation Gravity Missions". In: *International Symposium on Advancing Geodesy in a Changing World*. Ed. by Jeffrey T. Freymueller and Laura Sánchez. Cham: Springer International Publishing, 2019, pp. 85–89. ISBN: 978-3-030-12915-6.

[Chw+16]   M Chwalla et al. "Design and construction of an optical test bed for LISA imaging systems and tilt-to-length coupling". In: *Classical and Quantum Gravity* 33.24 (Nov. 2016), p. 245015. DOI: 10.1088/0264-9381/33/24/245015.

[Chw+20]   M. Chwalla et al. "Optical Suppression of Tilt-to-Length Coupling in the LISA Long-Arm Interferometer". In: *Phys. Rev. Applied* 14 (1 July 2020), p. 014030. DOI: 10.1103/PhysRevApplied.14.014030.

[CJ04]   J. L. Crassidis and J L Junkins. *Optimal Estimation of Dynamic Systems.* CRC Press LLC, 2004.

[CL19]   B. F. Chao and J. R. Liau. "Gravity Changes Due to Large Earthquakes Detected in GRACE Satellite Data via Empirical Orthogonal Function Analysis". In: *Journal of Geophysical Research: Solid Earth* 124.3 (2019), pp. 3024–3035. DOI: 10.1029/2018JB016862.

[Cli14]   Intergovernmental Panel on Climate Change. *Climate Change 2013 – The Physical Science Basis: Working Group I Contribution to the Fifth Assessment Report of the Intergovernmental Panel on Climate Change.* Cambridge University Press, 2014. DOI: 10.1017/CBO9781107415324.

[Con+21]   Lorcan Conlon et al. *Enhancing the precision limits of interferometric satellite geodesy missions.* 2021. DOI: 10.48550/ARXIV.2109.07666.

[Cos+21]   Fabiana Cossavella et al. "Attitude Control on GRACE Follow-On - Experiences from the first years in orbit". In: *16th International Conference on Space Operations.* May 2021.

[CP01]   Changmook Chun and F. C. Park. "Dynamics-Based Attitude Determination Using the Global Positioning System". In: *Journal of Guidance, Control, and Dynamics* 24.3 (2001), pp. 466–473. DOI: 10.2514/2.4767.

[CS13]   Stefano Cesare and Gianfranco Sechi. "Next Generation Gravity Mission". In: *Distributed Space Missions for Earth System Monitoring.* Ed. by Marco D'Errico. New York, NY: Springer New York, 2013, pp. 575–598. ISBN: 978-1-4614-4541-8. DOI: 10.1007/978-1-4614-4541-8_20.

[CVS20]   E. Ciracì, I. Velicogna, and S. Swenson. "Continuity of the Mass Loss of the World's Glaciers and Ice Caps From the GRACE and GRACE Follow-On Missions". In: *Geophysical Research Letters* 47.9 (2020). DOI: 10.1029/2019GL086926.

[Dah+17]   C. Dahl et al. "Laser ranging interferometer on Grace follow-on". In: *International Conference on Space Optics — ICSO 2016.* Ed. by Bruno Cugny, Nikos Karafolas, and Zoran Sodnik. Vol. 10562. International Society for Optics and Photonics. SPIE, 2017, pp. 1133–1141. DOI: 10.1117/12.2297705.

[Dan+93]   K Danzmann et al. *LISA (laser interferometer space antenna),Proposal for a laser-interferometer gravitational wave detector in space.* Tech. rep. Max Planck Gesellschaft, 1993.

[Dar+17]   N Darbeheshti et al. "Instrument Data Simulations for GRACE Follow-On: Observation and Noise Models". In: *Earth System Science Data* 9.2 (2017), pp. 833–848. DOI: 10.5194/essd-9-833-2017.

[DKL09]   Zhen Dai, Stefan Knedlik, and Otmar Loffeld. "A MATLAB toolbox for attitude determination with GPS multi-antenna systems". In: *GPS Solutions* 13.3 (July 2009), pp. 241–248. ISSN: 1521-1886. DOI: 10.1007/s10291-008-0108-x.

[Dob+13]   H. Dobslaw et al. "Simulating high-frequency atmosphere-ocean mass variability for dealiasing of satellite gravity observations: AOD1B RL05". In: *Journal of Geophysical Research: Oceans* 118.7 (2013), pp. 3704–3711. DOI: 10.1002/jgrc.20271.

[Dob+16]   Henryk Dobslaw et al. "Modeling of present-day atmosphere and ocean non-tidal de-aliasing errors for future gravity mission simulations". In: *Journal of Geodesy* 90.5 (May 2016), pp. 423–436. ISSN: 1432-1394. DOI: 10.1007/s00190-015-0884-3.

[DP17]   Ilias Daras and R. Pail. "Treatment of temporal aliasing effects in the context of next generation satellite gravimetry missions". In: *Journal of Geophysical Research: Solid Earth* 122 (July 2017). DOI: 10.1002/2017jb014250.

[DT+96]   Karsten Danzmann, LISA Study Team, et al. "LISA: laser interferometer space antenna for gravitational wave measurements". In: *Classical and Quantum Gravity* 13.11A (1996), A247.

[Els+14]   Basem Elsaka et al. "Comparing seven candidate mission configurations for temporal gravity field retrieval through full-scale numerical simulation". In: *Journal of Geodesy* 88.1 (Jan. 2014), pp. 31–43. ISSN: 1432-1394. DOI: 10.1007/s00190-013-0665-9.

[Fam14]   J. S. Famiglietti. "The global groundwater crisis". In: *Nature Climate Change* 4.11 (Nov. 2014), pp. 945–948. ISSN: 1758-6798. DOI: 10.1038/nclimate2425.

[FB16]   H. Fourati and D.E.C. Belkhiat. *Multisensor Attitude Estimation: Fundamental Concepts and Applications.* Devices, Circuits, and Systems. CRC Press, 2016. ISBN: 9781315351759. DOI: https://doi.org/10.1201/9781315368795.

[FBT08]   Jakob Flury, Srinivas Bettadpur, and Byron D. Tapley. "Precise accelerometry onboard the GRACE gravity field satellite mission". In: *Advances in Space Research* 42.8 (2008), pp. 1414–1423. ISSN: 0273-1177. DOI: https://doi.org/10.1016/j.asr.2008.05.004.

[FK]   F Flechtner and V Klemann. *GRACE and GRACE-FO related publications.* URL: http://www-app2.gfz-potsdam.de/pb1/op/grace/references/sort_date.html.

[Fle+14]   R Fleddermann et al. "Testing the GRACE Follow-On Triple Mirror Assembly". In: *Classical and Quantum Gravity* 31.19 (2014), p. 195004. DOI: 10.1088/0264-9381/31/19/195004.

[Fle+16]   F Flechtner et al. "What Can be Expected from the GRACE-FO Laser Ranging Interferometer for Earth Science Applications?" In: *Surveys in Geophysics* (2016).

[Fle15]   F Flechtner. *AOD1B Product Description Document for Product Release 05.* Tech. rep. GFZ German Research Centre for Geosciences, 2015.

[Fol+10]   W M Folkner et al. *Laser Frequency Stabilization for GRACE-II.* Tech. rep. NASA, 2010.

[Gat16]   P Gath. "Entwicklung, Integration und Test der GRACE Follow-On Satelliten". In: *Deutscher Luft- und Raumfahrtkongress* (2016).

[GI]   International Union of Geodesy and Geophysics (IUGG). *Satellite missions inventory.* URL: http://www.ggos.org/en/bureaus/bno/committee-satellite-missions/satellite-missions-inventory/. (accessed: 11.05.2020).

[Gio17]   Gabriele Giorgi. "Attitude Determination". In: *Springer Handbook of Global Navigation Satellite Systems.* Ed. by Peter J.G. Teunissen and Oliver Montenbruck. Cham: Springer International Publishing, 2017, pp. 781–809. ISBN: 978-3-319-42928-1. DOI: 10.1007/978-3-319-42928-1_27.

[GN14]   Th. Gruber and Team NGGM-D. "Next generation satellite gravimetry mission study (NGGM-D)". In: *European Geosciences Union General Assembly.* Wien, May 2014.

[Gos+18]   S. Goswami et al. "Analysis of Attitude Errors in GRACE Range-Rate Residuals—A Comparison Between SCA1B and the Fused Attitude Product (SCA1B + ACC1B)". In: *IEEE Sensors Letters* 2.2 (2018), pp. 1–4.

[Gos+21]   Sujata Goswami et al. "Analysis of GRACE Follow-On Laser Ranging Interferometer Derived Inter-Satellite Pointing Angles". In: *IEEE Sensors Journal* 21.17 (2021), pp. 19209–19221. DOI: 10.1109/JSEN.2021.3090790.

[Gos18]   S Goswami. "Understanding the sensor noise in the GRACE range-rate observations by analyzing their residuals". PhD thesis. Leibniz Universität Hannover, 2018.

[GPS02]   H. Goldstein, C.P. Poole, and J.L. Safko. *Classical Mechanics*. Addison Wesley, 2002. ISBN: 9780201657029.

[Han+06]   Shin-Chan Han et al. "Crustal Dilatation Observed by GRACE After the 2004 Sumatra-Andaman Earthquake". In: *Science* 313.5787 (2006), pp. 658–662. ISSN: 0036-8075. DOI: 10.1126/science.1128661.

[Har16]   Nate Harvey. "GRACE star camera noise". In: *Advances in Space Research* 58 (2016), pp. 408–414.

[Hei18]   G Heinzel. *LRI phase jump modeling*. Tech. rep. Albert Einstein Institute, Hannover, Germany, July 2018.

[Her+04]   J Herman et al. "Attitude control for GRACE - The first low-flying satellite formation". In: *18th International Symposium on Space Flight Dynamics*. Vol. 548. 2004, p. 27.

[Her+12]   J Herman et al. *Life with a weak Heart - Prolonging the GRACE Mission despite degraded Batteries*. June 2012.

[HM67]   W A Heiskanen and H Moritz. *Physical Geodesy*. W.H. Freeman, San Francisco, USA, 1967.

[Hor+11]   M Horwath et al. "Improved GRACE Science Results after Adjustment of Geometric Biases in the Level-1B K-Band Ranging Data". In: *Journal of Geodesy* (2011).

[HRS02]   G Heinzel, A Rüdiger, and R Schilling. *Spectrum and spectral density estimation by the Discrete Fourier transform (DFT), including a comprehensive list of window functions and some new flat-top windows*. eDoc 395068. Max Planck Gesellschaft, 2002.

[HS12]   J Herman and M Steinhoff. "Balancing, Turning, Saving - Special AOCS Operations to extend the GRACE Mission". In: *SpaceOps 2012 Conference*. June 2012. DOI: 10.2514/6.2012-1275114.

[HS19]   Nate Harvey and Carly Sakumura. "Results from a GRACE/GRACE-FO attitude reconstruction Kalman filter". In: *Journal of Geodesy* 93.10 (Oct. 2019), pp. 1881–1896. ISSN: 1432-1394. DOI: 10.1007/s00190-019-01289-z.

[HSW22]   M S Hartig, S Schuster, and G Wanner. "Geometric tilt-to-length coupling in precision interferometry: mechanisms and analytical descriptions". In: *(paper in preparation)* (2022).

[HTF09]   T Hastie, R Tibshirani, and J Friedman. *The Elements of Statistical Learning*. Springer, 2009.

[HW17]   Wen-Rui Hu and Yue-Liang Wu. "The Taiji Program in Space for gravitational wave physics and the nature of gravity". In: *National Science Review* 4.5 (Oct. 2017), pp. 685–686. ISSN: 2095-5138. DOI: 10.1093/nsr/nwx116.

[Iná+15]   Pedro Inácio et al. "Analysis of star camera errors in GRACE data and their impact on monthly gravity field models". In: *Journal of Geodesy* 89.6 (June 2015), pp. 551–571. ISSN: 1432-1394. DOI: `10.1007/s00190-015-0797-1`.

[Jäg+19]   Adrian Jäggi et al. "European Gravity Service for Improved Emergency Management (EGSIEM)—from concept to implementation". In: *Geophysical Journal International* 218.3 (May 2019), pp. 1572–1590. ISSN: 0956-540X. DOI: `10.1093/gji/ggz238`.

[Jen09]   O. Jennrich. "LISA technology and instrumentation". In: *Classical and Quantum Gravity - CLASS QUANTUM GRAVITY* 26 (Aug. 2009). DOI: `10.1088/0264-9381/26/15/153001`.

[JPL]   JPL. *GRACE-FO.* `https://gracefo.jpl.nasa.gov/`. Accessed: 2021-06-14.

[Kea81]   J Keat. "Analysis of Least-Squares Attitude Determination Routine DOAOP". In: *Computer Sciences Corporation Report* (1981), p. 117.

[KL09]   Jeongrae Kim and Seung-Woo Lee. "Flight performance analysis of GRACE K-band ranging instrument with simulation data". In: *Acta Astronautica* 65 (Dec. 2009), pp. 1571–1581. DOI: `10.1016/j.actaastro.2009.04.010`.

[KM]   B Klipstein and K McKenzie. *Phasemeter development for LISA at JPL.* URL: `https://pcos.gsfc.nasa.gov/studies/L3/PhasemeterForELISAfinal.pdf`.

[KM16]   Beate Klinger and Torsten Mayer-Gürr. "The role of accelerometer data calibration within GRACE gravity field recovery: Results from ITSG-Grace2016". In: *Advances in Space Research* 58.9 (2016), pp. 1597–1609. ISSN: 0273-1177. DOI: `https://doi.org/10.1016/j.asr.2016.08.007`.

[Ko08]   U D Ko. "Analysis of the characteristics of GRACE dual one-way ranging system". PhD thesis. University of Texas at Austin, 2008.

[Koc+18]   Alexander Koch et al. "Line of sight calibration for the laser ranging interferometer on-board the GRACE Follow-On mission: on-ground experimental validation". In: *Opt. Express* 26.20 (Oct. 2018), pp. 25892–25908. DOI: `10.1364/OE.26.025892`.

[Koc07]   Karl-Rudolf Koch. *Introduction to Bayesian Statistics.* Springer-Verlag, 2007.

[Koc99]   Karl-Rudolf Koch. *Parameter Estimation and Hypothesis Testing in Linear Models.* Springer-Verlag, 1999.

[Kor+19]   R P Kornfeld et al. "GRACE-FO: The Gravity Recovery and Climate Experiment Follow-On Mission". In: *Journal of Spacecraft and Rockets* 56.3 (2019), pp. 931–951. DOI: `10.2514/1.A34326`.

[Lan+]   F Landerer et al. *GRACE Follow-On Science Data System Newsletter Reports.* `https://www.gfz-potsdam.de/en/section/global-geomonitoring-and-gravity-field/projects/gravity-recovery-and-climate-experiment-follow-on-grace-fo-mission/news/`. Accessed: 2020-06-26.

[Lan+20]   Felix W. Landerer et al. "Extending the Global Mass Change Data Record: GRACE Follow-On Instrument and Science Data Performance". In: *Geophysical Research Letters* 47.12 (2020). DOI: `10.1029/2020GL088306`.

[Löw+19]   S Löw et al. "Attitude and Orbit Control of the Grace Satellites at extremely low power". In: *70th International Astronautical Congress (IAC)*. Oct. 2019.

[Luo+16]   Jun Luo et al. "TianQin: a space-borne gravitational wave detector". In: *Classical and Quantum Gravity* 33.3 (Jan. 2016), p. 035010. DOI: `10.1088/0264-9381/33/3/035010`.

[Luo+20]   Ziren Luo et al. "The Taiji program: A concise overview". In: *Progress of Theoretical and Experimental Physics* 2021.5 (July 2020). 05A108. ISSN: 2050-3911. DOI: `10.1093/ptep/ptaa083`.

[Mah14]   Christoph Mahrdt. "Laser Link Acquisition for the GRACE Follow-On Laser Ranging Interferometer". PhD thesis. Leibniz Universität Hannover, 2014.

[Mar88]   F L Markley. "Attitude Determination Using Vector Observations and the Singular Value Decomposition". In: *Journal of the Astronautical Sciences* 36 (1988), pp. 245–258.

[Mar93]   F L Markley. "Attitude Determination Using Vector Observations: A Fast Optimal Matrix Algorithm". In: *The Journal of the Astronautical Sciences* 41 (1993), pp. 261–280.

[May+21]   Torsten Mayer-Gürr et al. "GROOPS: A software toolkit for gravity field recovery and GNSS processing". In: *Computers & Geosciences* 155 (2021), p. 104864. ISSN: 0098-3004. DOI: `https://doi.org/10.1016/j.cageo.2021.104864`.

[MC14]   F L Markley and J L Crassidis. *Fundamentals of Spacecraft Attitude Determination and Control*. Springer, 2014.

[McC+19]   C M McCullough et al. *Description of Calibrated GRACE-FO Accelerometer Data Products (ACT)*. Tech. rep. PL D-103863. Jet Propulsion Laboratory, California Institute of Technology, and Center for Space Research, University of Texas at Austin, May 2019.

[Mis19]   Malte Misfeldt. "Data Processing and Investigations for the GRACE Follow-On Laser Ranging Interferometer". MA thesis. Germany: Leibniz Universität Hannover, 2019.

[MM20]   M Misfeldt and V Müller. *Far-Field Beam Intensities & TMA co-alignment estimates*. Tech. rep. Max Planck Institute for Gravitational Physics (Albert Einstein Institute), Jan. 2020.

[MNR12]   Thomas Müller-Gronbach, Erich Novak, and Klaus Ritter. "Numerische Integration". In: *Monte Carlo-Algorithmen*. Berlin, Heidelberg: Springer Berlin Heidelberg, 2012, pp. 245–310. ISBN: 978-3-540-89141-3. DOI: `10.1007/978-3-540-89141-3_7`.

[Mon00]   O Montenbruck. *Satellite Orbits - Models, Methods, Applications*. Springer-Verlag, 2000.

[Mor+94]   Euan Morrison et al. "Automatic alignment of optical interferometers". In: *Appl. Opt.* 33.22 (Aug. 1994), pp. 5041–5049. DOI: `10.1364/AO.33.005041`.

[Mor95a]   D Mortari. "Energy Approach Algorithm for Attitude Determination from Vector Observations". In: *Advances in Astronautical Sciences* 89 (1995), pp. 773–784.

[Mor95b]   D Mortari. "Euler-2 and Euler-n Algorithms for Attitude Determination from Vector Observations". In: *IFAC Space Technology International Conference on Intelligent Autonomous Control in Aerospace*. 1995, pp. 213–218.

[Mül+19]   Kay Müller et al. "End–of–Life Power Management on the Grace Satellites with several failed Battery Cells". In: Oct. 2019.

[Mül13]   Vitali Müller. "Simulations for LISA and GRACE Follow-On". MA thesis. Germany: Leibniz Universität Hannover, 2013.

[Mül17]   Vitali Müller. "Design Considerations for Future Geodesy Missions and for Space Laser Interferometry". PhD thesis. Germany: Leibniz Universität Hannover, 2017.

[MVa08]   P McNamara, S Vitale, and K Danzmann and. "LISA Pathfinder". In: *Classical and Quantum Gravity* 25.11 (May 2008), p. 114034. DOI: `10.1088/0264-9381/25/11/114034`.

[NAS18]   NASEM. In: *Thriving on our changing planet: A decadal strategy for earth observation from space*. National Academies of Sciences, Engineering, and Medicine, 2018. DOI: `https://doi.org/10.17226/24938`.

[Nic+17]   K. Nicklaus et al. "Optical bench of the laser ranging interferometer on grace follow-on". In: *International Conference on Space Optics — ICSO 2014*. Ed. by Zoran Sodnik, Bruno Cugny, and Nikos Karafolas. Vol. 10563. International Society for Optics and Photonics. SPIE, 2017, pp. 738–746. DOI: `10.1117/12.2304195`.

[Pan+13]   I. Panet et al. "Earth System Mass Transport Mission (e.motion): A Concept for Future Earth Gravity Field Measurements from Space". In: *Surveys in Geophysics* 34.2 (May 2013), pp. 141–163. ISSN: 1573-0956. DOI: `10.1007/s10712-012-9209-8`.

[Pav+12]   N K Pavlis et al. "The development and evaluation of the Earth Gravitational Model 2008 (EGM2008)". In: *Journal of Geophysical Research: Solid Earth* 117.B4 (2012). DOI: `10.1029/2011JB008916`.

[Pei+22]   Athina Peidou et al. "Spatiotemporal Characterization of Geophysical Signal Detection Capabilities of GRACE-FO". In: *Geophysical Research Letters* 49.1 (2022). DOI: `https://doi.org/10.1029/2021GL095157`.

[Pet10]   N Peterseim. "Acceleration Disturbances onboard of GRACE Satellites due to Magnetic Torquers". Diplomarbeit. Leibniz Universität Hannover, 2010.

[Pet14]   N Peterseim. "TWANGS - High-Frequency Disturbing Signals in 10 Hz Accelerometer Data of the GRACE Satellites". PhD thesis. Technische Universität München, 2014.

[PFS12]   Nadja Peterseim, Jakob Flury, and Anja Schlicht. "Magnetic torquer induced disturbing signals within GRACE accelerometer data". In: *Advances in Space Research* 49.9 (2012), pp. 1388–1394. ISSN: 0273-1177. DOI: `https://doi.org/10.1016/j.asr.2012.02.013`.

[Pie+12]   R. Pierce et al. "Stabilized Lasers for Space Applications: A High TRL Optical Cavity Reference System". In: *Conference on Lasers and Electro-Optics 2012*. Optical Society of America, 2012, JW3C.3. DOI: `10.1364/CLEO_AT.2012.JW3C.3`.

[PL10]   G Petit and B Luzum. *IERS Conventions (2010)*. Tech. rep. International Earth Rotation and Reference Systems Service (IERS), 2010.

[PP19]   Anna F Purkhauser and Roland Pail. "Next generation gravity missions: near-real time gravity field retrieval strategy". In: *Geophysical Journal International* 217.2 (Feb. 2019), pp. 1314–1333. ISSN: 0956-540X. DOI: `10.1093/gji/ggz084`.

[Rod+18]   M. Rodell et al. "Emerging trends in global freshwater availability". In: *Nature* 557.7707 (May 2018), pp. 651–659. ISSN: 1476-4687. DOI: `10.1038/s41586-018-0123-1`.

[Ros+20]   M. P. Ross et al. "Limits on the stochastic gravitational wave background and prospects for single-source detection with GRACE Follow-On". In: *Phys. Rev. D* 101 (10 May 2020), p. 102004. DOI: `10.1103/PhysRevD.101.102004`.

[RVF09]   Matthew Rodell, Isabella Velicogna, and James S. Famiglietti. "Satellite-based estimates of groundwater depletion in India". In: *Nature* 460.7258 (Aug. 2009), pp. 999–1002. ISSN: 1476-4687. DOI: `10.1038/nature08238`.

[Sas+10]   I. Sasgen et al. "Satellite gravimetry observation of Antarctic snow accumulation related to ENSO". In: *Earth and Planetary Science Letters* 299.3 (2010), pp. 352–358. ISSN: 0012-821X. DOI: https://doi.org/10.1016/j.epsl.2010.09.015.

[Sch+14]   D Schütze et al. "Retroreflector for GRACE follow-on: Vertex vs. point of minimal coupling". In: *Opt. Express* 22.8 (2014), pp. 9324–9333. DOI: 10.1364/OE.22.009324.

[Sch+15a]   B Schlepp et al. "Flight Dynamics Challenges for the GRACE Follow-On Mission". In: *25th International Symposium on Space Flight Dynamics (ISSFD)*. Institute of Transport Research, DLR, Oct. 2015.

[Sch+15b]   Sönke Schuster et al. "Vanishing tilt-to-length coupling for a singular case in two-beam laser interferometers with Gaussian beams". In: *Appl. Opt.* 54.5 (Feb. 2015), pp. 1010–1014. DOI: 10.1364/AO.54.001010.

[Sch+16]   Sönke Schuster et al. "Experimental demonstration of reduced tilt-to-length coupling by a two-lens imaging system". In: *Opt. Express* 24.10 (May 2016), pp. 10466–10475. DOI: 10.1364/OE.24.010466.

[Sch00]   Markus Schelkle. *The GRACE Cold Gas Attitude and Orbit Control System*. Tech. rep. Astrium GmbH, 2000.

[Sch15]   Daniel Schütze. "Intersatellite laser interferometry: Test Environments for GRACE Follow-On". PhD thesis. Germany: Leibniz Universität Hannover, 2015.

[Sch17]   S Schuster. "Tilt-to-length coupling and diffraction aspects in satellite interferometry". PhD thesis. Germany: Leibniz Universität Hannover, 2017.

[She+12]   B S Sheard et al. "Intersatellite Laser Ranging Instrument for the GRACE Follow-On Mission". In: *Journal of Geodesy* 86.12 (2012), pp. 1083–1095. DOI: 10.1007/s00190-012-0566-3.

[She78]   Stanley W. Shepperd. "Quaternion from Rotation Matrix". In: *Journal of Guidance and Control* 1.3 (1978), pp. 223–224. DOI: 10.2514/3.55767b.

[Sil+12]   P. Silvestrin et al. "The Future of the Satellite Gravimetry After the GOCE Mission". In: *Geodesy for Planet Earth*. Ed. by Steve Kenyon, Maria Christina Pacino, and Urs Marti. Berlin, Heidelberg: Springer Berlin Heidelberg, 2012, pp. 223–230. ISBN: 978-3-642-20338-1.

[SL92]   B. L. Stevens and F. L. Lewis. *Aircraft Control and Simulation*. John Wiley & Sons, 1992.

[SLL12]   B. R. Scanlon, L. Longuevergne, and D. Long. "Ground referencing GRACE satellite estimates of groundwater storage changes in the California Central Valley, USA". In: *Water Resources Research* 48.4 (2012). DOI: 10.1029/2011WR011312.

[SO81]   M Shuster and S Oh. "Three-Axis Attitude Determination from Vector Observations". In: *Journal of Guidance and Control* 4 (1981), pp. 70–77.

[Spe21]   Robert Spero. "Point-mass sensitivity of gravimetric satellites". In: *Advances in Space Research* 67.5 (Mar. 2021), pp. 1656–1664. DOI: 10.1016/j.asr.2020.12.019.

[Stu20]   David Stuhrmann. "Characterization of Attitude Thruster within GRACE Follow-On Laser Ranging Interferometer Data". MA thesis. Germany: Leibniz Universität Hannover, 2020.

[Tap+04a]   B D Tapley et al. "GRACE Measurements of Mass Variability in the Earth System". In: *Science* 305.5683 (2004), pp. 503–505. DOI: 10.1126/science.1099192.

[Tap+04b]   B. D. Tapley et al. "The gravity recovery and climate experiment: Mission overview and early results". In: *Geophysical Research Letters* 31.9 (2004). DOI: 10.1029/2004GL019920.

[Tap+19]   Byron D. Tapley et al. "Contributions of GRACE to understanding climate change". In: *Nature Climate Change* 9.5 (May 2019), pp. 358–369. ISSN: 1758-6798. DOI: 10.1038/s41558-019-0456-2.

[TD20]   Massimo Tinto and Sanjeev V. Dhurandhar. "Time-delay interferometry". In: *Living Reviews in Relativity* 24.1 (Dec. 2020). DOI: 10.1007/s41114-020-00029-6.

[tea19]   GRACE-FO AOCS team. personal communication. Oct. 11, 2019.

[tea21]   GRACE-FO Science Data System (SDS) team. personal communication. Sept. 15, 2021.

[TFW99]   Pierre Touboul, Bernard Foulon, and Eric Willemenot. "Electrostatic space accelerometers for present and future missions11Based on paper IAF.96.J1.02 presented at the 47th International Astronautical Congress, 7–11 October, 1996, Beijing, China." In: *Acta Astronautica* 45.10 (1999), pp. 605–617. ISSN: 0094-5765. DOI: https://doi.org/10.1016/S0094-5765(99)00132-0.

[TH05]   M Tröbs and G Heinzel. "Improved spectrum estimation from digitized time series on a logarithmic frequency axis". In: *Measurement* 39.2 (2005), pp. 120–129. DOI: 10.1016/j.measurement.2005.10.010.

[Tho+11]   R. Thompson et al. "A flight-like optical reference cavity for GRACE follow-on laser frequency stabilization". In: *2011 Joint Conference of the IEEE International Frequency Control and the European Frequency and Time Forum (FCS) Proceedings.* 2011, pp. 1–3.

[Tou+12]   P. Touboul et al. "CHAMP, GRACE, GOCE Instruments and Beyond". In: *Geodesy for Planet Earth.* Ed. by Steve Kenyon, Maria Christina Pacino, and Urs Marti. Berlin, Heidelberg: Springer Berlin Heidelberg, 2012, pp. 215–221. ISBN: 978-3-642-20338-1.

[Tou+99]   P Touboul et al. "Accelerometers for CHAMP, GRACE and GOCE space missions: synergy and evolution". In: *Bolletino di Geofisica Teorica ed Applicata* 40 (1999).

[TP12]   Chonrat Tatiyaworanun and S. Purivigraipong. "An operational algorithm for satellite attitude determination from GPS carrier phase". In: *2012 9th International Conference on Electrical Engineering/Electronics, Computer, Telecommunications and Information Technology* (2012), pp. 1–4.

[Trö+18]   M Tröbs et al. "Reducing tilt-to-length coupling for the LISA test mass interferometer". In: *Classical and Quantum Gravity* 35.10 (Apr. 2018), p. 105001. DOI: 10.1088/1361-6382/aab86c.

[VDS18]   Bramha Vishwakarma, Balaji Devaraju, and Nico Sneeuw. "What Is the Spatial Resolution of GRACE Satellite Products for Hydrology?" In: *Remote Sensing* 10 (May 2018). DOI: 10.3390/rs10060852.

[Vel+20]   Isabella Velicogna et al. "Continuity of Ice Sheet Mass Loss in Greenland and Antarctica From the GRACE and GRACE Follow-On Missions". In: *Geophysical Research Letters* 47.8 (2020). DOI: 10.1029/2020GL087291.

[Vel09]   I Velicogna. "Increasing Rates of Ice Mass Loss from the Greenland and Antarctic Ice Sheets Revealed by GRACE". In: *Geophysical Research Letters* (2009).

[VW05]   Isabella Velicogna and John Wahr. "Greenland mass balance from GRACE". In: *Geophysical Research Letters* 32.18 (2005). DOI: 10.1029/2005GL023955.

[VW06]   Isabella Velicogna and John Wahr. "Measurements of Time-Variable Gravity Show Mass Loss in Antarctica". In: *Science* 311.5768 (2006), pp. 1754–1756. ISSN: 0036-8075. DOI: 10.1126/science.1123785.

[Wa17]   Gudrun Wanner and Nikolaos Karnesis and. "Preliminary results on the suppression of sensing cross-talk in LISA Pathfinder". In: *Journal of Physics: Conference Series* 840 (May 2017), p. 012043. DOI: 10.1088/1742-6596/840/1/012043.

[Wah65]   Grace Wahba. "A Least Squares Estimate of Satellite Attitude". In: *SIAM Review* 7.3 (1965), pp. 409–409. DOI: 10.1137/1007077.

[Wan+10]   F Wang et al. "Determination of Center-of-Mass of Gravity Recovery and Climate Experiment Satellite". In: *Journal of Spacecraft and Rockets* 47.2 (2010). DOI: 10.2514/1.46086.

[Wan+12]   Lei Wang et al. "Coseismic and postseismic deformation of the 2011 Tohoku-Oki earthquake constrained by GRACE gravimetry". In: *Geophysical Research Letters* 39.7 (2012). DOI: 10.1029/2012GL051104.

[Wan00]   F Wang. *GRACE CG Offset Determination by Magnetic Torquers During the in-flight Phase*. Tech. rep. NASA Jet Propulsion Laboratory, 2000.

[Wan03]   F Wang. "Study on Center of Mass Calibration and K-Band Ranging System Calibration of the GRACE Mission". PhD thesis. The University of Texas at Austin, 2003.

[War+14]   R L Ward et al. "The Design and Construction of a Prototype Lateral-transfer Retro-reflector for Inter-satellite Laser Ranging". In: *Class. Quantum Grav.* (2014).

[Weg+20a]   H Wegener et al. *Coupling of Pointing Angles and Angular Rates in the GRACE Follow-On Laser Ranging Interferometer*. Oct. 26, 2020. URL: https://doi.org/10.5194/gstm2020-46.

[Weg+20b]   H Wegener et al. "Tilt-to-Length Coupling in the GRACE Follow-On Laser Ranging Interferometer". In: *Journal of Spacecraft and Rockets* 57.6 (2020), pp. 1362–1372. DOI: 10.2514/1.A34790.

[Weg19]   H Wegener. "Towards a Tilt-to-Length Coupling Calibration on the GRACE Follow-On Laser Ranging Instrument". In: *SPIE Proceedings of the International Conference on Space Optics – ICSO 2018* 11180 (2019). DOI: 10.1117/12.2536070.

[Wen+19]   Y W Wen et al. *Gravity Recovery and Climate Experiment Follow-On (GRACE-FO) Level-1 Data Product User Handbook*. Tech. rep. JPL D-56935 (URS270772). NASA Jet Propulsion Laboratory, California Institute of Technology, May 2019.

[Wer78]   J R Wertz. *Spacecraft Attitude Determination and Control*. Kluwer Academic Publishers, 1978.

[WGM19]   Bert Wouters, Alex S. Gardner, and Geir Moholdt. "Global Glacier Mass Loss During the GRACE Satellite Mission (2002-2016)". In: *Frontiers in Earth Science* 7 (2019), p. 96. ISSN: 2296-6463. DOI: 10.3389/feart.2019.00096.

[WNL12]   D. N. Wiese, R. S. Nerem, and F. G. Lemoine. "Design considerations for a dedicated gravity recovery satellite mission consisting of two pairs of satellites". In: *Journal of Geodesy* 86.2 (Feb. 2012), pp. 81–98. ISSN: 1432-1394. DOI: 10.1007/s00190-011-0493-8.

[Woe21]   Florian Woeske. "Gravity Field Recovery from GRACE Satellite Data and Investigation of Sensor, Environment and Processing-Option Influences by Closed Loop Mission Simulation". PhD thesis. Universität Bremen, 2021.

[Wol69]   Milo Wolff. "Direct measurements of the Earth's gravitational potential using a satellite pair". In: *Journal of Geophysical Research (1896-1977)* 74.22 (1969), pp. 5295–5300. DOI: https://doi.org/10.1029/JB074i022p05295.

[Wou+14] B Wouters et al. "GRACE, time-varying gravity, Earth system dynamics and climate change". In: *Reports on Progress in Physics* 77.11 (2014), p. 116801. DOI: 10.1088/0034-4885/77/11/116801.

[Yan+21] Yihao Yan et al. "Revisiting the light time correction in gravimetric missions like GRACE and GRACE follow-on". In: *Journal of Geodesy* 95.5 (Apr. 2021), p. 48. ISSN: 1432-1394. DOI: 10.1007/s00190-021-01498-5.

[Yan+22] Fan Yang et al. "Attitude Determination for GRACE-FO: Reprocessing the Level-1A SC and IMU Data". In: *Remote Sensing* 14.126 (2022). ISSN: 2072-4292. DOI: 10.3390/rs14010126.

[Yan12]   Y. Yang. "Spacecraft attitude determination and control: Quaternion based method". In: *Annual Reviews in Control* 36.2 (2012), pp. 198–219. ISSN: 1367-5788. DOI: https://doi.org/10.1016/j.arcontrol.2012.09.003.

[YBM08]   X Yun, E R Bachmann, and R B Mcghee. "Quaternion-Based Algorithm for Orientation Estimation from Earth Gravity and Magnetic Field Measurements". In: *IEEE Transactions on Instrumentation on Measures* 57 (2008), pp. 638–650.

Acknowledgements

There is grandeur in this view of life, with its several powers, having been originally breathed into a few forms or into one; and that, whilst this planet has gone cycling on according to the fixed law of gravity, from so simple a beginning endless forms most beautiful and most wonderful have been, and are being, evolved.

– Charles Darwin, On the Origin of Species

PERSONAL DETAILS

Full Name	Henry Paul Wegener
Current Address	Laportestraße 24 A, 30449 Hannover, Germany
Date of Birth	4 November 1987
Place of Birth	Langenhagen, Germany

EDUCATION AND EMPLOYMENT

21 March 2022	PhD Thesis Defense
	Thesis Title: „Analysis of Tilt-to-Length Coupling in the GRACE Follow-On Laser Ranging Interferometer"
Since 02/2015	Research Scientist and PhD Student at Albert Einstein Institute, Hannover, Germany
10/2011 to 07/2012	Study abroad, Erasmus Program University of Bristol, UK
July 2014 04/2011 to 07/2014	Master of Science passed, mark 1,6 Master of Science Mathematics (major), Economics (minor) Gottfried Wilhelm Leibniz Universität Hannover
April 2011 10/2007 to 03/2011	Bachelor of Science passed, mark 1,9 Bachelor of Science Mathematics (major), Economics (minor) Gottfried Wilhelm Leibniz Universität Hannover
June 2007 2000-2007	'Abitur' passed, mark 1,9 Leibniz Gymnasium Hannover

Publications

Peer-reviewed publications

M. Misfeldt et al., "Scale Factor Determination for the GRACE-Follow On Laser Ranging Interferometer" (paper in preparation)

H. Wegener, V. Müller, G. Heinzel, M. Misfeldt, "Tilt-to-Length Coupling in the GRACE Follow-On Laser Ranging Interferometer". In: Journal of Spacecraft and Rockets 57.6 (2020), pp. 1362–1372. doi: 10.2514/1.A34790.

K. Abich et al., "In-Orbit Performance of the GRACE Follow-On Laser Ranging Interferometer". In: Phys. Rev. Lett. 123.3 (July 2019), p.031101. doi: 10.1103/PhysRevLett.123.031101.

N. Darbeheshti, **H. Wegener**, V. Müller, M. Naeimi, G. Heinzel, M. Hewitson, "Instrument Data Simulations for GRACE Follow-On: Observation and Noise Models". In: Earth System Science Data 9.2 (2017), pp. 833–848. doi: 10.5194/essd-9-833-2017.

Conference proceedings

H. Wegener, "Towards a Tilt-to-Length Coupling Calibration on the GRACE Follow-On Laser Ranging Instrument". In: SPIE Proceedings of the International Conference on Space Optics – ICSO 2018 11180 (2019). doi: 10.1117/12.2536070.

Awards

NASA Group Achievement Award

to

GRACE-FO Laser Ranging Interferometer German Team

„For the German Team's dedication and excellence in developing and successfully deploying the Laser Ranging Interferometer instrument on the GRACE Follow-On mission."